

**Monodisperse Mesoporous Silica**  
**Nanoparticles: Preparation, Characterization**  
**and Application**

**Dissertation**

der Mathematisch-Naturwissenschaftlichen Fakultät

der Eberhard Karls Universität Tübingen

zur Erlangung des Grades eines

Doktors der Naturwissenschaften

(Dr. rer. nat.)

vorgelegt von

M. Sc. Leilei Luo

aus Wuhu, P. R. China

Tübingen

2018

Gedruckt mit Genehmigung der Mathematisch-Naturwissenschaftlichen Fakultät der  
Eberhard Karls Universität Tübingen.

Tag der mündlichen Qualifikation: 25.07.2018

Dekan:

Prof. Dr. Wolfgang Rosenstiel

1. Berichterstatter:

Prof. Dr. Reiner Anwander

2. Berichterstatter:

Prof. Dr. Hermann A. Mayer





---

## Acknowledgement

This PhD thesis has been achieved with the kind help and support from the people who are acknowledged here.

My first gratitude goes to Prof. Dr. Reiner Anwander and Dr. Yucang Liang, who accepted me into the research group. The enlightening guidance and constant encouragement from them throughout these years enabled me to develop my research expertise and to gain scientific experience in material science. Without their profound knowledge and invaluable supervisions, it would have not been impossible to complete this thesis.

The thanks also go to the members from the material science part of the research group. Dr. Ning Yuan, Andrea Sonström, Lorenz Bock, Dr. Yanzhong Zhen and Xin Ning are appreciated for their fruitful discussions about my research. The cooperation with Andrea and Lorenz in the nanoscience lab course gives me fascinating memories.

I am grateful to Elke Nadler for conducting numerous SEM and TEM measurements. The interesting and inspiring chats with her enabled me to gain lots of knowledge about electron microscopy. I thank Egil Severin Erichsen for doing TEM measurements in Bergen. I also would like to thank Wolfgang Bock for conducting the elemental analysis, and Kristina Strohmaier for performing the solid-state NMR measurements. Dr. Cécilia Maichle-Mössmer, Karl-Heinz Ableitner, Tobias Wolf, Heinz-Jürgen Kolb, Sabine Ehrlich and Elke Niquet are appreciated for their works that provided me with a clean, comfortable lab environment.

The kindness and help from the group members supported me in every important stage of my PhD life in Germany. I greatly appreciate all my colleagues of the Anwander group, Dr. Tatiana Spallek, Benjamin Wolf, Verena Birkelbach, Dr. Dorothea Schädle, Jochen Friedrich, Dr. Sonja König, Damir Barisic, Martin Bonath, Uwe Bayer, Dr. Daniel Werner, Dominic Diether, Dr. David Schneider, Christoph Otto Hollfelder, Dr. Nicole Dettenrieder, Christoph Stuhl, Renita Thim, Dr. Lars Jende, Dennis Buschmann, Alexandros Mortis and Simon Trzmiel.

I appreciate the University of Tübingen for providing me with the scholarship and my cooperative partners from the EXPAND program, Carla Lorenz, Leyla Guluzada and Elisabeth Früh for their collaboration.

I wish to thank my Chinese friends, Dr. Xi Chen, Dr. Yuan Fang, Xinyao Liu, Feiyang Li, Dr. Huiying Wang and Juncheng Yang, who are together with me in every funny moment.

I would like to express my great thanks to my family, especially, my wife Xiaohan Wang who moved to Germany to support my studies and encouraged me all the time. I am deeply grateful for your contribution to our small family.



---

# Contents

<b>Acknowledgement</b> .....	<b>i</b>
<b>Contents</b> .....	<b>iii</b>
<b>Abbreviations</b> .....	<b>vii</b>
<b>Summary</b> .....	<b>xi</b>
<b>Zusammenfassung</b> .....	<b>xv</b>
<b>1 Introduction</b> .....	<b>1</b>
1.1 Mesoporous Silica Nanospheres (MSNSs).....	3
1.1.1 Modified Stöber Method.....	3
1.1.2 MSNSs Prepared by Controlling the Reaction Kinetics.....	6
1.1.3 MSNSs Prepared by Other Methods.....	12
1.2 Mesoporous Silica Nanorods (MSNRs) and Nanofibers (MSNFs).....	13
1.3 Hollow Mesoporous Silica Nanoparticles (HMSNs).....	15
1.3.1 Soft Template Method.....	15
1.3.2 Hard Template Method.....	18
1.3.3 Self-templating Method.....	19
1.3.4 HMSNs Prepared by Other Methods.....	20
1.4 Core-Shell Structured Mesoporous Silica Nanoparticles (CSMSNs).....	21
1.4.1 CSMSNs with a Metal Nanoparticle as the Core.....	21
1.4.2 CSMSNs with a Magnetic Nanoparticle as the Core.....	24
1.4.3 CSMSNs with a Porous Nanoparticle as the Core.....	26
1.5 Yolk-Shell Structured Mesoporous Silica Nanoparticles (YSMSNs).....	27
1.5.1 Bottom-up Method Based on Soft Template Assembly.....	27
1.5.2 Selective Etching Method.....	28
1.6 Mesoporous Organosilica Nanoparticles (MONs).....	29
1.7 Mesoporous Organosilica Nanorods (MONRs) and Nanofibers (MONFs).....	31
1.8 Hollow Mesoporous Organosilica Nanoparticles (HMONs).....	33
1.8.1 Soft Template Method.....	33
1.8.2 Hard Template Method.....	34
1.9 Core-Shell Structured Mesoporous Organosilica Nanoparticles (CSMONs).....	35
1.10 Yolk-Shell Structured Mesoporous Organosilica Nanoparticles (YSMONs).....	37
1.11 Applications.....	40

---

1.11.1 Adsorption .....	40
1.11.2 Biomedical Applications .....	41
1.11.3 Catalysis .....	44
1.11.4 Formation of Colloidal Crystals .....	46
1.12 References .....	47
<b>2 Monodisperse Mesoporous Silica Nanoparticles of Distinct Topology .....</b>	<b>55</b>
2.1 Introduction .....	55
2.2 Experimental Section .....	56
2.2.1 Synthesis of Monodisperse and Uniform Cubic Mesoporous Silica Nanoparticles (CMSN-n).....	56
2.2.2 Characterization.....	57
2.3 Results and Discussion.....	57
2.3.1 Effect of Ethanol.....	57
2.3.2 Effect of CTAB .....	63
2.3.3 Formation of Surfactant-Silicate Frameworks .....	68
2.3.4 Mesophase Formation and Morphology Evolution.....	70
2.3.5 <sup>29</sup> Si CP MAS NMR Spectroscopy for HMSN-n, H/CMSN-n, CMSN-n and C/LMSN-n.....	75
2.4 Conclusions .....	77
2.5 References .....	78
<b>3 Hierarchical Mesoporous Organosilica/Silica Core-Shell Nanoparticles Capable of Controlled Fungicide Release .....</b>	<b>81</b>
3.1 Introduction .....	81
3.2 Experimental Section .....	82
3.2.1 Chemicals .....	82
3.2.2 Synthesis of HSMSCSNs .....	82
3.2.3 Adsorption and Controlled Release of Propiconazole.....	83
3.2.4 Characterization.....	83
3.3 Results and Discussion.....	83
3.3.1 Synthesis and Characterization of HSMSCSNs with Ethylene-Bridged PMO Core and MS Shell .....	83
3.3.2 Control of Shell Thickness, Core Size and Pore Diameter .....	91
3.3.3 Control of Composition and Topology: Methylene-Bridged HSMSCSNs .....	95
3.3.4 Formation Mechanism of Materials HSMSCSN .....	97
3.3.5 Adsorption and Controlled Release of Propiconazole on Material HSMSCSN ....	99



---

3.4 Conclusions .....	103
3.5 References .....	104
<b>4 Ultrafast Myoglobin Adsorption into Double-Shelled Hollow Mesoporous Silica Nanospheres .....</b>	<b>107</b>
4.1 Introduction .....	107
4.2 Experimental Section .....	108
4.2.1 Chemicals .....	108
4.2.2 Synthesis of $s\text{SiO}_2$ .....	108
4.2.3 Synthesis of HS-DS-HMSN .....	108
4.2.4 Characterization.....	109
4.2.5 Myoglobin (Mb) Adsorption .....	109
4.3 Results and Discussion.....	109
4.3.1 Synthesis and Characterization of HS-DS-HMSN .....	109
4.3.2 Formation Mechanism of HS-DS-HMSN .....	112
4.3.3 Control of HS-DS-HMSN Structural Properties .....	119
4.3.4 Myoglobin Adsorption onto HS-DS-HMSN.....	120
4.4 Conclusions .....	123
4.5 References .....	123
<b>5 Gold-loaded Mesoporous Organosilica-Silica Core-Shell Nanoparticles as Catalytic Nanoreactors .....</b>	<b>127</b>
5.1 Introduction .....	127
5.2 Experimental Section .....	128
5.2.1 Chemicals .....	128
5.2.2 Synthesis of Thiol Group-Functionalized Mesoporous Organosilica Nanoparticles (SH-MON).....	128
5.2.3 Synthesis of Core-Shell-Structured SH-MON@MS Nanoparticles.....	129
5.2.4 Synthesis of Au-loaded SH-MON@MS .....	129
5.2.5 Catalytic Reduction of 4-Nitrophenol .....	129
5.2.6 Catalytic Aerobic Oxidation of Benzyl Alcohol .....	130
5.2.7 Characterization .....	130
5.3 Results and Discussion.....	130
5.4 Conclusions .....	139
5.5 References .....	140

<b>6 Appendix</b> .....	<b>143</b>
6.1 Publications .....	143
6.2 Presentations.....	143
6.3 Curriculum Vitae.....	145

## Abbreviations

APTES	(3-aminopropyl)triethoxysilane
B50-6600	(PEO) <sub>39</sub> (PBO) <sub>47</sub> (PEO) <sub>39</sub>
BET	Brunauer-Emmett-Teller
BJH	Barret-Joyner-Haldenda
Brij-56	polyoxyethylene (10) cetyether
Brij-58	polyoxyethylene (20) cetyether
BTEE	bis(triethoxysilyl)ethane
BTEM	bis(triethoxysilyl)methane
BTME	bis(trimethoxysilyl)ethane
C/LMSN	mixed cubic/lamellar mesoporous silica nanoparticle
C <sub>10</sub> TMAB	decyltrimethylammonium bromide
CMC	critical micelle concentration
CMSN	cubic mesoporous silica nanoparticle
C <sub>n</sub> TMAX	alkyltrimethylammonium halide
CSMON	core-shell structured mesoporous organosilica nanoparticle
CSMSN	core-shell structured mesoporous silica nanoparticle
CSN	core-shell nanoparticles
CTA <sup>+</sup>	cetyltrimethylammonium cation
CTAB	cetyltrimethylammonium bromide
CTAC	cetyltrimethylammonium chloride
Cyt C	cytochrome c
DDA	dodecylamine
DLS	Dynamic Light Scattering
DMHA	<i>N,N</i> -dimethylhexadecylamine
DMOA	<i>N,N</i> -dimethyloctylamine
DOX	doxorubicin
DRIFT	Diffuse Reflectance Infrared Fourier Transform
ED	Electron Diffraction
EG	ethylene glycol
EISA	evaporation induced self-assembly
EtOH	ethanol
F108	(PEO) <sub>128</sub> (PPO) <sub>54</sub> (PEO) <sub>128</sub>
F127	(PEO) <sub>100</sub> (PPO) <sub>65</sub> (PEO) <sub>100</sub>
F68	(PEO) <sub>76</sub> (PPO) <sub>29</sub> (PEO) <sub>76</sub>
FC-4	C <sub>3</sub> F <sub>7</sub> O(CFCF <sub>3</sub> CF <sub>2</sub> O) <sub>2</sub> CFCF <sub>3</sub> CONH-(CH <sub>3</sub> )N <sup>+</sup> (C <sub>2</sub> H <sub>5</sub> ) <sub>2</sub> CH <sub>3</sub> I
FC-4911	CF <sub>3</sub> (CF <sub>2</sub> ) <sub>3</sub> SO <sub>2</sub> NH(CH <sub>2</sub> ) <sub>3</sub> N <sup>+</sup> (CH <sub>3</sub> ) <sub>3</sub> I

FDU	Fudan University
FFT	fast Fourier transform
GSH	glutathione
H/CMSN	mixed hexagonal/cubic mesoporous silica nanoparticle
HIFU	high intensity focused ultrasound
HKUST	Hong Kong University of Science and Technology
HMON	hollow mesoporous organosilica nanoparticle
HMSN	hollow mesoporous silica nanoparticle
HRTEM	High Resolution Transmission Electron Microscopy
HS-DS-HMSN	hierarchically structured double-shelled hollow mesoporous silica nanosphere
HSMSCSN	hierarchically structured mesoporous silica core-shell nanoparticle
HSSMS	hollow silica sphere with mesostructured shell
IBN	Institute of Bioengineering and Nanotechnology
IgG	immunoglobulin G
KIT	Korea Advanced Institute of Science and Technology
Mb	myoglobin
MCM	Mobile Composition of Matter
MeOH	methanol
MOF	metal-organic framework
MON	mesoporous organosilica nanoparticle
MONF	mesoporous organosilica nanofiber
MONR	mesoporous organosilica nanorod
MPTMS	(3-mercaptopropyl)trimethoxysilane
<i>m</i> SiO <sub>2</sub>	mesoporous silica
MSN	mesoporous silica nanoparticle
MSNF	mesoporous silica nanofiber
MSNR	mesoporous silica nanorod
MSNS	mesoporous silica nanosphere
nm	nanometer
P123	(PEO) <sub>20</sub> (PPO) <sub>70</sub> (PEO) <sub>20</sub>
P65	(PEO) <sub>19</sub> (PPO) <sub>29</sub> (PEO) <sub>19</sub>
P85	(PEO) <sub>25</sub> (PPO) <sub>40</sub> (PEO) <sub>25</sub>
PEG	poly(ethylene glycol)
PFOA	perfluorooctanoic acid
pK <sub>a</sub>	logarithmic acid dissociation constant
PMMA	polymethyl methacrylate
PMO	periodic mesoporous organosilica
PMS	periodic mesoporous silica

---

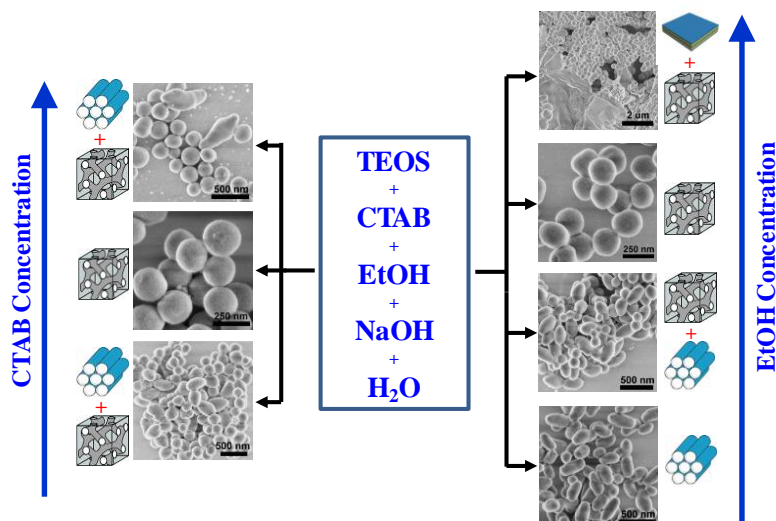
PMSN	periodic mesoporous silica nanoparticles
PNIPAM	poly( <i>N</i> -isopropyl acrylamide)
PS	polystyrene
PS- <i>b</i> -PAA	polystyrene- <i>b</i> -poly(acrylic acid)
PS- <i>co</i> -P4VP	polystyrene- <i>co</i> -poly(4-vinylpyridine)
PVP	poly(vinylpyrrolidone)
PXRD	powder X-ray diffraction
RF	resorcinol-formaldehyde
RhB	rhodamine B
rpm	rotations per minute
SBA	Santa Barbara amorphous
SDA	structure-directing agent
SDBS	dodecylbenzene sulfonate
SDS	sodium dodecylsulfate
SEM	Scanning Electron Microscopy
Si(OR) <sub>4</sub>	tetraalkoxysilane
<i>s</i> SiO <sub>2</sub>	solid silica
TBOS	tetrabutoxysilane
TEA	triethanolamine
TEM	Transmission Electron Microscopy
TEOS	tetraethyl orthosilicate
TIPB	triisopropylbenzene
TMB	1,3,5-trimethylbenzene
TMOS	tetramethyl orthosilicate
TMP	2,2,4-trimethylpentane
TPOS	tetrapropoxysilane
TTAB	tetradecyltrimethylammonium bromide
UCNP	upconversion nanoparticle
UiO	Universitetet i Oslo
YSMON	yolk-shell structured mesoporous organosilica nanoparticle
YSMSN	yolk-shell structured mesoporous silica nanoparticle
ZIF	zeolitic imidazolate framework
β-Gal	β-galactosidase
μm	micrometer



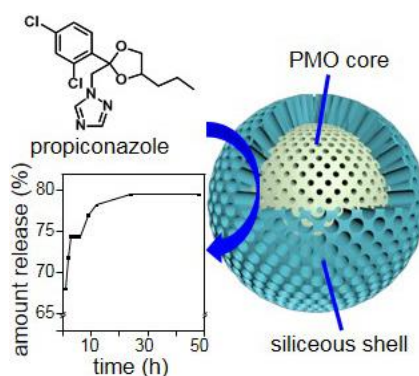
## Summary

As one of the most attractive materials in the past decades, mesoporous silica has proven a vast amount of applications in catalysis, separation, adsorption, biomedicine, photonics etc. Morphology and size greatly affect the properties and functions of mesoporous silica. Mesoporous silica nanoparticles (MSNs) with the size of several hundred nanometers provide enhanced pore accessibility, faster molecular diffusion, better dispersibility in aqueous and organic solvents and highly improved biocompatibility compared to their bulky counterparts. This thesis focuses on developing new synthesis methods for the preparation of MSNs with well controllable morphology, particle size, uniformity and dispersity. Four types of MSNs with various pore symmetries and diverse nanostructures were successfully synthesized. Furthermore, the applications of the obtained MSNs in the adsorption of biomolecules, controlled release of fungicides and catalysis are also demonstrated. Hence this thesis comprises an introduction about the research background of the present topic and four main research work sections described as follows.

In the first part, monodisperse and uniform MCM-48-type cubic mesoporous silica nanoparticles (CMSNs) were readily prepared by simply optimizing the molar ratio of ethanol and surfactant in the system TEOS-CTAB-NaOH-H<sub>2</sub>O-EtOH. In the absence of ethanol only hexagonal mesoporous silica with ellipsoidal and spherical morphology was obtained. The presence of ethanol drives a mesophase transformation from hexagonal to mixed hexagonal/cubic, further to purely cubic, and finally to a mixed cubic/lamellar. This is accompanied by a morphology evolution involving a mixture of ellipses/spheres, regular rods, uniform spheres, and finally a mixture of spheres/flakes. Moreover, the quality of the CMSNs could also be controlled by changing the surfactant concentration or adjusting the stirring rate. All MSNs were characterized using PXRD, TEM, SEM, and N<sub>2</sub> physisorption. The monodispersity of the CMSNs was verified by the statistical particle size distribution from SEM/TEM images and dynamic light scattering (DLS). The mesophase transformation can be rationalized on the basis of an ethanol-driven change of the surfactant packing structure and charge matching at the surfactant/silicate interface. The corresponding morphology evolution can be elucidated by an ethanol-controlled hydrolysis rate of TEOS and degree of condensation of oligomeric silicate species via a nucleation and growth process.



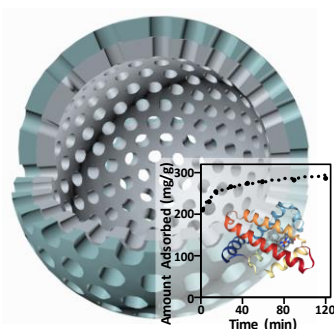
In the second part, a new class of hierarchically structured mesoporous silica core-shell nanoparticles (HSMSCSNs) with a periodic mesoporous organosilica (PMO) core and a mesoporous silica (MS) shell was prepared. The applied one-pot two-step strategy allows for a rational control over the core/shell chemical composition, topology and pore/particle size, simply by adjusting the reaction conditions in the presence of CTAB as a structure-directing agent (SDA) under basic conditions. The spherical ethylene- or methylene-bridged PMO cores feature hexagonal ( $p6mm$ ) or cage-like cubic symmetry ( $Pm-3n$ ) depending on the organosilica precursor. The hexagonal MS shell was obtained by an *n*-hexane-induced controlled hydrolysis of TEOS followed by a directional co-assembly/condensation process of silicate/CTAB composites at the PMO cores. The HSMSCSN feature a hierarchical pore structure with pore diameters in the range of ca. 2.7 nm and 5.6 nm in the core and shell domains, respectively. The core sizes and shell thicknesses are adjustable in the range of 90-275 nm and 15-50 nm, respectively. The adsorption and controlled release of fungicide propiconazole on the HSMSCSN revealed a three-stage release profile.



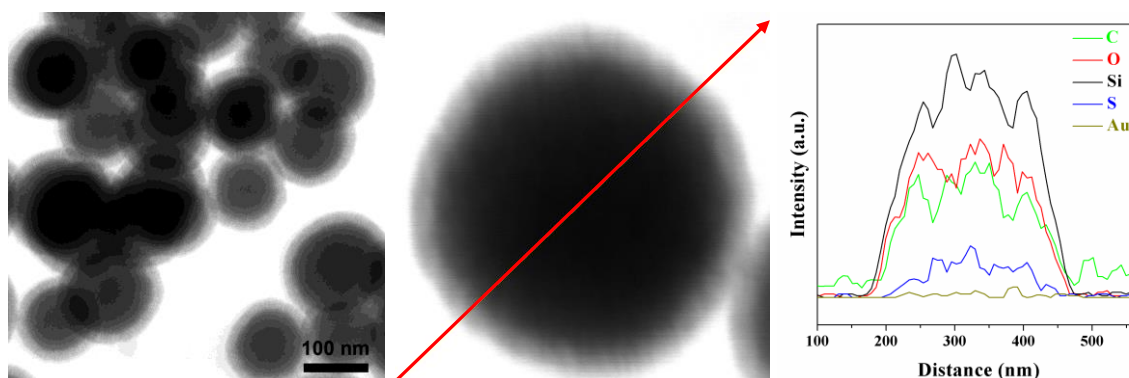
In the third part, a facile preparation approach was developed to synthesize hierarchically structured double-shelled hollow mesoporous silica nanospheres (HS-DS-HMSN). The HS-DS-HMSN-type materials obtained show high monodispersibility in aqueous solution, uniform



particle size, perpendicularly aligned mesochannels, adjacent double-shelled structures with hierarchically adjustable pore sizes and high surface area as well as large pore volume. On the basis of structure and morphology evolutions as well as unambiguous experimental data, a mechanism for the formation of such HS-DS-HMSN-type materials is proposed. The proposed mechanism features the dissolution of solid silica spheres under basic conditions and a co-surfactant-expanded micelle-assisted self-assembly process via a heterogeneous nucleation deposition. The syntheses of a series of HS-DS-HMSN-type materials with controlled structure properties on particle size and inner/outer shell thickness as well as pore size have verified the practicability and effectiveness of this facile preparation approach. Due to the structure advantages, the HS-DS-HMSN-type materials show an unusual ultrafast adsorption of myoglobin with a high adsorption amount.



In the fourth part, hierarchically structured core-shell nanoparticles consisting of thiol group-functionalized mesoporous organosilica as the core and mesoporous silica as the shell (SH-MON@MS) were synthesized. The distinct composition between the core and shell enables a specific loading of Au nanoparticles in the core domain by the interaction of thiol groups with Au(III) ions from  $\text{HAuCl}_4$ . The resultant material Au/SH-MON@MS possesses a hierarchical pore structures with 1.4 nm core pore size and 5.0 nm shell pore size. The large pore size in the shell facilitates the easy access and diffusion of reactant and product, and the mesoporous organosilica core provides a hydrophobic microenvironment. Due to the superior structure properties, the Au/SH-MON@MS material exhibits excellent catalytic performance in the reduction of 4-nitrophenol to 4-aminophenol and the aerobic oxidation of benzyl alcohol to benzaldehyde.





## Zusammenfassung

Als eines der interessantesten Materialien der letzten Jahrzehnte hat sich mesoporöses Siliciumdioxid in einer Vielzahl von Anwendungen bewährt. Sei es in der Katalyse, in der Trennung, in der Biomedizin oder in der Photonik, die Liste der Beispiele für den Einsatz von mesoporösem Siliciumdioxid ist lang. Die Eigenschaften sowie Funktionen von mesoporösem Siliciumdioxid werden vor allem durch seine Morphologie und Größe beeinflusst. Mesopörses Siliciumdioxidnanopartikeln (MSNs) mit einer Größe von einigen hundert Nanometern bieten eine schnellere molekulare Diffusion, eine bessere Dispergierbarkeit in wässrigen und organischen Lösemitteln sowie eine stark verbesserte Biokompatibilität im Vergleich zu ihren sperrigen Gegenstücken. Der Schwerpunkt dieser Arbeit liegt insbesondere in der Entwicklung neuer Syntheseverfahren von MSNs mit gut kontrollierbarer Morphologie, Partikelgröße, Gleichmäßigkeit und Dispersität. Es ist gelungen, vier Arten von MSNs mit verschiedenen Porensymmetrien und unterschiedlichen Nanostrukturen zu synthetisieren. Darüberhinaus wurden die Anwendungen der erhaltenen MSNs bei der Adsorption von Biomolekülen, der kontrollierten Freisetzung von Fungiziden und der Katalyse demonstriert. Somit umfasst diese Arbeit eine Einführung in den Forschungshintergrund des vorliegenden Themas und vier Hauptforschungsbereiche, die im Folgenden beschrieben werden.

Im ersten Teil dieser Arbeit wurden monodisperse und einheitliche kubische mesoporöse Siliciumdioxidnanopartikeln (CMSNs) vom MCM-48-Typ durch Optimierung des Molverhältnisses von Ethanol und Tensid im System TEOS-CTAB-NaOH-H<sub>2</sub>O-EtOH hergestellt. In Abwesenheit von Ethanol wurde nur hexagonales mesoporöses Siliciumdioxid mit ellipsoider und sphärischer Morphologie erhalten. Die Anwesenheit von Ethanol führte zu einer Mesophasenumwandlung von Hexagonal zu gemischt Hexagonal/Kubisch, weiter zu rein Kubisch und schließlich zu gemischt Kubisch/Lamellar. Diese Transformation wurde von einer Morphologieentwicklung begleitet, die eine Mischung aus Ellipsen/Kugeln, regelmäßigen Stäbchen, gleichförmigen Kugeln und schließlich einer Mischung von Kugeln/Flocken beinhaltet. Zudem konnte die Qualität der CMSNs auch durch Veränderung der Tensidkonzentration oder der Rührgeschwindigkeit kontrolliert werden. Alle MSNs wurden unter Verwendung von PXRD-, TEM-, SEM-, und N<sub>2</sub>-Physisorption charakterisiert. Die Monodispersität der CMSNs wurde durch statische Partikelgrößenverteilung aus SEM/TEM-Bildern und dynamischer Lichtstreuung (DLS) verifiziert. Die Mesophasenumwandlung kann auf der Basis einer ethanolgetriebenen Änderung der Tensidpackungsstruktur und der Ladungsanpassung an der Grenzfläche zwischen Tensid und Silikat erklärt werden. Die entsprechende Morphologieentwicklung kann durch eine ethanolgesteuerte hydrolysegeschwindigkeit von TEOS und den Kondensationsgrad von oligomeren Silicatspezies über einen Keimbildungs- und Wachstumsprozess aufgeklärt werden.

Im zweiten Teil dieser Arbeit wurde eine neue Klasse hierarchisch strukturierter mesoporöser Siliciumdioxid-Kern-Schale-Nanopartikel (HSMSCSNs) mit einem periodischen mesoporösen Organosiliciumkern (PMO) und einer Schale aus mesoporösem Siliziumdioxid (MS) hergestellt. Die angewandte Eintopf-Zwei-Schritt-Strategie ermöglicht eine rationale Kontrolle über die chemische Zusammensetzung von Kern/Schale, Topologie und Poren/Partikelgröße, welches durch Anpassung der Reaktionsbedingungen in Gegenwart von CTAB als strukturdirigierendes Agens (SDA) unter basischen Bedingungen realisiert wurde. Die kugelförmigen Ethylen- oder Methylen-verbrückten PMO-Kerne weisen abhängig vom Organosilikapräkursor eine hexagonale ( $p6mm$ ) oder käfigartige kubische Symmetrie ( $Pm-3n$ ) auf. Die hexagonale MS-Schale wurde durch eine  $n$ -Hexan induzierte Hydrolyse von TEOS erhalten, gefolgt von einem gerichteten Co-Assembly/Kondensationsprozess von Silikat/CTAB-Verbunde an den PMO-Kernen. Die HSMSCSN weisen eine hierarchische Porenstruktur mit Porendurchmessern im Bereich von ca. 2,7 nm und 5,6 nm in der Kern- bzw. Schalebereich. Die Kerngrößen und Schalendicken sind im Bereich von 90-275 nm bzw 15-50 nm einstellbar. Die Adsorption und kontrollierte Freisetzung vom Fungizid Propiconazol auf dem HSMSCSN ergab ein dreistufiges Freisetzungsprofil.

Im dritten Teil dieser Arbeit wurde ein einfacher Ansatz zur Synthese hierarchisch strukturierter doppelschaliger hohler mesoporöser Siliziumdioxidnanokugeln (HS-DS-HMSN) entwickelt. Die erhaltenen HS-DS-HMSN-artigen Materialien zeigen in wässriger Lösung eine hohe Monodispersibilität, einheitliche Partikelgröße, senkrecht ausgerichtete Mesokanäle, benachbarte Doppelschalenstrukturen mit hierarchisch einstellbaren Porengrößen und großer Oberfläche sowie großes Porenvolumen. Auf der Basis von Struktur- und Morphologieentwicklungen sowie eindeutigen experimentellen Daten wird ein Mechanismus zur Bildung solcher HS-DS-HMSN-artiger Materialien vorgeschlagen. Der vorgeschlagene Mechanismus beinhaltet die Auflösung von festen Siliziumdioxidkugeln unter basischen Bedingungen und einem durch Co-Tensid erweiterten Mizellen-unterstützten Self-Assembly-Prozess. Dieser wiederum wird über eine heterogene Keimbildung ausgelöst. Die Synthese von einer Reihe solcher HS-DS-HMSN-artigen Materialien mit kontrollierten Struktureigenschaften bezüglich der Partikelgröße, der Dicke der inneren/äußeren Schale und der Porengröße haben die Praktikabilität und Wirksamkeit dieses Ansatzes der einfachen Herstellung bestätigt. Aufgrund der Strukturvorteile zeigen die HS-DS-HMSN-Materialien eine ungewöhnliche ultraschnelle Adsorption von Myoglobin mit einer hohen Adsorptionsmenge.

Im vierten Teil dieser Arbeit wurden hierarchisch strukturierte Kern-Schale-Nanopartikel synthetisiert, die aus mesoporösen Organosilika mit Thiolgruppen als Kern und mesoporösem Siliziumdioxid als Schale bestehen (SH-MON@MS). Die ausgeprägte Zusammensetzung zwischen Kern und Schale ermöglicht eine spezifische Beladung von Au-Nanopartikeln in der Kerndomäne durch die Wechselwirkung von Thiolgruppen mit Au(III)-Ionen aus  $\text{HAuCl}_4$ . Das resultierende Material Au/SH-MON@MS besitzt eine hierarchische Porenstruktur mit einer

Kernporengröße von 1,4 nm und einer Porengröße von 5,0 nm. Die große Porengröße in der Schale erleichtert den Zugang und die Diffusion von Reaktant und Produkt, und der mesoporöse Organosilikakern liefert eine hydrophobe Mikroumgebung. Aufgrund der überlegenen Struktureigenschaften zeigt das Au/S<sub>H</sub>-MON@MS-Material eine ausgezeichnete katalytische Leistung bei der Reduktion von 4-Nitrophenol zu 4-Aminophenol und die aerobe Oxidation von Benzylalkohol zu Benzaldehyd.



# 1 Introduction

New technology based on nanoscale machines and devices is envisioned as the dominant tool to solve the problems in energy, environment and diseases etc.<sup>1</sup> Key to the realization of this nanotechnology will rely on efficient methods that convert the organizing building-blocks (molecules, molecular clusters, polymers) into precise and predesigned nanostructures. Nature has shown us examples of intricately organized architectures, such as the marine organisms diatoms and radiolarian, which are preserved in silica or calcium carbonate. These natural microstructures are often formed by biomineralization,<sup>2</sup> a template-assisted self-assembly process, in which the pre-organized organic composites regulate the nucleation, growth and morphology of inorganic materials. To date, various synthesis pathways used as mimics for biomineralization have been widely explored to prepare patterned materials.<sup>3,4</sup> Among them, zeolites prepared using alkylammonium salts as structure-directing agents (SDA) have microporous crystalline network structures with pore diameters less than 2 nm. This small pore size greatly limits the growing demand for applications such as adsorption of large molecules. In 1992, Mobil scientists used long-chain ammonium cationic surfactants as templates to synthesize mesoporous aluminosilicates with long-range ordered pore arrays and narrow pore size distribution.<sup>5,6</sup> These materials are often called M41S family that includes the one-dimensional (1D) hexagonal channel-like MCM-41 with  $p6mm$  symmetry, the three-dimensional (3D) cubic MCM-48 consisting of two interpenetrating continuous networks of chiral channels with  $Ia-3d$  symmetry, and the lamellar MCM-50. This new kind of material extended the range of pore diameter from microporous (< 2 nm) to mesoporous (2 ~ 50 nm). The open frameworks and tunable porosities endow mesoporous materials with accessibility to ions, molecules and even larger guest species.<sup>7</sup> Therefore, mesoporous materials exhibit a broad potential for applications in catalysis, sensors, electronics, biology, nanodevices, separation etc. In 1999, a class of novel mesoporous silica, denoted as Periodic Mesoporous Organosilica (PMO), which integrates organic functional groups into the framework structures, has been reported.<sup>8-12</sup> Compared with periodic mesoporous silica (PMS), the organic functional groups in PMOs are uniformly distributed in the framework at the molecular level. The featured organic moieties in the framework enable PMOs to have virtually unlimited applications based on the reactivities of the organic functional groups, modulation of hydrophilicity/hydrophobicity of the pore and the crystal-like features.<sup>12,13</sup>

Although much efforts have been devoted to fabricating new mesoporous materials, characterizing the mesostructures, understanding the mechanism of formation, synthesizing new mesoporous materials and applying mesoporous silicas,<sup>7,14-17</sup> tailoring the particle size of PMSs and PMOs to nanoscale, the preparation of nanostructured morphology- and particle-size-controlled monodisperse PMSs and PMOs is much more challenging and has been less studied.<sup>12,18-20</sup> Mesoporous silica nanoparticles (MSNs) and mesoporous organosilica

nanoparticles (MONs) provide even more pore accessibility, faster molecular diffusion, higher dispersibility in aqueous and organic solvents and improved biocompatibility than their bulk counterparts, and therefore greatly promote the application potentials. The term MSNs was popularized by Victor Lin to represent mesoporous silica nanospheres.<sup>21</sup> Furthermore, MSNs and MONs with particle sizes less than 500 nm can be easily taken up by the cell through endocytosis,<sup>22</sup> thus providing desired biocompatible delivery platforms for a broad range of applications in therapeutics, pharmaceuticals and diagnosis.<sup>23,24</sup> Lots of approaches have been used to synthesize MSNs with various morphologies, dimensions, pore sizes, and pore structures. Unger and co-workers were the first ones to prepare sphere-like MSNs using the modified Stöber method.<sup>25</sup> Mann and co-workers prepared MSNs with the size of several tens of nanometers by suppressing the particle growth through acid quenching.<sup>26</sup> Cui and co-workers as well as Ostafin and co-workers reported the preparation of MSNs in a low concentration of surfactant.<sup>27,28</sup> Since then, various MSNs have been extensively prepared.<sup>29-31</sup> Although the synthesis of MONs is quite similar to that of MSNs, namely based on sol-gel chemistry via the self-assembly of hydrolyzed/condensed bissilylated organosilane precursor in the presence of SDA, the organic fragments within the bissilylated organosilane precursors usually show unfavorable impact on the self-assembly of hydrolyzed/condensed organosilane precursors with SDA.<sup>20</sup> Therefore, any rational controls over the mesoporous structure and morphology are relatively difficult to achieve compared with the synthesis of MSNs.

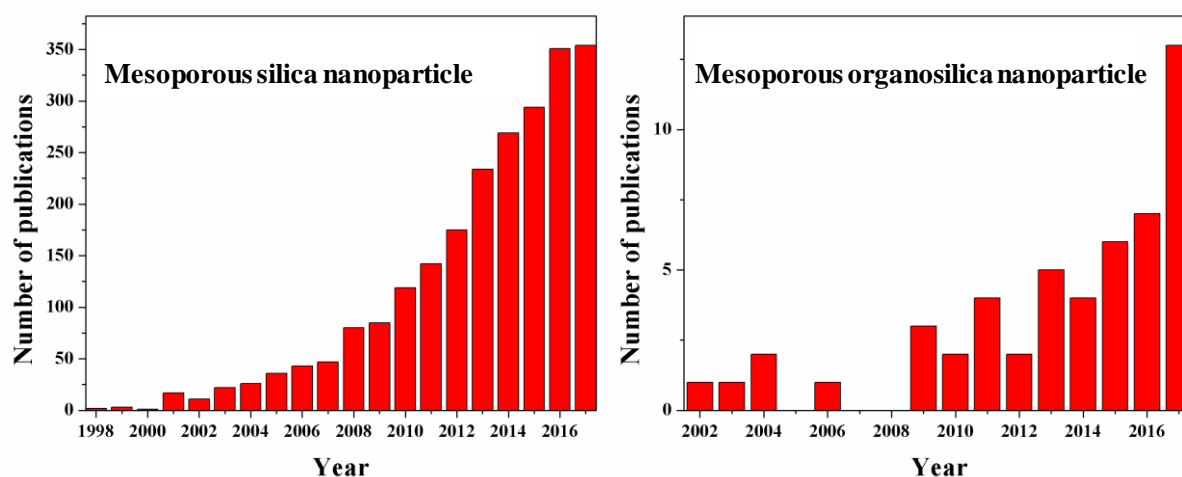


**Figure 1.1** Time-evolution of the scientific interests in MSNs and MONs as illustrated by the number of publications in each year. Data included only for complete years, hence not covering 2018. These data are based on the publications recorded in ISI Web of knowledge which contain the key words listed in the images.

The advances in synthesizing MSNs and MONs over the last years have been tremendous (Figure 1.1). This is due to the development and improvement of the synthesis methods and their potential advantages in various applications. There are several reviews focusing on the syntheses and applications of MSNs and MONs.<sup>12,18-20,22,24,29-31</sup> In this introduction section, main synthesis pathways for the fabrication of MSNs and MONs will be dominantly reviewed,



and the types of MSNs and MONs will be classified by their morphology and characteristic nanostructure. In addition, the applications of MSNs and MONs in adsorption, catalysis, biomedicine and the formation of colloidal crystals are also briefly addressed.

## 1.1 Mesoporous Silica Nanospheres (MSNSs)

### 1.1.1 Modified Stöber Method

In 1968, Stöber and co-workers first reported the synthesis of monodisperse solid silica ( $s\text{SiO}_2$ ) spheres by means of hydrolysis of alkoxy silanes and subsequent condensation of silicic acid in a mixture of alcohol, ammonia and water.<sup>32</sup> Following this seminal work, this method was widely applied for the preparation of monodisperse nanoparticles, and is commonly called Stöber method. When cationic surfactants like cetyltrimethylammonium bromide (CTAB) or cetyltrimethylammonium chloride (CTAC) are added into the preparation solution via a Stöber method, MSNSs with hexagonal pore structure were formed.<sup>25</sup> This process is called modified Stöber method and has been used as a most efficient method for the preparation of MSNSs. In general, MSNSs synthesized by a modified Stöber method tend to form particle sizes larger than 30 nm. The resultant nanospheres exhibit a large amount of silanol groups that impart a good dispersity in aqueous solution due to their high surface charge. Particle characteristics like size, morphology and composition can be easily controlled by changing synthesis conditions.

During the preparation of MSNSs by the modified Stöber method, the use of alcohol played a dual role as co-solvent and inhibitor, enabling the reaction to take place in a homogeneous environment and ensure the formation spherical MSNs.<sup>33</sup> Jacobs and co-workers used high-resolution transmission electron microscope (HRTEM) and electron diffraction (ED) to investigate the pore structure of MSNSs prepared by the modified Stöber method, indicating radially distributed pore arrays and an observable hexagonal pore structure in the middle of the nanoparticle. This implied that the growth of the MSNSs in the modified Stöber method started with the formation of a hexagonal core and subsequent radial growth to form the final particles.<sup>34</sup> Similar results have also been reported by other researchers.<sup>27,28</sup> These investigations revealed that the morphology and mesostructure of MSNSs were markedly influenced by chemical composition of the gel such as ethanol, base and surfactant. Based on the observations, the basic process was proposed as follows: i) the formation of MSNSs started with the formation of primary particles generated by the self-assembly of silicate species with surfactant micelles; ii) the silicate-surfactant composites then deposited on the surface of the primary particles along the packing pathway depended on the synthesis condition to form the MSNSs with various mesostructures and morphologies. From then on, the modified Stöber method was widely applied to the preparation of various MSNSs. Mou and co-workers synthesized fluorescent MSNSs with an average particle size of 110 nm by co-condensation of tetraethyl orthosilicate (TEOS) and fluorescent alkoxy silane in a mixed solution of ethanol, water and ammonia.<sup>35</sup> Yano and co-workers prepared monodisperse MSNSs with radially

distributed pore structure and adjustable particle size ranging from 520 to 1250 nm in a tetramethoxysilane (TMOS)-NaOH-H<sub>2</sub>O-MeOH-C<sub>10</sub>TMAB system.<sup>36,37</sup> Small primary particles were reported to be formed by the self-assembly of silicate oligomer and surfactants, while the residual silica precursors reacted preferentially with the surface silanols on these existing particles as the core to afford monodisperse MSNSs.<sup>38</sup> This formation process prevented the generation of new particles and ensured the monodispersity of the final nanoparticles. By precisely adjusting the pH (11.52 ~ 10.68) of the reaction solutions, MSNSs with tunable size (280 ~ 30 nm) and ordered hexagonal mesostructure were obtained (Figure 1.2).<sup>39</sup> When ethylene glycol (EG) replaced ethyl alcohol according to the modified Stöber method for the preparation of amino-functionalized MSNSs via the co-condensation strategy,<sup>40</sup> the resultant MSNSs showed a hexagonal pore structure and various particle sizes ranging from 70 to 110 nm. Carboxylic-functionalized MSNSs were synthesized through the one-pot method by adding carboxyethylsilanetriol sodium as both carboxylic group source and base.<sup>41</sup> The batch-addition of TEOS was beneficial for the formation of uniform carboxylic-functionalized

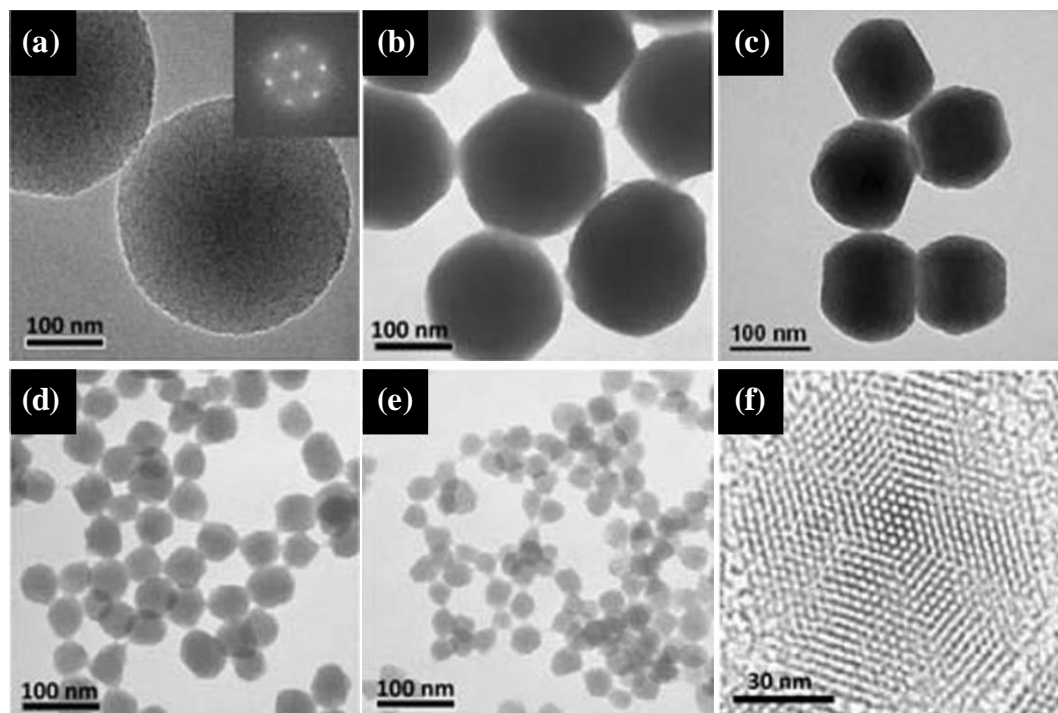


**Figure 1.2** Transmission Electron Microscopy (TEM) images of MSNSs synthesized at different pH values with average particle size of (a) 280 nm, the inset is the corresponding fast Fourier transform (FFT) diffractogram, (b) 170 nm, (c) 110 nm, (d) 50 nm, (e) 30 nm, and (f) high-resolution TEM image of a single particle in (c), reproduced from reference 39.

MSNSs due to the separated nucleation and growth processes. The particle size of carboxylic-functionalized MSNSs could be controlled from 140 to 60 nm by changing the amount of water in the reaction mixture. By replacing alcohol with *n*-hexane as the solvent in the modified Stöber method, large pore MSNSs with nanocube morphology and *Pm-3n* pore symmetry were obtained (Figure 1.3).<sup>42</sup> Moreover, mesoporous silicas with distinct morphology (truncated

nanocubes, core-shell microspheres and twisted nanorods) and different mesostructures were obtained by changing the amounts of ammonia solution and *n*-hexane in the reaction system via a nonpolar solvent-assisted modified Stöber method.

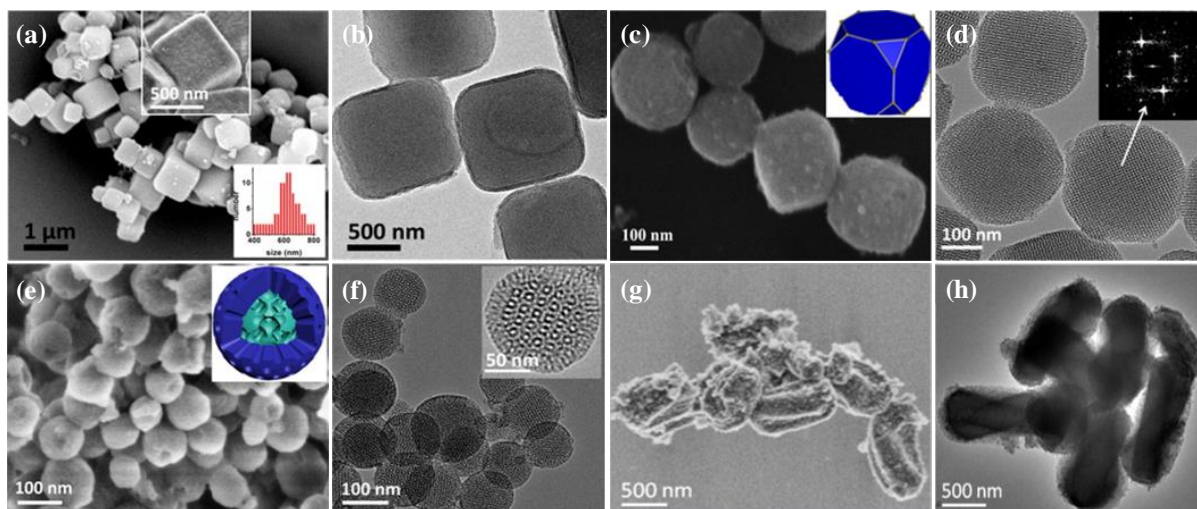


**Figure 1.3** Scanning Electron Microscopy (SEM) and TEM images of (a, b) mesoporous silica nanocubes, (c, d) truncated mesoporous silica nanocubes, (e, f) core-shell structured mesoporous silica microspheres, and (g, h) twisted mesoporous silica nanorods synthesized with different amounts of ammonia solution and *n*-hexane, reproduced from reference 42.

Compared to 1D channel-like MSNSs with hexagonal mesopore structure, 3D mesoporous silicas have the advantage in mass diffusion and transport because of their interconnecting networks. These 3D mesoporous silicas include cubic MCM-48 (*Ia-3d*),<sup>43</sup> cubic SBA-1 (*Pm-3n*),<sup>44</sup> hexagonal SBA-2<sup>45</sup> and SBA-12 (*P6<sub>3</sub>/mmc*),<sup>46</sup> cubic SBA-16<sup>47</sup> and FDU-1 (*Im-3m*),<sup>48</sup> and cubic KIT-5 (*Fm-3m*)<sup>49</sup>. In these 3D mesoporous silicas, MCM-48 displays a 3D channel-like pore structure, others adopt a cage-like mesopore structure. Also, cubic *Ia-3d* MSNs are expected to form via the simple and convenient modified Stöber method. Unger and co-workers first used the modified Stöber method to synthesize MCM-48 nanospheres.<sup>50</sup> Compared with MCM-41 nanospheres synthesized by the same method,<sup>25</sup> high concentrations of base and surfactant were beneficial for the formation of the cubic *Ia-3d* pore structure. This novel method could also produce metal (aluminum, vanadium and titanium)-substituted MCM-48 nanospheres.<sup>51</sup> MCM-48 nanoparticles with irregular morphology could also be obtained by adjusting the amount of ethanol in the reaction solution.<sup>52</sup> The successful formation of MCM-48 nanoparticles was attributed to the co-surfactant behavior of ethanol, which could penetrate into the surfactant micelles and thereby induced phase transformation. By optimizing the synthesis parameters, uniform spherical MCM-48 nanoparticles could be prepared in very short time (30 min).<sup>53</sup> Although this method could provide access to ordered cubic MCM-48 nanoparticles, the nanoparticle aggregation was often observed and the particle sizes were not really uniform. Lin and co-workers improved this strategy and used poly(ethylene oxide)-*b*-poly(propylene oxide)-*b*-poly(ethylene oxide) (PEO-PPO-PEO) triblock copolymer F127

((PEO)<sub>100</sub>(PPO)<sub>65</sub>(PEO)<sub>100</sub>) as an agent to promote the formation of monodisperse spherical MCM-48 nanoparticles in a diluted solution.<sup>54</sup> The average size of cubic MSNSs could be controlled over the range of 70-500 nm by changing the amount of F127 in the reaction solution. Moreover, the type of silica precursor and solvent had remarkable effects on the mesostructure of MSNSs.<sup>55</sup> Monodisperse MSNSs with various pore structures were prepared by adjusting the weight ratio of water/methanol/ethanol. With the gradual increase of the amount of ethanol, the pore structure of MSNSs changed from hexagonal to mixed hexagonal/cubic symmetry, with the *Ia-3d* pore structure was observed in the center of the particle while the hexagonal pore structure formed near the surface. MSNSs with overall cubic *Ia-3d* mesostructure were obtained using tetrakis(3-hydroxypropyl)orthosilicate as the precursor under high concentration of ethanol.<sup>55</sup>

### 1.1.2 MSNSs Prepared by Controlling the Reaction Kinetics

Both the hydrolysis rate of silane and condensation of the siloxane bond depend strongly on the synthesis parameters, such as type of silane precursor, pH value, temperature, solvent etc.<sup>56</sup> Therefore, it is possible to control the hydrolysis and condensation kinetics for adjusting the nucleation and growth of MSNSs. Another effective method to obtain monodisperse MSNSs is to add capping agents into the synthesis solution. The capping agent molecules are adsorbed on the surface of the nanoparticle and stabilize the particle as a colloid.

Mann and co-workers first synthesized MSNSs in diluted reaction mixtures.<sup>26</sup> The particle aggregation was reduced by using a large amount of water to quench the reaction which was then neutralized with 2 M HCl, overall changing the nucleation condition and promoting burst nucleation during the dilution process. The resultant particle size of MSNSs could be controlled in the range of 23-100 nm. Similarly, MSNSs with the average particle size of 30, 50 and 70 nm were also conveniently synthesized from a highly diluted aqueous solution of NaOH-Na<sub>2</sub>SiO<sub>3</sub>-H<sub>2</sub>SO<sub>4</sub>(CH<sub>3</sub>CH<sub>2</sub>COOH)-C<sub>n</sub>TMAX (alkyltrimethylammonium halide, n = 14-18; X = Br or Cl) with a pH value of 5.5, 7.0 and 9.0, respectively.<sup>57</sup> By quickly changing the pH value of the reaction solution, MSNSs with 20-50 nm in diameter were synthesized with the assistance of F127 as a particle growth inhibitor.<sup>58</sup> This synthesis process involved the prehydrolysis of TEOS under acidic conditions and subsequent addition of ammonia solution. The slow silicate condensation rate and weak interaction between silicate species and surfactant provided an appropriate condition for the formation of silicate-surfactant composites. The subsequent addition of ammonia solution induced a fast condensation rate and rapid nucleation. Meanwhile, the presence of F127 micelles covered the nanoparticles, suppressing the grain growth and stabilizing the ordered mesostructures.<sup>58</sup> Moreover, TEOS was added into a CTAB aqueous solution acidified with nitric acid to form an aqueous solution containing silicate species.<sup>59</sup> This solution was then poured into a large amount of buffer solution (NaOH-CH<sub>3</sub>CO<sub>2</sub>Na) or ammonium solution to form MSNs with different morphologies and sizes under various acidic or basic conditions.<sup>59</sup> The alterations of morphology and pore structure were

attributed to the different interactions between hydrolyzed silicate species and surfactant under various acidic or basic conditions.

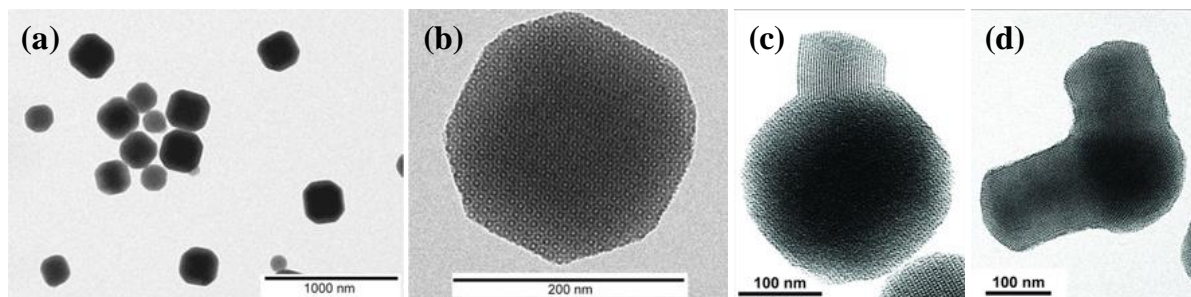


**Figure 1.4** TEM images of (a, b) octahedrally truncated amino-functionalized MSNs, reproduced from reference 60; (c) multicompartiment MSNs consisting of a core of cube-like mesoporous silica and a branch of hexagonal mesoporous silica, and (d) two hexagonal mesoporous silica branches emanated from the core, reproduced from reference 62.

Highly aminated MSNs with cubic  $Pm-3n$  pore symmetry were synthesized via the co-condensation of TEOS and (3-aminopropyl)triethoxysilane (APTES) under basic conditions.<sup>60</sup> The nanoparticles showed truncated-octahedral shape with an average particle size of 220 nm and pore size of 2.7 nm (Figure 1.4a, b). By adding a pore expander molecule (1,3,5-trimethylbenzene (TMB)), the pore size could be enlarged to 5.3 nm while the average particle size decreased to 110 nm. Moreover, it was found that the mesostructure and the morphology of the nanoparticles depended on the amount of APTES used.<sup>61</sup> Oval-like elongated nanoparticles with hexagonal  $p6mm$  pore structure were obtained in the APTES molar ratio of 0-49 (with respect to total silane used). Truncated-octahedral nanoparticles with cubic  $Pm-3n$  pore symmetry were obtained with 54-65 mol% APTES, these nanoparticles formed by the aggregation of small silicate-surfactant micelle clusters and grew into the final shape by the anisotropic addition of the residual clusters. When the reaction system contained 69 mol% APTES, the resultant nanoparticles showed irregular morphology and a disordered pore structure. It was noted that when an appropriate amount of ethyl acetate was added into this reaction system the multicompartimental MSNs with hexagonal  $p6mm$  branches on the cubic  $Pm-3n$  core were obtained (Figure 1.4c, d).<sup>62</sup> Hydrolysis of ethyl acetate produced acetic acid decreasing the pH value of the solution, thus influencing the state of amino group of APTES. This synthesis condition favored the formation of MSNs with  $Pm-3n$  pore symmetry. Along with the hydrolysis of ethyl acetate, the pH value decreased below the  $pK_a$  of APTES, thus the predominant state of the amino group was positively charged, repelling the charged head groups of the CTAB cation. The change in the charge state of APTES might induce a structural change in the CTAB micelle. This process was associated with the hydrolysis and condensation of TEOS and APTES, resulting in the formation of hexagonal MSNs as the branches in the facets of (111) of preformed truncated nanoparticles.

Owing to the size effect of macromolecules, monodisperse MSNs with large pore size are a desirable carrier for the separation and transport of biomacromolecules, such as proteins or

DNA. Hence some chemical agents are often used as expanders to enlarge the pore size of MSNSs. Shi and co-workers used *N,N*-dimethylhexadecylamine (DMHA) as pore size mediator to obtain MSNSs with a pore size of 4.6 nm and particle size of 110-130 nm.<sup>63</sup> The pore enlargement mainly relied on how many DMHA molecules self-assembled into an inverted cylindrical micelle inside the cationic surfactants micelle. The presence of F127 as the particle growth inhibitor in this synthesis system was beneficial for the formation of MSNSs with small particle size (down to 80 nm).

Weakly basic conditions (pH 7-11) during the synthesis of MSNSs can effectively control the hydrolysis and condensation rate of silica precursors in a favorable manner, making it possible to prepare stable colloidal solutions of MSNSs at a high concentration. Such weak base, such as triethanolamine (TEA),<sup>64</sup> and lysine,<sup>65</sup> tends to attach on the surface of nanoparticles, thus limiting growth and preventing from aggregation. Bein and co-workers used the weak base triethanolamine (TEA) to replace the commonly used base NaOH or ammonia solution for preparing MSNSs.<sup>64</sup> Due to the weakly basic characteristic and the buffering capability of TEA, the preparation solution had a relatively low pH value of about 11 during the reaction. Moreover, TEA could also act as a complexing agent for silica species. These factors induced slow hydrolysis and condensation rates of TEOS in the concentrated reaction solutions. As a result, size-controlled MSNSs were obtained in the range of 50-100 nm. Various organic groups (vinyl, benzyl, phenyl, cyano, mercapto, amino) functionalized MSNSs with a particle size range of 40-150 nm were readily prepared through the co-condensation strategy using the same preparation method.<sup>66,67</sup> Furthermore, MSNSs were also synthesized in the buffer solution in the pH range of 6.0-10.0, and the particle size was influenced by the degree of acidity and basicity.<sup>68</sup> The hydrolysis and condensation rates of silica precursors are generally affected by pH value and reaction temperature. Under an identical condition, decrease of the pH value from 10.0 to 6.0 led to an increase of the size of MSNSs obtained from 30 to 85 nm. This cause was probably attributed to the decreased silicate condensation rate. Except for the preparation of MSNSs under acidic or basic condition, MSNSs were also synthesized under neutral conditions.<sup>69</sup> The size of the resultant MSNSs was affected by reaction temperature, surfactant concentration, and addition of co-surfactant as well as of multistep silica precursor. By adjusting the synthesis parameters monodisperse MSNSs with a size ranging from 42 to 617 nm could be readily obtained. In addition, arginine and lysine were also used as the base catalysts for the preparation of MSNSs.<sup>70</sup> The weakly basic reaction condition (pH = 9.7) led to the slow hydrolysis of TEOS but fast condensation of silicate species, while the size of the obtained MSNSs could be controlled in the range of 15-200 nm. When weakly basic sodium acetate was used as a catalyst for the formation of MSNSs, uniform MSNSs were obtained, the particle size of which could be adjusted within the range of 50 to 100 nm by increasing the reaction temperature from 40 to 80 °C.<sup>71</sup>

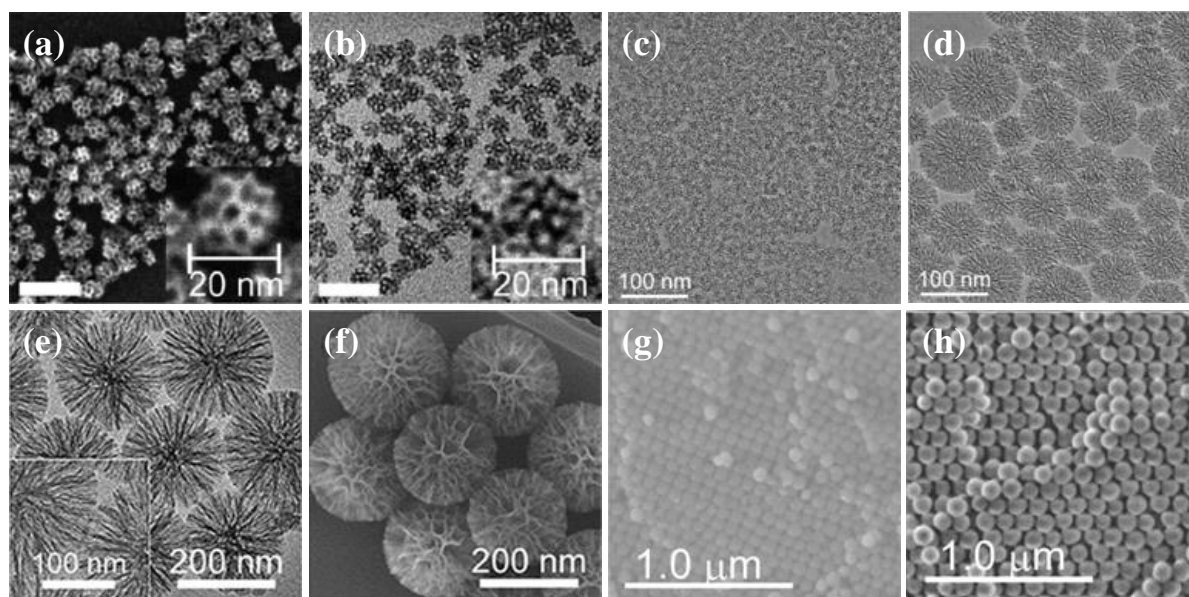


**Figure 1.5** (a) SEM and (b) TEM images of colloidal MSNSs (scale bar: 50 nm), the insets are the HRTEM images, reproduced from reference 72; (c) TEM image of colloidal MSNSs with average size of 20 nm synthesized using TMOS as silica precursor, (d) TEM image of colloidal MSNSs with average size of 30 nm using tetrabutoxysilane (TBOS) as silica precursor, reproduced from reference 73; (e) TEM image and (f) SEM image of colloidal MSNSs using tetrapropoxysilane (TPOS) as silica precursor and TMB as a pore expander, reproduced from reference 76; colloidal crystals composed of (g) 82 nm, and (h) 108 nm MSNSs, respectively, reproduced from reference 77.

Note that the colloidal MSNSs were successfully synthesized under weakly basic conditions (Figure 1.5).<sup>72-77</sup> Stable colloidal MSNSs less than 20 nm in diameter were prepared in a TMOS-TEA-CTAB-H<sub>2</sub>O system and the surfactant was readily removed by dialysis (Figure 1.5a, b).<sup>72</sup> Such small colloidal MSNSs showed a high stability due to the use of TMOS and a weakly basic reaction system as well as a high ratio of CTAB/Si. The formation of such small MSNSs was caused by the fast hydrolysis rates of TMOS, the corresponding rapid nucleation and grain growth reactions, and weaker basic conditions. Moreover, the relatively high surfactant/Si molar ratio (0.5) was found to afford good dispersion of MSNSs due to the protective interaction of surfactant on the surface of colloidal MSNSs. If different tetraalkoxysilanes (Si(OR)<sub>4</sub>, R = Me, Et, Pr and Bu) were used as the silica precursor, different hydrolysis rates led to the formation of MSNSs with 20-80 nm in diameter (Figure 1.5c, d).<sup>73</sup> In general, nucleation and particle growth were markedly influenced by the hydrolysis rate of the silica precursor, and the corresponding particle size increased with the gradually decreasing hydrolysis rate. In addition, the size of MSNSs could be further controlled by adding alcohols into the synthesis solution. Much larger MSNSs were prepared by adding alcohols with different alkyl chains to slow down the hydrolysis rate of tetraalkoxysilanes.<sup>74</sup> MSNSs with size as large as 700 nm were obtained by using tetrabutoxysilane as a silica precursor in the presence of butanol. The hydrolysis and the subsequent formation rates of silicate species were the slowest in this case, which contributed to the preferential particle growth of MSNSs rather

than the nucleation. The effects of surfactant/Si molar ratio on the mesostructure, the particle size and the dispersity of as-synthesized MSNSs were also systematically investigated.<sup>75</sup> Worm-like pore structure with incomplete passing through the outer surface of the nanoparticle was observed when the surfactant/Si molar ratio was lower than 0.035. The mesostructure extended into the overall nanoparticle when the surfactant/Si molar ratio ranged from 0.043-0.11. In both cases, the surfactant acted as the SDA for the pore formation and the as-synthesized MSNSs were aggregated together to form 100 nm or larger particles. Further increasing the surfactant/Si molar ratio (0.13-0.5) resulted in the formation of monodisperse MSNSs with average particle size of 30 nm. The reduction of particle size was due to the increased nucleation rate at high surfactant/Si molar ratio. In the case of a high surfactant/Si molar ratio, the surfactant not only acted as the SDA for the formation of the mesostructure, but also adsorbed on the surface of MSNSs, enhancing the electrostatic repulsion between nanoparticles and making a stable colloidal solution. The pore/particle size and morphology of MSNSs were also tuned by adding trialkylbenzene as the modifying agent (such as expander).<sup>76</sup> Addition of 1,3,5-triisopropylbenzene (TIPB) and TMB with different molecular size and hydrophobicity to the reaction system gave rise to distinct effects on pore/particle size of the resultant MSNSs. When tetrapropoxysilane (TPOS) and TMB were used in the preparation, MSNSs with uniform particle size, radial aligned mesopores, and large pore size were obtained (Figure 1.5e, f). This method has also been applied for the further growth of size-controlled MSNSs.<sup>77</sup> Monodisperse MSNSs with 40 nm in diameter were prepared and used as the seeds for the growth of larger MSNSs. After 2 and 4 cycles of growth under weakly basic conditions, the size of MSNSs increased to 82 and 108 nm, respectively. Due to the uniform shapes and relatively smooth surfaces, these two kinds of MSNSs could be packed to form colloidal crystals (Figure 1.5g, h).

Ultrasub-10 nm MSNs with single pores were prepared in a TMOS-CTAB-NH<sub>3</sub>-H<sub>2</sub>O system with an initial pH value of 9.2.<sup>78</sup> The successful synthesis of such small MSNSs relied on the fast hydrolysis of silica precursor, slow silica condensation rate of silicate species and termination of particle growth via poly(ethylene glycol) (PEG)-silane to quench the further silicate condensation on the surface of MSNSs. The precise adjustment of the synthesis conditions, such as different base catalysts (L-lysine, and ammonium hydroxide), pH, concentration of TMOS, reaction temperature and appropriate time for adding PEG-silane as an efficient capping agent to terminate particle growth, could effectively control the particle size from 6 nm to 15 nm.<sup>79</sup> Zhang and co-workers first reported the synthesis of monodisperse MSNSs smaller than 130 nm in diameter at the kilogram scale under weakly basic conditions (pH 7-10).<sup>80</sup> Depending on the surfactants and the concentrations of organic amines in the synthesis mixture, MSNSs with different pore sizes (2.3 nm, 10-20 nm) and various mesostructures (stellate, raspberry and worm-like) were obtained. In the same reaction system, the size of stellate MSNSs was tailored by adding ionic liquid as cosurfactant or F127 as



particle growth inhibitor.<sup>81</sup> MSNSs with average particle size in the ranges of 100-300 nm and 40-100 nm were obtained by adjusting the amounts of ionic liquid and F127, respectively.

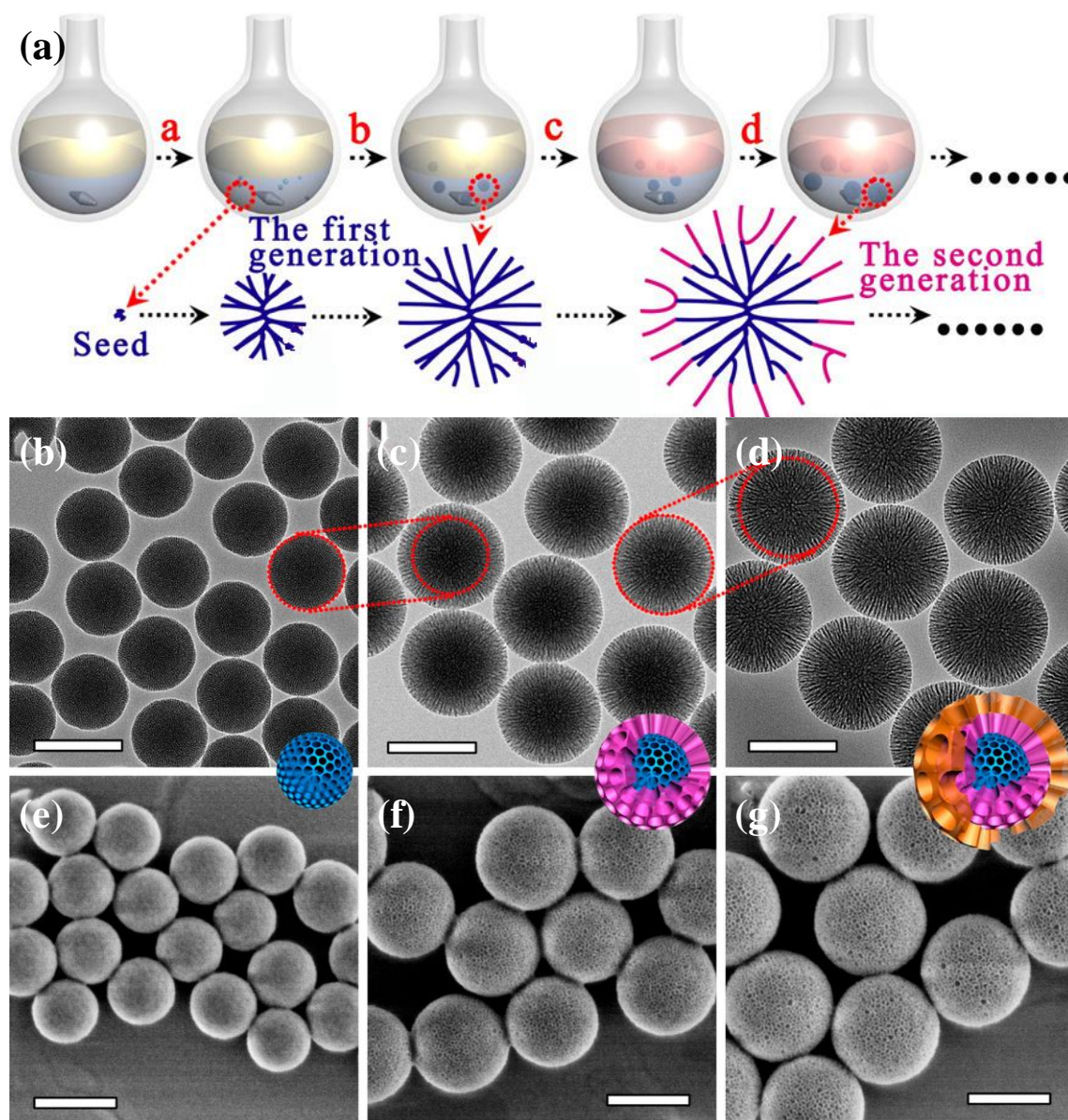


**Figure 1.6** (a) Schematic illustration of the synthesis process for 3D dendritic MSNSs using a biphasic reaction system; TEM and SEM images of 3D dendritic MSNSs after (b,e) one, (c, f) two and (d, g) three generations preparation via the biphasic reaction (scale bar: 200 nm), reproduced from reference 82.

A novel biphasic reaction system was developed by Zhao and co-workers for the preparation of 3D dendritic MSNSs (Figure 1.6).<sup>82,83</sup> The reaction system consisted of an aqueous phase containing CTAC and TEA at the bottom and an oil phase of TEOS dissolved in the organic solvent at the top.<sup>82</sup> The hydrophobic organic solvent not only provided a storage medium for TEOS, but also interacted and assembled with the surfactant molecules at the interface to form expanded micelles, enabling the formation of large pores (pore size of 2.8-13 nm depending on the type of organic solvent used). The size of the MSNSs relied on the reaction time or the amount of TEOS used. The pore size and particle size of MSNSs could also be controlled by

multistep growth (Figure 1.6b-g). By applying this synthesis approach, 3D dendritic MSNSs with particle size of 125 nm and pore size of 6 nm were prepared using cyclohexane as an organic solvent.<sup>83</sup> Amino groups were then anchored onto the mesopore channels by post-grafting in order to homogeneously immobilize Pd nanoparticles with ~1.2 nm in diameter. In addition, core-cone structured monodisperse MSNSs were also synthesized using the biphasic reaction approach, in which TEA and CTAC were dissolved in water and chlorobenzene was used as an organic solvent for TEOS.<sup>84</sup> The primary mesostructured silica nanoparticles first formed in the aqueous phase acted as the core for the subsequent growth of chlorobenzene-expanded lamellar structures. The resultant nanoparticles had an average diameter of 180 nm and shell pore size as large as 45 nm.

### 1.1.3 MSNSs Prepared by Other Methods

Brinker and co-workers used an aerosol-assisted self-assembly process for the synthesis of MSNSs with spherical morphology and various mesostructures (hexagonal, cubic and vesicular).<sup>85</sup> The synthesis was performed in a homogeneous aqueous solution containing TEOS, CTAB, polyoxyethylene (10) cetyether (Brij-56) (or polyoxyethylene (20) cetyether (Brij-58), or triblock polymer Pluronic P123 ((PEO)<sub>20</sub>(PPO)<sub>70</sub>(PEO)<sub>20</sub>), H<sub>2</sub>O, EtOH and HCl with an initial surfactant concentration much lower than the critical micelle concentration (CMC), followed by dispersing this mixed solution in the form of aerosol, heating, drying and collecting. The solvent evaporation induced the micelle formation and successive co-assembly of silica-surfactant micellar species into a liquid-crystalline mesophase. Various metal-silica, dye-silica and polymer-silica nanoparticles could also be prepared using this procedure, through the incorporation of extra metal colloids, dyes and polymer precursors into the initial solutions.

Uniform mesoporous silica particles with a large pore size (8 nm) were prepared through the interface-directed co-assembly approach.<sup>86</sup> Closely packed *s*SiO<sub>2</sub> colloidal crystals fabricated by using monodisperse silica nanospheres via sedimentation were used as the hard template for the formation of 3D macroporous carbon by nanocasting. Macroporous carbons were then soaked into the precursor solution containing TEOS-P123-HCl-EtOH-H<sub>2</sub>O which was used for the fabrication of mesoporous silica. The gradual evaporation of solvent and the hydrolysis of TEOS induced the cooperative assembly of a silicate-micelle composite at the solid-liquid interface, which further nucleated and grew along the macropore carbon wall to form assembled silica-surfactant mesostructured spheres. Due to macropore confinement, the rod-like silicate-micelle composites adapted a curved morphology and assembled into 2D hexagonal mesostructure in the same direction along the macropore walls. Finally, uniform and ordered mesoporous silica spheres with circularly arranged mesopore channels were obtained after the removal of organic composites by calcination at high temperature, while the particle size was controlled by the pore size of the macroporous carbon. Similarly, when F127 instead of P123 was used as a surfactant, cubic mesostructured silica spheres were obtained. If the

amount of precursor or the soaking time was controlled, hemispherical and hollow mesoporous silica particles were prepared. This preparation strategy was also applicable for the formation of core-shell structured MSNSs with magnetic  $\text{Fe}_3\text{O}_4$  core and mesoporous silica shell.

MSNSs with various mesostructures ( $Im-3m$ ,  $Fm-3m$ ,  $p6mm$ , foam-like) were synthesized in a weakly acidic solution of cationic fluorocarbon surfactant (FC-4,  $\text{C}_3\text{F}_7\text{O}(\text{CF}_2\text{CF}_2)_2\text{CF}_2\text{CONH}(\text{CH}_3)\text{N}^+(\text{C}_2\text{H}_5)_2\text{CH}_3\text{I}$ ) and nonionic triblock copolymer surfactant (F127, P65 or P123).<sup>87</sup> In some cases, TMB was also added to adjust the pore size or vary the mesostructure. Due to the hydrophobic and lipophobic nature of FC-4, it was immiscible with the copolymer surfactants and acted as a particle growth inhibitor. The weakly acidic condition promoted the hydrolysis of TEOS and the co-assembly with the copolymer surfactant, which finally resulted in the mesoporous silica nanoparticles with relatively uniform size (50-300 nm), tunable pore size (5-30 nm) and controllable mesostructures.

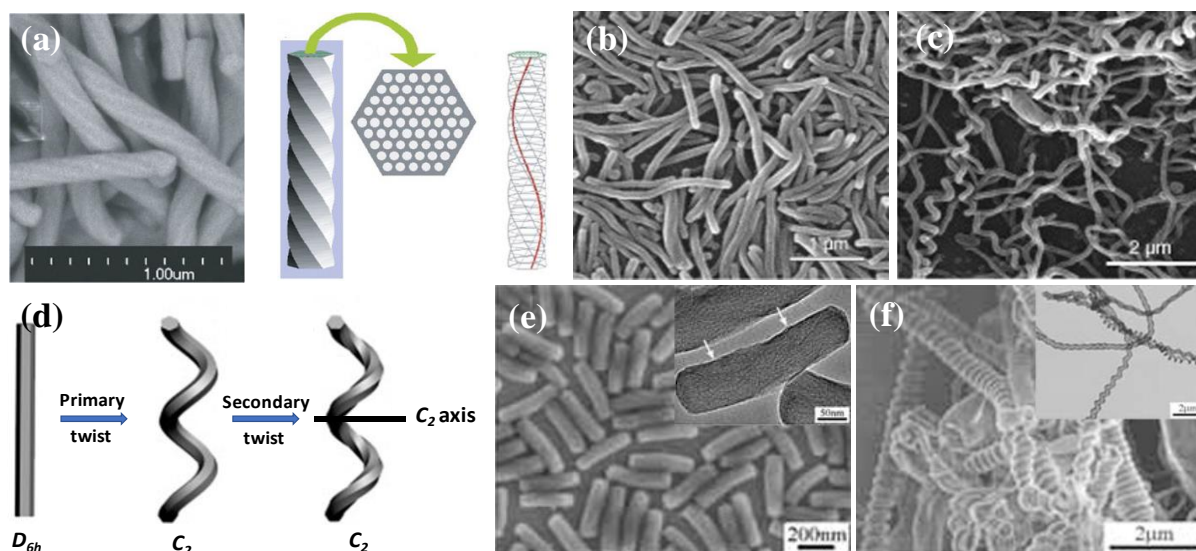


**Figure 1.7** (a) SEM image and schematic drawing of the structural model of chiral MSNRs, reproduced from reference 90; (b) SEM image of chiral MSNFs, reproduced from reference 94; (c) SEM image and (d) schematic illustration of the formation process of dual-axis chiral MSNFs, reproduced from reference 94; (e) SEM image of chiral MSNRs, the inset is HRTEM image, reproduced from reference 96; and (f) SEM image of chiral mesoporous silica nanotubes, the inset is HRTEM image, reproduced from reference 96.

## 1.2 Mesoporous Silica Nanorods (MSNRs) and Nanofibers (MSNFs)

1D MSNRs and MSNFs have great application potentials in electronics, optics, biosensing, etc.<sup>88</sup> MSNRs with hexagonal pore structure were prepared by using P123 as the SDA in the presence of an inorganic salt (KCl).<sup>89</sup> This synthesis approach produced high-yield ( $\approx 100\%$ ) MSNRs with a relatively uniform length (1-2  $\mu\text{m}$ ) and long-range ordered pore structure with  $p6mm$  symmetry as well as high condensation degree. Twisted helical MSNRs and MSNFs with chiral pore structures were often observed. A twisted rod-like hexagonal mesoporous silica showed width of 130-180 nm and length of 1-6  $\mu\text{m}$  (Figure 1.7a).<sup>90</sup> The formation of this twisted morphology is due to the hexagonally ordered chiral channels winding around the

central axis of the nanorod, and the well-ordered mesopore silica structures based on the self-assembly of chiral anionic surfactant and silica precursor (TEOS) by using aminosilane (APTES) as the co-structure-directing agent. The size and shape of the obtained twisted MSNRs as well as the chiral structure and helical pitch length could be controlled by the stirring rate.<sup>91</sup> When the stirring rate increased from 200 to 800 rotations per minute (rpm), the obtained silica particles showed decreased length, increased width and the helical pitch length. However, when the stirring rate was faster than 1200 rpm, a non-helical morphology was observed. In addition, racemic helical MSNRs were produced by using achiral surfactant sodium dodecyl sulfate as the SDA,<sup>92</sup> suggesting that the inherent chirality of the surfactant molecule was not necessary and other driving forces, existing in such reaction system, are a key factor to control the formation of chiral mesostructures. However, the use of a chiral surfactant led to more left-handed nanorods than right-handed ones,<sup>90</sup> indicating that the chiral surfactant might play a pivotal role in the breaking of the racemization of the obtained MSNRs. Yang and co-workers suggested an interfacial interaction mechanism to explain the spontaneous formation of helical MSNRs synthesized in the presence of achiral surfactants.<sup>93</sup> The origin of the chiral mesostructure might be attributed to a morphology transformation from cylindrical to helical induced by the reduction in surface free energy. While the curvature of the helical morphology was limited by the increasing bending energy, the resultant pore structure changed from perfectly hexagonal to helical. Hence, the reduction in surface free energy drove the spontaneous formation of the spiral morphology, and a purely interfacial interaction mechanism was suggested to explain the formation of such helical mesostructures.

Chiral MSNFs have also been synthesized in a  $\text{Na}_2\text{SiO}_3$ -CTAB- $\text{CH}_3\text{CO}_2\text{CH}_2\text{CH}_3$ - $\text{H}_2\text{O}$  system.<sup>94</sup> The twisted morphology around the axis endowed MSNFs with chiral channels (Figure 1.7b). The length and the width of the nanofibers increased with the concentrations of CTAB and silicate, respectively. By decreasing the amount of ethyl acetate, nanofibers twisted in two different axes were obtained, one positioned outside the nanofiber, and the other one in the center of the nanofiber (Figure 1.7c, d). It was proposed that the chirality of MSNFs was attributed to the chiral nuclei in the solution or the chiral silicate- $\text{CTA}^+$  species formed during the self-assembly process. These chiral composites induced the co-assembly of silicate and  $\text{CTA}^+$  into chiral aggregates. In 2007, Han and co-workers reported the synthesis of entropy-driven helical mesostructures using CTAB as the surfactant in a concentrated ammonia solution.<sup>95</sup> The surfactant micelles were believed to take on a helical conformation to maximize the entropy of the system, while the resultant MSNRs possessed twisted morphology and chiral mesoporous channels. In 2010, Ye and co-workers used nonionic triblock copolymer F127 and cationic surfactant CTAB as the SDA to prepare uniform chiral MSNRs with length of 250-380 nm and width of 80-110 nm through the ammonia-catalyzed hydrolysis of TEOS in the presence of F127 and CTAB (Figure 1.7e).<sup>96</sup> The cationic surfactant CTAB contributed to the pore structure of the nanorod, while nonionic surfactant F127 controlled the size and the twisted

morphology. By replacing ammonia with HCl in the same synthesis system, helical mesoporous silica nanotubes with diverse morphologies were obtained (Figure 1.7f).

### 1.3 Hollow Mesoporous Silica Nanoparticles (HMSNs)

Hollow mesoporous silica nanoparticles (HMSNs) have the advantages of both a hollow structure and mesoporous structure.<sup>97</sup> For instance, the large specific surface area from exterior and interior could provide more adsorption or reaction sites for functional substances than that of MSNSs. The relatively large voids also increase the amount of substances encapsulated and protect them from damage or decomposition. The mesopores in the shell are adjustable in terms of pore structure, pore size and composition, which endow HMSNs accessible channels for various substance into the interior space. HMSNs have been synthesized by using various approaches which can be categorized into soft template method, hard template method and self-template method (Figure 1.8).

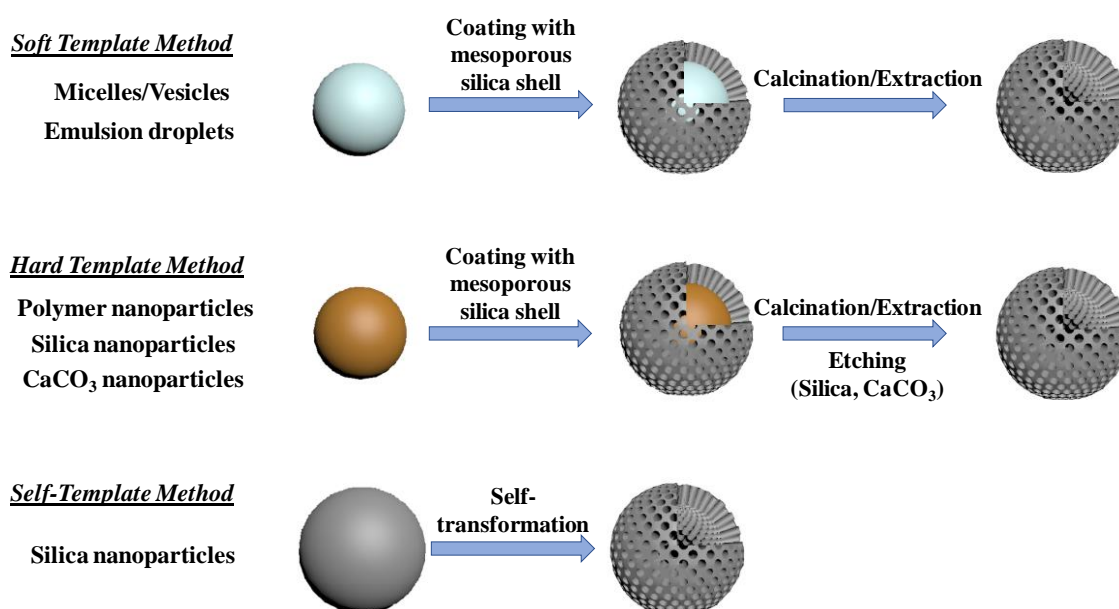


**Figure 1.8** Schematic illustration of the preparation of HMSNs by various methods.

#### 1.3.1 Soft Template Method

Emulsion droplets involving oil-in-water and water-in-oil can be used as the soft templates for the fabrication of HMSNs. For example, Schüth and co-workers used oil (TMB)-in-water emulsions as the template to prepare HMSNs with particle size range of 1-100  $\mu\text{m}$ .<sup>98</sup> The stirring rate was crucial during the formation of the hollow structure. Under slow stirring conditions, mesoporous silica with fiber-like morphology was obtained. High stirring rates created a CTAB-stabilized oil-in-water emulsion and TEOS dissolved and located in the oil droplets. TEOS was subsequently hydrolyzed at the oil-water interface to form silicate species including silicate oligomers. These silicate species further self-assembled with surfactant to form a mesoporous shell at the interfacial area. Mesoporous aluminosilicate hollow spheres

with 3D *Ia-3d* pore structure were synthesized by using oil(TEOS)-in-water emulsion as the template.<sup>99</sup> Note that the hydrolysis temperature of TEOS for this case was a key to control the successful formation of hollow spheres with ordered cubic structures. When the hydrolysis temperature of TEOS was less than 18 °C, the partially hydrolyzed TEOS condensed along the interface of the TEOS droplets and prevented TEOS in the droplet from further hydrolysis. When the temperature was raised during hydrothermal treatment, the gradual diffusion out and hydrolysis of TEOS in the center of the droplets formed the hollow core. When the hydrolysis temperature was higher than 18 °C, complete hydrolysis of TEOS in the droplets led to the formation of solid mesoporous silica nanoparticles without hollow structure. The oil-in-water emulsion of a triblock copolymer F68 (EO<sub>76</sub>PO<sub>29</sub>EO<sub>76</sub>) stabilized TMB droplet in a HCl-acidified aqueous solution was used as the template to prepare well-defined hollow silica spheres with the average size of ~ 1 μm and multilamellar shell structure.<sup>100</sup>

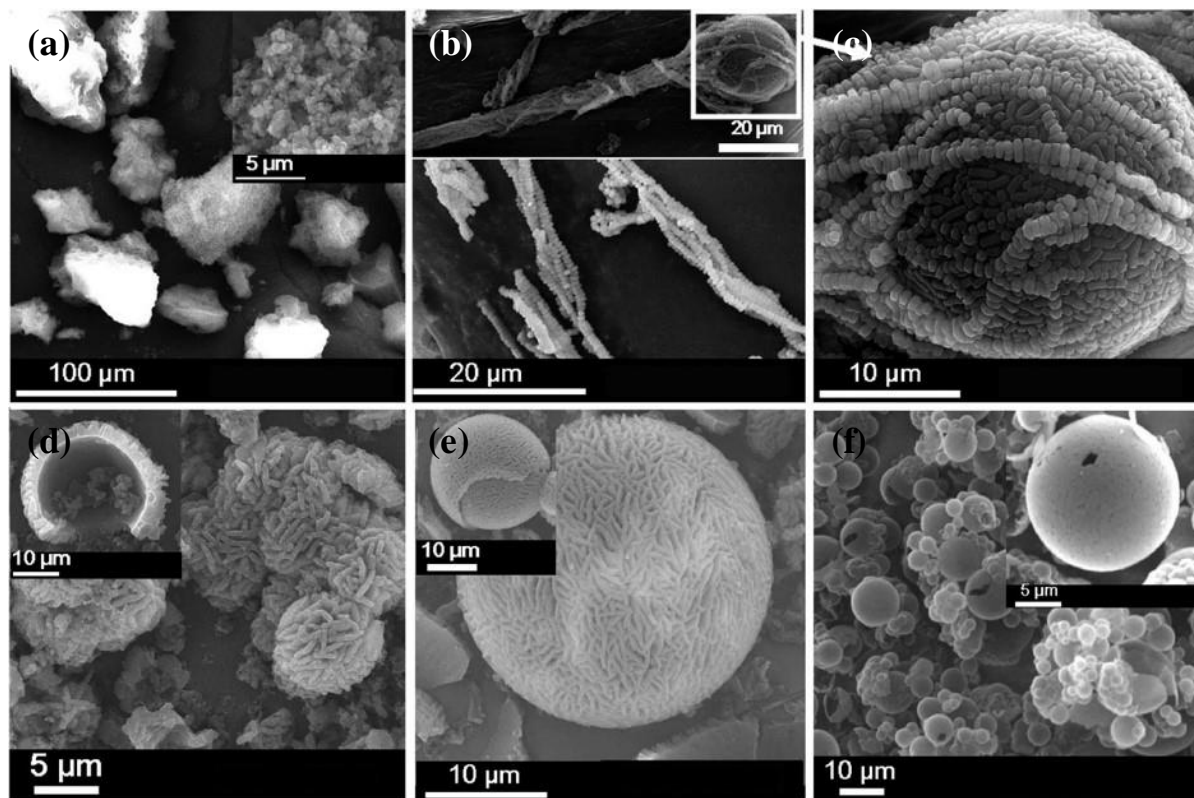


**Figure 1.9** SEM images of mesoporous silica synthesized with different weight ratios of 2,2,4-trimethylpentane (TMP)/P123 under acidic conditions, (a) TMP/P123 = 0, (b, c) TMP/P123 = 0.5, (d) TMP/P123 = 1, (e) TMP/P123 = 3, and (f) TMP/P123 = 6, reproduced from reference 102.

In addition, water-in-oil emulsions can also be used in the preparation of HMSNs. Aqueous solution of triblock copolymer surfactant B50-6600(EO<sub>39</sub>BO<sub>47</sub>EO<sub>39</sub>) was added into TMB to form a stable water-in-oil emulsion.<sup>101</sup> The subsequent hydrolysis and condensation of TEOS at the water-oil interface resulted in HMSNs with particle size of 1-4 μm and large pore of 50 nm in the shell. Liu and co-workers systematically investigated the influence of organic solvent on the morphology and mesostructure of the obtained HMSNs (Figure 1.9).<sup>102</sup> As shown in

Figure 1.9, the preparation was conducted in a buffer solution (pH = 4.4) with P123 as the SDA and TMOS as the silica precursor. Aggregation of mesoporous silica with pore size of 9.3 nm was observed in the absence of 2,2,4-trimethylpentane (TMP) (Figure 1.9a). With increasing amount of TMP in the preparation solution, the morphologies of mesoporous silica obtained evolved from bundles of rope and gigantic spheres intertwined with ropes, to hollow particles composed of aggregated nanorods with smoothly interior surface, to hollow spheres with a smoothly interior surface and irregular particle size on the external surface, finally to hollow spheres with smooth external surface (Figure 1.9b-f). Note that the pore sizes of these mesoporous silicas could be changed from 11 nm to 27.5 nm in the presence of TMP and simultaneous alteration of the initial reaction temperature and ageing temperature. In these cases, TMP could diffuse into the hydrophobic core of the P123 micelles, resulting in a pore enlargement. However, the amount of TMP dissolved in the P123 micelles was limited and the remaining TMP formed an oil-in-water emulsion, which acted as the template for the assembly of primary rod-like MSNs. Simultaneously, the hydrolysis of TMOS was influenced by TMP effecting the growth of mesoporous silica and thereby leading to the formation of various shaped mesoporous silicas.

Based on the nature of surfactant, surfactant aggregations (micelles, vesicles, liquid crystal phases) with various shapes can be formed. The thermodynamically stable micelles/vesicles can be considered as the template for the preparation of HMSNs. Vesicles-templated HMSNs were first reported in 1996.<sup>103</sup> Multilamellar vesicles prepared with 1,12-diaminododecane were used as the template under neutral condition to form HMSNs with pillared lamellar structure in the shell. Poly(vinylpyrrolidone) (PVP) and CTAB or dodecylamine (DDA) were used as co-templates for the fabrication of the HMSNs.<sup>104,105</sup> Hollow silica spheres with mesostructured shells (HSSMS) were prepared by using a mixture of CTAB, sodium dodecyl sulfate (SDS) and Pluronic P123 (CTAB-SDS-EO<sub>20</sub>PO<sub>70</sub>EO<sub>20</sub>) in the range of SDS/CTAB ratio of 0.6-0.8 as a vesicle template via a fast silicification in dilute silicate solution at pH  $\approx$  5.0.<sup>106</sup> In this synthesis system, P123 anchored onto the surface of CTA<sup>+</sup>-DS<sup>-</sup> vesicles acted as the template for the preparation of HMSNs with particle size of 100-500 nm and pore size of 5.5-7.5 nm. Thermosensitive polymer poly(*N*-isopropylacryamide) could also be used as a template to prepare HMSNs with mesoporous shells.<sup>107</sup> Note that the polymer aggregates could be easily removed by cooling the reaction solution to room temperature due to a reversible dissolution under the lower critical solution temperature. In addition, a mixture of [C<sub>3</sub>F<sub>7</sub>O(CFCF<sub>3</sub>CF<sub>2</sub>O)<sub>2</sub>CFCF<sub>3</sub>CONH-(CH<sub>2</sub>)<sub>3</sub>N<sup>+</sup>(C<sub>2</sub>H<sub>5</sub>)<sub>2</sub>CH<sub>3</sub>I] (FC-4) and EO<sub>106</sub>PO<sub>70</sub>EO<sub>106</sub> (F127) was used as a vesicle template to fabricate multi-shelled HMSNs.<sup>108</sup> Both the number of shells (1~4 layers) and shell thickness (7-20 nm) were facilely controlled by adjusting the synthesis parameters. Yu and co-workers synthesized HMSNs with particle size of 50 nm by the self-assembly of triblock copolymer EO<sub>39</sub>BO<sub>47</sub>EO<sub>39</sub> (B50-6600) vesicles and silica oligomers in acidic solution.<sup>109</sup> Further hydrothermal treatment could effectively enlarge the pore size in the shell. The results showed that the hydrothermal temperature induced the

formation of pore sizes less than 3.9 nm at 40-90 °C and of large pore of 6-34 nm at 100-180 °C in the shell.

### 1.3.2 Hard Template Method

Any bulk or monodisperse solid matters with regular shape or pore arrays or uniform size can be theoretically used as a hard template for the fabrication of novel materials, but these hard templates should be readily removable after being used. Due to the difference of composition or structure, these hard templates include polymer nanospheres, metal oxide or carbonate and (non)porous silicas spheres. According to the aim and requirement of the envisaged materials, different hard templates were selected and used. Herein, the preparation of HMSNs focuses on the use of hard templates. The facile and easy scale-up preparation of uniform polystyrene (PS) spheres and *s*SiO<sub>2</sub> spheres with variable size makes these materials good candidates as the hard templates for the synthesis of HMSNs. Generally, HMSNs with well-defined spherical morphology and smooth surface are easily obtained by using the hard template method.

HMSNs with hexagonally ordered mesoporous shell were synthesized using PS spheres as the hard template and CTAB as the SDA in a mixture of ammonia and water.<sup>110</sup> The obtained HMSNs showed a hollow cavity of 350 nm in size similar to the diameter of the PS spheres and shell thickness of 124 nm. This process could also be applied to the preparation of monodisperse HMSNs with ordered mesoporous silica shells.<sup>111</sup> Ethanol in the reaction system played an essential role to decrease the reactivity of silica in forming monodisperse hollow particles. In this case, the presence of ethanol was quite similar to the coating of PS particles with porous silica layer via the modified Stöber method. Both the size of the hollow cavity and the thickness of mesoporous silica shell were adjustable by using PS spheres with different size and changing the amount of TEOS, respectively. Kato and co-workers systematically investigated the effects of water/ethanol ratio and surfactant concentration on the monodispersity of HMSNs templated by PS spheres.<sup>112</sup> Monodisperse HMSNs of various sizes (570-75 nm) and shell thicknesses (140-20 nm) were obtained under the optimized conditions. HMSNs with macropores ( $\geq 50$  nm) in the shell were also fabricated through a PS templating route.<sup>113</sup> The primary silica nanoparticles were deposited on the surface of PS particles by hydrolysis and condensation of TEOS in an ammonia-ethanol-water solution. The subsequent growth and coalescence of the primary silica nanoparticles formed an intact shell consisting of interconnected nanoparticles. The uncovered areas on PS particles became macroporous pores in the shell after the removal of the PS spheres.

Shi and co-workers reported the synthesis of HMSNs by using *s*SiO<sub>2</sub> spheres as the template via an etching strategy.<sup>114-116</sup> *s*SiO<sub>2</sub> spheres synthesized using the Stöber method were first coated with mesoporous silica (*m*SiO<sub>2</sub>) layer in the same preparation solution in the presence of surfactant, resulting in the *s*SiO<sub>2</sub>@*m*SiO<sub>2</sub> core-shell structured nanoparticles. The *s*SiO<sub>2</sub> core was then removed by simply treating the as-synthesized core-shell structured nanoparticles



with weak base at elevated temperature. The selective etching of the *s*SiO<sub>2</sub> core based on the structural difference between the *s*SiO<sub>2</sub> and *m*SiO<sub>2</sub> was due to the higher condensation degree and stability of *m*SiO<sub>2</sub> than *s*SiO<sub>2</sub>. Furthermore, the mesopores in the shell could be modulated from 3.2 nm to larger than 10 nm by partial breaking Si-O bonds in the shell during the core etching process.<sup>115</sup> This strategy of producing HMSNs based on “structural difference etching” was also conducted under acidic conditions.<sup>117,118</sup> Because the byproducts of the alkaline etching were avoided under acidic conditions, monodisperse HMSNs with uniform particle size were obtained.

Apart from PS and *s*SiO<sub>2</sub> spheres, calcium carbonate nanoparticles were also used as the template for the formation of HMSNs. Hollow porous silica nanoparticles with 60-70 nm in diameter and a shell thickness of 10 nm were synthesized by using calcium carbonate nanoparticles as the hollow structure template.<sup>119</sup> However, the obtained HMSNs had micropores in the shell due to the absence of surfactant in the shell formation process. HMSNs with pore size of 4-5 nm in the shell were synthesized by adding CTAB as the mesopore template.<sup>120</sup> The shell thickness of these HMSNs was controllable in the range of 15-45 nm by adjusting the weight ratio of Na<sub>2</sub>SiO<sub>3</sub>·9H<sub>2</sub>O/CaCO<sub>3</sub>. Magnetic HMSNs containing Fe<sub>3</sub>O<sub>4</sub> nanoparticles in the hollow space were also obtained when CaCO<sub>3</sub>/Fe<sub>3</sub>O<sub>4</sub> composite particles were used as the hollow structure template.<sup>121</sup>

### 1.3.3 Self-templating Method

Direct synthesis of HMSNs without the need of additional hollow structure templates is preferred in practical applications due to the significantly reduced production cost and ease of up-scaling. Yin and co-workers reported a simple and scalable self-templating method for the formation of hollow silica spheres based on the dissolution and regrowth process (Figure 1.10).<sup>122</sup> A spontaneous structure change from solid to hollow spheres occurred when *s*SiO<sub>2</sub> spheres were dispersed in an aqueous solution of NaBH<sub>4</sub>. Due to the high basicity of the NaBH<sub>4</sub> solution, *s*SiO<sub>2</sub> spheres would gradually dissolve to produce soluble monosilicate and polysilicate species, which were released into solution to eventually become supersaturated. Meanwhile, the concentration of NaBO<sub>2</sub> gradually increased as a result of the decomposition of NaBH<sub>4</sub>, causing the silicate species to precipitate and redeposit on the core surfaces. The shell further grew at the expense of the core through Ostwald ripening, leading to the production of hollow silica spheres. Zheng and co-workers developed a cationic surfactant-assisted selective etching strategy for the synthesis of HMSNs.<sup>123</sup> The *s*SiO<sub>2</sub> spheres were treated with Na<sub>2</sub>CO<sub>3</sub> in the presence of CTAB. The anionic silicate species produced by *s*SiO<sub>2</sub> dissolution under basic conditions were captured by cationic CTA<sup>+</sup> and re-deposited on the surface of *s*SiO<sub>2</sub> core. HMSNs were finally obtained after *s*SiO<sub>2</sub> was totally transformed into the mesoporous silica shell. Hollow mesoporous aluminosilica nanospheres with radially aligned mesoporous shell were later reported by using the same preparation strategy.<sup>124</sup> By treating with a hot alkaline solution in the presence of sodium aluminate and CTAB, *s*SiO<sub>2</sub>

spheres were converted into hollow mesoporous aluminosilicate spheres with perpendicular pore channels. Dumbbell shaped silica particles consisting of a large  $s\text{SiO}_2@m\text{SiO}_2$  spherical core-shell part and a small HMSNs lobe were synthesized by Mayer and co-workers via a self-templating dissolution and re-deposition process.<sup>125</sup>

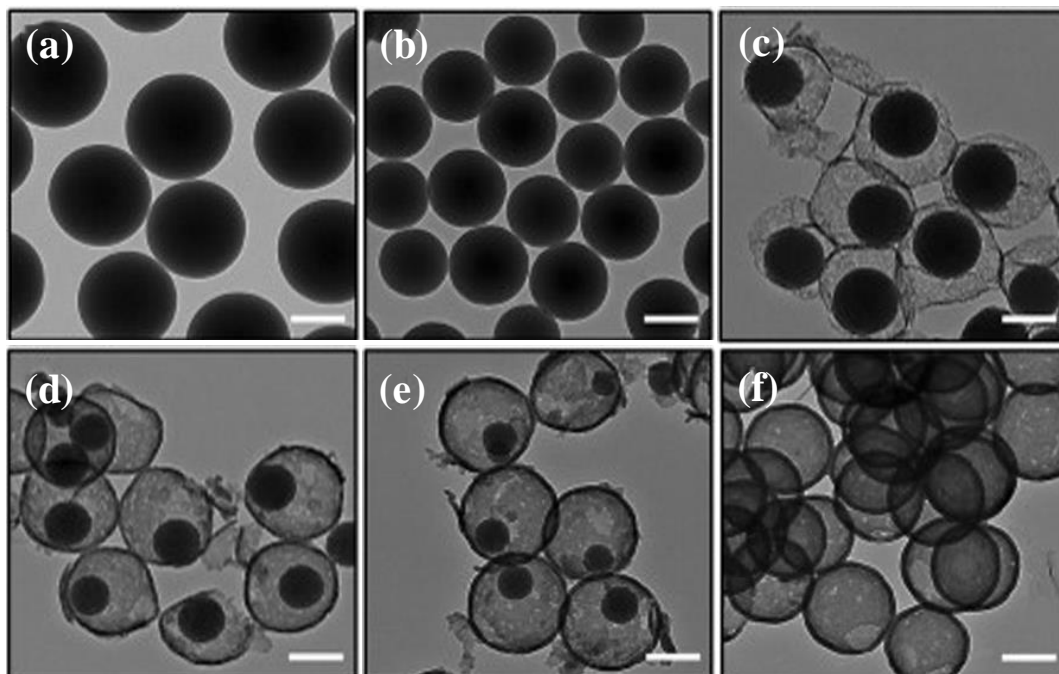


**Figure 1.10** The formation of hollow silica spheres via a dissolution and regrowth process. TEM images of (a) as-made  $s\text{SiO}_2$  spheres, and samples after reacting with 0.06 g/mL  $\text{NaBH}_4$  at ambient temperature for (b) 2 days, (c) 3 days, (d) 5 days, (e) 6 days, and (f) 10 days. Scale bars are 200 nm, reproduced from reference 122.

### 1.3.4 HMSNs Prepared by Other Methods

Brinker and co-workers reported the preparation of HMSNs through an aerosol evaporation induced self-assembly (EISA) process.<sup>126</sup> The precursor solution containing TEOS, CTAB, HCl and  $(\text{NH}_4)_2\text{SO}_4$  in a water/ethanol mixture was converted into an aerosol. During the heating process, fast solvent evaporation initiated the self-assembly between CTAB and silicate species and the nucleation of  $(\text{NH}_4)_2\text{SO}_4$  in the central space of the aerosol droplets. The subsequent decomposition of  $(\text{NH}_4)_2\text{SO}_4$  at high temperature resulted in the formation of hollow nanoparticles with mesoporous shell.

Zeng and co-workers used the concept of Ostwald ripening to produce HMSNs.<sup>127</sup> It was believed that MSNSs formed by the modified Stöber method were the aggregation of small silica particles. Due to the rapid hydrolysis and condensation reactions at the beginning of the reaction, the initially formed silica particles in the central of MSNSs were small in size, while the subsequently aggregated silica particles were comparatively bigger. The small silica particles in the central part of MSNSs would easily dissolve under solvothermal conditions owing to the higher surface energy and regrow on the outer silica particles, creating a hollow

part in the interior of MSNSs. The size of the hollow cavity depended on the temperature and treatment time of such solvothermal reactions.

Lu and co-workers reported a spontaneous self-transformation approach for the preparation of HMSNs.<sup>128</sup> MSNSs synthesized by a modified Stöber method could be spontaneously transformed into HMSNs after incubation with water. The solid-to-hollow transformation was attributed to the higher condensation degree of silica in the outer layer than those in the inner part of MSNSs. Therefore, the inner part of MSNSs was more easily attacked by water to dissolve, and a hollow space was formed in the center of MSNSs.

Yu and co-workers synthesized HMSNs with rough surface and named this as silica nanopollens.<sup>129</sup> The preparation involved the polymerization of resorcinol and formaldehyde as well as the hydrolysis and condensation of TEOS in the Stöber solution.<sup>130-132</sup> Resorcinol-formaldehyde (RF) nanoparticles were first formed by adding polymer precursors at the beginning of the reaction. With the following additions of TEOS and polymer precursors, silica-polymer composites would deposit on the surface of primary polymer nanoparticles, forming a core-shell structure. After removing the polymer by calcination, silica nanopollens consisting of a hollow space, one layer of dense silica and one layer of porous silica were obtained. Both the thickness of the silica shell and the pore size were adjustable by controlling the amount of TEOS added at different stages.

#### **1.4 Core-Shell Structured Mesoporous Silica Nanoparticles (CSMSNs)**

Core-shell structured mesoporous silica nanoparticles (CSMSNs) integrate various functional cores and a mesoporous silica shell into one unit.<sup>133,134</sup> Compared with single component counterparts, CSMSNs exhibit improved physical and chemical properties (e.g., multi-functionality, improved stability, high and adaptable dispersibility). More importantly, CSMSNs provide new active interfaces and potential synergistic effects between the core and mesoporous silica shell, making them promising candidates for use as catalysts and many other applications. Therefore, CSMSNs have attracted considerable attention and have become an increasingly important interdisciplinary research field in chemistry, material science, biology and engineering.

##### **1.4.1 CSMSNs with a Metal Nanoparticle as the Core**

Metal nanoparticles, like Au, Ag and Pt nanoparticles, have potential applications in pollution treatment and organic synthesis due to their high catalytic activities in CO oxidation, partial oxidation, combustion reactions etc. However, metal nanoparticles tend to sinter at high temperature during the catalytic processes, which severely limits their applications. Directly coating metal nanoparticles with a mesoporous silica shell to form a core-shell structure not only makes the metal nanoparticles easily accessible through the mesoporous channels, but also inhibits the possible aggregation of metal nanoparticles. In the early studies, Au@mSiO<sub>2</sub> core-shell structured nanoparticles were synthesized using Au nanoparticles as the seeds for

the further growth of mesoporous silica shells under basic condition<sup>135</sup> or by treating Au@mSiO<sub>2</sub> core-shell structured nanoparticles under the hydrothermal conditions in the presence of CTAB via a pseudomorphic transformation approach.<sup>136</sup> In both cases, Au nanoparticles need to be modified with mercaptopropyl trimethoxysilane to make a vitreophilic surface and facilitate silica coating. This surface modification process is tedious and could not be extended to synthesize CSMSNs with other metal cores. A simple method for the directly coating of single Au nanorod with a mesoporous silica shell was reported.<sup>137</sup> CTAB-capped Au nanorods were synthesized with CTAB as the stabilizer in aqueous solution. The coating with mesoporous silica was conducted by directly adding TEOS into the basic Au nanorod colloidal solution. During the coating process, CTAB on the surface of the Au nanorods acted as the SDA for the formation of the mesoporous silica shell. This coating strategy could be generally extended to other CTAB-capped nanoparticles. The dual-function of surfactant in the synthesis of CSMSNs has also been demonstrated by Somorjai and co-workers. They synthesized Pt@mSiO<sub>2</sub> core-shell structured nanoparticles in order to obtain a Pt catalyst for high-temperature reactions (Figure 1.11).<sup>138</sup> The core-shell structure was formed by using tetradecyltrimethylammonium bromide (TTAB) as both capping agent for Pt nanoparticles and SDA molecule for the mesoporous silica shell (Figure 1.11a). Most of the nanoparticles still preserved the core-shell structure even after calcination at high temperatures (Figure 1.11b-d). TTAB has also been used as the surfactant in the preparation of Au@mSiO<sub>2</sub> core-shell structured nanoparticles through a quite similar synthesis process.<sup>139</sup>

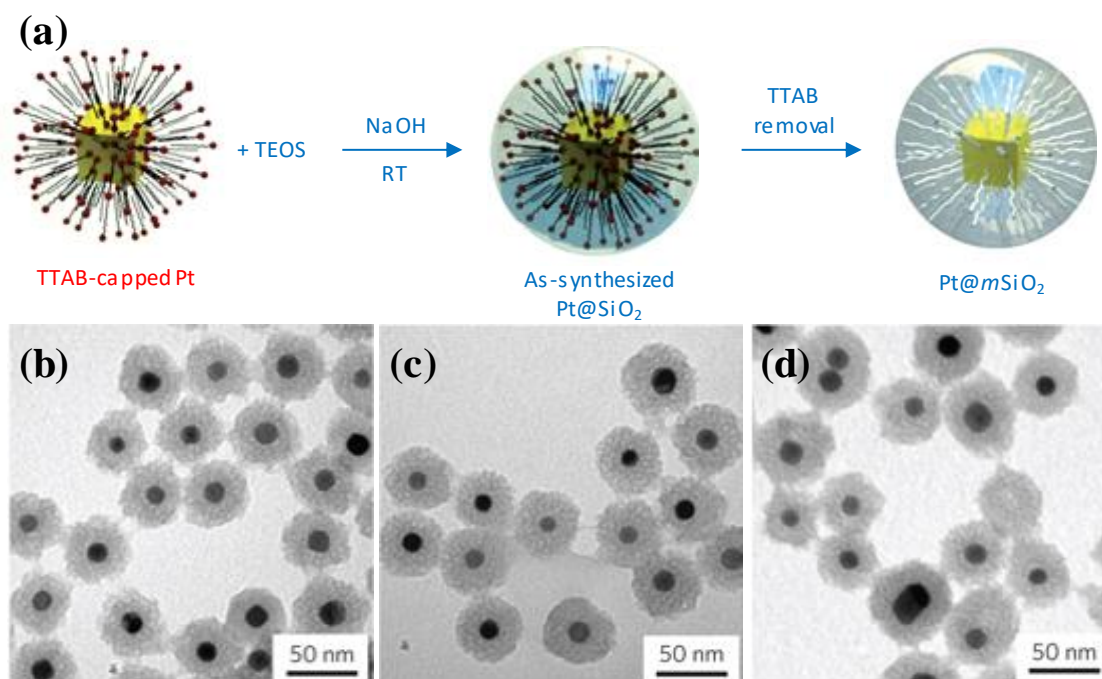


**Figure 1.11** (a) Schematic illustration of the preparation process of Pt@mSiO<sub>2</sub> core-shell structured nanoparticles, TEM images of Pt@mSiO<sub>2</sub> after calcination at (b) 350 °C, (c) 550 °C, and (d) 750 °C, reproduced from reference 138.

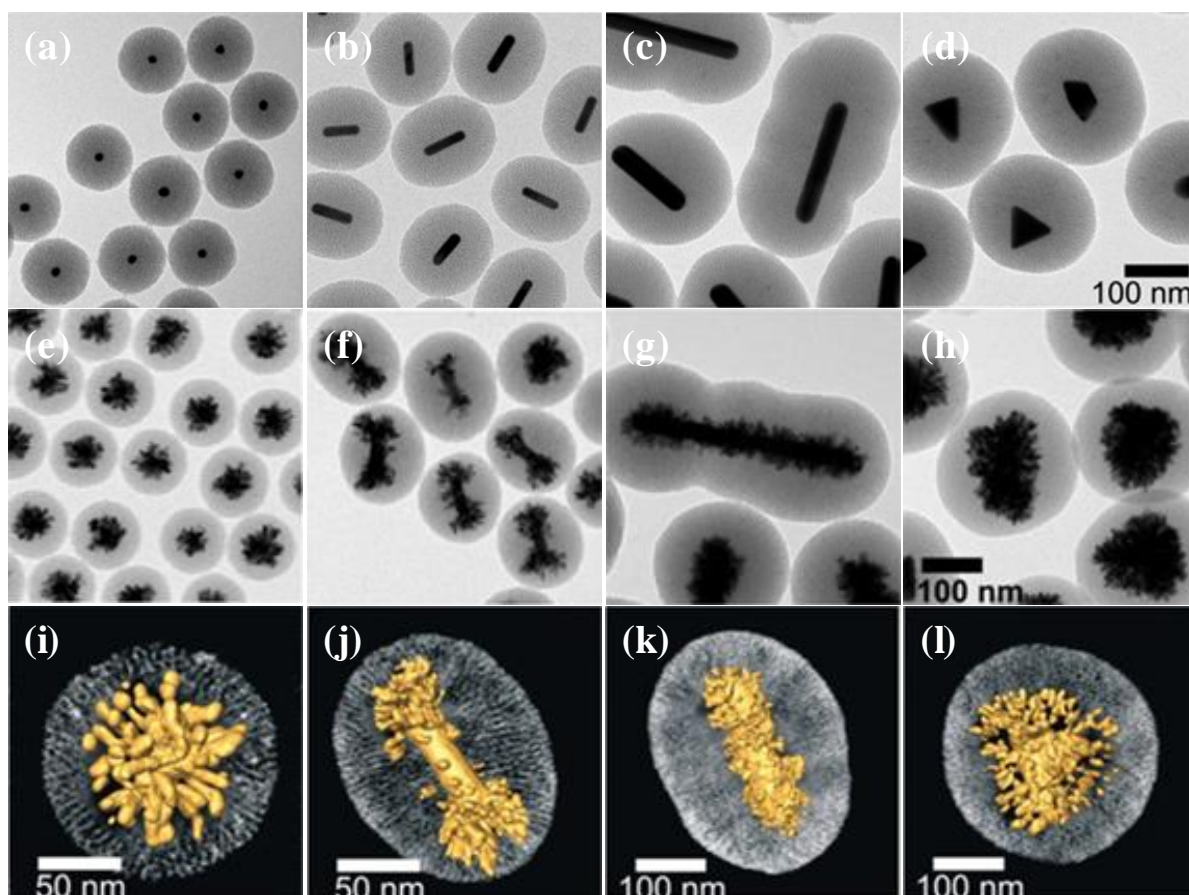


**Figure 1.12** TEM images of Au@mSiO<sub>2</sub> core-shell structured nanoparticles containing Au nanoparticles with various shapes before and after growing Au tips into the mesoporous silica channels, (a, e) nanospheres, (b, f) single-crystal nanorods, (c, g) penta-twinned nanorods, (d, h) nanotriangles, (i-l) 3D reconstruction images of corresponding core-shell structured nanoparticles after Au tips growth. (all the images in the first and second line were obtained at the same magnification), reproduced from reference 140.

Liz-Marzán and co-workers synthesized Au@mSiO<sub>2</sub> core-shell structured nanoparticles using Au nanoparticles with different morphologies (nanospheres, single-crystal nanorods, penta-twinned nanorods and nanotriangles) as the cores (Figure 1.12a-d).<sup>140</sup> All of the Au nanoparticles were capped with CTAB by adsorption prior to the growth of uniform mesoporous silica shells. The adsorption of CTAB improved the interaction between the Au nanoparticles and silicate species, inducing the formation of the mesoporous structure. It is interesting to observe that the mesoporous silica shells of obtained Au@mSiO<sub>2</sub> core-shell structured nanoparticles could be employed as the template for the growth of Au tips branching out from the core (Figure 1.12e-l). The growth of Au tips from the central Au cores was templated by the mesoporous channels and its shape was regardless of the Au core morphology. It is noted that when using a chiral surfactant as the SDA molecules, a novel CSMSNs with Au nanorod as the core and chiral mesoporous silica as the shell was obtained by Che and co-workers.<sup>141</sup>

Au@mSiO<sub>2</sub> core-shell structured nanoparticles could also be synthesized by a one-pot method.<sup>142</sup> Au nanoparticles with size of 32 nm were formed by the reduction of HAuCl<sub>4</sub> with

formaldehyde solution in the presence of CTAB as the stabilizing agent. Further addition of TEOS into the same preparation solution initiated the formation of a mesoporous silica shell around Au cores using CTAB as the template, giving rise to core-shell structured nanoparticles with particle size of 120 nm. The size of the Au core was controlled by the amount of  $\text{HAuCl}_4$ . A similar procedure could be used for the preparation of  $\text{Ag}@m\text{SiO}_2$  core-shell structured nanoparticles.<sup>143</sup> Small Ag nanoparticles were first formed by the reduction of silver nitrate with CTAB as the stabilizing agent. The addition of TEOS induced the formation of MSNs along the surface of CTAB-stabilized primary small Ag nanoparticles. With the growth of MSNs, the primary small Ag nanoparticles transferred and aggregated and formed a large Ag core in an incompact mesostructured silica framework.

Sandwich-structured  $\text{Ag}@s\text{SiO}_2@m\text{SiO}_2$  nanoparticles were prepared and used to fabricate the multifunctional Au nanocage@ $m\text{SiO}_2$ @PNIPAM (PNIPAM: poly(*N*-isopropyl acrylamide)) core-shell structured nanoparticles (Figure 1.13).<sup>144</sup> The  $s\text{SiO}_2$  layer was selectively etched to form Ag nanocube@ $m\text{SiO}_2$  yolk-shell structured nanoparticles (Figure 1.13b, c). The Au cage@ $m\text{SiO}_2$  core-shell structured nanoparticles were obtained based on a galvanic replacement reaction between the silver nanocubes and  $\text{HAuCl}_4$  (Figure 1.13d). After surface modification with PNIPAM, the final Au nanocage@ $m\text{SiO}_2$ @PNIPAM (Figure 1.13e) was used as a drug carrier for light-controlled release.

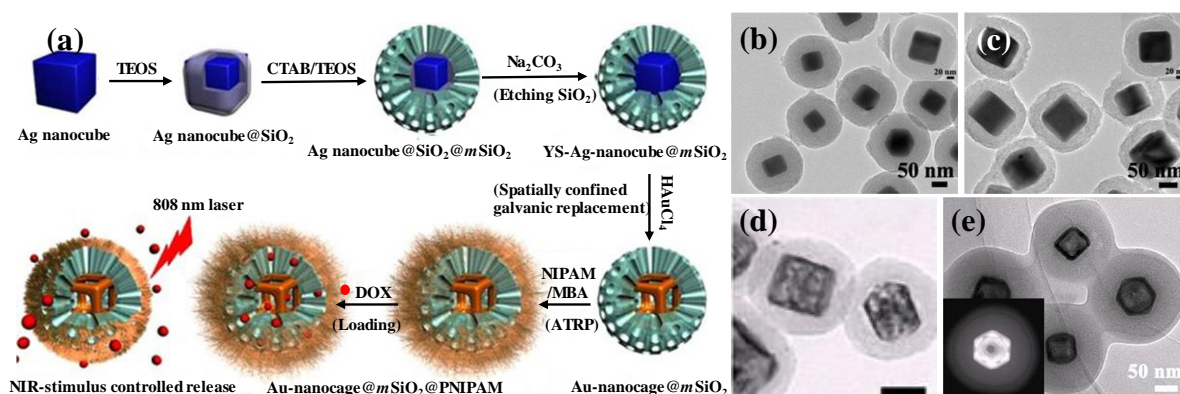


**Figure 1.13** (a) Schematic illustration of the preparation process of Au nanocage@ $m\text{SiO}_2$ @PNIPAM core-shell structured nanoparticles, TEM images of (b) Ag nanocube@ $s\text{SiO}_2@m\text{SiO}_2$  core-shell structured nanoparticles, (c) Ag nanocube@ $m\text{SiO}_2$  yolk-shell structured nanoparticles, (d) Au nanocage@ $m\text{SiO}_2$  core-shell structured nanoparticles obtained by a galvanic replacement reaction with  $\text{HAuCl}_4$  (scale bar is 50 nm), and (e) Au nanocage@ $m\text{SiO}_2$ @PNIPAM core-shell structured nanoparticles, the insets are the HRTEM image in (b) and (c), and the scanning transmission electron microscope (STEM) image in (e), reproduced from reference 144.

#### 1.4.2 CSMSNs with a Magnetic Nanoparticle as the Core

Magnetic nanocrystals with controllable size and regular crystallite morphology, prepared through the thermal decomposition of organometallic precursors, could be used as the cores to fabricate magnetic CSMSNs. It is known that nanocrystals are usually obtained in the presence of hydrophobic capping agent. Due to poor dispersibility in polar solution such as water, these nanoparticles are very difficult to be coated with a mesoporous silica shell via the sol-gel

approach. Heyon and co-workers proposed an approach to transfer hydrophobic magnetite nanocrystals and quantum dots into aqueous solution with the assistance of CTAB.<sup>145</sup> The water-dispersible nanocrystals were obtained by adding a nanocrystal chloroform solution into a CTAB aqueous solution, followed by the evaporation of the organic solvent. CTAB interacted with the organic capping agent on the surface of nanocrystals to generate a “homogeneously” nanocrystals-dispersed aqueous phase. The subsequent nanocrystals were coated by a mesoporous silica shell via a sol-gel reaction of TEOS in the presence of CTAB as the template forming the 150 nm sized nanospheres with several nanocrystals embedded in each MSN. By using a similar synthesis strategy, monodisperse magnetic CSMSNs with one Fe<sub>3</sub>O<sub>4</sub> nanocrystal in each nanosphere were prepared.<sup>146</sup> The size of CSMSNs could be easily adjusted below 100 nm. Multifunctional nanoparticles with magnetic and fluorescent properties could also be obtained by incorporating fluorescence dyes into the silica wall.

Magnetic CSMSNs with a large magnetic nanosphere core have also been investigated. Uniform magnetic CSMSNs with sandwich structure were first synthesized by Shi and co-workers.<sup>147</sup> Hematite (Fe<sub>2</sub>O<sub>3</sub>) nanoparticles with average size of 120 nm were prepared and coated with a 20 nm thickness *s*SiO<sub>2</sub> layer to protect the cores from leaching under acidic conditions. Further growth of a mesoporous silica shell was conducted in a mixture of water, ethanol and ammonia using TEOS and *n*-octadecyltrimethoxysilane as the silica precursors and SDA, respectively. The nonmagnetic hematite core was reduced to produce the final magnetic CSMSNs. Zhao and co-workers used a stepwise coating approach to produce magnetic Fe<sub>3</sub>O<sub>4</sub>@*s*SiO<sub>2</sub>@*m*SiO<sub>2</sub> nanoparticles consisting of a *s*SiO<sub>2</sub> coated magnetite core and a mesoporous silica shell with perpendicularly oriented channels.<sup>148</sup> Multifunctional Fe<sub>3</sub>O<sub>4</sub>@*s*SiO<sub>2</sub>-Au@*m*SiO<sub>2</sub> microspheres were developed later, which possessed a *s*SiO<sub>2</sub> coated magnetite nanoparticle core, a transitional layer of active Au nanoparticles and an outer shell of ordered mesoporous silica.<sup>149</sup> The mesoporous silica shell not only protected the Au nanoparticles from leaching into the solution, but also ensured effective mass diffusion to the active Au nanoparticles during the catalytic reactions. Magnetic Fe<sub>3</sub>O<sub>4</sub>@C-Pd(Pt)@*m*SiO<sub>2</sub> nanoparticles made of a carbon-coated magnetite nanoparticle core, a transitional layer of Pd (or Pt) nanoparticles and an outer layer of ordered mesoporous silica were also synthesized.<sup>150</sup> In addition, Fe<sub>3</sub>O<sub>4</sub>@*s*SiO<sub>2</sub>@*m*SiO<sub>2</sub> nanoparticles with magnetic and fluorescent properties could also be obtained using the stepwise coating approach.<sup>151</sup> The channels of the mesoporous silica shell were modified with YVO<sub>4</sub>:Eu<sup>3+</sup> phosphors, providing the nanoparticles with fluorescent properties. Magnetic CSMSNs synthesized by using CTAB as SDA always have pore size about 2.5 nm, which greatly limited the further application involving loading of large biomolecules such as proteins and DNA. By replacing CTAB with triblock copolymer P123, Fe<sub>3</sub>O<sub>4</sub>@*s*SiO<sub>2</sub>@*m*SiO<sub>2</sub> nanoparticles with a pore size of 4.5 nm in the shell were obtained.<sup>152</sup> Another alternative pathway for fabricating large pore CSMSNs is to employ a biphasic reaction system, which has been demonstrated to produce large pore MSNs,<sup>82</sup> such as magnetic Fe<sub>3</sub>O<sub>4</sub>@RF@*m*SiO<sub>2</sub> nanoparticles with tunable large mesopores (5.0-18.8 nm) in the shell (RF:

resorcinol formaldehyde),<sup>153</sup> and large pore magnetic sandwich-structured mesoporous aluminosilicate nanoparticles.<sup>154</sup> In this case, organic solvents such as hexane was used as an expander for extending the surfactant micelles.

### 1.4.3 CSMSNs with a Porous Nanoparticle as the Core

When porous nanoparticles are used as the core of CSMSNs, hierarchically porous nanoparticles with bimodal pores are obtained. Dual-pore CSMSNs have been synthesized by using two different surfactants, polystyrene-*b*-poly(acrylic acid) (PS-*b*-PAA) and CTAB, as the templates and TEOS as the silica source via a one-pot method.<sup>155</sup> The resultant material possessed smaller pores (2.0 nm) in the shell and larger tunable pores (12.8-18.5 nm) in the core.<sup>155</sup> In this case, rod-like PS-*b*-PAA micelles, coupled with CTAB micelles via electrostatic interaction between CTA<sup>+</sup> and PAA<sup>-</sup>, templated the large pore in the core domain. The residual CTAB in the solution assembled with silicate species and deposited on the surface of the core, leading to the formation of an outer shell with smaller pores surrounding the cores. The pore size in the core was controlled by the hydrophobic block (PS) length of PS-*b*-PAA and the shell thickness was tuned by the amount of TEOS.

More interestingly, the combination of microporous zeolite and mesoporous silica can construct a new type of core-shell structure at the nanoscale,<sup>156-158</sup> as shown for example, by coating of the titanosilicate zeolite TS-1 nanoparticles with a mesoporous silica shell.<sup>158</sup> In order to improve the interaction between core and silicate species, the TS-1 nanoparticles were modified with polydiallyldimethylammonium chloride yielding a positively charged external surface, which was beneficial for the formation of mesoporous silica shell. The shell thickness of the resultant CSMSNs could be controlled by the amount of TEOS used.

Metal-organic frameworks (MOFs) can also be used as the core for preparing CSMSNs. The coating of MOFs with a mesoporous silica shell can effectively improve their mechanical properties.<sup>159</sup> Four MOFs (ZIF-8, ZIF-7, UiO-66, and HKUST-1) have been chosen as the cores to fabricate mesoporous silica-coated MOFs in a mixed solution of methanol and water under mild basic conditions. The resultant MOFs@*m*SiO<sub>2</sub> core-shell structured nanoparticles could be further coated with an additional MOFs phase to form more complicated MOFs@*m*SiO<sub>2</sub>@MOFs core-shell structures. In addition, core-shell structured metal-*m*SiO<sub>2</sub>@MOF nanoparticles were also successfully prepared (Figure 1.14).<sup>160</sup> *s*SiO<sub>2</sub> nanoparticles (Figure 1.14b) were first transformed into *s*SiO<sub>2</sub>@*m*SiO<sub>2</sub> core-shell structured nanoparticles (Figure 14c) through a dissolution-reconstruction process. After loading the metal nanoparticles (Pd, Pt, Ru, Ag, Pt<sub>53</sub>Ru<sub>47</sub>) in the mesopore channels (Figure 1.14d), the core-shell structured nanoparticles were further modified with anionic polymer (poly(sodium-4-styrenesulfonate)) to make a negatively charged surface. Afterwards, the coating with ZIF-8 shell was conducted in diluted condition in the presence of PVP as the stabilizer to produce metal-*m*SiO<sub>2</sub>@ZIF-8 nanoparticles (Figure 1.14e) possessing a hierarchical pore system which



consisted of metal-loaded mesoporous silica as the middle shell and the microporous ZIF-8 as the outer shell.

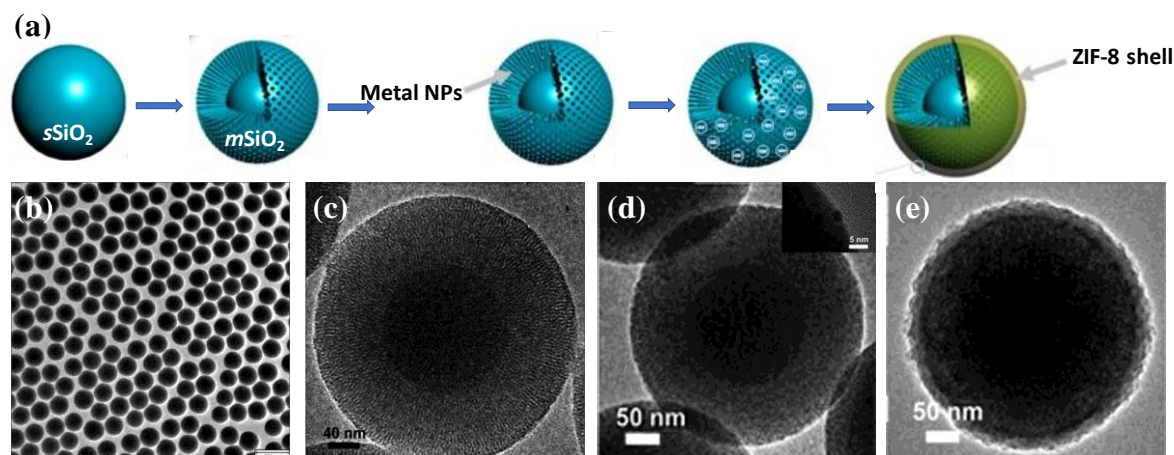


**Figure 1.14** (a) Schematic illustration of the preparation process of metal- $m\text{SiO}_2@ZIF-8$  core-shell nanoparticles, TEM images of (b)  $s\text{SiO}_2$  nanoparticles, (c) CSMSNs transformed from  $s\text{SiO}_2$  nanoparticles through the dissolution-regrowth process, (d) Pt-loaded CSMSNs, the inset is the HRTEM image, and (e) Pt- $m\text{SiO}_2@ZIF-8$  core-shell nanoparticles, reproduced from reference 160.

## 1.5 Yolk-Shell Structured Mesoporous Silica Nanoparticles (YSMSNs)

Yolk-shell structured mesoporous silica nanoparticles (YSMSNs) represent a new class of special core-shell structures with a distinctive core@void@ $m\text{SiO}_2$  configuration.<sup>161</sup> Compared with CSMSNs, the core particles of YSMSNs are freely movable in the shells, affording more exposed active sites. It is beneficial for molecular diffusion through the mesoporous silica shell to make the confined reaction environment inside of YSMSNs very close to one prevailing in homogeneous catalysis. Furthermore, YSMSNs featuring a large cavity between the core and the shell are particularly suitable for the loading of guest molecules, such as proteins, fluorescent or drug molecules. In this case, the YSMSNs can be employed as delivery vehicles.

### 1.5.1 Bottom-up Method Based on Soft Template Assembly

Micelles, vesicles or microemulsions formed by surfactants are usually used as soft templates to assemble inorganic materials. A soft template composed of CTAB and sodium dodecylbenzene sulfonate (SDBS) was used to fabricate magnetic YSMSNs.<sup>162</sup> Polymethyl methacrylate (PMMA) spheres infiltrated with several magnetic  $\text{Fe}_3\text{O}_4$  nanoparticles were suspended in an aqueous solution, and the pre-mixed CTAB and SDBS micelles were adsorbed onto these particle surface. A mesoporous silica shell was then coated onto the micelle-nanoparticle complex to form  $\text{Fe}_3\text{O}_4\text{-PMMA}@m\text{SiO}_2$  yolk-shell structured nanoparticles after the surfactants removal.  $s\text{SiO}_2$  nanoparticles, MSNs,  $\text{Fe}_3\text{O}_4$  nanoparticles, and Au nanoparticles could also be used as various cores to synthesize YSMSNs with tunable shell thickness by a vesicle templating approach (Figure 1.15).<sup>163</sup> The fluorocarbon surfactant FC-4, nonionic triblock polymer F127 and the core materials first formed the core-vesicle complex by

electrostatic interactions and a synergetic effect. Then by a vesicle-templating approach and the simultaneous sol-gel polymerization of TEOS, a mesoporous silica shell was deposited and further condensed on the surface of the vesicle-core complex to form YSMSNs. After removal of the surfactant vesicle template by calcination, the final yolk-shell structured nanoparticles were obtained. The shell thickness could be well controlled by tailoring the amount of TEOS or adjusting the FC-4/F127 molar ratio.

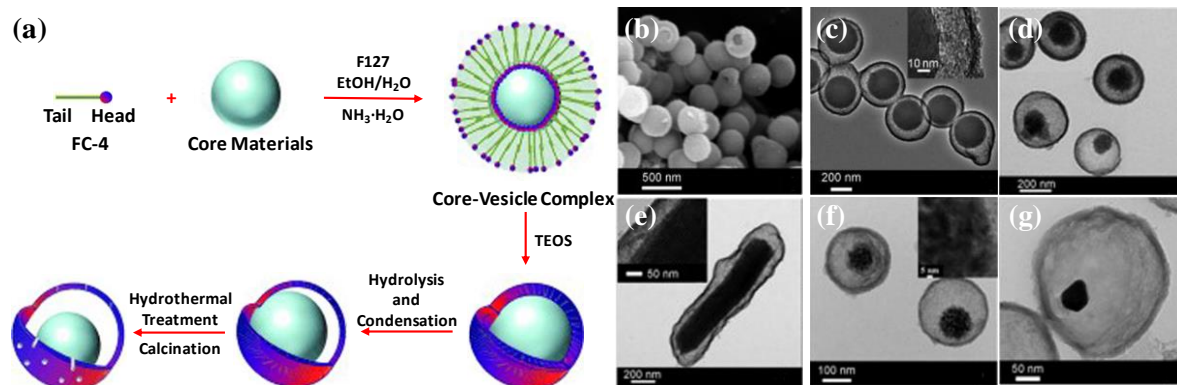


**Figure 1.15** (a) Schematic illustration of the preparation of YSMSNs with various cores, SEM and TEM images of resultant YSMSNs with cores of (b, c) 260 nm  $s\text{SiO}_2$  nanoparticles, (d) 100 nm MSNs, (e) SBA-15 nanorods, (f)  $\text{Fe}_3\text{O}_4$  nanoparticles, and (g) Au nanoparticles, reproduced from reference 163.

### 1.5.2 Selective Etching Method

The selective etching method is an effective route for the preparation of YSMSNs. In the selective etching process, the pre-synthesized core materials are first coated with a transitional layer, followed by further coating with mesoporous silica. Then the inner shell is selectively removed.

Magnetic  $\text{Fe}_3\text{O}_4@m\text{SiO}_2$  yolk-shell structured nanoparticles were prepared by selective removal of carbon spheres.<sup>164</sup> Monodisperse carbon spheres absorbed with iron precursor were prepared by the hydrothermal method. The subsequent coating with a mesoporous silica shell gave rise to the  $\text{carbon}@m\text{SiO}_2$  core-shell structured nanoparticles in the presence of a templating agent. During the calcination process, both the carbon spheres and the organic SDA were removed and the  $\alpha\text{-Fe}_2\text{O}_3$  core with a size of 100 nm was formed in the meantime in each YSMSNs. After reducing under hydrogen atmosphere, magnetic YSMSNs with a shell thickness of 100 nm and cavity size of 900 nm were obtained. Further investigations demonstrated that the cavity size, shell thickness and the  $\text{Fe}_3\text{O}_4$  content were all controllable by adjusting the synthesis parameters.<sup>165</sup> Polystyrene-*co*-poly(4-vinylpyridine) (PS-*co*-P4VP) nanospheres loaded with 2 nm Au nanoparticles were coated with mesoporous silica shell to form  $\text{Au}@m\text{SiO}_2$  yolk-shell structured nanoparticles. During the calcination process, initial small Au nanoparticles were aggregated into a single 50 nm Au nanoparticle in  $\text{Au}@m\text{SiO}_2$  YSMSNs.<sup>166</sup> Shi and co-workers synthesized monodisperse YSMSNs by using the structural difference-based selective etching strategy.<sup>114,167</sup>  $\text{Au}@s\text{SiO}_2@m\text{SiO}_2$ ,  $\text{Fe}_3\text{O}_4@s\text{SiO}_2@m\text{SiO}_2$

and  $\text{Fe}_2\text{O}_3@_s\text{SiO}_2@m\text{SiO}_2$  core-shell structured nanoparticles were prepared by stepwise coating. The  $s\text{SiO}_2$  shell was selectively etched under weakly basic conditions by using the structural difference between  $s\text{SiO}_2$  and  $m\text{SiO}_2$ .<sup>114</sup> The obtained YSMSNs could be further coated with another layer of mesoporous silica, giving rise to  $s\text{SiO}_2@m_1\text{SiO}_2@m_2\text{SiO}_2$  and  $\text{Fe}_2\text{O}_3@m_1\text{SiO}_2@m_2\text{SiO}_2$  yolk-shell structured nanoparticles.<sup>168</sup> Zheng and co-workers found that the etching of  $s\text{SiO}_2$  shell of the core-shell structured nanoparticles ( $\text{Au}@_s\text{SiO}_2$ ,  $\text{Fe}_3\text{O}_4@_s\text{SiO}_2$  and  $\alpha\text{-Fe}_2\text{O}_3@_s\text{SiO}_2$ ) under basic conditions in the presence of CTAB led to the corresponding YSMSNs ( $\text{Au}@_m\text{SiO}_2$ ,  $\text{Fe}_3\text{O}_4@m\text{SiO}_2$  and  $\alpha\text{-Fe}_2\text{O}_3@m\text{SiO}_2$ ).<sup>124</sup> The selective etching of  $s\text{SiO}_2$  approach has also been applied to synthesize polymer nanospheres@ $m\text{SiO}_2$  yolk-shell structured nanoparticles.<sup>169</sup> Monodisperse mesoporous phenolic polymer nanospheres were used as the core and coated with  $s\text{SiO}_2$  and then  $m\text{SiO}_2$  layers to form a polymer@ $s\text{SiO}_2@m\text{SiO}_2$  core-shell structured nanoparticle. The selective etching of  $s\text{SiO}_2$  under weakly basic conditions produced polymer@ $m\text{SiO}_2$  yolk-shell structured nanoparticles with a uniform particle size of 200 nm and bimodal pore sizes of 5.8 nm and 3.1 nm in the core and shell, respectively. The polymeric cores were carbonized, resulting in hierarchical YSMSNs with hydrophobic carbon cores and hydrophilic silica shells. YSMSNs consisting of  $\text{Fe}_3\text{O}_4@_s\text{SiO}_2$  nanoparticle as core and mesoporous silica as shell were prepared by selective removal of resorcinol-formaldehyde (RF) layer of  $\text{Fe}_3\text{O}_4@_s\text{SiO}_2@\text{RF}@_m\text{SiO}_2$  core-shell structured nanoparticles.<sup>170</sup>  $\text{Fe}_3\text{O}_4@_s\text{SiO}_2@\text{RF}@_m\text{SiO}_2$  nanoparticles with different RF shell thickness resulted in the final YSMSNs with different cavity size.

Moreover, a surface-protected etching strategy was reported to afford YSMSNs.<sup>171</sup> Core-shell structured  $\text{Au}@_s\text{SiO}_2$  nanoparticles were adsorbed with PVP molecules prior to the etching process. The stability of silica near the surface was improved due to the strong hydrogen bonding between the carbonyl groups of PVP molecules and hydroxyl groups of silica. Therefore, the interior silica was selectively etched under basic conditions, leading to the  $\text{Au}@_m\text{SiO}_2$  yolk-shell structured nanoparticles with similar particle size as pristine  $\text{Au}@_s\text{SiO}_2$  core-shell structured nanoparticles.

## 1.6 Mesoporous Organosilica Nanoparticles (MONs)

PMOs have advantages over mesoporous silica materials, such as excellent hydrothermal and mechanical stabilities, a hydrophobic environment inside the pore and wall, and a high concentration of organic functional group in the framework. Mesoporous organosilica nanoparticles (MONs) in the size range of 30-500 nm have not only the aforementioned advantages, but also additional properties like fast mass transport, effective adhesion to substance and good suspensibility in the solution.

Ethylene-bridged MONs with average particle size of 100 nm have been synthesized using F108 as the SDA and FC-4 as the particle size controller.<sup>87</sup> A similar co-templating strategy has also been applied for the synthesis of phenylene-bridged MONs.<sup>172</sup> Poly(ethylene oxide)-poly(DL-lactic acid-co-glycolic acid)-poly(ethylene oxide) and FC-4 were used as the template

and 1,4-bis(triethoxysilyl)benzene (BTEB) as an organosilica precursor under acidic conditions, resulting in the formation of core-shell structured MONs with a particle size of 50-1000 nm. These two methods produced markedly aggregated MONs that were not suitable for further applications. Monodisperse ethylene-bridged MONs with single crystal morphologies were obtained by adjusting the ammonia amount,<sup>173</sup> featuring sizes of 480 nm and 1  $\mu$ m for cube and truncated-cube morphologies, respectively. Kuroda and co-workers reported the synthesis of colloidal MONs with ethenylene-bridged silsesquioxane frameworks with a uniform diameter of  $\sim$ 20 nm using BTEE as an organosilica precursor in the presence of CTAB in weakly basic aqueous solution (TEA).<sup>174</sup> This preparation method also produced methylene-, and ethylene-bridged MONs, but was not applicable for phenylene-bridged MONs. Huo and co-workers reported a synthesis process for fabricating monodisperse methylene-, ethylene-, ethenylene-, and phenylene-bridged MONs with highly ordered pore structures and a particle size of 100-200 nm.<sup>175</sup> These MONs were produced in aqueous solution using CTAB as the SDA and ammonia as the catalyst. The particle size of MONs was controlled by the amounts of ammonia and cosolvent (*n*-propanol). In addition, porphyrin-functionalized ethenylene-bridged MONs in the particle size range of 200-600 nm and a pore size of 2.5 nm were synthesized by the co-condensation reaction of a zinc porphyrin derivative possessing eight triethoxysilyl groups and 1,2-bis(triethoxysilyl)ethylene under basic conditions.<sup>176</sup>

MONs with large pores are in general suitable for applications involving adsorption or loading of large biomacromolecules. Yu and co-workers applied a biphasic reaction system to synthesize 50 nm phenylene-bridged MONs with large pores.<sup>177</sup> Toluene was used as the oil phase to dissolve the organosilane precursor. The slow hydrolysis rate of the organosilica precursor at the interface led to a low concentration of organosilicate species in the aqueous solution, which contributed to the silicate species-surfactants assembly and eventually the formation of MONs. Moreover, the surfactant micelle was expanded by toluene applying slow stirring conditions. Therefore, MONs with enlarged mesopores (4.6 nm) were obtained. The results showed that the pore of phenylene-bridged MONs could be further enlarged to 7.6 nm by adding isopropanol as a co-swelling agent.

The hybrid MONs, composed of one to several ethenylene-bridged organosilica pods branching out from the phenylene-bridged organosilica core, were synthesized by Durand and co-workers (Figure 1.16) in a one-pot two-step process.<sup>178</sup> This process involved the formation of benzene-based spherical PMO cores followed by the condensation of ethylene-based rod-shaped PMO pods on these cores.<sup>178</sup> These hybrid MONs possessed a core with one pod or multipods as branches. This synthesis strategy was extended to the preparation of multipodal MONs with multiple organic hybridization. In this case, ethenylene-disulfide-based organosilica pods were grown onto the surface of phenylene-bridged organosilica cores by co-condensation of bis(triethoxysilyl)ethenylene and bis(3-triethylsilylpropyl) disulfide precursors in the second coating step. The results confirmed that the multipodal phenylene-bridged MONs were produced under the same synthesis condition at low stirring rates.<sup>179</sup> The

formation of multipodal structures was dependent on the precursor. Nanospheres without branching pods were obtained by replacing 1,4-bis(triethoxysilyl)benzene with 1,3-bis(triethoxysilyl)benzene. Based on these observations, Janus nanoparticles comprising of a phenylene-bridged MON core and a phenylene-ethylene-mixed organosilica pod were prepared.

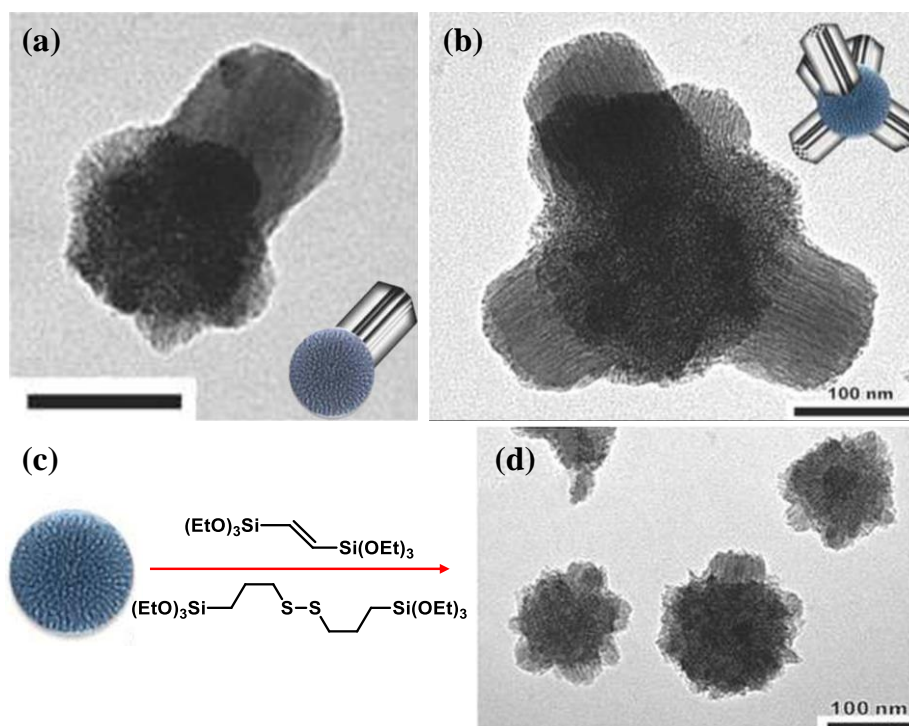


**Figure 1.16** (a) TEM image of hybrid MONs with one pod, (b) TEM image of hybrid MONs with several pods, (c) the formation process, and (d) TEM image of hybrid MONs with ethylene-disulfide-based pods. The inset in (a) and (b) is the schematic illustration, reproduced from reference 178.

### 1.7 Mesoporous Organosilica Nanorods (MONRs) and Nanofibers (MONFs)

Lu and co-workers first reported the synthesis of ethylene-bridged MONRs using P123 as the SDA under acidic conditions.<sup>180</sup> The obtained nanorods displayed a highly ordered hexagonal pore structure, uniform length of 1-2  $\mu\text{m}$  and pore size of 8 nm. When octaethoxy-1,3,5-trisilapentate((EtO)<sub>3</sub>Si-CH<sub>2</sub>-Si(OEt)<sub>2</sub>-CH<sub>2</sub>-Si(OEt)<sub>3</sub>) was used as the organosilane precursor and P123 as a SDA under acidic conditions, special nanorice-shaped MONRs were obtained and showed 600  $\times$  200 nm in length and width.<sup>181</sup> Note that the aspect ratio of the nanorice particles was dependent on the amount of organosilane precursor used during the reaction.<sup>182</sup> With increasing amounts of organosilane precursor, the aspect ratio of MONRs could be systematically varied over a wide range from 2 : 1 to > 20 : 1. In addition, when a mixture of fluorinated surfactant CF<sub>3</sub>(CF<sub>2</sub>)<sub>3</sub>SO<sub>2</sub>NH(CH<sub>2</sub>)<sub>3</sub>N<sup>+</sup>(CH<sub>3</sub>)<sub>3</sub>I<sup>-</sup> (FC-4911) and CTAB was employed as the SDA, chiral ethenylene-bridged MONRs with twisted hexagonal rod-like morphology and phenylene-bridged MONRs with spiral hexagonal rod-like morphology were produced, respectively.<sup>183</sup> Both MONRs had very similar pore size of about 2 nm. The presence

of fluorinated surfactant was probably responsible for the formation of chiral structures. Such chiral ethylene-bridged MONRs could also be prepared using  $C_{18}TAB$  as a template and perfluorooctanoic acid (PFOA) as an additive as well as BTEE as the organosilica precursor under basic condition.<sup>184</sup> By increasing the weight ratio of perfluorooctanoic acid (PFOA)/ $C_{18}TAB$  in the reaction system, the morphology and pore structure arrays of MONRs obtained transformed from short non-helical to long helical nanorods with hexagonal symmetry, and finally to irregular small particles with concentric circular pore structure. For such case, on the one hand, PFOA molecules interacted with  $C_{18}TAB$  in the composite micelles affecting the mesostructure of MONRs. On the other hand, PFOA reduced the surface free energy of nanoparticles contributing to the formation of MONRs with increased aspect ratio. The long helical MONRs formed by twisting greatly reduced the surface free energy.<sup>93</sup> Moreover, by using (*S*)- $\beta$ -citronellol and CTAB as the co-structure-directing agents, helical ethylene-bridged MONFs with length of 0.2-2.0  $\mu m$  and diameter of 100-200 nm were obtained under basic conditions.<sup>185</sup> TEM images revealed that the MONFs had a hexagonal pore structure inside,

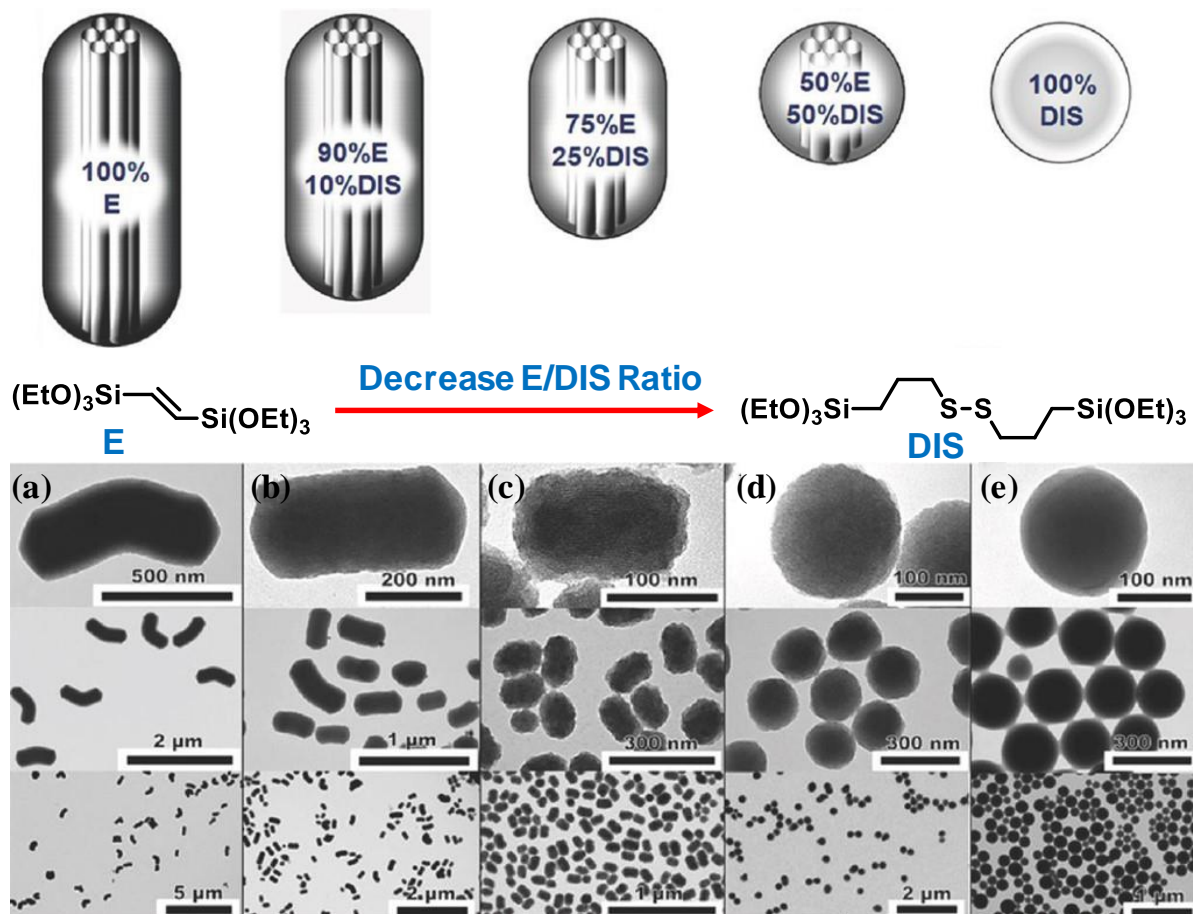


**Figure 1.17** Schematic illustration of MONRs and MONs with different morphologies and particle sizes synthesized by varying the weight ratio of E/DIS, (a-e) TEM images of MONRs and MONs constituted of weight ratio of E/DIS of 100/0, 90/10, 75/25, 50/50, and 0/100, respectively, reproduced from reference 187.

while a lamellar structure was formed on the surface. The lamellar structure was proposed to be formed by merging the hexagonally arranged cylinder-like micelles. When the ethylene-

bridge group of the organosilica precursor was replaced by methylene- or phenylene-bridge groups, methylene- and phenylene-bridged MONFs with helical morphologies were also obtained using the same templating agents.<sup>186</sup> Note that the co-condensation reaction of bis(triethoxysilyl)-ethene (E) and bis(propyl)disulfide (DIS) with different weight ratios led to the formation of ethenylene-bis(propyl)disulfide-based MONRs with various morphologies and particle sizes (Figure 1.17).<sup>187</sup> In the absence of DIS in the starting reaction system, a rod-like PMO material with 700 nm in length and 200 nm in diameter were obtained (Figure 1.17a). However, a single DIS precursor as an organosilica source only led to the formation of nonporous nanospheres with 200 nm in diameter (Figure 1.17e). In addition, the variation on the weight ratio of E/DIS markedly influenced the length and diameter of the MONRs as well as the monodispersity of MONs (Figure 1.17b-d).

## 1.8 Hollow Mesoporous Organosilica Nanoparticles (HMONs)

### 1.8.1 Soft Template Method

Similar to HMSNs, HMONs could also be synthesized by the soft template method. A partially fluorinated cationic surfactant ( $\text{CF}_3(\text{CF}_2)_7(\text{CH}_2)_2\text{PyCl}$  (Py: pyridinium) was used as the template for the formation of ethylene-bridged hollow organosilica nanoparticles.<sup>188</sup> The results confirmed that a hollow structure could only be produced using BTEE as the precursor, while bulky PMO materials were obtained using BTME as the precursor, due to the fast hydrolysis rate of BTME in the reaction system. Moreover, this fluorinated surfactant could also template octylene-bridged hollow organosilica nanoparticles with partially collapsed hollow structure. In addition, when using nonionic triblock copolymer F127 micelles as the hollow template, ethylene-bridged hollow organosilica nanoparticles could be synthesized in a neutral phosphate buffer solution.<sup>189</sup> The condensation of silicate oligomers around the individual micelle resulted in the formation of hollow nanoparticles with 18 nm in diameter and a hollow cavity about 5 nm as well as micropores of about 0.5 - 1.2 nm in the shell. When an appropriate amount of 1,3,5-trimethylbenzene (TMB) was used as an expander, the hollow cavity size could be enlarged to 15 nm.<sup>190</sup> By using FC-4 and CTAB as co-structure directing agents and BTME as the organosilica precursor, ethylene-bridged HMONs were obtained.<sup>191</sup> This novel vesicle and liquid crystal dual templating approach resulted in HMONs, showing highly ordered mesoporous wall structure, tunable particle size, and controllable wall thickness. Only by using CTAB as the SDA non-hollow MONs were produced.<sup>191</sup> The results revealed that the hollow cavity size increased with the increasing molecular ratio of FC-4/CTAB. HMONs with hollow cavity size of 50-100 nm and wall thickness of 20 nm were obtained at a FC-4/CTAB molecular ratio of 1.2. In addition, multilamellar shell structured ethylene-bridged HMONs could be fabricated using triblock copolymer P85 as the SDA under mild acidic conditions.<sup>192</sup> Both the mesostructure and the number of layers could be effectively controlled by changing the synthesis pH value. The resultant multilamellar organosilica vesicles featured

interconnected sponge-like walls with relatively large pores centered at 6 nm, making a convenient access of guest molecules.

HMONs could also be prepared by using emulsion droplets as the template and different organosilanes as the organosilica precursor. For example, BTEE was dispersed in a mixture of water and ethanol to form a stable oil (BTEE)-in-water emulsion, the hydrolysis of BTEE at the interface of the droplet generated organosilicate species simultaneously assembling with CTAB surfactant molecules to form HMONs.<sup>193</sup> In this process, CTAB not only stabilized the emulsion droplets, but also acted as the SDA for the formation of the mesoporous shell. The particle/cavity size and shell thickness of HMONs were readily controlled by the volume ratio of ethanol and water in the reaction mixture. Similarly, when a CTAB-stabilized oil (*n*-decane)-in-water emulsion was used as the hollow template and BTEE as the organosilica precursor, the hydrolyzed silicate species self-assembled with cationic surfactant around *n*-decane droplets to form HMONs.<sup>194</sup> Such HMONs displayed a particle size of 560 nm and a cavity size of 400 nm as well as radial oriented mesochannels in the shell after the removal of *n*-decane and CTAB by solvent extraction.

### 1.8.2 Hard Template Method

Any readily removable metal oxide/hydroxide/carbonate spheres or nonporous nonmetallic spheres can be used as a hard template. Similar to the preparation of HMSNs, the formation of HMONs often undergoes two steps. In general, the core-shell structured  $s\text{SiO}_2@PMO$  nanoparticles were first fabricated using  $s\text{SiO}_2$  spheres as the hard template, followed by removing the  $s\text{SiO}_2$  to form HMONs (Figure 1.18).<sup>195</sup> Due to the similarity of chemical structures between silicon alkoxides and bissilylated organic precursors, the preparation of  $s\text{SiO}_2@PMO$  nanoparticles was conducted by a one-pot, two-step procedure. The  $s\text{SiO}_2$  spheres could be selectively etched and the PMO shell was retained by treating as-made  $s\text{SiO}_2@PMO$  core-shell structured nanoparticles with either an alkaline solution or HF (Figure 1.18b, c). Various organic group (ethylene-/phenylene-/ethenylene)-bridged HMONs have been prepared by this strategy. Such organic group-bridged HMONs could be easily converted into hollow mesoporous carbonaceous nanocapsules by pyrolysis. Moreover, multiple-hybridized HMONs with varied organic functional groups which homogeneously incorporated into the framework were prepared by using the same procedure.<sup>196</sup> The resultant different organic groups (such as thioether, phenylene, ethylene, ethenylene, biphenyl) were uniformly incorporated into the PMO frameworks to form multifunctionalized HMONs, while hollow structure and monodispersity were preserved after removal of the hard template (Figure 1.18d). In addition, the pore size of HMONs could be enlarged. For example, phenylene-bridged HMONs obtained after etching  $s\text{SiO}_2$  were further hydrothermally treated to enlarge the pore size from initial 4.0 nm to as large as 20.4 nm in the shell, due to the selectively breakage of Si-C bonds in the frameworks and subsequent merging of small mesopores.<sup>197</sup>



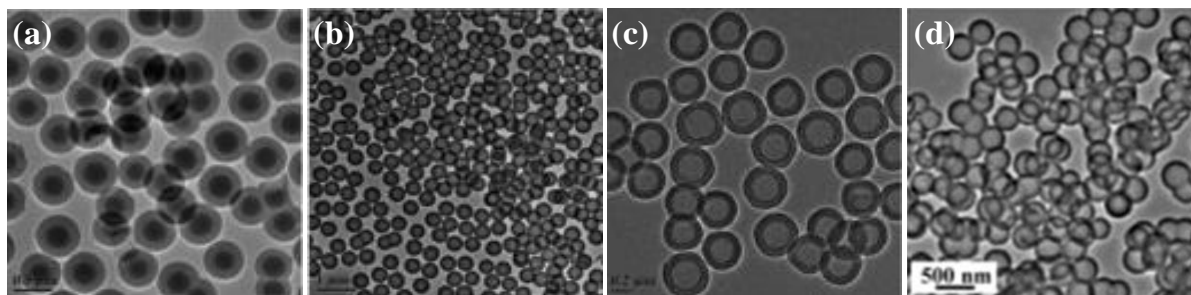


**Figure 1.18** TEM images of (a)  $s\text{SiO}_2$ @PMO core-shell structured nanoparticles, (b) HMONS obtained by treating  $s\text{SiO}_2$ @PMO nanoparticles with sodium carbonate, (c) HMONS obtained by treating  $s\text{SiO}_2$ @PMO nanoparticles with HF, reproduced from reference 195; (d) HMONS with thioether, phenylene, ethane, ethylene, biphenyl groups incorporated into the framework, reproduced from reference 196.

PS spheres could also be used as the template for the synthesis of ethylene-bridged HMONS.<sup>198</sup> Core-shell structured PS@PMO nanoparticles were formed first by coating PS spheres with a PMO shell using CTAB as the SDA. After removal of the PS spheres and CTAB molecules, monodisperse HMONS with a particle size of 240 nm and cavity size of 140 nm were obtained. In addition, metal oxides such as hematite ( $\text{Fe}_2\text{O}_3$ ) nanoparticles could also be used as the hard template to fabricate phenylene-bridged HMONS, which incorporated azidopropyl groups in the framework by co-condensation of the respective precursors around hematite nanoparticles.<sup>199</sup> After removal of the CTAB template and hematite nanoparticles via a solvent extraction process, the resulting HMONS featured a particle size of 100-200 nm and cavity size of 90 nm. Note that the incomplete removal of metal oxide can effectively affect the physical and chemical properties of HMONS.

### 1.9 Core-Shell Structured Mesoporous Organosilica Nanoparticles (CSMONs)

In 2010, Fröba and co-workers reported the preparation of CSMONs with  $s\text{SiO}_2$  core and phenylene-bridged PMO shell and found that the  $s\text{SiO}_2$  core could be partially dissolved under hydrothermal conditions, while the shell thickness and overall particle size remained unchanged.<sup>200</sup> CSMONs with  $\text{Co}_3\text{O}_4$  nanoparticle core and ethylene-bridged PMO shell were reported in 2012.<sup>201</sup>  $\text{Co}_3\text{O}_4$  nanoparticles with size of 10-20 nm were dispersed in an aqueous solution with the adsorbed CTAB molecules on their surface. The negatively charged silicate species derived from the hydrolysis and condensation of organosilane precursor assembled with CTAB molecules to form 130 nm sized core-shell structured nanoparticles. A two-photon photosensitizer with 4 trialkoxysilyl groups (2PS) was used as the organosilane precursor to fabricate core-shell structured nanoparticles (Au@MONs) with several Au nanoparticles embedded in the resultant nanoparticles (Figure 1.19a).<sup>202</sup> The construction of Au@MONs was conducted by a one-pot method with Au nanoparticles formed by autoreduction and subsequent coating with an organosilica shell in the same preparation solution. Due to the plasmonic resonance upon two-photons excitation, the obtained Au@MONs exhibited an enhanced two-photo absorption cross-section, making Au@MONs promising for bio-applications. By replacing 2PS with 1,2-bis(triethoxysilyl)ethylene or BTEB, CSMONs with one Au

nanoparticle in each ethylene- or phenylene-bridged MONs were obtained, respectively (Figure 1.19b, c).<sup>203</sup> The synthesis of Au@MONs could be further modified by co-condensation of 2PS with BTEE or BTEB to obtain the core-shell structured nanoparticles with mixed organic bridging groups in the shell (Figure 1.19d, e).

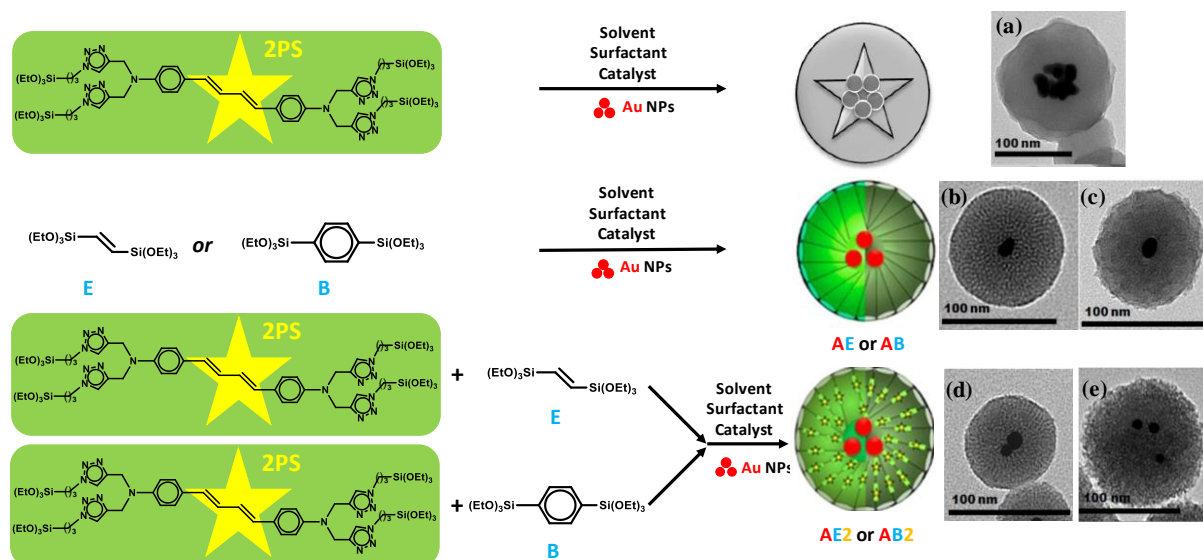


**Figure 1.19** Schematic illustrations and corresponding TEM images of Au@MONs core-shell structured nanoparticles with (a) 2PS, reproduced from reference 202; (b) ethylene-bridged PMO, (c) phenylene-bridged PMO, (d) 2PS-ethylene-mixed PMO, and (e) 2PS-phenylene-mixed PMO as shells, reproduced from reference 203.

Nonporous silica-coated magnetic  $\text{Fe}_3\text{O}_4$  nanoparticles  $\text{Fe}_3\text{O}_4@s\text{SiO}_2$  were used as the core to construct CSMONs  $\text{Fe}_3\text{O}_4@s\text{SiO}_2@PMO$  with ethylene-bridged PMO single crystals as the shell (Figure 1.20a).<sup>204</sup> In contrast to most core-shell structured nanoparticles with spherical morphology, the obtained  $\text{Fe}_3\text{O}_4@s\text{SiO}_2@PMO$  nanoparticles had an asymmetrical morphology with the  $\text{Fe}_3\text{O}_4@s\text{SiO}_2$  core partly covered with PMO cubes (Figure 1.20b-d). The positions of the cores were either in the middle or at a corner of the PMO cube. The same preparation solution was used to produce PMO nanocubes in the absence of  $\text{Fe}_3\text{O}_4@s\text{SiO}_2$  nanoparticles.<sup>173</sup> Therefore, the formation of this strange core-shell structure was attributed to a heterogeneous nucleation of PMO nanoparticles on parts of the surface of  $\text{Fe}_3\text{O}_4@s\text{SiO}_2$  nanoparticles and then an anisotropic growth of single crystal-like PMO nanocubes. By replacing the  $\text{Fe}_3\text{O}_4@s\text{SiO}_2$  core-shell structured nanoparticles with  $\text{UCNP}@s\text{SiO}_2@m\text{SiO}_2$  sandwich-structured nanoparticles (UCNP: upconversion nanoparticles), Janus mesoporous silica nanocomposites  $\text{UCNP}@s\text{SiO}_2@m\text{SiO}_2\&PMO$  containing a functional sandwich-structured mesoporous silica and a PMO nanocube were obtained (Figure 1.21).<sup>205</sup> The dual independent mesopores with distinct hydrophobicity/hydrophilicity were integrated into one unit. The UCNP core also endowed the nanocomposites with fluorescence and upconversion properties.

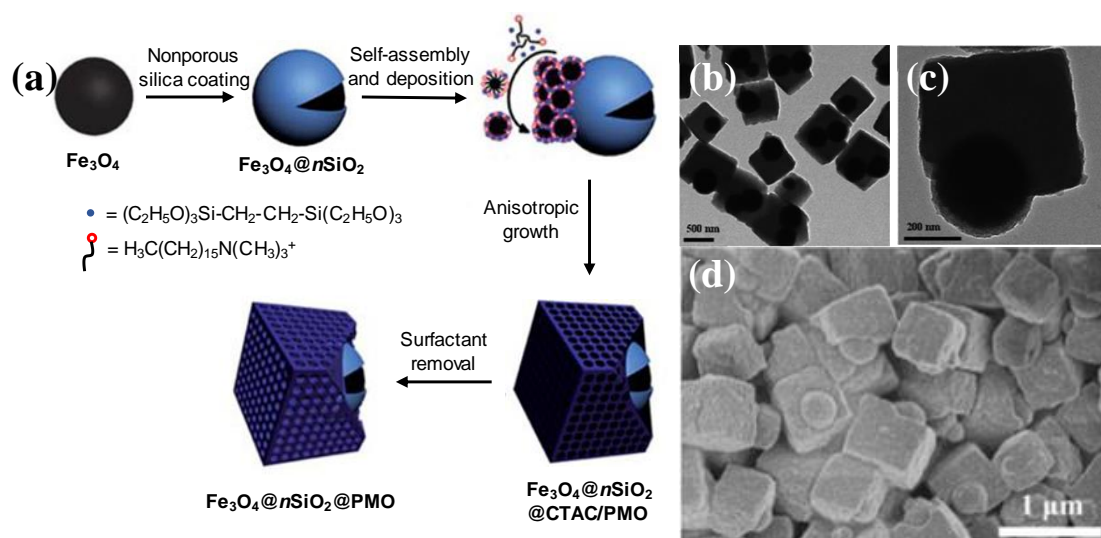


**Figure 1.20** (a) Schematic illustration of the preparation process of  $\text{Fe}_3\text{O}_4@s\text{SiO}_2@PMO$  nanoparticles with partly coated magnetic cores, and (b, c) TEM and (d) SEM images of the resultant  $\text{Fe}_3\text{O}_4@n\text{SiO}_2@PMO$  nanoparticles, reproduced from reference 204.

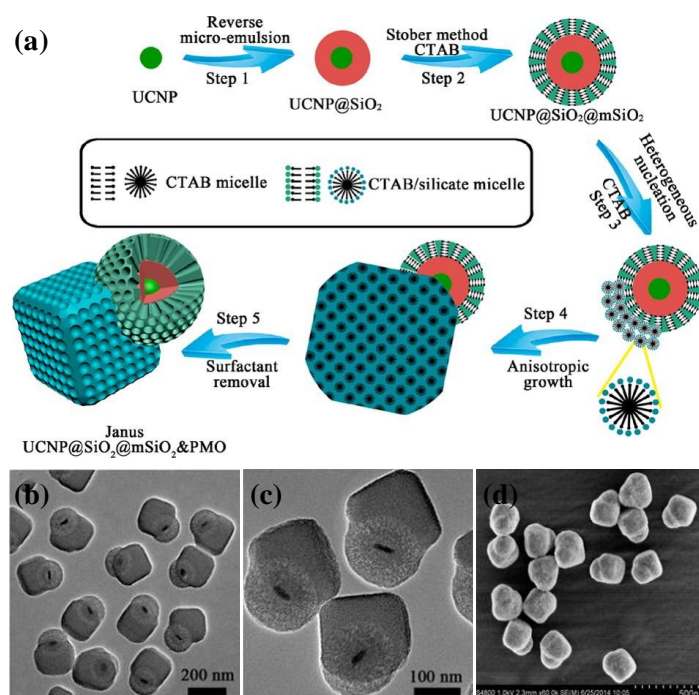


**Figure 1.21** (a) Schematic illustration of the preparation process of Janus  $\text{UCNP}@s\text{SiO}_2@m\text{SiO}_2@PMO$  nanocomposites, and (b, c) TEM and (d) SEM image, reproduced from reference 205.

### 1.10 Yolk-Shell Structured Mesoporous Organosilica Nanoparticles (YSMONs)

Lu and co-workers extended the vesicle approach of preparing HMONs to the synthesis of magnetic YSMONs with an ethylene-bridged organosilica shell.<sup>206</sup> FC-4 vesicles-encapsulated CTAB-stabilized magnetic  $\text{Fe}_3\text{O}_4$  nanocrystals were coated via the addition of BTME under basic conditions to form composite micelles surrounding the vesicles. These further condensed to fabricate a novel PMO magnetic hollow sphere (PMO-MHS),  $\text{Fe}_3\text{O}_4@MONs$ . Along with

the self-assembly of silicate species with CTAB around the vesicles, Fe<sub>3</sub>O<sub>4</sub> nanocrystals were entrapped into the hollow cavity of the resultant Fe<sub>3</sub>O<sub>4</sub>@MONs yolk-shell structured nanoparticles. For Fe<sub>3</sub>O<sub>4</sub>@MONs, TEM images and PXRD pattern confirmed that the PMO shell had an ordered hexagonal mesostructure. With increasing amounts of FC-4 from 0.3 to 0.75 g in the starting reaction system, the particle size and shell thickness decreased from 230 to 130 nm and from 75 to 15 nm, respectively.

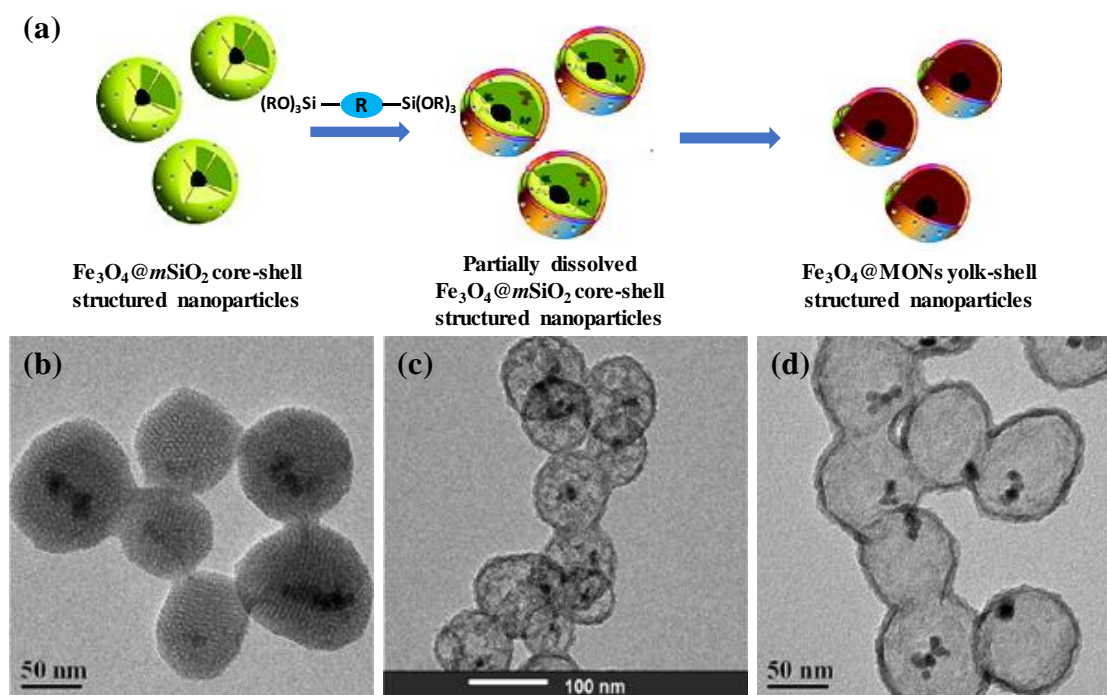


**Figure 1.22** (a) Schematic illustration of the formation of Fe<sub>3</sub>O<sub>4</sub>@MONs yolk-shell structured nanoparticles, TEM images of (b) Fe<sub>3</sub>O<sub>4</sub>@mSiO<sub>2</sub> core-shell structured nanoparticles, and nanoparticles after adding BTMM for (c) 5 min and (d) 60 min, reproduced from reference 207.

An organosilane-assisted etching approach was developed by Yang and co-workers for the transformation of core-shell structured nanoparticles to yolk-shell structured nanoparticles (Figure 1.22).<sup>207</sup> Fe<sub>3</sub>O<sub>4</sub>@mSiO<sub>2</sub> core-shell structured nanoparticles could transform into yolk-shell structured nanoparticles Fe<sub>3</sub>O<sub>4</sub>@MONs after adding an organosilane precursor (bis(trimethoxy-silyl)methane (BTMM) or BTEB) into the same preparation solution. The structure transformation was achieved within 60 min but the average particle sizes kept almost constant at 100 nm (Figure 1.22b, d). Detailed investigations revealed that the formation of the mesoporous organosilica shell was accompanied by the gradual dissolution of mesoporous silica (Figure 1.22c). The selective etching of the mesoporous silica shell during the transformation process was attributed to the unbalance between hydrolysis and condensation of mesoporous silica in the synthesis system. The addition of organosilane into the synthesis system induced the gradual hydrolysis of preformed mesoporous silica into silicate oligomers, which further re-condensed with organosilica to form the shell around Fe<sub>3</sub>O<sub>4</sub>@mSiO<sub>2</sub> core-shell structured nanoparticles. This synthesis strategy for YSMONs has been applied to prepare

yolk-shell structured nanoparticles  $m\text{SiO}_2@\text{PMO}$ ,<sup>208</sup>  $\text{Au}@\text{phenylene-bridged MONs}$ <sup>209</sup> and  $\text{Fe}_3\text{O}_4@\text{MONs}$ <sup>210</sup> as well as hollow structured ethylene-bridged HMONs.<sup>209</sup>

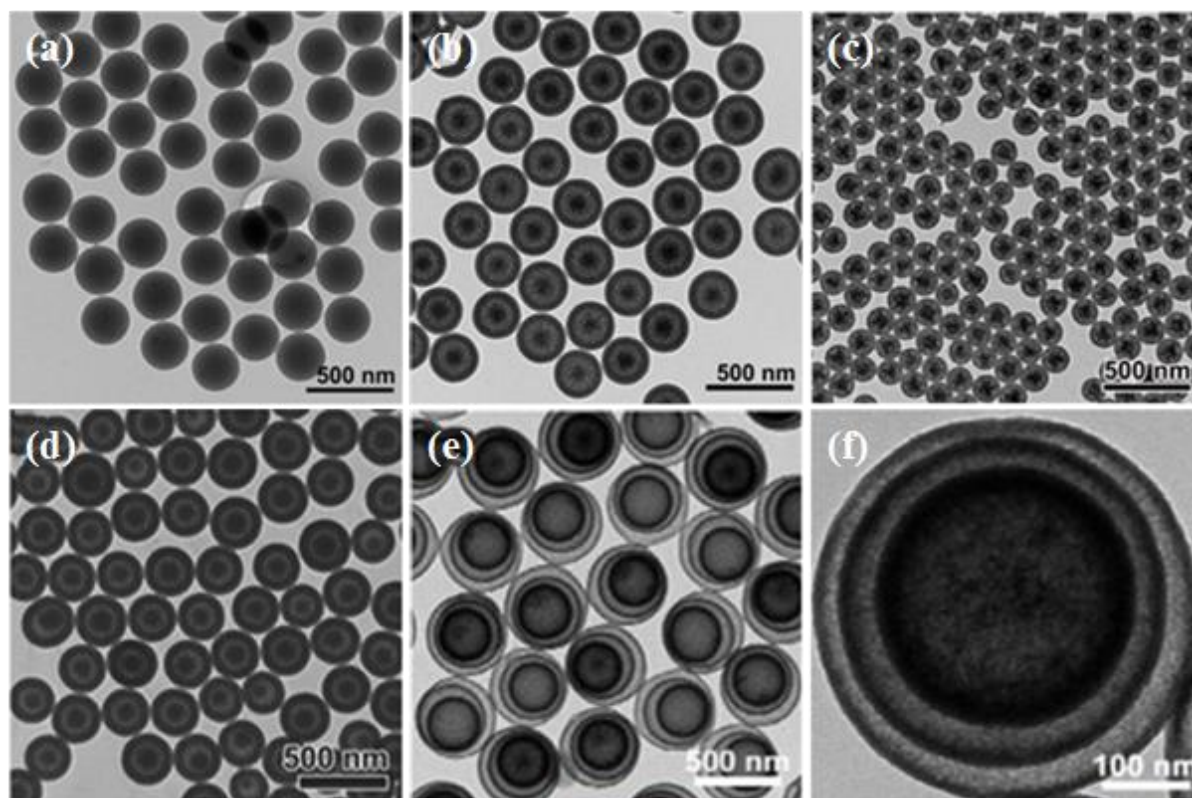


**Figure 1.23** TEM images of (a) as-synthesized organic-inorganic hybrid nanospheres, and (b) after incubating in water at 70 °C for 12 h, reproduced from reference 211; (c) yolk-shell structured nanospheres with thioether-bridged group incorporated in the framework, reproduced from reference 212; (d) yolk-shell structured nanospheres with ethylene, thioether, and phenylene bridged groups incorporated in the framework, reproduced from reference 213; (e, f) triple-shelled nanospheres, reproduced from reference 214.

The dissolution and re-assembly of silicate species is another method for preparing YSMONs.<sup>211</sup> Organic-inorganic hybrid nanospheres with uniform size of 270 nm and radially oriented pore structure were first prepared by using TEOS and BTEE as precursors and CTAB as SDA via the modified Stöber method (Figure 1.23a). After incubation with water at 70 °C for 12 h, the spheres transformed into a yolk-shell structure with original uniform morphology and particle size (Figure 1.23b). Both the core and shell were composed of organic-inorganic hybrid silica. Such transformation of nanospheres from solid into yolk-shell structure was attributed to the dissolution of silicate-CTAB composites with low condensation degree in the inner part of the nanosphere. The dissolved silicate-CTAB composites then re-assembled into the core and shell regions, producing the final yolk-shell structured nanospheres. The particle/core size and shell thickness of the yolk-shell structured nanospheres were controllable in the ranges of 380-120/120-50 nm and 50-13 nm, respectively, by adjusting the reaction parameters including CTAB concentration, ethanol/water ratio and precursor content. By using bis(triethoxysilyl)propane tetrasulfide as the organosilane precursor, yolk-shell structured

nanospheres with thioether-bridged functional groups in the framework were obtained (Figure 1.23c).<sup>212</sup> Triple-hybridized yolk-shell structured nanospheres containing ethylene-, thioether-, and phenylene-bridged functional groups incorporated into the framework have also been prepared by using the corresponding bridged silanes as precursors (Figure 1.23d).<sup>213</sup> When the as-synthesized hybrid spheres were prepared by stepwise adding TEOS and BTEE into the Stöber solution, hollow spheres with multi-shells were obtained after hydrothermal treatment (Figure 1.23e, f).<sup>214</sup> The number of the shells (1-4) depended on the addition time of the silane precursors. The organic bridged functional groups in each shell could also be varied by changing the organosilane in each adding sequence.

## 1.11 Applications

Owing to the high surface area, tunable pore diameter, large pore volume, various pore structures and modifiable surface physical and chemical properties, mesoporous silica nanostructured materials have been extensively used as adsorbent for small molecules or biomacromolecules, as support for preparing heterogeneous catalysts, as carrier for drug delivery and release, and as a template for fabricating new materials. Especially, monodisperse mesoporous silica nanospheres exhibit excellent application potentials in biomedicine due to their biocompatibility. In this section, the applications of monodisperse mesoporous (organo)silica nanoparticles will be addressed as follows.

### 1.11.1 Adsorption

It is well known that mesoporous (organo)silica nanostructured materials with tailorable mesostructure, large surface area and high pore volume are promising for the adsorption of various molecules. Note that the adsorption amount depends on the surface hydrophilicity and functional groups of MSNs. For example, when template of as-made MSNs was removed by solvent extraction. The obtained MSNs showed a high Rhodamine B (RhB) adsorption capacity (124 mg/g) compared to that (70 mg/g) of MSNs gained by calcination at high temperature.<sup>42</sup> This was caused by the highly hydrophilic surface of solvent-extracted MSNs. For both solvent-extracted and calcined MSNs the adsorption behaviors were in good agreement with a pseudo-second-order kinetic model, indicating that the interaction between the negatively charged pore surface and positively charged RhB molecules was the rate-determining step of adsorptions. Ethylene-bridged HMONs could rapidly adsorb toluene from aqueous solution, due to the high surface area, hollow structure and amphiphilic frameworks.<sup>209</sup> It is well known that phosphate is one of the major nutrients in water and causes the eutrophication. As an outstanding adsorbent, sandwich-structured magnetic  $\text{Fe}_3\text{O}_4@\text{sSiO}_2$ @mesoporous aluminosilicate nanoparticles could efficiently remove phosphate from waste water compared to  $\text{Fe}_3\text{O}_4@\text{sSiO}_2$ @dendritic  $m\text{SiO}_2$  with the same pore size, due to the strong acidic sites of Al-incorporated mesoporous aluminosilicate frameworks.<sup>154</sup> Microcystins are extremely toxic disocyclic heptapeptides that exist in eutrophic water. Hence, the removal of microcystins is of

considerable importance in terms of environment protection. Mesoporous silica nanomaterials with similar pore size as the hydrodynamic size of microcystin of around 3.0 nm could adsorb microcystin into the mesoporous silica channels. Sandwich-structured  $\text{Fe}_3\text{O}_4@s\text{SiO}_2@m\text{SiO}_2$  nanoparticles could effectively remove more than 95% of microcystins in aqueous solution within 60 s.<sup>148</sup> The magnetic property of the nanoparticles made easy separation from the solution and the high removal efficiency was still retained even after eight times reuse.

The pore size of mesoporous silica has a significant impact on the immobilization of biomacromolecules, such as proteins or DNA.<sup>215</sup> Cytochrome c (Cyt C) with a molecular dimension of  $2.6 \times 3.2 \times 3.3$  nm was immobilized into MSNs.<sup>63</sup> It was found that the loading amount of Cyt C depended on the pore size of MSNs. With increasing pore size from 2.7 to 4.0 nm, the loading amount of Cyt C gradually increased from 32 to 230  $\text{mg g}^{-1}$ . However, when the pore size of MSNs reached to 4.6 nm, the loading amount decreased to 190  $\text{mg g}^{-1}$ . A similar adsorption tendency has also been observed for a series of ethylene-bridged PMO nanorods with same pore symmetry ( $p6mm$ ) and pore sizes of 2.6-7.3 nm for peptide (E7 peptide) enrichment.<sup>216</sup> The highest enrichment performance was achieved by nanorods with a pore size of 5.8 nm. Oppositely, for nanorods with larger pore size, a lower loading amount was attributed to an easy escape of adsorbed peptide from pores. The pore volume is another factor for influencing the adsorption of biomacromolecules. For example, the increase of pore volume also led to the increase of loading capacities for immunoglobulin G (IgG) and  $\beta$ -galactosidase ( $\beta$ -Gal).<sup>84</sup> The effect of pore volume could also embody on HMSNs for the loading of protein. HMSNs with the largest pore volume resulted in the highest loading amount of Cyt C.<sup>109</sup> It is noted that the morphology of MSNs also influenced the adsorption rate. HMSNs with regular morphology showed much faster lysozyme adsorption rate than those with large and irregular shaped morphologies.<sup>102</sup> It is believed that the uniform morphology enables short mass transport path through the pores into the hollow interior of HMSNs.<sup>114</sup> The adsorption capacities of mesoporous silica and PMO towards Cyt C were compared by using SBA-15 nanorods and PMO nanorods with similar pore size and pore structure as the adsorbents.<sup>180</sup> The results demonstrated a higher loading capacity for SBA-15 nanorods than that of PMO nanorods and the maximum loading amounts were reached around the isoelectric point of Cyt C in both cases, implying the electrostatic interaction between Cyt C and adsorbent was more dominant than the hydrophobic interaction in the immobilization process. The stability and activity of protein were improved after immobilization on the mesoporous (organo)silica nanomaterials. The resultant protein-mesoporous (organo)silica hybrid materials could be used in catalysis,<sup>201</sup> and size-selective enzymolysis of low molecular proteins.<sup>153</sup>

### 1.11.2 Biomedical Applications

Another area of great interest for monodisperse mesoporous (organo)silica nanomaterials is concerned with biomedical applications. The adjustable particle size, tunable morphology and controllable mesostructure enable the modulation of biological interactions. For example,

MSNs could be internalized by cell with the uptake amount depended on the particle size.<sup>39</sup> It was found that the maximum uptake by cells occurred at a nanoparticle size of 50 nm. Surface PEG-modified MSNs could prevent from particle aggregation and improve the stability in physiological environment.<sup>60</sup> The co-condensation of TEOS and fluorescent silane resulted in fluorescent MSNs, making the nanoparticles easily detectable after cellular uptake.<sup>35,39,60</sup> Compared with MSNs, MONs showed low hemolytic activity and improved biocompatibility due to the lower density and lower acidity of silanol groups on the surface.<sup>174</sup>

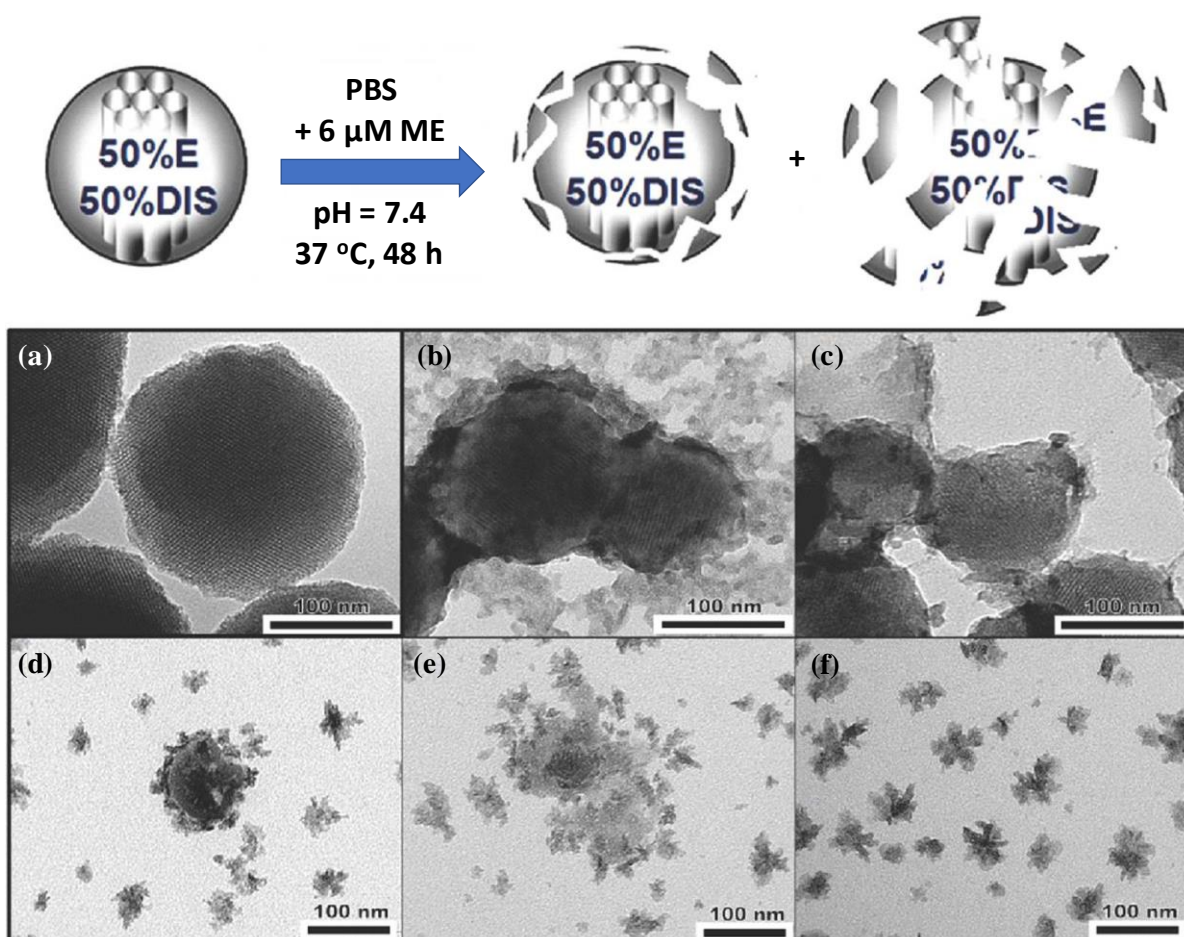


**Figure 1.24** TEM images of ethylene-bis(propyl)disulfide-based MONs EDIS 50/50 nanoparticles (a) before and (b-f) after 48 h of degradation in physiological conditions, reproduced from reference 187.

Both MSNs and MONs have been exploited as drug delivery agents for potential biomedical applications. Among these drug delivery systems, the degradation of nanoparticles induced drug delivery is quite interesting and promising.<sup>82,187,196</sup> Ethylene-bis(propyl)disulfide-based MONs (EDIS 50/50) could be quickly degraded into small fragments after incubation in physiological conditions for 48 h (Figure 1.17, Figure 1.24).<sup>187</sup> In contrast, pure ethylene-bridged MONs were not degraded under identical conditions. The fast degradation of EDIS 50/50 was due to the presence of the disulfide bond within the framework, which could be easily broken under the weakly acidic physiological conditions. When the cancer killing drug doxorubicin (DOX) was loaded into the MONs, the degradation of nanoparticles under acidic



conditions initiated the controlled release of DOX. The pH responsive release was proved by a no release in neutral solution, while instantaneous DOX release occurred when the pH value of the solution was adjusted to 5.5. It was also observed that the DOX loaded MONs were endocytosed by the cancer cells and mainly located in the lysosomes. The weakly acidic condition in the lysosomal compartments induced the degradation of MONs and DOX release in the cancer cell. A significant cancer cell death was therefore detected.

The release of guest molecules can be achieved by a controlled and programmed sequence through the design of the core/yolk-shell structure.<sup>155,217</sup> Yolk-shell structured MSNs with IBN-1 typed MSNs as the core and mesoporous silica as the shell were used as a delivery agent of ibuprofen.<sup>217</sup> A three-stage release profile was observed. The rapid release during the first 5 h was due to ibuprofen adsorbed on the external surface of MSNs. The second release stage from 5 to 8 h was attributed to the ibuprofen absorbed in the shell and inner hollow spaces. The release of ibuprofen absorbed in the core contributed to the last stage of release. A quite similar three-stage release profile was also observed when using hierarchical core-shell structured MSNs as a delivery agent.<sup>155</sup> The ibuprofen molecules adsorbed on different locations of MSNs had distinct release rates, and therefore contributed to the stage release profile. In addition, the release rates of ibuprofen could be controlled by changing the shell thickness of the core-shell structured MSNs, further proving that the release was affected by the structure of MSNs.

Shi and co-workers applied phenylene-tetrasulfide-based HMONS in the multi-responsive controlled release of DOX (Figure 1.25).<sup>196</sup> The incorporation of phenylene and tetrasulfide within the framework of HMONS facilitated the loading of DOX via both  $\pi$ - $\pi$  stacking and hydrophobic-hydrophobic interactions, which contributed to a loading amount as high as 148 mg g<sup>-1</sup>. The breakage of thioether bonds (-S-S-) in the framework could be induced by the reductant glutathione (GSH). Therefore, the  $\pi$ - $\pi$  stacking and hydrophobic-hydrophobic interaction between DOX molecules and the HMONS framework would be disturbed, triggering the substantial release of DOX. The release rate of DOX depended on the concentration of GSH in the solution (Figure 1.25b). Furthermore, the thioether bond could also be broken by ultrasonic cavitation. The application of high-intensity focused ultrasound (HIFU) induced the controlled release of DOX with the release amount easily controlled by the intensity and the ON/OFF status of ultrasound (Figure 1.25c).

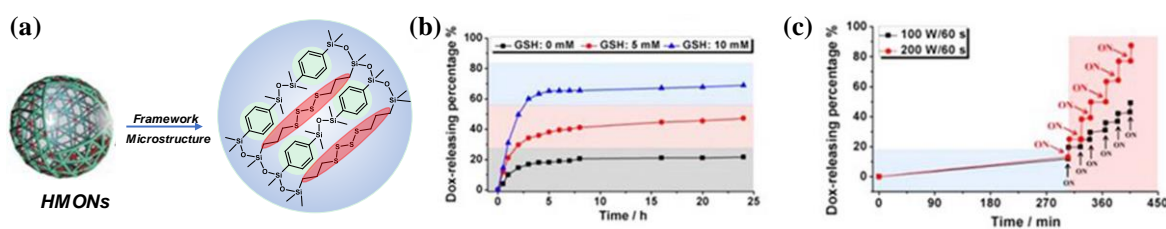


**Figure 1.25** (a) Schematic illustration of the framework composition of HMONS, (b) cumulative DOX release profiles at the GSH concentrations of 0, 5, and 10 mM, respectively, and (c) HIFU-triggered DOX release profiles at different power densities, reproduced from reference 196.

### 1.11.3 Catalysis

The application of MSNs in catalysis involves the derivatization with catalytic units through surface functionalization,<sup>218,219</sup> metal substitution within the silica framework,<sup>70</sup> or grafting metallic nanoparticles onto the mesochannel. Monodisperse sulfonic acid-functionalized MSNs were used as a catalyst in the condensation reaction of acetone and 2-methylfuran.<sup>218</sup> It was found that the catalytic activity highly depended on the particle size and morphology. Compared with mesoporous silica with irregular morphology, monodisperse MSNs with radially aligned pore structure provided more pore entrances, and thus showed an enhanced catalytic activity. The particle size influenced the diffusion rates of reactants and products. Smaller particles enabled faster diffusion through the shortened mesopore channels and contributed to higher catalytic activity. For example, Ti-substituted MSNs-catalyzed alkene epoxidation confirmed that a smaller particle size led to higher catalytic activity due to a beneficial mass transport.<sup>70</sup> Au-loaded amino group-modified MSNs displayed an excellent catalytic performance in 4-nitrophenol reduction.<sup>81</sup> Pd-loaded amino group-modified MSNs demonstrated a high and stable activity in the catalytic Suzuki-Miyaura cross-coupling reaction of bromobenzene with phenylboronic acid.<sup>83</sup> The particle size of all Au and Pd was 1-2 nm.

Catalytically active units, such as Au and Pt nanoparticles,<sup>124,138,139,166,171</sup> zeolites and metal loaded zeolites,<sup>156-158</sup> as well as MOFs<sup>159</sup> could be encapsulated by a mesoporous silica shell to form core-shell or yolk-shell structures. The roles of the mesoporous silica shell was embodied in i) preventing the core nanoparticles from aggregation at high reaction temperature and therefore improved catalytic performance,<sup>138</sup> ii) enhancing a high catalytic selectivity due to the synergetic interactions between mesoporous silica shell and porous core,<sup>156</sup> and iii) greatly increasing the mechanical strength of core nanoparticle MOFs.<sup>159</sup> Moreover, the mesoporous shell could also be modified with catalytically active species by Al substitution<sup>124</sup> and grafting of metallic nanoparticles.<sup>158,199</sup> In some cases, the core/yolk-shell structured MSNs with functional core and modified mesoporous shell adapted different roles in the multistep catalytic reactions.<sup>124,158,208</sup> For example, yolk-shell structured Au/Pd@mesoporous aluminosilica nanoparticles (Pd/Au@[Na]-HMAS) were employed in the sequence reaction involving the reaction of 4-nitrobenzaldehyde and 1,2-phenylenediamine to 2-(4-nitrophenyl)-1*H*-benzimidazole, and further to 2-(4-aminophenyl)-1*H*-benzimidazole catalyzed by the aluminosilica shell and Au/Pd core, respectively (Figure 1.26).<sup>124</sup> The conversion of the reaction was nearly 100% with 92% yield of final product. In contrast, the absence of either the acidic aluminosilica shell or the Au/Pd nanoparticles as core did not give the conversion of the reactants into the final product. Furthermore, the catalytic activity was still retained in five successive cycles. In the study reported by Xu and co-workers, TS-1 zeolite particles were encapsulated by mesoporous silica, forming core-shell structured TS-1@MSNs nanoparticles.<sup>158</sup> After the grafting of Au nanoparticles onto the mesoporous silica shell, the core-shell structured nanoparticles served as a bifunctional catalyst in the direct epoxidation of

propylene with  $H_2$  and  $O_2$ . The reaction involved the *in situ* formation of  $H_2O_2$  as an intermediate catalyzed by Au nanoparticles, and the subsequent oxidation of propylene with  $H_2O_2$  catalyzed by the TS-1 core. Yang and co-workers demonstrated the deacetalization-Henry cascade reaction catalyzed by the yolk-shell structured nanoparticles with an amino-functionalized mesoporous silica core and a sulfonic acid-functionalized mesoporous organosilica shell.<sup>208</sup> The deacetalization reaction was first catalyzed by the sulfonic acid group in the shell, followed by the Henry reaction catalyzed by the amino group in the core. The sequential reactions occurring in one yolk-shell nanostructure displayed 100% conversion and selectivity.

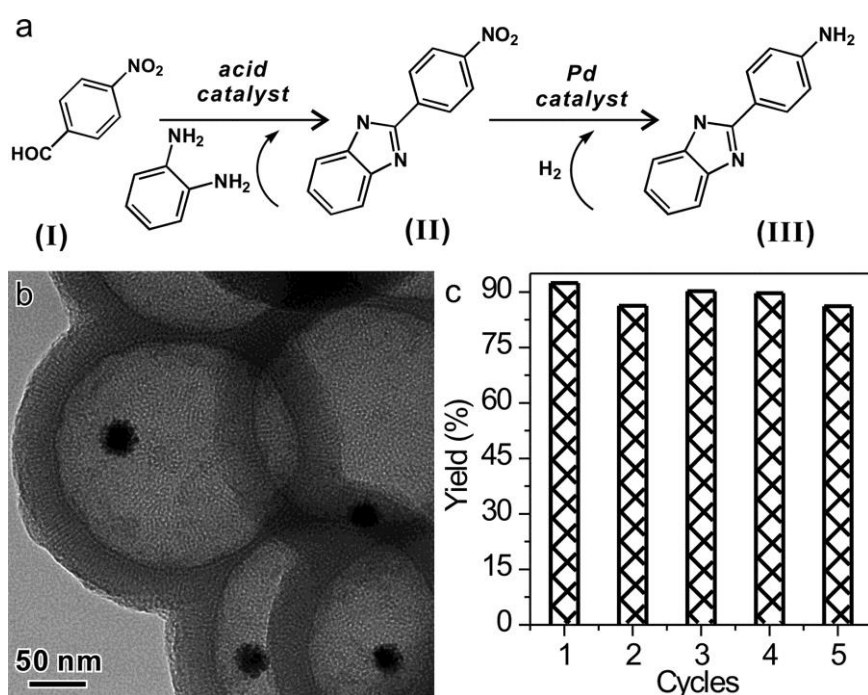


**Figure 1.26** (a) Schematic illustration of the two-step sequence reaction involving an acid catalysis and subsequent catalytic reduction for the synthesis of 2-(4-aminophenyl)-1H-benzimidazole, (b) TEM images of Pd/Au@[Na]-HMAS, and (c) synthesis yield of 2-(4-aminophenyl)-1H-benzimidazole in five successive reactions with Pd/Au@[Na]-HMAS, reproduced from reference 124.

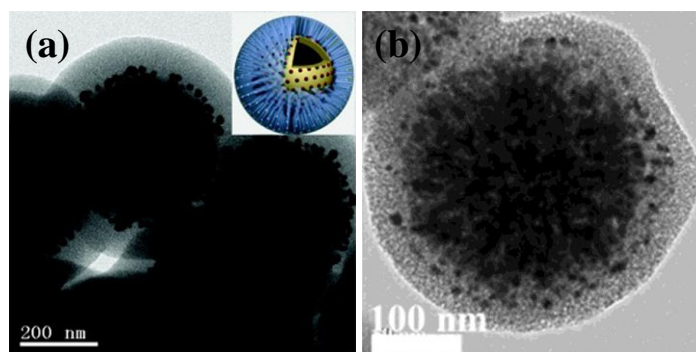


**Figure 1.27** TEM images of core-shell structured nanoparticles with a transitional layer of metal nanoparticles: (a)  $Fe_3O_4@sSiO_2-Au@mSiO_2$ , reproduced from reference 149; (b)  $Fe_3O_4@C-Pd@mSiO_2$ , reproduced from reference 150.

Catalytically active metallic nanoparticles could be immobilized as a layer in core-shell structured nanoparticles (Figure 1.27).<sup>149,150</sup> Magnetically separable catalysts made of a  $s\text{SiO}_2$ /carbon-coated magnetite nanoparticle core, transitional layer of active metal (Au, Pd, Pt) nanoparticles and an outer shell of ordered mesoporous silica were synthesized. The magnetic core endowed the core-shell structured nanoparticles with a convenient separability from the catalysis system. The mesoporous silica shell not only protected the immobilized metal nanoparticles from detaching, but also enabled easy access of the substrate through the mesochannels to the metallic nanoparticles. These multifunctional nanoparticles were used as the catalysts in the epoxidation of styrene, reduction of 4-nitrophenol, and Suzuki-Miyaura cross-coupling reaction, demonstrating excellent and stable catalytic performances.

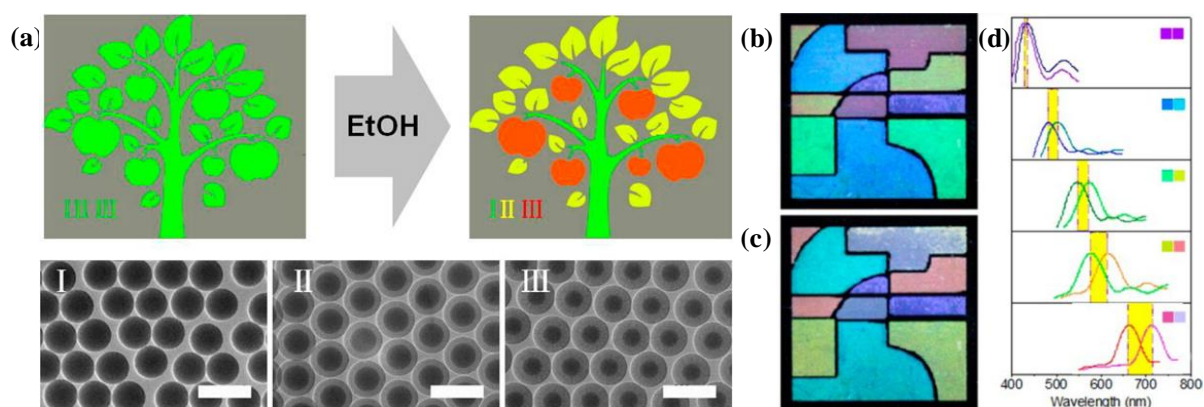


**Figure 1.28** (a) An implicit image made of  $s\text{SiO}_2$  nanospheres and  $s\text{SiO}_2@m\text{SiO}_2$  core-shell structured nanoparticles that exhibits distinct colors in ethanol atmosphere; image made of multicolor colloidal photonic crystals in (b) nitrogen and (c) saturated ethanol atmospheres, (d) reflection spectra of the multicolor colloidal photonic crystals in nitrogen and saturated ethanol atmospheres, each reflection spectrum was marked by colors of corresponding patterns in (b) and (c), reproduced from reference 221.

#### 1.11.4 Formation of Colloidal Crystals

Due to their three-dimensionally periodic refractive indices and interstitial ordered pores, colloidal crystals prepared by the assembly of colloidal particles have been investigated for various applications such as photonic crystals, sensors, and templates.<sup>77</sup> For colloidal crystals composed of MSNSs, hierarchical pore structures consisted of interstitial pores formed by the stacking of MSNSs, while the mesopores of MSNSs provided more opportunities for effective use of colloidal crystals. A series of MSNSs with sizes less than 110 nm were synthesized by Yamada and co-workers through the seed-growth process, in which spontaneous nucleation and aggregation of nanoparticles were avoided.<sup>77</sup> The resultant MSNSs with uniform sizes and smooth surfaces were compacted into colloidal crystals by simply drying the colloidal suspensions. For the preparation of such colloidal crystals, the MSNs should meet two requirements: i) monodispersity in terms of uniform size and shape, and ii) colloidal stability to enable thermodynamically favorable assemblies. Monodisperse MSNSs with an average size of 473 nm and a size standard deviation of 4.0% were compacted into a colloidal crystal film.<sup>220</sup>

Because of the condensation of water vapor into the mesoporous channels, the optical color of the colloidal crystal film could be adjusted by exposing it to water vapor with different relative pressures. The film exhibited pale blue and pale pink color when exposed to water vapor with relative pressure of 0.2 and 0.8, respectively. The color change could be reversed over 5 cycles by varying the relative pressure between 0.2 and 0.8. In contrast, no color change occurred in the case of the colloidal crystal film fabricated from  $s\text{SiO}_2$ . If  $s\text{SiO}_2@m\text{SiO}_2$  core-shell structured nanoparticles were used to fabricate colloidal photonic crystals (Figure 1.28),<sup>221</sup> the resultant crystals showed different colors in nitrogen and saturated ethanol atmospheres. The color change was caused by vapor condensation into the mesopores, resulting in the great increase of the reflection index of the core-shell structured nanoparticles  $s\text{SiO}_2@m\text{SiO}_2$ . Furthermore, the original color and the vapor-induced color of colloidal photonic crystals could be precisely controlled by adjusting the size and mesopore proportion of the core-shell structured nanoparticles. The implicit images fabricated by multicolor colloidal photonic crystals with distinct vapor-induced colors could exhibit the hidden information when exposed to a different atmosphere.

## 1.12 References

1. C. J. Brinker, Y. F. Lu, A. Sellinger and H. Y. Fan, *Adv. Mater.*, **1999**, 11, 579-585.
2. S. Mann, *Nature*, **1993**, 365, 499-505.
3. I. A. Aksay, M. Trau, S. Manne, I. Honma, N. Yao, L. Zhou, P. Fenter, P. M. Eisenberger and S. M. Gruner, *Science*, **1996**, 273, 892-898.
4. A. H. Heuer, D. J. Fink, V. J. Laraia, J. L. Arias, P. D. Calvert, K. Kendall, G. L. Messing, J. Blackwell, P. C. Rieke, D. H. Thompson, A. P. Wheeler, A. Veis and A. I. Caplan, *Science*, **1992**, 255, 1098-1105.
5. C. T. Kresge, M. E. Leonowicz, W. J. Roth, J. C. Vartuli and J. S. Beck, *Nature*, **1992**, 359, 710-712.
6. J. S. Beck, J. C. Vartuli, W. J. Roth, M. E. Leonowicz, C. T. Kresge, K. D. Schmitt, C. T. W. Chu, D. H. Olson, E. W. Sheppard, S. B. McCullen, J. B. Higgins and J. L. Schlenker, *J. Am. Chem. Soc.*, **1992**, 114, 10834-10843.
7. Y. Wan and D. Zhao, *Chem. Rev.*, **2007**, 107, 2821-2860.
8. S. Inagaki, S. Guan, Y. Fukushima, T. Ohsuna and O. Terasaki, *J. Am. Chem. Soc.*, **1999**, 121, 9611-9614.
9. T. Asefa, M. J. MacLachlan, N. Coombs and G. A. Ozin, *Nature*, **1999**, 402, 867-871.
10. B. J. Melde, B. T. Holland, C. F. Blanford and A. Stein, *Chem. Mater.*, **1999**, 11, 3302-3308.
11. N. Mizoshita, T. Tani and S. Inagaki, *Chem. Soc. Rev.*, **2011**, 40, 789-800.
12. J. G. Croissant, X. Cattoën, M. W. C. Man, J.-O. Durand and N. M. Khashab, *Nanoscale*, **2015**, 7, 20318-20334.
13. A. Comotti, S. Bracco, P. Valsesia, M. Beretta and P. Sozzani, *Angew. Chem. Int. Ed.*, **2010**, 49, 1760-1764.
14. X. S. Zhao, G. Q. M. Lu and G. J. Millar, *Ind. Eng. Chem. Res.*, **1996**, 35, 2075-2090.
15. U. Ciesla and F. Schüth, *Microporous Mesoporous Mater.*, **1999**, 27, 131-149.
16. H. P. Lin and C. Y. Mou, *Acc. Chem. Res.*, **2002**, 35, 927-935.
17. C. T. Kresge and W. J. Roth, *Chem. Soc. Rev.*, **2013**, 42, 3663-3670.
18. S.-H. Wu, C.-Y. Mou and H.-P. Lin, *Chem. Soc. Rev.*, **2013**, 42, 3862-3875.
19. E. Yamamoto and K. Kuroda, *Bull. Chem. Soc. Jpn.*, **2016**, 89, 501-539.

20. Y. Chen and J. Shi, *Adv. Mater.*, **2016**, 28, 3235-3272.
21. C.-Y. Lai, B. G. Trewyn, D. M. Jeftinija, K. Jeftinija, S. Xu, S. Jeftinija and V. S. Y. Lin, *J. Am. Chem. Soc.*, **2003**, 125, 4451-4459.
22. A. Popat, S. B. Hartono, F. Stahr, J. Liu, S. Z. Qiao and G. Q. Lu, *Nanoscale*, **2011**, 3, 2801-2818.
23. S. Angelos, M. Liong, E. Choi and J. I. Zink, *Chem. Eng. J.*, **2008**, 137, 4-13.
24. B. G. Trewyn, S. Giri, I. I. Slowing and V. S. Y. Lin, *Chem. Commun.*, **2007**, 3236-3245.
25. M. Grün, I. Lauer and K. K. Unger, *Adv. Mater.*, **1997**, 9, 254-257.
26. C. E. Fowler, D. Khushalani, B. Lebeau and S. Mann, *Adv. Mater.*, **2001**, 13, 649-652.
27. Q. Cai, Z. S. Luo, W. Q. Pang, Y. W. Fan, X. H. Chen and F. Z. Cui, *Chem. Mater.*, **2001**, 13, 258-263.
28. R. I. Nooney, D. Thirunavukkarasu, Y. M. Chen, R. Josephs and A. E. Ostafin, *Chem. Mater.*, **2002**, 14, 4721-4728.
29. B. G. Trewyn, I. I. Slowing, S. Giri, H.-T. Chen and V. S. Y. Lin, *Acc. Chem. Res.*, **2007**, 40, 846-853.
30. Y. Chen, H. Chen and J. Shi, *Adv. Mater.*, **2013**, 25, 3144-3176.
31. J. M. Rosenholm, C. Sahlgren and M. Linden, *Nanoscale*, **2010**, 2, 1870-1883.
32. W. Stöber, A. Fink and E. Bohn, *J. Colloid Interface Sci.*, **1968**, 26, 62-69.
33. M. Grün, K. K. Unger, A. Matsumoto and K. Tsutsumi, *Microporous Mesoporous Mater.*, **1999**, 27, 207-216.
34. B. Pauwels, G. Van Tendeloo, C. Thoelen, W. Van Rhijn and P. A. Jacobs, *Adv. Mater.*, **2001**, 13, 1317-1320.
35. Y. S. Lin, C. P. Tsai, H. Y. Huang, C. T. Kuo, Y. Hung, D. M. Huang, Y. C. Chen and C. Y. Mou, *Chem. Mater.*, **2005**, 17, 4570-4573.
36. K. Yano and Y. Fukushima, *J. Mater. Chem.*, **2003**, 13, 2577-2581.
37. K. Yano and Y. Fukushima, *J. Mater. Chem.*, **2004**, 14, 1579-1584.
38. T. Nakamura, M. Mizutani, H. Nozaki, N. Suzuki and K. Yano, *J. Phys. Chem. C*, **2007**, 111, 1093-1100.
39. F. Lu, S.-H. Wu, Y. Hung and C.-Y. Mou, *Small*, **2009**, 5, 1408-1413.
40. J. Gu, W. Fan, A. Shimojima and T. Okubo, *Small*, **2007**, 3, 1740-1744.
41. J. Gu, J. Liu, Y. Li, W. Zhao and J. Shi, *Langmuir*, **2013**, 29, 403-410.
42. X. Wang, Y. Zhang, W. Luo, A. A. Elzatahry, X. Cheng, A. Alghamdi, A. M. Abdullah, Y. Deng and D. Zhao, *Chem. Mater.*, **2016**, 28, 2356-2362.
43. V. Alfredsson and M. W. Anderson, *Chem. Mater.*, **1996**, 8, 1141-1146.
44. S. Che, Y. Sakamoto, O. Terasaki and T. Tatsumi, *Chem. Mater.*, **2001**, 13, 2237-2239.
45. M. Pérez-Mendoza, J. Gonzalez, P. A. Wright and N. A. Seaton, *Langmuir*, **2004**, 20, 9856-9860.
46. Y. Sakamoto, I. Díaz, O. Terasaki, D. Zhao, J. Pérez-Pariente, J. M. Kim and G. D. Stucky, *J. Phys. Chem. B*, **2002**, 106, 3118-3123.
47. O. C. Gobin, Y. Wan, D. Zhao, F. Kleitz and S. Kaliaguine, *J. Phys. Chem. C*, **2007**, 111, 3053-3058.
48. C. Yu, Y. Yu and D. Zhao, *Chem. Commun.*, **2000**, 575-576.
49. C.-Y. Wu, Y.-T. Hsu and C.-M. Yang, *Microporous Mesoporous Mater.*, **2009**, 117, 249-256.
50. K. Schumacher, M. Grün and K. K. Unger, *Microporous Mesoporous Mater.*, **1999**, 27, 201-206.
51. K. Schumacher, C. D. von Hohenesche, K. K. Unger, R. Ulrich, A. Du Chesne, U. Wiesner and H. W. Spiess, *Adv. Mater.*, **1999**, 11, 1194-1198.
52. S. Q. Liu, P. Cool, O. Collart, P. Van der Voort, E. F. Vansant, O. I. Lebedev, G. Van Tendeloo and M. H. Jiang, *J. Phys. Chem. B*, **2003**, 107, 10405-10411.
53. B. Boote, H. Subramanian and K. T. Ranjit, *Chem. Commun.*, **2007**, 4543-4545.
54. T.-W. Kim, P.-W. Chung and V. S. Y. Lin, *Chem. Mater.*, **2010**, 22, 5093-5104.
55. K. Yano, M. B. Katz, X. Pan and N. Tatsuda, *J. Colloid Interface Sci.*, **2014**, 418, 61-65.

- 
56. C. J. Brinker and G. W. Scherer, *Sol-Gel Science*, Academic Press, San Diego, **1990**.
57. H. P. Lin and C. P. Tsai, *Chem. Lett.*, **2003**, 32, 1092-1093.
58. K. Suzuki, K. Ikari and H. Imai, *J. Am. Chem. Soc.*, **2004**, 126, 462-463.
59. M. C. Chao, H. P. Lin and C. Y. Mou, *Chem. Lett.*, **2004**, 33, 672-673.
60. T. Suteewong, H. Sai, R. Cohen, S. T. Wang, M. Bradbury, B. Baird, S. M. Gruner and U. Wiesner, *J. Am. Chem. Soc.*, **2011**, 133, 172-175.
61. T. Suteewong, H. Sai, M. Bradbury, L. A. Estroff, S. M. Gruner and U. Wiesner, *Chem. Mater.*, **2012**, 24, 3895-3905.
62. T. Suteewong, H. Sai, R. Hovden, D. Muller, M. S. Bradbury, S. M. Gruner and U. Wiesner, *Science*, **2013**, 340, 337-341.
63. J. Gu, K. Huang, X. Zhu, Y. Li, J. Wei, W. Zhao, C. Liu and J. Shi, *J. Colloid Interface Sci.*, **2013**, 407, 236-242.
64. K. Moeller, J. Kobler and T. Bein, *Adv. Funct. Mater.*, **2007**, 17, 605-612.
65. T. Yokoi, Y. Sakamoto, O. Terasaki, Y. Kubota, T. Okubo and T. Tatsumi, *J. Am. Chem. Soc.*, **2006**, 128, 13664-13665.
66. K. Moeller, J. Kobler and T. Bein, *J. Mater. Chem.*, **2007**, 17, 624-631.
67. J. Kobler, K. Moeller and T. Bein, *ACS Nano*, **2008**, 2, 791-799.
68. Z.-A. Qiao, L. Zhang, M. Guo, Y. Liu and Q. Huo, *Chem. Mater.*, **2009**, 21, 3823-3829.
69. Q. He, X. Cui, F. Cui, L. Guo and J. Shi, *Microporous Mesoporous Mater.*, **2009**, 117, 609-616.
70. T. Yokoi, T. Karouji, S. Ohta, J. N. Kondo and T. Tatsumi, *Chem. Mater.*, **2010**, 22, 3900-3908.
71. M. Yu, L. Zhou, J. Zhang, P. Yuan, P. Thorn, W. Gu and C. Yu, *J. Colloid Interface Sci.*, **2012**, 376, 67-75.
72. C. Urata, Y. Aoyama, A. Tonegawa, Y. Yamauchi and K. Kuroda, *Chem. Commun.*, **2009**, 5094-5096.
73. H. Yamada, C. Urata, Y. Aoyama, S. Osada, Y. Yamauchi and K. Kuroda, *Chem. Mater.*, **2012**, 24, 1462-1471.
74. H. Yamada, C. Urata, H. Ujiie, Y. Yamauchi and K. Kuroda, *Nanoscale*, **2013**, 5, 6145-6153.
75. H. Yamada, C. Urata, S. Higashitamori, Y. Aoyama, Y. Yamauchi and K. Kuroda, *ACS Appl. Mater. Interfaces*, **2014**, 6, 3491-3500.
76. H. Yamada, H. Ujiie, C. Urata, E. Yamamoto, Y. Yamauchi and K. Kuroda, *Nanoscale*, **2015**, 7, 19557-19567.
77. E. Yamamoto, M. Kitahara, T. Tsumura and K. Kuroda, *Chem. Mater.*, **2014**, 26, 2927-2933.
78. K. Ma, H. Sai and U. Wiesner, *J. Am. Chem. Soc.*, **2012**, 134, 13180-13183.
79. K. Ma, U. Werner-Zwanziger, J. Zwanziger and U. Wiesner, *Chem. Mater.*, **2013**, 25, 677-691.
80. K. Zhang, L.-L. Xu, J.-G. Jiang, N. Calin, K.-F. Lam, S.-J. Zhang, H.-H. Wu, G.-D. Wu, B. Albela, L. Bonneviot and P. Wu, *J. Am. Chem. Soc.*, **2013**, 135, 2427-2430.
81. Y.-J. Yu, J.-L. Xing, J.-L. Pang, S.-H. Jiang, K.-F. Lam, T.-Q. Yang, Q.-S. Xue, K. Zhang and P. Wu, *ACS Appl. Mater. Interfaces*, **2014**, 6, 22655-22665.
82. D. Shen, J. Yang, X. Li, L. Zhou, R. Zhang, W. Li, L. Chen, R. Wang, F. Zhang and D. Zhao, *Nano Lett.*, **2014**, 14, 923-932.
83. D. Shen, L. Chen, J. Yang, R. Zhang, Y. Wei, X. Li, W. Li, Z. Sun, H. Zhu, A. M. Abdullah, A. Al-Enizi, A. A. Elzatahry, F. Zhang and D. Zhao, *ACS Appl. Mater. Interfaces*, **2015**, 7, 17450-17459.
84. C. Xu, M. Yu, O. Noonan, J. Zhang, H. Song, H. Zhang, C. Lei, Y. Niu, X. Huang, Y. Yang and C. Yu, *Small*, **2015**, 11, 5949-5955.
85. Y. F. Lu, H. Y. Fan, A. Stump, T. L. Ward, T. Rieker and C. J. Brinker, *Nature*, **1999**, 398, 223-226.
86. M. Wang, Z. Sun, Q. Yue, J. Yang, X. Wang, Y. Deng, C. Yu and D. Zhao, *J. Am. Chem. Soc.*, **2014**, 136, 1884-1892.
87. Y. Han and J. Y. Ying, *Angew. Chem. Int. Ed.*, **2005**, 44, 288-292.

88. D. Zhao, Y. Wan and W. Zhou, *Ordered mesoporous materials*, Wiley-VCH, Weinheim, **2013**.
89. C. Z. Yu, J. Fan, B. Z. Tian, D. Y. Zhao and G. D. Stucky, *Adv. Mater.*, **2002**, 14, 1742-1745.
90. S. Che, Z. Liu, T. Ohsuna, K. Sakamoto, O. Terasaki and T. Tatsumi, *Nature*, **2004**, 429, 281-284.
91. H. Y. Jin, Z. Liu, T. Ohsuna, O. Terasaki, Y. Inoue, K. Sakamoto, T. Nakanishi, K. Ariga and S. N. Che, *Adv. Mater.*, **2006**, 18, 593-596.
92. X. W. Wu, H. Y. Jin, Z. Liu, T. Ohsuna, O. Terasaki, K. Sakamoto and S. N. Che, *Chem. Mater.*, **2006**, 18, 241-243.
93. S. Yang, L. Zhao, C. Yu, X. Zhou, J. Tang, P. Yuan, D. Chen and D. Zhao, *J. Am. Chem. Soc.*, **2006**, 128, 10460-10466.
94. B. Wang, C. Chi, W. Shan, Y. H. Zhang, N. Ren, W. L. Yang and Y. Tang, *Angew. Chem. Int. Ed.*, **2006**, 45, 2088-2090.
95. Y. Han, L. Zhao and J. Y. Ying, *Adv. Mater.*, **2007**, 19, 2454-2459.
96. J. Ye, H. Zhang, R. Yang, X. Li and L. Qi, *Small*, **2010**, 6, 296-306.
97. Y. Si, M. Chen and L. Wu, *Chem. Soc. Rev.*, **2016**, 45, 690-714.
98. S. Schacht, Q. Huo, I. G. Voigt-Martin, G. D. Stucky and F. Schüth, *Science*, **1996**, 273, 768-771.
99. Y. S. Li, J. L. Shi, Z. L. Hua, H. R. Chen, M. L. Ruan and D. S. Yan, *Nano Lett.*, **2003**, 3, 609-612.
100. Q. Y. Sun, P. J. Kooyman, J. G. Grossmann, P. H. H. Bomans, P. M. Frederik, P. Magusin, T. P. M. Beelen, R. A. van Santen and N. Sommerdijk, *Adv. Mater.*, **2003**, 15, 1097-1100.
101. C. Z. Yu, B. H. Tian, J. Fan, G. D. Stucky and D. Y. Zhao, *Chem. Lett.*, **2002**, 31, 62-63.
102. J. Liu, C. M. Li, Q. H. Yang, J. Yang and C. Li, *Langmuir*, **2007**, 23, 7255-7262.
103. P. T. Tanev and T. J. Pinnavaia, *Science*, **1996**, 271, 1267-1269.
104. Y. Zhu, J. Shi, W. Shen, H. Chen, X. Dong and M. Ruan, *Nanotechnology*, **2005**, 16, 2633-2638.
105. L. Du, S. Liao, H. A. Khatib, J. F. Stoddart and J. I. Zink, *J. Am. Chem. Soc.*, **2009**, 131, 15136-15142.
106. Y. Q. Yeh, B. C. Chen, H. P. Lin and C. Y. Tang, *Langmuir*, **2006**, 22, 6-9.
107. B. Du, Z. Cao, Z. Li, A. Mei, X. Zhang, J. Nie, J. Xu and Z. Fan, *Langmuir*, **2009**, 25, 12367-12373.
108. J. Liu, S. B. Hartono, Y. G. Jin, Z. Li, G. Q. Lu and S. Z. Qiao, *J. Mater. Chem.*, **2010**, 20, 4595-4601.
109. J. Zhang, S. Karmakar, M. Yu, N. Mitter, J. Zou and C. Yu, *Small*, **2014**, 10, 5068-5076.
110. B. Tan and S. E. Rankin, *Langmuir*, **2005**, 21, 8180-8187.
111. H. Blas, M. Save, P. Pasetto, C. Boissiere, C. Sanchez and B. Charleux, *Langmuir*, **2008**, 24, 13132-13137.
112. N. Kato, T. Ishii and S. Koumoto, *Langmuir*, **2010**, 26, 14334-14344.
113. L. Li, J. Ding and J. Xue, *Chem. Mater.*, **2009**, 21, 3629-3637.
114. Y. Chen, H. Chen, L. Guo, Q. He, F. Chen, J. Zhou, J. Feng and J. Shi, *ACS Nano*, **2010**, 4, 529-539.
115. Y. Chen, C. Chu, Y. Zhou, Y. Ru, H. Chen, F. Chen, Q. He, Y. Zhang, L. Zhang and J. Shi, *Small*, **2011**, 7, 2935-2944.
116. Y. Chen, H.-R. Chen and J.-L. Shi, *Acc. Chem. Res.*, **2014**, 47, 125-137.
117. Y. Chen, Y. Gao, H. Chen, D. Zeng, Y. Li, Y. Zheng, F. Li, X. Ji, X. Wang, F. Chen, Q. He, L. Zhang and J. Shi, *Adv. Funct. Mater.*, **2012**, 22, 1586-1597.
118. M. Wu, Y. Chen, L. Zhang, X. Li, X. Cai, Y. Du, L. Zhang and J. Shi, *J. Mater. Chem. B*, **2015**, 3, 766-775.
119. J. F. Chen, H. M. Ding, J. X. Wang and L. Shao, *Biomaterials*, **2004**, 25, 723-727.
120. Z. Z. Li, S. A. Xu, L. X. Wen, F. Liu, A. Q. Liu, Q. Wang, H. Y. Sun, W. Yu and J. F. Chen, *J. Control. Release*, **2006**, 111, 81-88.



- 
121. J. Zhou, W. Wu, D. Caruntu, M. H. Yu, A. Martin, J. F. Chen, C. J. O'Connor and W. L. Zhou, *J. Phys. Chem. C*, **2007**, 111, 17473-17477.
122. T. Zhang, J. Ge, Y. Hu, Q. Zhang, S. Aloni and Y. Yin, *Angew. Chem. Int. Ed.*, **2008**, 47, 5806-5811.
123. X. Fang, C. Chen, Z. Liu, P. Liu and N. Zheng, *Nanoscale*, **2011**, 3, 1632-1639.
124. X. Fang, Z. Liu, M.-F. Hsieh, M. Chen, P. Liu, C. Chen and N. Zheng, *ACS Nano*, **2012**, 6, 4434-4444.
125. J. Maisch, F. Jafarli, T. Chassé, F. Blendinger, A. Konrad, M. Metzger, A. J. Meixner, M. Brecht, L. Dähne and H. A. Mayer, *Chem. Commun.*, **2016**, 52, 14392-14395.
126. X. Jiang, T. L. Ward, Y.-S. Cheng, J. Liu and C. J. Brinker, *Chem. Commun.*, **2010**, 46, 3019-3021.
127. D. P. Wang and H. C. Zeng, *Chem. Mater.*, **2011**, 23, 4886-4899.
128. Z. Teng, X. Su, Y. Zheng, J. Sun, G. Chen, C. Tian, J. Wang, H. Li, Y. Zhao and G. Lu, *Chem. Mater.*, **2013**, 25, 98-105.
129. H. Song, Y. A. Nor, M. Yu, Y. Yang, J. Zhang, H. Zhang, C. Xu, N. Mitter and C. Yu, *J. Am. Chem. Soc.*, **2016**, 138, 6455-6462.
130. A. B. Fuertes, P. Valle-Vigon and M. Sevilla, *Chem. Commun.*, **2012**, 48, 6124-6126.
131. H. Zhang, M. Yu, H. Song, O. Noonan, J. Zhang, Y. Yang, L. Zhou and C. Yu, *Chem. Mater.*, **2015**, 27, 6297-6304.
132. H. Zhang, O. Noonan, X. Huang, Y. Yang, C. Xu, L. Zhou and C. Yu, *ACS Nano*, **2016**, 10, 4579-4586.
133. W. Li and D. Y. Zhao, *Adv. Mater.*, **2013**, 25, 142-149.
134. J. Liu, S. Z. Qiao, Q. H. Hu and G. Q. Lu, *Small*, **2011**, 7, 425-443.
135. R. I. Nooney, T. Dhanasekaran, Y. M. Chen, R. Josephs and A. E. Ostafin, *Adv. Mater.*, **2002**, 14, 529-532.
136. P. Botella, A. Corma and M. T. Navarro, *Chem. Mater.*, **2007**, 19, 1979-1983.
137. I. Gorelikov and N. Matsuura, *Nano Lett.*, **2008**, 8, 369-373.
138. S. H. Joo, J. Y. Park, C. K. Tsung, Y. Yamada, P. D. Yang and G. A. Somorjai, *Nat. Mater.*, **2009**, 8, 126-131.
139. C. Wu, Z.-Y. Lim, C. Zhou, W. G. Wang, S. Zhou, H. Yin and Y. Zhu, *Chem. Commun.*, **2013**, 49, 3215-3217.
140. M. N. Sanz-Ortiz, K. Sentosun, S. Bals and L. M. Liz-Marzán, *ACS Nano*, **2015**, 9, 10489-10497.
141. W. Liu, Z. Zhu, K. Deng, Z. Li, Y. Zhou, H. Qu, Y. Gao, S. Che and Z. Tang, *J. Am. Chem. Soc.*, **2013**, 135, 9659-9664.
142. J. Chen, R. Zhang, L. Han, B. Tu and D. Zhao, *Nano Res.*, **2013**, 6, 871-879.
143. L. Han, H. Wei, B. Tu and D. Y. Zhao, *Chem. Commun.*, **2011**, 47, 8536-8538.
144. J. Yang, D. Shen, L. Zhou, W. Li, X. Li, C. Yao, R. Wang, A. M. El-Toni, F. Zhang and D. Zhao, *Chem. Mater.*, **2013**, 25, 3030-3037.
145. J. Kim, J. E. Lee, J. Lee, J. H. Yu, B. C. Kim, K. An, Y. Hwang, C. H. Shin, J. G. Park, J. Kim and T. Hyeon, *J. Am. Chem. Soc.*, **2006**, 128, 688-689.
146. J. Kim, H. S. Kim, N. Lee, T. Kim, H. Kim, T. Yu, I. C. Song, W. K. Moon and T. Hyeon, *Angew. Chem. Int. Ed.*, **2008**, 47, 8438-8441.
147. W. R. Zhao, J. L. Gu, L. X. Zhang, H. R. Chen and J. L. Shi, *J. Am. Chem. Soc.*, **2005**, 127, 8916-8917.
148. Y. Deng, D. Qi, C. Deng, X. Zhang and D. Zhao, *J. Am. Chem. Soc.*, **2008**, 130, 28-29.
149. Y. H. Deng, Y. Cai, Z. K. Sun, J. Liu, C. Liu, J. Wei, W. Li, C. Liu, Y. Wang and D. Y. Zhao, *J. Am. Chem. Soc.*, **2010**, 132, 8466-8473.
150. Z. K. Sun, J. P. Yang, J. X. Wang, W. Li, S. Kaliaguine, X. F. Hou, Y. H. Deng and D. Y. Zhao, *J. Mater. Chem. A*, **2014**, 2, 6071-6074.

151. P. P. Yang, Z. W. Quan, Z. Y. Hou, C. X. Li, X. J. Kang, Z. Y. Cheng and J. Lin, *Biomaterials*, **2009**, 30, 4786-4795.
152. Z. K. Sun, Q. Yue, Y. Liu, J. Wei, B. Li, S. Kaliaguine, Y. H. Deng, Z. X. Wu and D. Y. Zhao, *J. Mater. Chem. A*, **2014**, 2, 18322-18328.
153. Q. Yue, J. L. Li, W. Luo, Y. Zhang, A. A. Elzatahry, X. Q. Wang, C. Wang, W. Li, X. W. Cheng, A. Alghamdi, A. M. Abdullah, Y. H. Deng and D. Y. Zhao, *J. Am. Chem. Soc.*, **2015**, 137, 13282-13289.
154. J. P. Yang, D. K. Shen, Y. Wei, W. Li, F. Zhang, B. A. Kong, S. H. Zhang, W. Teng, J. W. Fan, W. X. Zhang, S. X. Dou and D. Y. Zhao, *Nano Res.*, **2015**, 8, 2503-2514.
155. D. C. Niu, Z. Ma, Y. S. Li and J. L. Shi, *J. Am. Chem. Soc.*, **2010**, 132, 15144-15147.
156. X. F. Qian, J. M. Du, B. Li, M. Si, Y. S. Yang, Y. Y. Hu, G. X. Niu, Y. H. Zhang, H. L. Xu, B. Tu, Y. Tang and D. Y. Zhao, *Chem. Sci.*, **2011**, 2, 2006-2016.
157. X. F. Qian, D. S. Xiong, A. M. Asiri, S. B. Khan, M. M. Rahman, H. L. Xu and D. Y. Zhao, *J. Mater. Chem. A*, **2013**, 1, 7525-7532.
158. L. Xu, Y. J. Ren, H. H. Wu, Y. M. Liu, Z. D. Wang, Y. T. Zhang, J. J. Xu, H. G. Peng and P. Wu, *J. Mater. Chem.*, **2011**, 21, 10852-10858.
159. Z. Li and H. C. Zeng, *J. Am. Chem. Soc.*, **2014**, 136, 5631-5639.
160. B. Xi, Y. C. Tan and H. C. Zeng, *Chem. Mater.*, **2016**, 28, 326-336.
161. J. Liu, S. Z. Qiao, J. S. Chen, X. W. Lou, X. R. Xing and G. Q. Lu, *Chem. Commun.*, **2011**, 47, 12578-12591.
162. F. Lan, H. Hu, W. Jiang, K. Liu, X. Zeng, Y. Wu and Z. Gu, *Nanoscale*, **2012**, 4, 2264-2267.
163. J. Liu, S. Z. Qiao, S. Budi Hartono and G. Q. Lu, *Angew. Chem. Int. Ed.*, **2010**, 49, 4981-4985.
164. Y. Zhu, E. Kockrick, T. Ikoma, N. Hanagata and S. Kaskel, *Chem. Mater.*, **2009**, 21, 2547-2553.
165. Y. Zhu, T. Ikoma, N. Hanagata and S. Kaskel, *Small*, **2010**, 6, 471-478.
166. S. Wang, M. Zhang and W. Zhang, *ACS Catalysis*, **2011**, 1, 207-211.
167. Y. Chen, H. Chen, D. Zeng, Y. Tian, F. Chen, J. Feng and J. Shi, *ACS Nano*, **2010**, 4, 6001-6013.
168. Y. Chen, H. Chen, M. Ma, F. Chen, L. Guo, L. Zhang and J. Shi, *J. Mater. Chem.*, **2011**, 21, 5290-5298.
169. Y. Fang, G. Zheng, J. Yang, H. Tang, Y. Zhang, B. Kong, Y. Lv, C. Xu, A. M. Asiri, J. Zi, F. Zhang and D. Zhao, *Angew. Chem. Int. Ed.*, **2014**, 53, 5366-5370.
170. Q. Yue, Y. Zhang, C. Wang, X. Wang, Z. Sun, X.-F. Hou, D. Zhao and Y. Deng, *J. Mater. Chem. A*, **2015**, 3, 4586-4594.
171. Q. Zhang, T. Zhang, J. Ge and Y. Yin, *Nano Lett.*, **2008**, 8, 2867-2871.
172. E.-B. Cho, D. Kim and M. Jaroniec, *Microporous Mesoporous Mater.*, **2009**, 120, 252-256.
173. J. Li, Y. Wei, Y. Deng, D. Gu, X. Yang, L. Zhang, B. Tu and D. Zhao, *J. Mater. Chem.*, **2010**, 20, 6460-6463.
174. C. Urata, H. Yamada, R. Wakabayashi, Y. Aoyama, S. Hirose, S. Arai, S. Takeoka, Y. Yamauchi and K. Kuroda, *J. Am. Chem. Soc.*, **2011**, 133, 8102-8105.
175. B. Guan, Y. Cui, Z. Ren, Z.-a. Qiao, L. Wang, Y. Liu and Q. Huo, *Nanoscale*, **2012**, 4, 6588-6596.
176. C. Mauriello-Jimenez, J. Croissant, M. Maynadier, X. Cattoën, M. W. C. Man, J. Vergnaud, V. Chaleix, V. Sol, M. Garcia, M. Gary-Bobo, L. Raehm and J. O. Durand, *J. Mater. Chem. B*, **2015**, 3, 3681-3684.
177. Y. Yang, Y. Niu, J. Zhang, A. K. Meka, H. Zhang, C. Xu, C. X. C. Lin, M. Yu and C. Yu, *Small*, **2015**, 11, 2743-2749.
178. J. Croissant, X. Cattoën, M. W. C. Man, P. Dieudonne, C. Charnay, L. Raehm and J.-O. Durand, *Adv. Mater.*, **2015**, 27, 145-149.
179. J. G. Croissant, Y. Fatieiev, H. Omar, D. H. Anjum, A. Gurinov, J. Lu, F. Tamanoi, J. I. Zink and N. M. Khashab, *Chem. Eur. J.*, **2016**, 22, 9607-9615.

180. S. Z. Qiao, C. Z. Yu, W. Xing, Q. H. Hu, H. Djoputro and G. Q. Lu, *Chem. Mater.*, **2005**, *17*, 6172-6176.
181. P. Mohanty and K. Landskron, *Nanoscale Res. Lett.*, **2009**, *4*, 169-172.
182. P. Mohanty and K. Landskron, *Nanoscale Res. Lett.*, **2009**, *4*, 1524-1529.
183. X. Meng, T. Yokoi, D. Lu and T. Tatsumi, *Angew. Chem. Int. Ed.*, **2007**, *46*, 7796-7798.
184. P. Yuan, L. Z. Zhao, N. A. Liu, G. F. Wei, Y. Zhang, Y. H. Wang and C. Z. Yu, *Chem. Eur. J.*, **2009**, *15*, 11319-11325.
185. Y. Li, L. F. Bi, S. B. Wang, Y. L. Chen, B. Z. Li, X. L. Zhu and Y. G. Yang, *Chem. Commun.*, **2010**, *46*, 2680-2682.
186. M. Zhang, Y. Li, L. F. Bi, W. Zhuang, S. B. Wang, Y. L. Chen, B. Z. Li and Y. G. Yang, *Chin. J. Chem.*, **2011**, *29*, 933-941.
187. J. Croissant, X. Cattoën, M. W. C. Man, A. Gallud, L. Raehm, P. Trens, M. Maynadier and J. O. Durand, *Adv. Mater.*, **2014**, *26*, 6174-6180.
188. B. Tan, S. M. Vyas, H.-J. Lehmer, B. L. Knutson and S. E. Rankin, *Adv. Funct. Mater.*, **2007**, *17*, 2500-2508.
189. J. Liu, Q. Yang, L. Zhang, H. Yang, J. Gao and C. Li, *Chem. Mater.*, **2008**, *20*, 4268-4275.
190. J. Liu, S. Y. Bai, H. Zhong, C. Li and Q. H. Yang, *J. Phys. Chem. C*, **2010**, *114*, 953-961.
191. H. Djoputro, X. F. Zhou, S. Z. Qiao, L. Z. Wang, C. Z. Yu and G. Q. Lu, *J. Am. Chem. Soc.*, **2006**, *128*, 6320-6321.
192. Y. Zhang, M. Yu, L. Zhou, X. Zhou, Q. Zhao, H. Li and C. Yu, *Chem. Mater.*, **2008**, *20*, 6238-6243.
193. N. Ma, Y. Deng, W. Liu, S. Li, J. Xu, Y. Qu, K. Gan, X. Sun and J. Yang, *Chem. Commun.*, **2016**, *52*, 3544-3547.
194. X. Ma, J. Zhang, M. Dang, J. Wang, Z. Tu, L. Yuwen, G. Chen, X. Su and Z. Teng, *J. Colloid Interface Sci.*, **2016**, *475*, 66-71.
195. Y. Chen, P. F. Xu, H. R. Chen, Y. S. Li, W. B. Bu, Z. Shu, Y. P. Li, J. M. Zhang, L. X. Zhang, L. M. Pan, X. Z. Cui, Z. L. Hua, J. Wang, L. L. Zhang and J. L. Shi, *Adv. Mater.*, **2013**, *25*, 3100-3105.
196. Y. Chen, Q. S. Meng, M. Y. Wu, S. G. Wang, P. F. Xu, H. R. Chen, Y. P. Li, L. X. Zhang, L. Z. Wang and J. L. Shi, *J. Am. Chem. Soc.*, **2014**, *136*, 16326-16334.
197. M. Wu, Q. Meng, Y. Chen, L. Zhang, M. Li, X. Cai, Y. Li, P. Yu, L. Zhang and J. Shi, *Adv. Mater.*, **2016**, *28*, 1963-1969.
198. W. Guo, J. Wang, S.-J. Lee, F. Dong, S. S. Park and C.-S. Ha, *Chem. Eur. J.*, **2010**, *16*, 8641-8646.
199. J. Y. Shi, C. A. Wang, Z. J. Li, Q. Wang, Y. Zhang and W. Wang, *Chem. Eur. J.*, **2011**, *17*, 6206-6213.
200. S. Haffer, M. Tiemann and M. Froeba, *Chem. Eur. J.*, **2010**, *16*, 10447-10452.
201. W. Na, Q. Wei and Z. Nie, *J. Mater. Chem.*, **2012**, *22*, 9970-9974.
202. J. Croissant, M. Maynadier, O. Mongin, V. Hugues, M. Blanchard-Desce, A. Chaix, X. Cattoën, M. W. C. Man, A. Gallud, M. Gary-Bobo, M. Garcia, L. Raehm and J.-O. Durand, *Small*, **2015**, *11*, 295-299.
203. J. Croissant, D. Salles, M. Maynadier, O. Mongin, V. Hugues, M. Blanchard-Desce, X. Cattoën, M. W. C. Man, A. Gallud, M. Garcia, M. Gary-Bobo, L. Raehm and J.-O. Durand, *Chem. Mater.*, **2014**, *26*, 7214-7220.
204. J. Li, Y. Wei, W. Li, Y. H. Deng and D. Y. Zhao, *Nanoscale*, **2012**, *4*, 1647-1651.
205. X. Li, L. Zhou, Y. Wei, A. M. El-Toni, F. Zhang and D. Zhao, *J. Am. Chem. Soc.*, **2014**, *136*, 15086-15092.
206. L. Zhang, S. Qiao, Y. Jin, Z. Chen, H. Gu and G. Q. Lu, *Adv. Mater.*, **2008**, *20*, 805-809.
207. Y. Yang, J. Liu, X. Li, X. Liu and Q. Yang, *Chem. Mater.*, **2011**, *23*, 3676-3684.

208. Y. Yang, X. Liu, X. Li, J. Zhao, S. Bai, J. Liu and Q. Yang, *Angew. Chem. Int. Ed.*, **2012**, 51, 9164-9168.
209. H. Zou, R. Wang, X. Li, X. Wang, S. Zeng, S. Ding, L. Li, Z. Zhang and S. Qiu, *J. Mater. Chem. A*, **2014**, 2, 12403-12412.
210. Y. Wei, X. Li, A. A. Elzatahry, R. Zhang, W. Wang, X. Tang, J. Yang, J. Wang, D. Al-Dahyan and D. Zhao, *RSC Adv.*, **2016**, 6, 51470-51479.
211. Z. Teng, S. Wang, X. Su, G. Chen, Y. Liu, Z. Luo, W. Luo, Y. Tang, H. Ju, D. Zhao and G. Lu, *Adv. Mater.*, **2014**, 26, 3741-3747.
212. Z. Teng, X. Su, B. Lee, C. Huang, Y. Liu, S. Wang, J. Wu, P. Xu, J. Sun, D. Shen, W. Li and G. Lu, *Chem. Mater.*, **2014**, 26, 5980-5987.
213. Z. Teng, J. Zhang, W. Li, Y. Zheng, X. Su, Y. Tang, M. Dang, Y. Tian, L. Yuwen, L. Weng, G. Lu and L. Wang, *Small*, **2016**, 12, 3550-3558.
214. Z. Teng, X. Su, Y. Zheng, J. Zhang, Y. Liu, S. Wang, J. Wu, G. Chen, J. Wang, D. Zhao and G. Lu, *J. Am. Chem. Soc.*, **2015**, 137, 7935-7944.
215. S. Hudson, J. Cooney and E. Magner, *Angew. Chem. Int. Ed.*, **2008**, 47, 8582-8594.
216. K. Qian, F. Liu, J. Yang, X. D. Huang, W. Y. Gu, S. Jambhrunkar, P. Yuan and C. Z. Yu, *RSC Adv.*, **2013**, 3, 14466-14472.
217. J. Liu, S. Z. Qiao, S. B. Hartono and G. Q. Lu, *Angew. Chem. Int. Ed.*, **2010**, 49, 4981-4985.
218. T. M. Suzuki, T. Nakamura, E. Sudo, Y. Akimoto and K. Yano, *Microporous Mesoporous Mater.*, **2008**, 111, 350-358.
219. T. M. Suzuki, T. Nakamura, E. Sudo, Y. Akimoto and K. Yano, *J. Catal.*, **2008**, 258, 265-272.
220. Y. Yamada, T. Nakamura, M. Ishi and K. Yano, *Langmuir*, **2006**, 22, 2444-2446.
221. L. Bai, Z. Xie, W. Wang, C. Yuan, Y. Zhao, Z. Mu, Q. Zhong and Z. Gu, *ACS Nano*, **2014**, 8, 11094-11100.

## 2 Monodisperse Mesoporous Silica Nanoparticles of Distinct Topology

### 2.1 Introduction

Since the first report from Mobil scientists,<sup>1</sup> periodic mesoporous silicas (PMSs) have attracted broad attention due to their long-range ordered pore structure exhibiting large surface area, high pore volume, and tunable pore diameter, which makes them ideally suited for surface functionalization.<sup>2</sup> Sticking out is the framework topology of PMS MCM-48 and its extended-pore variant KIT-6, which feature a bicontinuous cubic mesostructure of *Ia-3d* symmetry.<sup>3</sup> Such a uniquely interpenetrating and three-dimensional (3D) pore structure, promoting rapid diffusion of guest molecule without pore blockage, is believed to be beneficial for material design of relevance for adsorption, catalysis and controlled drug delivery.<sup>4</sup> In this regard, the feasibility of monodisperse mesoporous silica nanoparticles involving additional control of particle size, shape, and morphology, is equally important.<sup>5</sup> For example, monodisperse MCM-48 nanoparticles provide enhanced pore accessibility for guest molecules, as demonstrated by their use as the drug reservoirs for enzyme-responsive release.<sup>6</sup> Moreover, monodisperse mesoporous silica nanoparticles proved superior in assessing catalytic activity or diffusion kinetics<sup>7</sup> and can be used for the fabrication of mesoporous colloidal photonic crystals.<sup>8</sup>

Until now, several protocols have been applied for the synthesis of MCM-48 nanoparticles. Unger and co-workers were the first to use a modified Stöber method, however, the MCM-48 silica nanoparticles obtained seemed to show some degree of aggregation.<sup>9</sup> Also, Ranjit and co-workers reported a rapid and facile synthesis of nanoscale MCM-48 according to a modified Stöber process by adjusting the molar ratio of surfactant to silica precursor, stirring rate, reaction time, type of alcohol, silica precursor, surfactant chain length as well as base concentration.<sup>10</sup> Unfortunately, the authors did not provide details of the morphology and polydispersity of these MCM-48 materials as well as their mechanism of formation. Addition of triblock polymer F127 (EO<sub>106</sub>PO<sub>70</sub>EO<sub>106</sub>) as a dispersing agent (“particle size designer”) into the reaction mixture greatly improved the monodispersity of MCM-48 nanoparticles obtained (diameter can be controlled in the range 70–500 nm),<sup>11</sup> but the preparation was not facile. More recently, benzylcetyldimethylammonium chloride featuring a big head-group has been used as a structure-directing agent for the synthesis of MCM-48 nanoparticles, but a broad particle size distribution was observed (200–300 nm diameter).<sup>12</sup> In 2014, Tatsuda and co-workers used tetrakis(3-hydroxypropyl)orthosilicate as a silica precursor for the fabrication of monodisperse particles (413 nm diameter) with mixed hexagonal/cubic mesophases.<sup>13</sup> Therefore, the preparation of monodisperse and uniform MCM-48 nanoparticles using a simple and efficient method represents still a big challenge.

The scarcity of preparation methods for monodisperse MCM-48 nanoparticles might be a result of the inevitable simultaneous control of the formation of a long-range ordered pore

structure and particle morphology both of which being enormously affected by the reaction conditions. For example, the formation of the MCM-48 structure is generally favoured by a high concentration of the structure-directing agent,<sup>14</sup> while the formation of monodisperse and uniform nanoparticles preferentially occurs in dilute solution.<sup>15</sup> Hence, the key challenge is to find appropriate reaction conditions for precisely tailoring both the cubic pore structure and monodisperse uniform nanoparticles. The energetically unstable character of the bicontinuous gyroid pore structure of MCM-48 requires that the template-silicate interaction should be given particular attention, compared with hexagonal mesoporous silica nanoparticles.<sup>16</sup> To address these problems, we report herein a simple and effective method for the synthesis of monodisperse and uniform MCM-48 nanoparticles applying the TEOS-NaOH-CTAB-H<sub>2</sub>O-EtOH system. We show that ethanol plays a dual role—the adjuster of pore structure and the controller of uniform nanoparticle growth. Overall, the implications of EtOH and CTAB concentration for the particle size, mesopore array, and monodispersity of nanoparticles are investigated in detail. Finally, a mechanism for the mesophase formation and morphology evolution of monodispersive mesoporous silica nanoparticles is proposed.

## 2.2 Experimental Section

### 2.2.1 Synthesis of Monodisperse and Uniform Cubic Mesoporous Silica Nanoparticles (CMSN-n)

All chemicals were used without further purification. MCM-48 nanoparticles were synthesized with the molar ratio of 2TEOS : xEtOH : yCTAB : 1NaOH : 2950H<sub>2</sub>O, where  $x = 225\text{--}275$  and  $y = 0.125\text{--}0.2$ . A typical procedure is as follows: cetyltrimethylammonium bromide (CTAB) (98%, Sigma-Aldrich) was dissolved in a solvent mixture of EtOH (99.9% Sigma-Aldrich) and deionized water, and subsequently a sodium hydroxide (NaOH) (98%, Sigma-Aldrich) aqueous solution (2 M) was added. After having stirred at a rate of 600 rotations per minute (rpm) at ambient temperature for 20 min and the formation of a clear solution, tetraethylorthosilicate (TEOS) (99%, Sigma-Aldrich) was added. The solution was stirred at the same speed at ambient temperature for 4 h and kept statically for another 24 h. The resulting nanoparticles were separated by centrifugation (20000 rpm, 7 min) and washed once with water and ethanol, respectively. The template was removed by stirring the as-made nanoparticles (1.0 g) in a hydrochloric acid (HCl) (37%, Fisher Chemical)-acidified EtOH solution (1 mL of 37% HCl and 80 mL of EtOH) at 75 °C for 18 h. An identical procedure was applied for the preparation of hexagonal or mixed hexagonal/cubic or cubic/lamellar mesoporous silica nanoparticles (HMSN-n, or H/CMSN-n, or C/LMSN-n), when the molar ratio of ethanol/2TEOS was less than 225 or higher than 275 and the molar ratio of CTAB/2TEOS was less than 0.125 or higher than 0.2.

## 2.2.2 Characterization

Low-angle powder X-ray diffraction (PXRD) patterns were obtained on a Bruker D8 Advance Diffractometer in the step/scan mode with a step width of 0.00825 and accumulation time of 2 s/step using monochromatic  $\text{CuK}\alpha$  radiation ( $\lambda = 1.5406 \text{ \AA}$ ) in the  $2\theta$  range of  $0.5\text{--}10.0^\circ$ . Nitrogen physisorption measurements were carried out on a Micrometrics ASAP2020 volumetric adsorption apparatus at  $77.4 \text{ K}$  [ $a_m(\text{N}_2, 77 \text{ K}) = 0.162 \text{ nm}^2$ ]. The samples were degassed at  $120 \text{ }^\circ\text{C}$  for 5 h under vacuum (ca.  $5 \text{ }\mu\text{mHg}$ ) prior to analysis. The surface area was calculated by the *Brunauer-Emmett-Teller* (BET) method from the adsorption data obtained from  $P/P_0$  between 0.05 and 0.2. The pore size distribution was obtained from the adsorption branch of the nitrogen isotherm from  $P/P_0$  between 0.05 and 0.995 using the *Barret-Joyner-Haldenda* (BJH) method. Dynamic Light Scattering (DLS) measurements were conducted on a Malvern Zetasizer Nano-ZS at ambient temperature, for which each sample was suspended in ethanol by sonication. The nanoparticle size distribution curves are presented in the intensity mode. Scanning Electron Microscopy (SEM) images were taken with a Hitachi SU 8030 microscope operated at an acceleration voltage of 1 kV. Transmission electron microscopy (TEM) images were obtained using a JEOL JEM 2010 microscope operated at 160 kV. The samples were prepared by dispersing the powdery material in ethanol; one drop of the suspension was dried on the copper grid covered with a holey carbon film.  $^{29}\text{Si}$  CP MAS NMR spectra were obtained at ambient temperature on a Bruker ASX 300 instrument equipped with MAS (magic angle spinning) hardware and using a  $\text{ZrO}_2$  rotor with an inside diameter of 7 mm.

## 2.3 Results and Discussion

### 2.3.1 Effect of Ethanol

Alcoholic additives have a strong influence on the morphology, symmetry and packing structure of surfactants,<sup>17-26</sup> and hence the surfactant-induced assembly of inorganic structures can also be affected by alcohols. While short-chain alcohols as polar cosolvents tend to disrupt the structural order of the hexagonal mesoporous phase, medium- or long-chain alcohols as co-surfactants can enhance the long-range ordering of hexagonal pore arrays in MCM-41.<sup>27,28</sup> When used as cosurfactants and expanders aliphatic alcohols can also induce mesophase transformations from hexagonal to lamellar or from hexagonal to lamellar via a cubic structure.<sup>29,30</sup> In fact, most of these investigations deal with the formation of hexagonal mesoporous silicas involving the micelle-forming properties of surfactants in low concentration and in the presence of alcohols.<sup>13,27-36</sup> This alcohol effect has been less studied with respect to monodisperse and high-quality periodic mesoporous silica nanoparticles (PMSNs) with *Ia-3d* symmetry. Although EtOH was previously found useful for the synthesis of cubic MCM-48 nanoparticles under highly basic conditions, its role was not addressed in detail.<sup>6,9,11,13</sup> The present work will focus on the alcohol effect on the formation of PMSNs and its influence on morphology and topology under very low surfactant and base concentrations.

This investigation markedly differs from a previous report.<sup>10</sup> The original molar ratio of the gel in our study was 2TEOS : xEtOH : 0.15CTAB : 1NaOH : 2950 H<sub>2</sub>O (x = 0-275). In this reaction system, when the molar ratio of EtOH/2TEOS was adjusted in the range from 0 to 200, PMSNs with hexagonal structure of *p6mm* symmetry (x = 0 and 175) or a mixed mesophase with *p6mm* and *Ia-3d* symmetries (x = 200) were obtained as evidenced by their PXRD patterns (Figure 2.1a, HMSN-1, HMSN-2, H/CMSN-3). This result implies that the addition of a small amount of ethanol does not affect the kinetics of mesophase formation, which is consistent with previous investigations.<sup>27-29</sup> When the EtOH/2TEOS molar ratio ranged from 225 to 275, pure and high-quality cubic PMSNs (CMSN-1, CMSN-2, and CMSN-3) with *Ia-3d* symmetry were obtained.

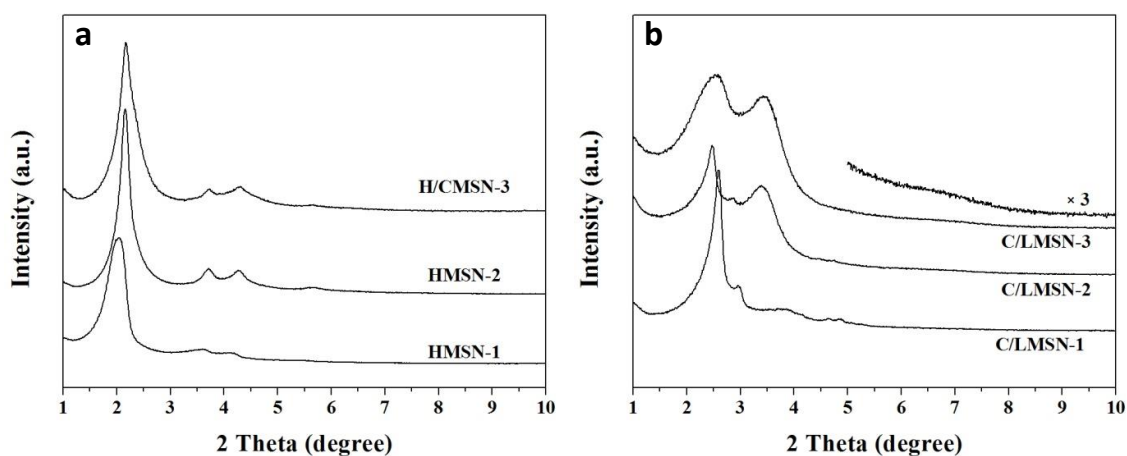


**Figure 2.1** PXRD patterns of periodic mesoporous silica prepared applying molar ratios of TEOS : EtOH : CTAB : NaOH : H<sub>2</sub>O = 2 : x : 0.15 : 1 : 2950. (a) x = 0 for HMSN-1; x = 175 for HSMN-2; x = 200 for H/CMSN-3, and (b) x = 303 for C/LMSN-1, x = 325 for C/LMSN-2, and x = 400 for C/LMSN-3. For HMSN and H/CMSN samples, the template was removed by washing with HCl-acidified ethanol, while C/LMSN samples were measured without template removal.

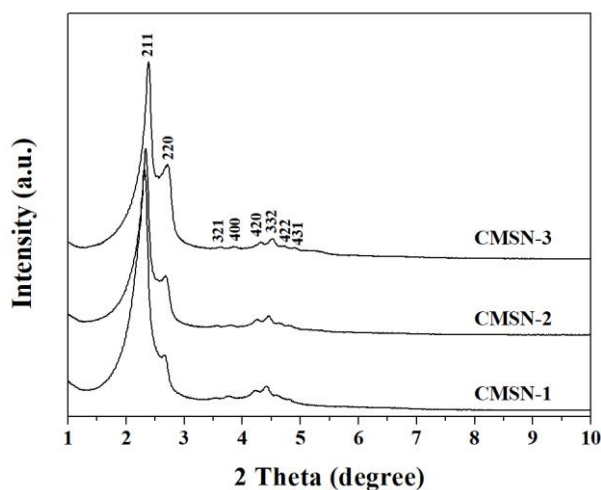


**Figure 2.2** PXRD patterns of materials CMSN-n (n = 1, 2, 3) prepared with the molar ratio of TEOS : EtOH : CTAB : NaOH : H<sub>2</sub>O = 2 : x : 0.15 : 1 : 2950; x = 225 for CMSN-1, x = 250 for CMSN-2, and x = 275 for CMSN-3.



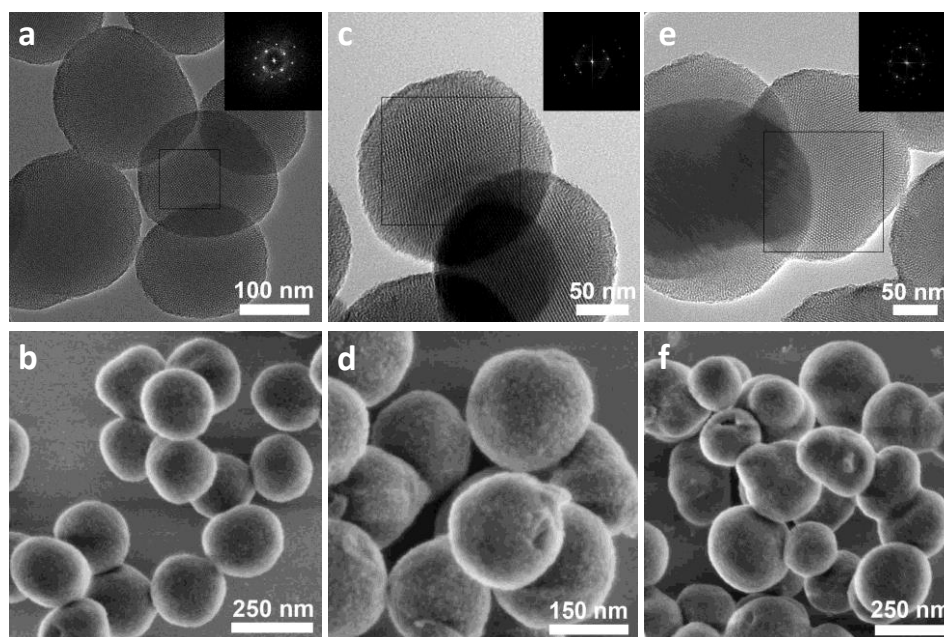


**Figure 2.3** Representative TEM images of (a) CMSN-1, (c) CMSN-2, and (e) CMSN-3 taken along the [100], [311] and [111] directions, respectively, and SEM images of (b) CMSN-1, (d) CMSN-2, and (f) CMSN-3. The insets are the corresponding Fast Fourier Transform (FFT) images.

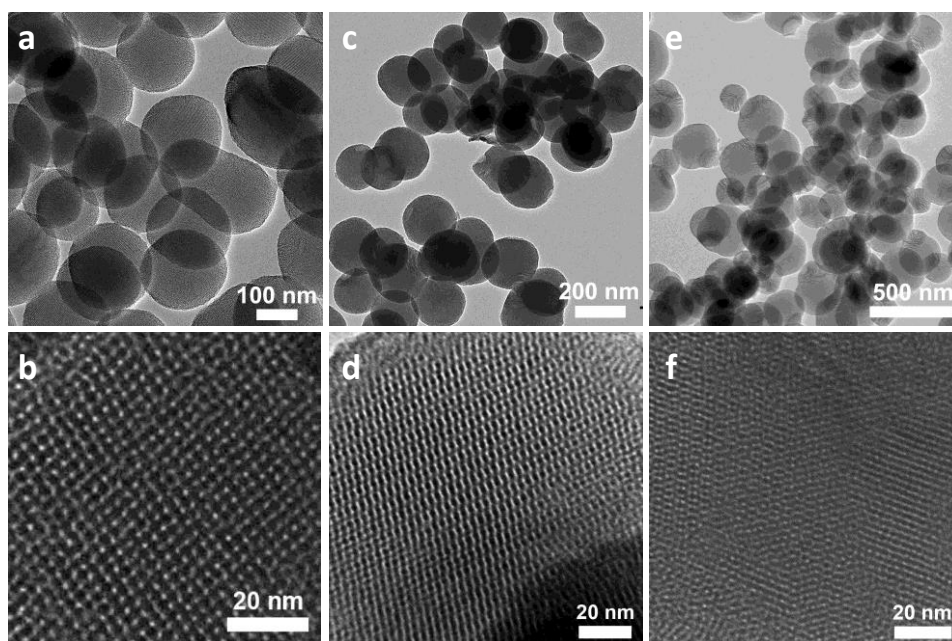


**Figure 2.4** TEM images with different magnifications of (a,b) CMSN-1, (c,d) CMSN-2 and (e,f) CMSN-3.

The PXRD patterns of all CMSN- $n$  ( $n = 1, 2, 3$ ) show eight well-resolved diffraction peaks in the range of  $1 < 2\theta < 5^\circ$  that could be indexed as (211), (220), (321), (400), (420), (332), (422) and (431) reflections of cubic  $Ia-3d$  symmetry, indicating the typical and highly ordered MCM-48 structure (Figure 2.2). The cubic structure could be corroborated by TEM analysis. Representative TEM images along the [100], [311] and [111] directions are shown in Figure 2.3 (a, c and e), demonstrating the long-range ordered 3D cubic pore arrays.<sup>3</sup> TEM images with

different magnifications show the monodisperse nanoparticles with cubic pore structures (Figure 2.4). When the molar ratio of EtOH/2TEOS was higher than 275, a mixed cubic and lamellar structure formed (Figure 2.1b, C/LMSN-1, C/LMSN-2, C/LMSN-3).

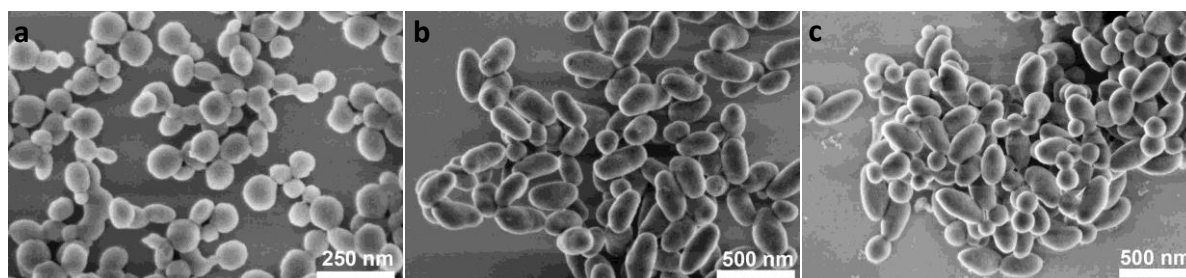


**Figure 2.5** SEM images of (a) HMSN-1, (b) HMSN-2, and (c) H/CMSN-3 obtained applying molar ratios of TEOS : EtOH : CTAB : NaOH : H<sub>2</sub>O = 2 : x : 0.15 : 1 : 2950, (a) x = 0, (b) x = 175, and (c) x = 200.

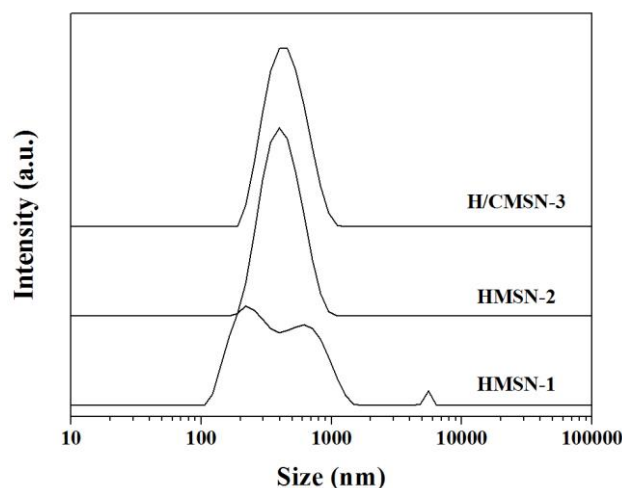


**Figure 2.6** DLS-derived particle size distribution of HMSN-1, HMSN-2, and H/CMSN-3 prepared by applying molar ratios of TEOS : EtOH : CTAB : NaOH : H<sub>2</sub>O = 2 : x : 0.15 : 1 : 2950. Herein x = 0 for HMSN-1, x = 175 for HMSN-2, and x = 200 for H/CMSN-3.

The change of PMSN topology upon variation of the EtOH/2TEOS molar ratio was also accompanied by an alteration of the morphology. The PMSN obtained show spherical and ellipsoidal shapes with multidispersive sizes for HMSN-1, rod-like shape with an average size of  $316 \pm 12.9$  nm  $159 \pm 3.7$  nm in length and width, respectively, for HMSN-2, and mixed morphologies for H/CMSN-3 – rod-like shape with an average size of  $353 \pm 15.1$  nm  $182 \pm 4.0$  nm in length and width and spherical shape with an average size of  $155 \pm 7.2$  nm (Figure 2.5). The morphology change is attributed to the EtOH effect.<sup>37</sup> Use of a small amount of ethanol cannot effectively change the cylindrical micelle structure of surfactant CTAB, but with increasing ethanol concentration surfactant aggregates slowly change from a cylindrical to a spherical structure, which is in agreement with the structure transformation previously observed for alcohol-induced CTAB surfactant aggregates.<sup>26</sup> Hence, variation of surfactant/aggregate structure leads to the formation of PMSNs with different morphologies and symmetries. The dynamic light scattering (DLS) analyses of the series HMSNs and

H/CMSNs show multi-peaks and broad particle size distribution (Figure 2.6) as well as much larger particle size compared to that from SEM and TEM analyses. This is probably due to a strong solvent effect, meaning solvent layers of the primary particles, affording a comparatively large hydrodynamic size. However, the cubic PMSs CMSN-*n* (*n* = 1, 2, 3) display a regular spherical shape (Figure 2.3, absence of rod-like morphologies) with narrow particle size distribution (Figure 2.7). With increasing molar ratio of EtOH/2TEOS ranging from 225 to 275, the average particle size of CMSN-1, CMSN-2 and CMSN-3 gradually increases from  $226 \pm 2.7$  nm to  $303 \pm 5.1$  nm as obtained by SEM measurements (Table 2.1). Since partial aggregation of nanoparticles is observed for CMSN-3, it seems that the use of a low amount of ethanol is beneficial to the formation of monodisperse CMSNs. In order to evaluate the monodispersity of the nanoparticles, 50 random CMSNs were chosen to determine their standard deviation on sizes by SEM/TEM (Table 2.1, Figure 2.7). These data clearly revealed that the monodispersity of the nanoparticles decreased with increasing EtOH amount, corroborating the detrimental influence of excessive ethanol. For all CMSNs, the DLS analyses (Figure 2.8) indicated a single peak, which gradually shifted to larger size with increasing EtOH amount used, reflecting the monodisperse nature and a gradually increasing particle size. This trend is in good agreement with the findings from SEM and TEM. The broadness of the DLS peak as characterized by its PDI (Polydispersity Index) gradually increases with increasing EtOH molar ratio (Table 2.1), implying broad particle size distribution of the nanoparticles. As observed for materials HMSNs and H/CMSNs the average hydrodynamic particle size from DLS analyses is higher than that from SEM.

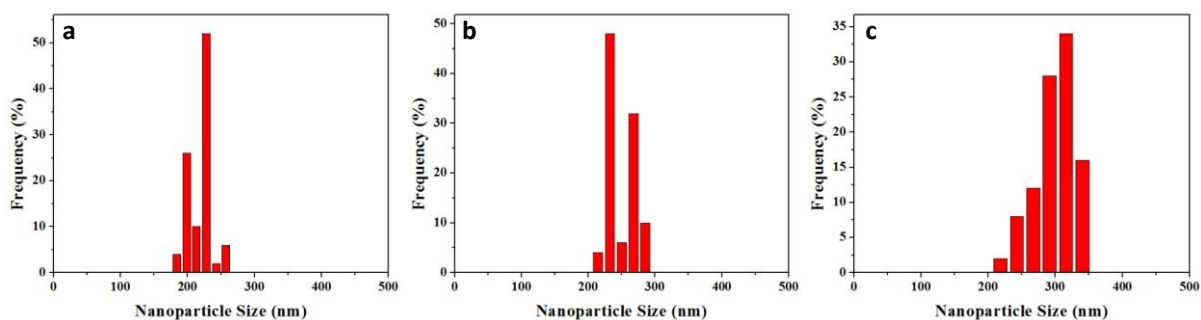


**Figure 2.7** Particle size distributions obtained by measuring 50 nanoparticles for (a) CMSN-1, (b) CMSN-2, and (c) CMSN-3 with average particle sizes of 226 nm, 251 nm, and 303 nm respectively.

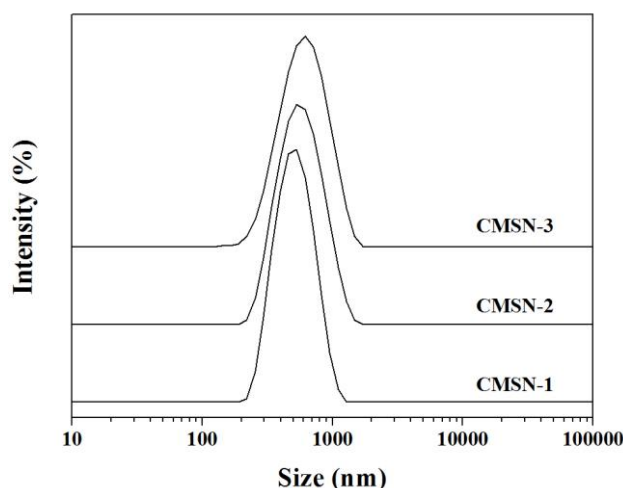


**Figure 2.8** DLS-derived particle size distribution of samples CMSN-1, CMSN-2, and CMSN-3 prepared by applying molar ratios of TEOS : EtOH : CTAB : NaOH : H<sub>2</sub>O = 2 : x : 0.15 : 1 : 2950. Herein x = 225 for CMSN-1, x = 250 for CMSN-2, and x = 275 for CMSN-3.

**Table 2.1** Pore parameters of MCM-48-type CMSN-n prepared with different CTAB and EtOH molar ratios.

Material	CTAB <sup>a</sup>	EtOH <sup>a</sup>	SEM/TEM		DLS		a <sub>BET</sub> (m <sup>2</sup> g <sup>-1</sup> ) <sup>e</sup>	d <sub>p</sub> (nm) <sup>f</sup>	V <sub>p</sub> (cm <sup>3</sup> g <sup>-1</sup> ) <sup>g</sup>
			Size (nm) <sup>b</sup>	St. Dev. <sup>c</sup>	Size (nm) <sup>d</sup>	PDI <sup>d</sup>			
CMSN-1	0.15	225	226/216	18.96/16.63	481	0.094	1127	2.6	1.06
CMSN-2	0.15	250	251/235	20.78/28.62	527	0.115	1139	2.7	1.10
CMSN-3	0.15	275	303/289	36.36/36.45	548	0.135	1160	2.5	1.08
CMSN-4	0.125	225	241/225	19.95/16.58	559	0.110	1137	2.5	1.06
CMSN-5	0.175	225	237/220	13.69/16.53	464	0.082	1152	2.6	1.07
CMSN-6	0.2	225	223/213	12.12/12.18	383	0.017	1173	2.6	1.14

<sup>a</sup> Molar ratio of CTAB or ethanol correspond to 2 mol of TEOS.

<sup>b</sup> Size calculated by averaging sizes of 50 random nanoparticles.

<sup>c</sup> St. Dev. (Standard Deviation) obtained by measuring sizes of 50 random nanoparticles.

<sup>d</sup> Size and PDI (Polydispersity Index) obtained from the DLS results in the intensity mode.

<sup>e</sup> Specific BET surface area.

<sup>f</sup> Pore diameter from the adsorption branch of the isotherm.

<sup>g</sup> Single point adsorption total pore volume of pores at relative pressure  $P/P_0 = 0.995$ .

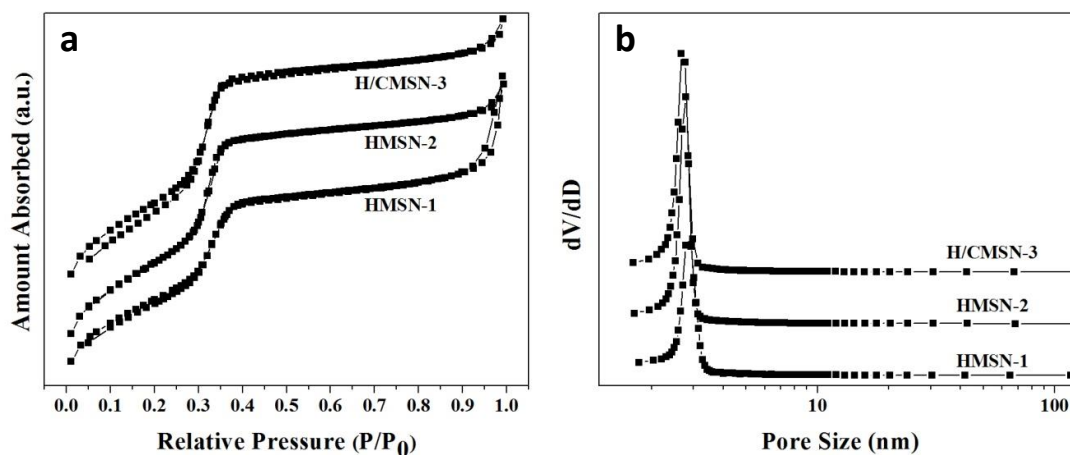


**Figure 2.9** (a) Nitrogen physisorption isotherms and (b) BJH pore size distributions of samples prepared by applying molar ratios of TEOS : EtOH : CTAB : NaOH : H<sub>2</sub>O = 2 : x : 0.15 : 1 : 2950. Herein, x = 0 for HMSN-1, x = 175 for HMSN-2, and x = 200 for H/CMSN-3.

Nitrogen physisorption analyses for HMSN-*n*, H/CMSN-*n* and CMSN-*n* revealed that all isotherms are of type IV without hysteresis loop (Figure. 2.9a and 2.10a), indicating typical characteristics of mesoporous architectures. The appearance of two capillary condensation steps at  $P/P_0$  of 0.28–0.35 and 0.95–1.0 can be attributed to framework-confined mesopores and interparticle textural pores. All MSNs exhibit narrow BJH pore size distributions regardless of the mesophase (Figure. 2.9b and 2.10b). All CMSN-*n* exhibit high BET surface areas of about 1130–1160  $\text{m}^2 \text{g}^{-1}$  and pore volumes of about 1.06–1.10  $\text{cm}^3 \text{g}^{-1}$ , as well as pore diameters of about 2.5–2.7 nm (cf., Tables 2.1 and 2.2).

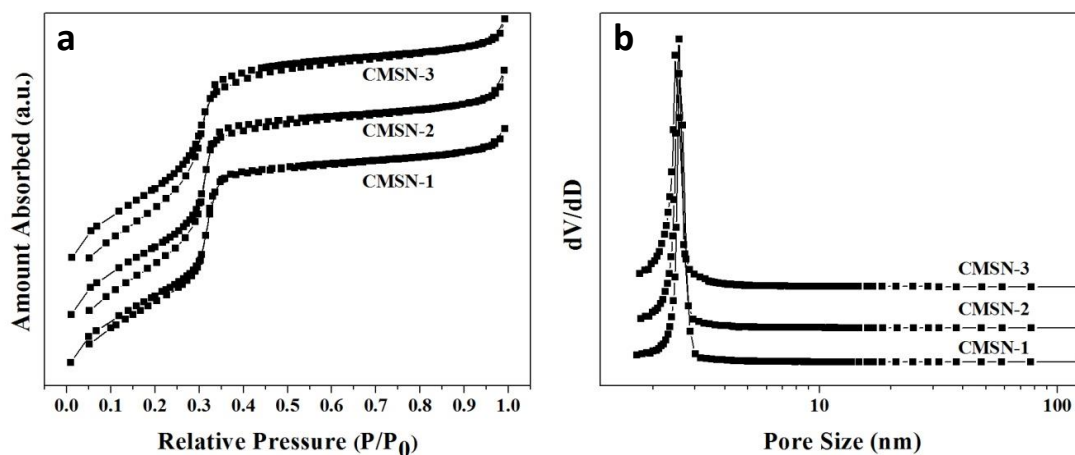


**Figure 2.10** (a) Nitrogen physisorption isotherms and (b) BJH pore size distributions of samples prepared by applying molar ratios of TEOS : EtOH : CTAB : NaOH : H<sub>2</sub>O = 2 : *x* : 0.15 : 1 : 2950. Herein *x* = 225 for CMSN-1, *x* = 250 for CMSN-2, and *x* = 275 for CMSN-3.

**Table 2.2** Pore parameters of HMSN and H/CMSN.

Material	CTAB <sup>a</sup>	EtOH <sup>a</sup>	$a_{\text{BET}}$ ( $\text{m}^2 \text{g}^{-1}$ ) <sup>b</sup>	$d_p$ (nm) <sup>c</sup>	$V_p$ ( $\text{cm}^3 \text{g}^{-1}$ ) <sup>d</sup>
HMSN-1	0.15	0	1008	2.7	1.12
HMSN-2	0.15	175	1144	2.8	1.03
H/CMSN-3	0.15	200	1146	2.6	1.05
H/CMSN-4	0.1	225	1119	2.5	0.90
H/CMSN-5	0.225	225	1240	2.5	1.10

<sup>a</sup> Molar ratio of CTAB/TEOS or ethanol/TEOS that correspond to 2 mol of TEOS;

<sup>b</sup> Specific BET surface area;

<sup>c</sup> Pore diameter from adsorption branch of the isotherm;

<sup>d</sup> Pore volume at relative pressure  $P/P_0 = 0.995$ .

### 2.3.2 Effect of CTAB

The surfactant concentration has been shown to be a vital parameter for the preparation of high-quality cubic MCM-48.<sup>38</sup> In the present study we also adjusted the molar ratio of CTAB/TEOS in the range from 0.1:2 to 0.225:2 while keeping a constant ratio of EtOH/TEOS of 225:2. PXRD measurements showed that mixed hexagonal-cubic PMSs were obtained when the molar ratio CTAB/TEOS is less than 0.125:2 or higher than 0.20:2 (Figure 2.11: H/CMSN-*n* (*n* = 4, 5)). When the CTAB/TEOS molar ratio ranged from 0.125:2 to 0.2:2, high-quality CMSN-*n* (*n* = 4, 5, 6) were formed, which were characterized by PXRD (Figure 2.12) and

TEM (Figure 2.13a, c and e, Figure 2.14), confirming characteristic mesoporous structures with  $Ia-3d$  symmetry. Mesoporous channels running perpendicular to the particle surface can be observed at the edge area of the nanoparticles in some TEM images (Figure. 2.3c, 2.13a, c and e). Similar mesoporous silica nanoparticles surrounded by a layer of mesopores oriented differently from the inner pore structure were reported previously,<sup>39</sup> especially in the intermediate state of the particle growth process.<sup>39b,39c</sup>

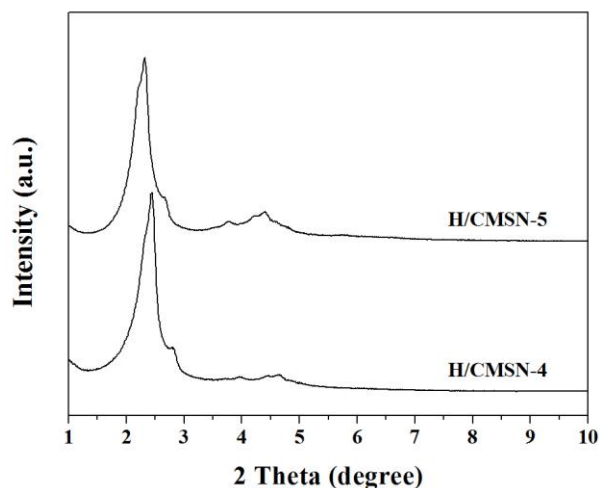


**Figure 2.11** PXR D patterns of H/CMSNs samples prepared by applying molar ratios of TEOS : EtOH : CTAB : NaOH : H<sub>2</sub>O = 2 : 225 : y : 1 : 2950. Herein y = 0.1 for H/CMSN-4, and y = 0.225 for H/CMSN-5.

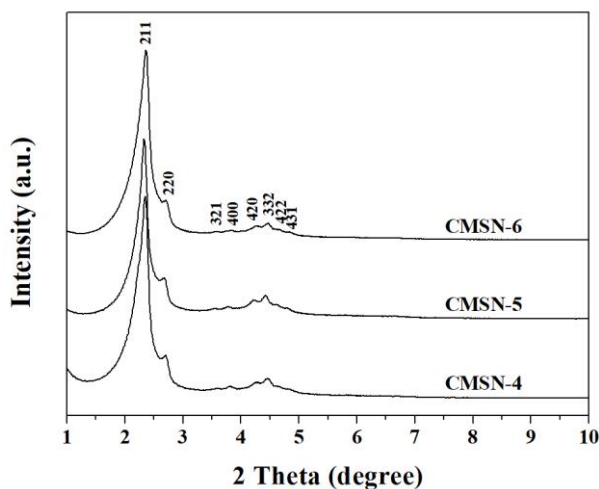


**Figure 2.12** PXR D patterns of CMSN-n (n = 4, 5, 6) prepared with molar ratios of TEOS : EtOH : CTAB : NaOH : H<sub>2</sub>O = 2 : 225 : y : 1 : 2950, y = 0.125 for CMSN-4, y = 0.175 for CMSN-5, and y = 0.2 for CMSN-6.

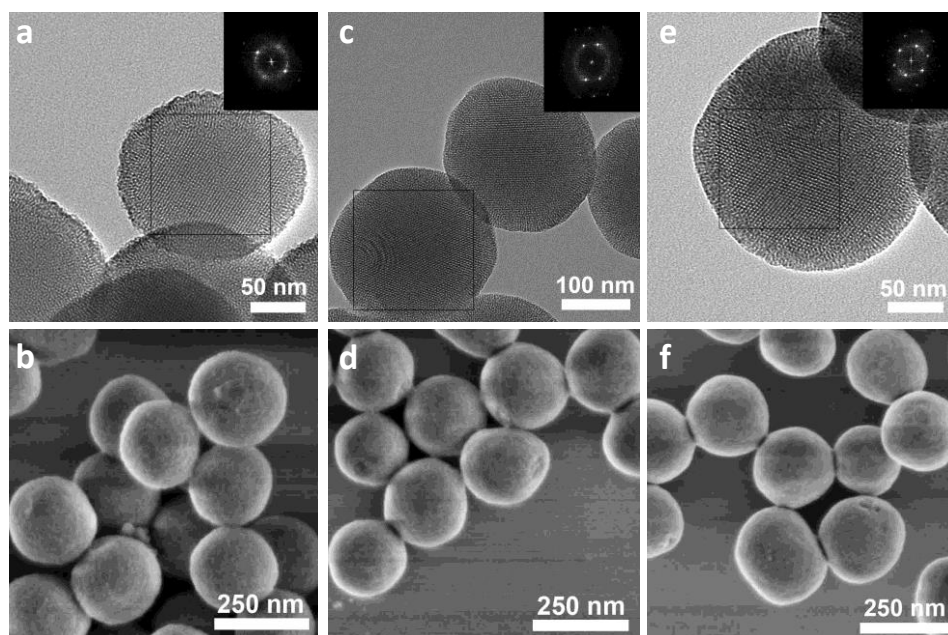


**Figure 2.13** Representative TEM images of (a) CMSN-4, (c) CMSN-5, and (e) CMSN-6 taken along the [100], [110] and [111] directions, respectively, as well as SEM images for (b) CMSN-4, (d) CMSN-5, and (f) CMSN-6. The insets are the corresponding Fast Fourier Transform (FFT) images.

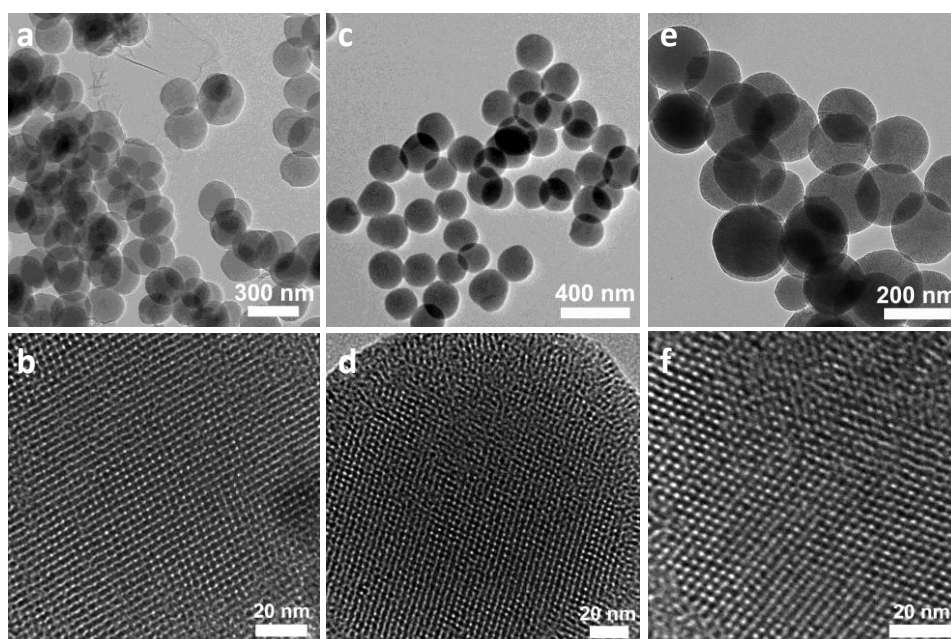


**Figure 2.14** TEM images with different magnifications of (a, b) CMSN-4, (c, d) CMSN-5 and (e, f) CMSN-6.

According to SEM analyses H/CMSN-4 and H/CMSN-5 are mixtures of rod-like and spherical nanoparticles (Figure 2.15). TEM and SEM images shown in Figure 2.13 demonstrate that all CMSN- $n$  ( $n = 4, 5, 6$ ) feature spherical morphologies with a narrow particle size distribution (Figure 2.16). The average particle size is  $241 \pm 2.8$  nm for CMSN-4,  $237 \pm 1.9$  nm for CMSN-5 and  $223 \pm 1.7$  nm for CMSN-6, revealing a slight decrease of the average particle size with increasing surfactant concentration. The monodispersity improved in the

same order (Table 2.1), which is also corroborated by DLS analyses (Figure. 2.17 and 2.18). The DLS curves of materials H/CMSN-n ( $n = 4, 5$ ) and CMSN-n ( $n = 4, 5, 6$ ) exhibited single peaks only. For CMSN-n, the DLS peaks shifted gradually to smaller particle size and became narrower with increasing surfactant concentration, also reflecting enhanced monodispersity.

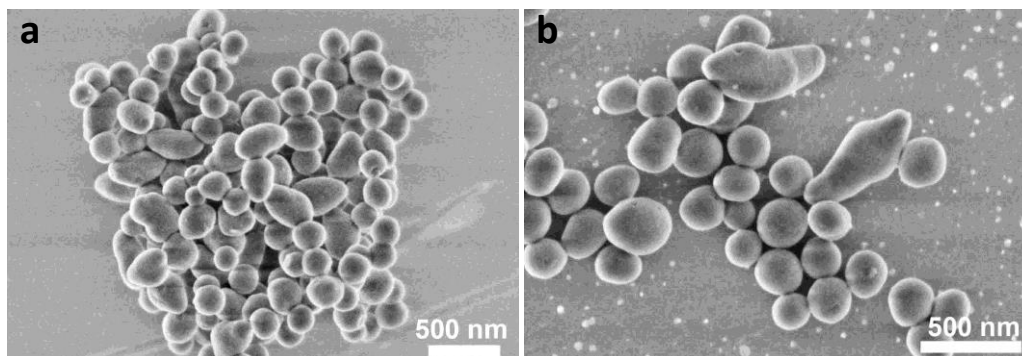


**Figure 2.15** SEM images of samples (a) H/CMSN-4 and (b) H/CMSN-5 prepared by applying molar ratios of TEOS : EtOH : CTAB : NaOH : H<sub>2</sub>O = 2 : 225 : y : 1 : 2950. Herein  $y = 0.1$  for H/CMSN-4 and  $y = 0.225$  for H/CMSN-5.

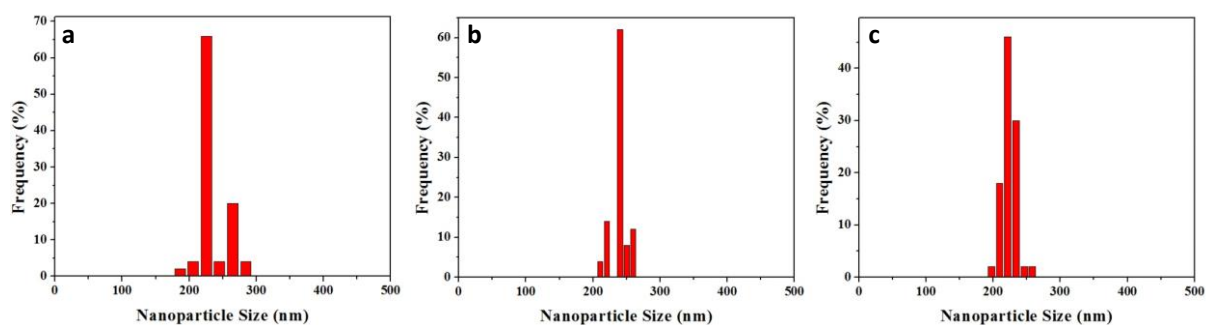


**Figure 2.16** Particle size distributions obtained by measuring 50 nanoparticles for (a) CMSN-4, (b) CMSN-5, and (c) CMSN-6 with average particle sizes of 241 nm, 237 nm and 223 nm, respectively.

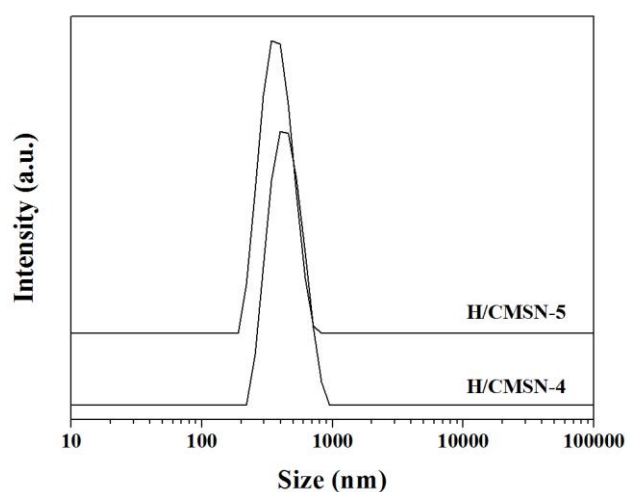


**Figure 2.17** DLS-derived particle size distribution of H/CMSN samples prepared by applying molar ratios of TEOS : NaOH : EtOH : CTAB : H<sub>2</sub>O = 2 : 1 : 225 : y : 2950. Herein  $y = 0.1$  for H/CMSN-4 and  $y = 0.225$  for H/CMSN-5.



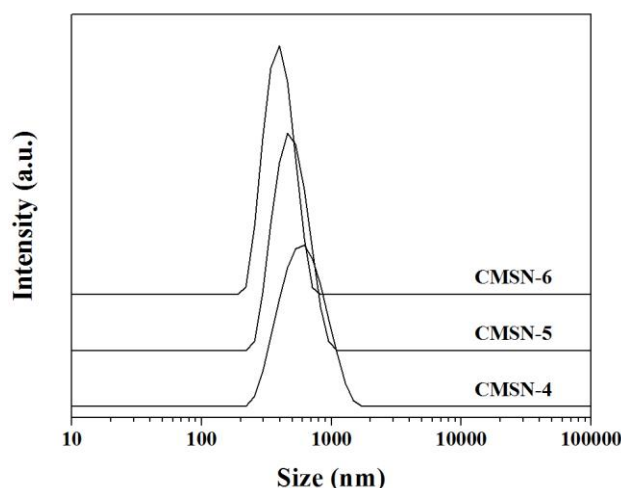


**Figure 2.18** DLS-derived particle size distribution of CMSN samples prepared by applying molar ratios of TEOS : NaOH : EtOH : CTAB : H<sub>2</sub>O = 2 : 1 : 225 : y : 2950. Herein y = 0.125 for CMSN-4, y = 0.175 for CMSN-5, and y = 0.2 for CMSN-6.

Nitrogen physisorption analyses showed that all H/CMSN-n (n = 4, 5) and CMSN-n (n = 4, 5, 6) have similar type IV isotherms (Figure. 2.19 and 2.20). With increasing surfactant concentration, the *BET* surface area for CMSN-n (n = 4, 5, 6) slightly increases and is accompanied by increase of the pore volume, but no remarkable change in pore diameter was observed (Table 2.1). Moreover, the narrow *BJH* pore size distributions (Figure. 2.19 and 2.20) also revealed a long-range ordering of pore arrays, which is in agreement with TEM and PXRD analyses.

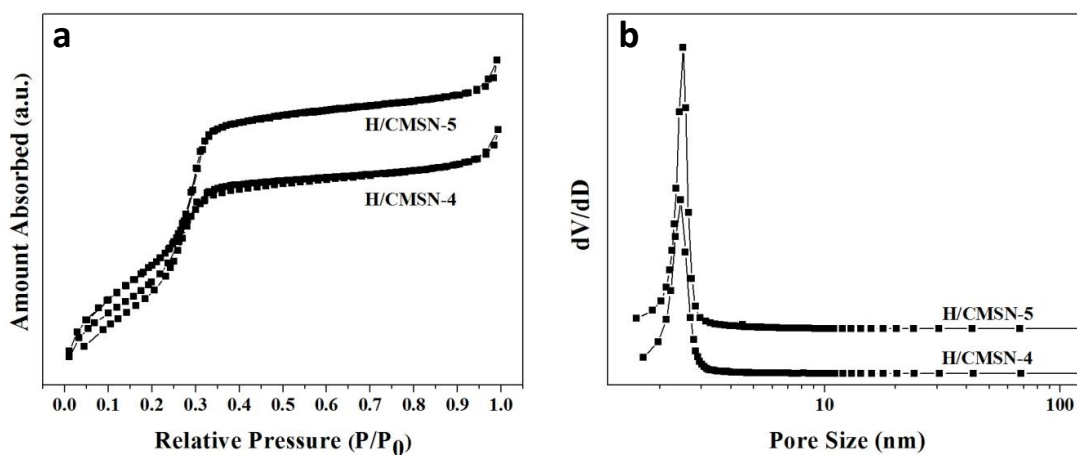


**Figure 2.19** (a) Nitrogen physisorption isotherms and (b) BJH pore size distributions of H/CMSN samples prepared by applying molar ratios of TEOS : NaOH : EtOH : CTAB : H<sub>2</sub>O = 2 : 1 : 225 : y : 2950. Herein, y = 0.1 for H/CMSN-4 and y = 0.225 for H/CMSN-5.

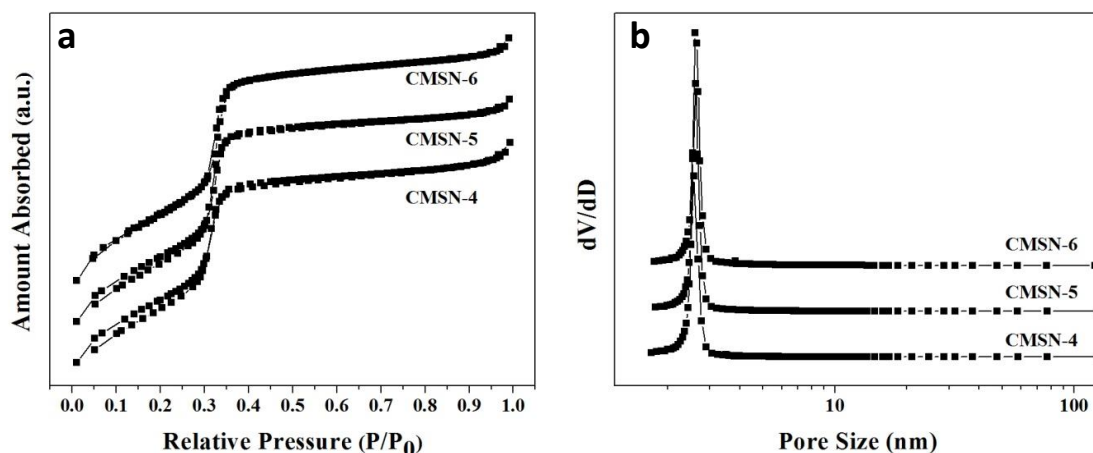


**Figure 2.20** (a) Nitrogen physisorption isotherms and (b) BJH pore size distributions of CMSNs prepared by applying molar ratios of TEOS : NaOH : EtOH : CTAB : H<sub>2</sub>O = 2 : 1 : 225 : y : 2950. Herein y = 0.125 for CMSN-4, y = 0.175 for CMSN-5, and y = 0.2 for CMSN-6.

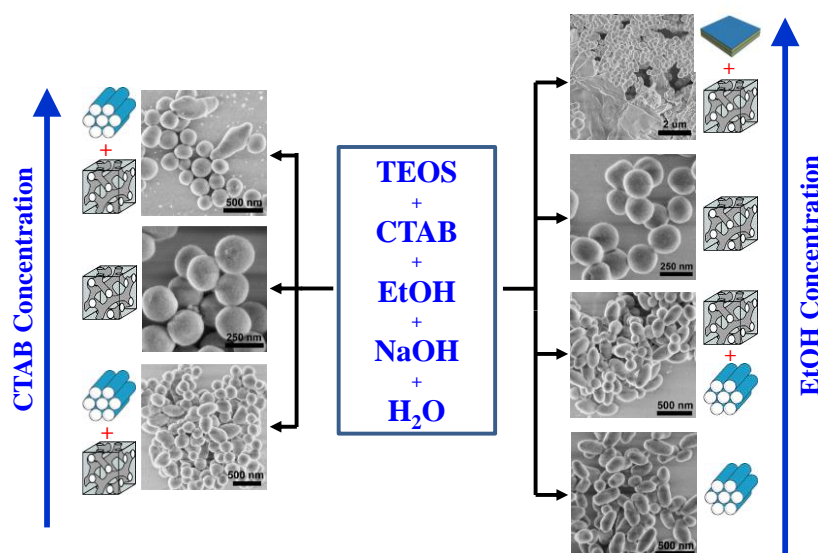


**Figure 2.21** Schematic illustration of the mesophase transformation and morphology evolution of MSNs by changing EtOH and CTAB concentrations.

### 2.3.3 Formation of Surfactant-Silicate Frameworks

The mesophase and morphology of the PMSNs could be readily adjusted by controlling the EtOH and CTAB concentrations. The overall results are schematized in Figure 2.21. The silica framework formation, mesophase transformation, and morphology evolution of the PMSNs under study were investigated in detail as follows. For comparison, the process of metal-based nanoparticle formation is well-known and established featuring nucleation and nanoparticle growth,<sup>40</sup> which is divided into three stages: (i) rapid increase of the concentration of constitute species, (ii) burst-nucleation, which in turn decreases the concentration of solute, (iii) slow growth of the seeds by diffusion. For mesoporous silica nanoparticles, the formation mechanism is supposed to be much more complicate because of the involvement of several factors, such as surfactant concentration, interactions between surfactant and inorganic silicate

frameworks, and condensation of ethoxysilanol species in aqueous solution involving pH control etc. The pH value of the reaction solution is an effective indicator for the progress hydrolysis and condensation in the synthesis system.<sup>41,42</sup>

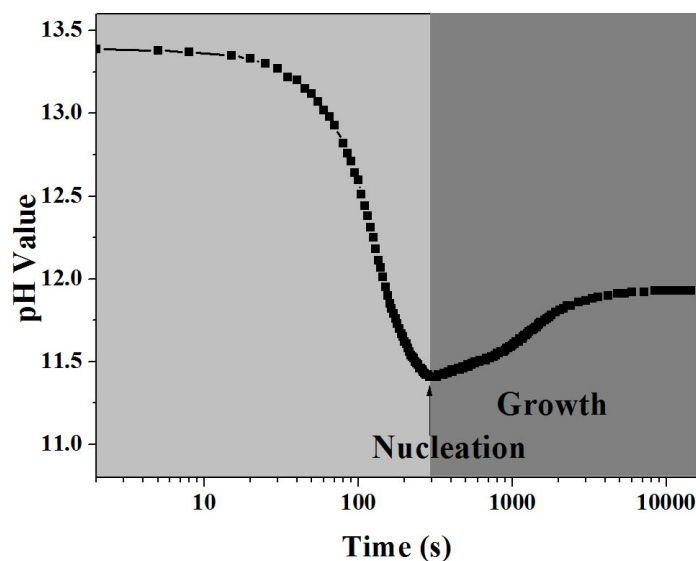
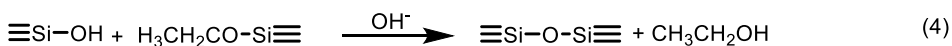
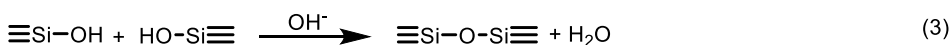
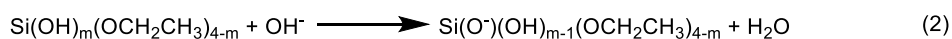
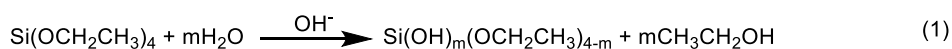


**Figure 2.22** Time-dependent pH development for the synthesis of CMSN-6 after addition of TEOS (molar ratio of TEOS : EtOH : CTAB : NaOH : H<sub>2</sub>O = 2 : 225 : 0.2 : 1 : 2950).

In Figure 2.22, we illustrate an *in-situ* time-dependent pH curve, obtained during the preparation of high-quality material CMSN-6. Any pH(pOH) alteration in the reaction system can directly reflect any changes occurring in the reaction mixture, since the concentration of the hydroxide anions (OH<sup>-</sup>) in solution depends on the hydrolysis of silica precursor TEOS and condensation of ethoxysilanol species. During the initial 10 s after addition of TEOS to the surfactant solution, no remarkable pH change was observed (Figure 2.22). At this stage, phase separation was observed in the mixture TEOS-CTAB-H<sub>2</sub>O-EtOH by turning off the stirring, while a turbid emulsion-like phase formed using stirring at a rate of 600 rotations per minute, implying that TEOS entered the hydrophobic area of the CTAB micelles. Afterwards, the turbid phase gradually converted into a clear solution, implying the hydrolysis of TEOS (caused by water molecules at the interface hydrophobic hydrocarbon chain/water) and migration of thus formed ethoxysilanol species from hydrophobic to hydrophilic regions. In the process of the gradual hydrolysis of TEOS (Eq. (1)), the formed ethoxysilanol species Si(OH)<sub>m</sub>(OCH<sub>2</sub>CH<sub>3</sub>)<sub>4-m</sub> (m is integer, m ≤ 4) can better dissolve in the aqueous solution and a transparent solution is observed which is accompanied by a pH decrease due to OH<sup>-</sup> consumption via deprotonation of silanol groups (Eq. (2)). On the one hand, the deprotonated silanol groups (CH<sub>3</sub>CH<sub>2</sub>O)<sub>4-m</sub>(HO)<sub>m-1</sub>SiO<sup>-</sup> can interact with cationic surfactants by electrostatic interaction. On the other hand, two neighbouring ethoxysilanol species containing hydroxyl or ethoxy groups can condense to form a bridged siloxane Si-O-Si- framework which in turn is accompanied by elimination of H<sub>2</sub>O or ethanol molecules (Eqs. (3) and (4)). At this stage, the rates of formation

of silanol groups by hydrolysis and consumption of silanol groups by deprotonation are higher than the rate of the condensation reactions, the pH value of solution thereby decreases. This is in accordance with previous findings.<sup>42</sup> Along with TEOS hydrolysis, the positive charge of the surfactant is balanced by deprotonated silicate species, generating a number of surfactant-silicate composites, the concentrations of which quickly increase and reach to the supersaturation state in solution. At this stage, the pH value reaches to a minimum and the nucleation of self-assembled surfactant-silicate composites occurs, and hence a turbid solution forms. Extensive condensation of silicate species leads to complicate and metastable siloxane frameworks,<sup>43</sup> while the pH value in the solution increases with the consumption of silanol group by condensation. At this point, nucleation comes to a halt and the proceeding condensation reaction generally causes the solution to become increasingly turbid while the pH value of the solution continuously increases. When the condensation reaction and the hydrolysis of the siloxane frameworks reached an equilibrium, which is at any time accompanied by charge matching between silicate oligomers and cationic surfactant molecules, the pH value in solution stays almost constant. Now, a stable silicate-surfactant composite is formed. Note that the plot of the pH versus time clearly demonstrates that the nucleation and growth of the silica nanoparticle occur at different stages. During the growth stage, no new surfactant-silicate fragments formed, ensuring the monodispersity of the eventual nanoparticles.



However, the above-mentioned only addresses the formation of surfactant-silicate frameworks, but how do the surfactant-silicate frameworks convert into a hexagonal or cubic phase with different morphologies during nanoparticle growth?

### 2.3.4 Mesophase Formation and Morphology Evolution

The formation of mesoporous silica with cubic or hexagonal symmetry is a complicate process involving silicate speciation reactions, surfactant-silicate self-assembly, and mesophase transformation from a metastable intermediate phase to a very stable hexagonal or cubic phase.<sup>43,44</sup> All these processes depend heavily on the synthesis conditions such as the molar ratio of the initial components, stirring rate, reaction temperature, ageing time, acidic or basic condition, and additives etc.<sup>14,45-47</sup> The previous investigations have elucidated in detail the formation of hexagonal or cubic PMSs using long-carbon chain quaternary ammonium salts as a structure-directing agent under basic conditions.<sup>1,14,45-48</sup> More recently, the growth or self-assembly mechanism and kinetics of PMSs were investigated using *in-situ* synchrotron small angle X-ray scattering,<sup>49-55</sup> whereas the mechanism of mesoporous silica formation has been discussed on the basis of time-resolved NMR spectroscopy and TEM studies.<sup>56-58</sup> Herein, we

focus on the influence of ethanol and surfactant on the mesophase formation of cubic PMSNs under otherwise identical conditions.

During the self-assembly of surfactant-silicate composites and continuous condensation of silicate species in solution, the charge-matching at the surfactant/silicate interface changes continuously. Depending on the size of these charge-matched surfactant-silicate entities, different interface curvatures are formed which decide the mesophase of the surfactant-silicate composite.<sup>46</sup> Further, the packing structure of the surfactant and the charge-matching between cationic surfactant and negative silicate species under basic condition are two key factors determining the mesostructure of the obtained silica. The pH value, cosolvent and counterions at the micelle interface influence charge matching while the reaction temperature and organic additives strongly affect the packing of surfactant chains, which is illustrated by the surfactant packing parameter  $g = V/(a_0l)$ .<sup>48,59</sup> Accordingly, low  $g$  values imply large interfacial surface curvatures, while high  $g$  values are beneficial to the preparation of MCM-48 or lamellar phase.<sup>48</sup> In our reaction system TEOS-NaOH-CTAB-H<sub>2</sub>O-EtOH, highly ordered hexagonal pore arrays for HMSN-1 were obtained in the absence of additional EtOH. When a small amount of EtOH was added to the reaction mixture, the resulting material HMSN-2 did not show any phase change. With increasing amount of EtOH, the mesophase switches from hexagonal (HMSN-n) to mixed hexagonal/cubic(H/CMSN-3), further to purely cubic (CMSN-n), and finally to mixed cubic/lamellar (C/LMSN-n) are clearly observed. This can be readily interpreted by change of the  $g$  value. The addition of a small amount of EtOH to a TEOS-NaOH-CTAB-H<sub>2</sub>O system is not enough to change the surfactant packing structure represented by the  $g$  value, and therefore no phase transformation occurred. In this case, EtOH likely acts as a co-solvent. Increasing amounts of EtOH partially or completely disrupt/disfavour the hexagonal surfactant micelle structure. The relatively greater increase of the total volume of surfactant and ethanol than that of the effective hydrophilic headgroup area at the micelle interface by EtOH, formally increases the  $g$  value and thereby leads to the formation of mixed hexagonal/cubic or purely cubic or cubic/lamellar phases. Hence the amount of EtOH used can be viewed as a switch to effectively control the formation of distinct mesophases. Moreover, the change of surfactant packing structure directly embodies on the alteration of surface curvature that markedly influences charge matching at surfactant/silicate interface. Hence the synergism of surfactant packing and charge matching decides the formation of different mesophases. In addition, at an identical EtOH concentration, alteration of the cationic surfactant concentration in the reaction system can also affect the formation of different mesophases. This mesophase transformation is caused by charge matching at the interface between cationic surfactant and silicate oligomer. The requirement for charge matching at the interface strongly drives the reorganization of the surfactant structure in order to match with the negative charge of oligomeric silicate species under basic conditions. In our system, a 3D cubic mesophase with *Ia-3d* symmetry can only form in a narrow range of surfactant concentration (the molar ratio of surfactant to TEOS ranged from 0.125 : 2 to 0.2 : 2, yielding

samples CMSN-4, CMSN-5, and CMSN-6, respectively). This is in good agreement with previous findings reported by Sayari and us.<sup>38</sup> Furthermore, the stirring rate and reaction time can also influence the formation and symmetry of the mesophase.<sup>10,11</sup> In the present reaction system, the high stirring rate was beneficial to the formation of the cubic mesophase at a very low surfactant concentration as well as a low base concentration (the molar ratio of surfactant/silica precursor and NaOH/silica precursor was 0.075 and 0.5, respectively). This can be rationalized by rapid diffusion of EtOH into the surfactant micelle, which decisively expands the total surfactant volume and thereby enables the formation of a bicontinuous cubic packed gyroidal micelle packing structure (Figure 2.23, HMSN-S1, CMSN-S2, CMSN-S3). The emerging oligomeric silicate species condense along the curved micellar surface to form the cubic mesophase at a high stirring rate.

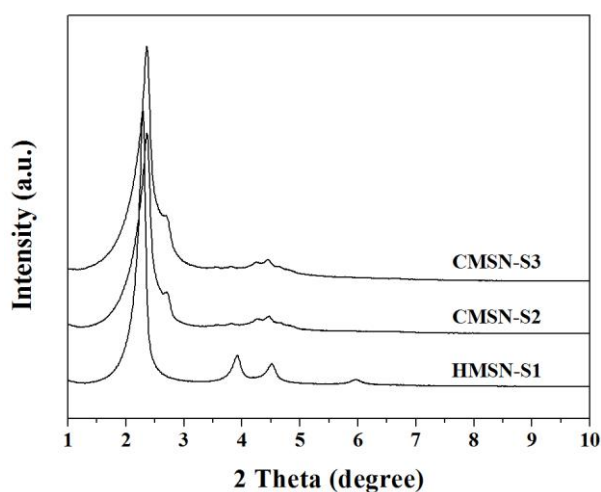


**Figure 2.23** PXRD patterns of HMSN and CMSN samples prepared by applying molar ratios of TEOS : NaOH : CTAB : H<sub>2</sub>O : EtOH = 2 : 1 : 0.15 : 2950 : 225 under stirring at 450 rpm for HMSN-S1, at 600 rpm for CMSN-S2, and at 750 rpm for CMSN-S3.

Next, how does the change of topology influence the morphology of the obtained PMSNs? SEM and TEM images shown in Figure 2.3, 2.5, 2.13 and 2.15 clearly display the evolution of distinct PMSN morphologies along with mesophase changes. Previous investigations have revealed that the PMSN morphology was influenced by the reaction conditions such as pH value,<sup>60</sup> temperature, and reaction time,<sup>38,61</sup> as well as auxiliary additives.<sup>44,62,63</sup> In our synthesis system, the absence/presence of EtOH directly influences PMSN morphology. Without EtOH, non-uniform ellipses and spheres with hexagonal mesostructure were obtained (HMSN-1, Figure 2.5a). Use of a small amount of ethanol led to the formation of uniform rod-like hexagonal mesoporous silica HMSN-2 (Figure 2.5b), implying that a low ethanol concentration could only change the shape of the mesoporous silica particle formed but not induce a mesophase transformation. Apparently, a small amount of ethanol only slightly expands the surfactant packing structure along a single direction within the original mesophase. Moreover, the addition of EtOH probably decreases the hydrolysis rate of TEOS and condensation rate of

silicate oligomers, facilitating a directed growth of nanoparticles at a low base concentration, at the same time minimizing the surface energy. Any change of conditions will influence the rate of the isotropic growth process from a nucleation point and thereby leads to the formation of irregular or more regular morphology with minimum surface energy. The final PMSN morphology depends on the balance between the condensation rate of inorganic silicate species and the rate of mesostructure formation.<sup>64,65</sup> The condensation rate of inorganic silicate oligomers in the HMSN-1 synthesis is evidently higher than the rate of mesostructure formation, resulting in non-uniformly aggregated nanoparticles (Figure 2.5a) with low long-range ordered mesostructure (Figure 2.1a). For HMSN-2, with more EtOH molecules penetrating into the surfactant micelle to form well-elongated micelles,<sup>24,30</sup> the slower hydrolysis and condensation rates provide enough time for the formation of cylindrical micelles and hence the assembly of a well-ordered hexagonal MCM-41 mesostructure (Figure 2.1a) with uniform rod-like morphology (Figure 2.5b). With further increase of the EtOH amount, the original surfactant micelles are partially broken up by the diffusion of a large number of ethanol into the surfactant packing structure, and thereby lead to the formation of new micelles that induce a phase transformation in order to rebalance charge matching at the interface between positively charged surfactants and negatively charged inorganic silicate oligomers. Thus, material H/CMSN-3 was obtained, featuring particles of mixed rodlike (from original phase) and spherical shape (from new phase) (Figure 2.1a and 2.5c), indicating that morphology evolution starts with the nucleation of new self-assembled micelles. Within the nucleation and growth process, the aggregation of surfactant micelles and the condensation of oligomeric silicate species along the curved micelles keep the final particles with a minimum surface energy. At a certain ethanol level, the original micelle structure is completely broken up and a new phase forms accompanied by a new morphology. In our system, CMSNs with a pure cubic mesophase of *Ia-3d* symmetry were obtained in the ethanol range from 225 to 275 corresponding to 2 mol TEOS, showing spherical shape with uniform particle size (Figure 2.3 and 2.7). Even higher levels of ethanol produced a mixed cubic/lamellar phase exhibiting spherical and flake-like particles (Figure 2.24). Based on above discussion, the presence of ethanol can effectively control the PMSN formation involving hexagonal, mixed hexagonal/cubic, cubic, and mixed cubic/lamellar mesophases and PMSN morphologies of ellipsoidal/spherical, rod-like, spherical, and spherical/flake-like shapes, respectively. Previous studies revealed that the use of ethanol can affect phase transformation from MCM-41 to MCM-48 via a high stirring rate or hydrothermal treatment.<sup>10,11,66</sup> Our own work and that of others showed that in the absence of ethanol the TEOS-CTAB-NaOH-H<sub>2</sub>O system affords mesoporous silica with high polydispersity, most likely due to the faster hydrolysis and condensation rate in the absence of EtOH, which further gives rise to rapid nucleation and increased formation of seeds for growth.<sup>12,67</sup> Note that the addition of ethanol markedly extends nucleation time which is beneficial to the formation of uniform and regular morphology. As seen in Table 2.3, with increasing amounts of ethanol, the nucleation was delayed while the particle size gradually

increased, indirectly confirming the decrease of the hydrolysis rate of TEOS and condensation rate of silicate oligomers. Moreover, we observed that nucleation in solution is accompanied by a temporary constant pH value (Figure. 2.22 and 2.25). Therefore, it seems easy to detect nucleation in solution by monitoring the pH value.

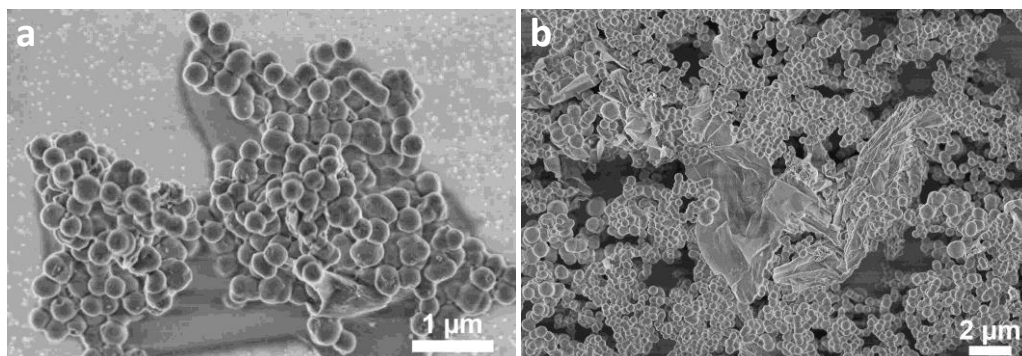


**Figure 2.24** SEM images of samples (a) C/LMSN-2 and (b) C/LMSNs-3 prepared by applying molar ratios of TEOS : EtOH : CTAB : NaOH : H<sub>2</sub>O = 2 : x : 0.15 : 1 : 2950. Herein x = 325 for C/LMSN-2 and x = 400 for C/LMSN-3.

**Table 2.3** Nucleation time and final nanoparticle size for the final molar gel composition TEOS : EtOH : CTAB : NaOH : H<sub>2</sub>O = 2 : x : 0.15 : 1 : 2950 (x = 225, 250 and 275).

Ethanol molar ratio	Nucleation time (s)	Nanoparticle size (nm)
225	275	226
250	290	251
275	310	303

<sup>a</sup> Molar ratio of EtOH/TEOS that corresponds to 2 mol of TEOS.

<sup>b</sup> The starting point of nucleation is set after reaching a constant pH value (Figure S2.19)

<sup>c</sup> From SEM

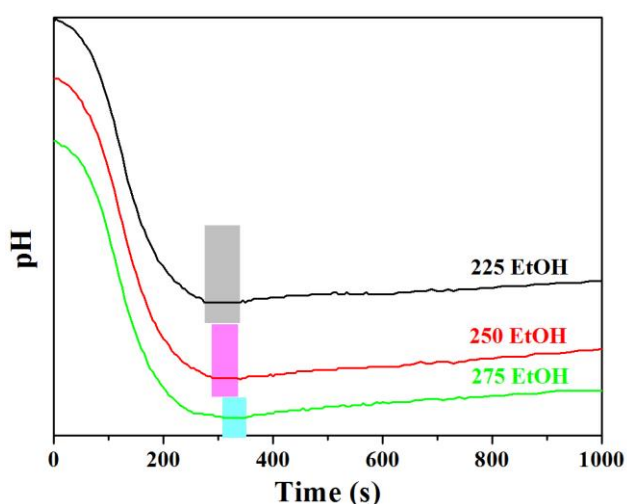


**Figure 2.25** Time-dependent pH curves of the solutions during the preparation of CMSN-n (n = 4, 5, 6) applying molar compositions of 2TEOS : 1NaOH : xEtOH : 2950H<sub>2</sub>O : 0.15CTAB (x = 225 for CMSN-4, x = 250 for CMSN-5, and x = 275 for CMSN-6). The colored areas in each curve indicate the stage of constant pH value.

In addition, we found that under otherwise identical conditions, the increase of CTAB concentration gives rise to the formation of spherical PMSs with particle sizes gradually



decreasing from 241 to 223 nm. This phenomenon is consistent with previous reports.<sup>68,69</sup> Our investigations showed that a pure cubic mesophase occurred only in a very narrow range of surfactant concentration (the molar ratio of surfactant/2TEOS ranged from 0.125 to 0.2), which implies only a small change of particle size. Apart from a smaller size, high CTAB concentration gives also rise to increasingly monodisperse MCM-48 nanoparticles as reflected by the DLS and SEM results.

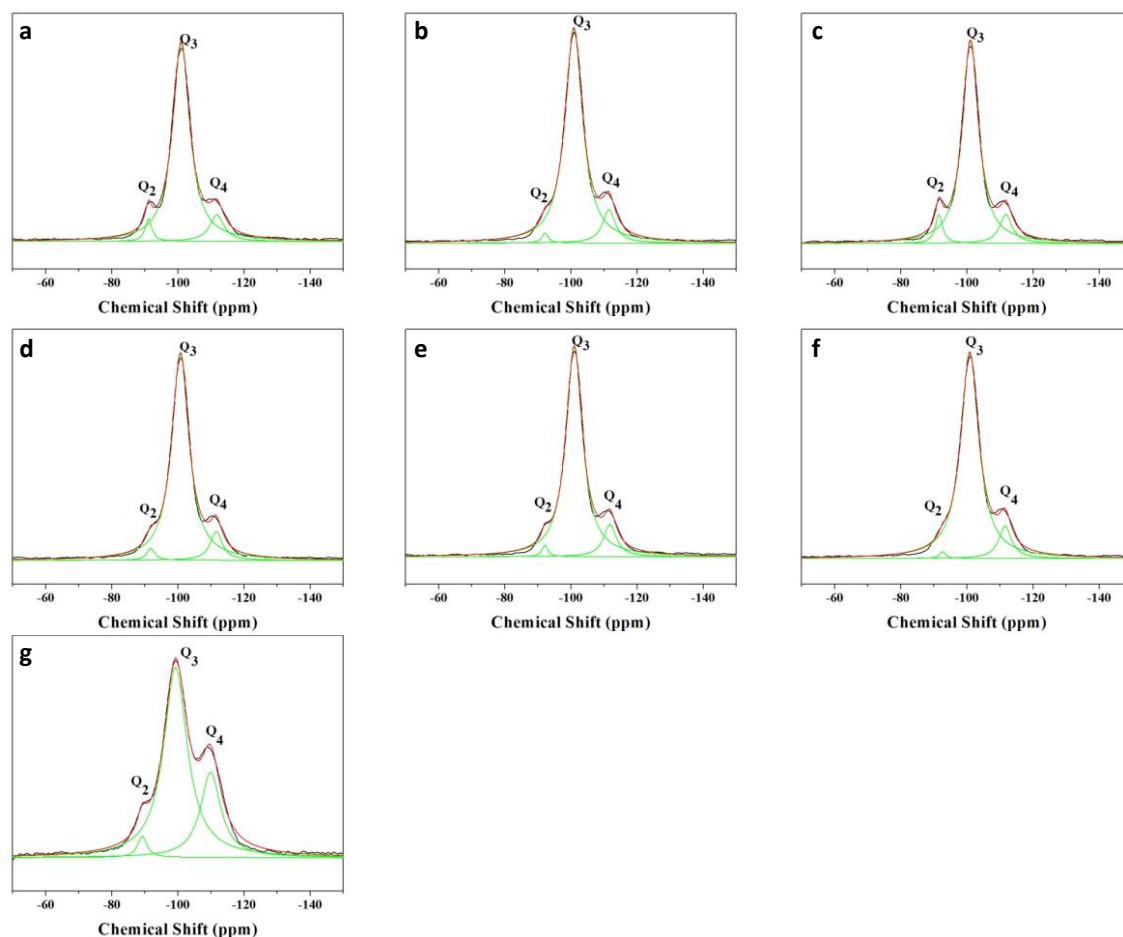


**Figure 2.26**  $^{29}\text{Si}$  CP MAS NMR spectra of PMS samples (a) HMSN-1, (b) HMSN-2, (c) H/CMSN-3, (d) CMSN-1, (e) CMSN-2, (f) CMSN-3, and (g) C/LMSN-2.

### 2.3.5 $^{29}\text{Si}$ CP MAS NMR Spectroscopy for HMSN-n, H/CMSN-n, CMSN-n and C/LMSN-n

Solid-state  $^{29}\text{Si}$  NMR spectra were recorded to examine the degree of silica framework condensation for the different mesophases and morphologies. As shown in Figure 2.26 and 2.27 as well as Table 2.4, almost all PMSNs indicate three characteristic peaks—two weak peaks assigned to  $\text{Q}^2$  ( $\text{Si}(\text{OSi})_2(\text{OX})_2$ ,  $\text{X} = \text{H}$  or  $\text{Et}$ ) (-91 ppm) and  $\text{Q}^4$  ( $\text{Si}(\text{OSi})_4$ ) (-110 to -111 ppm) species, and a very strong peak ascribed to  $\text{Q}^3$  ( $\text{Si}(\text{OSi})_3(\text{OX})$ ) (-101 to -102 ppm). The chemical shifts are quite similar to those reported previously,<sup>44,70,71</sup> but the ratio of  $\text{Q}^3/\text{Q}^4$ , that is used to determine the degree of condensation, and the concentration of silanol groups was quite different (which is plausible considering the different template removal).<sup>44,69</sup> Previous

investigations confirmed that the spherical morphology is more condensed than that of a fine powder<sup>69</sup> and that the cubic mesophase was more condensed than other mesophases.<sup>44,69</sup> However, the ratio of  $Q^3/Q^4$  listed in Table 2.4 is almost the same regardless of morphology and mesophase of MSNs, indicating a low degree of condensation of the silica framework. Moreover, the appearance of  $Q^2$  (with similar intensity as  $Q^4$ ) directly verifies the low condensation degree of the silica wall of the MSNs under study. The low condensation degree of PMSNs is probably attributable to the extraction process for template removal which is not beneficial to the further condensation of silica framework compared to high temperature calcination. However, the obtained CMSN is quite stable in the solvent *n*-hexane. The spherical morphology and average size are still remained after 1 day and even 7 days upon continuous stirring (Fig. 2.28). The preserved spherical morphology and stable mesostructure in organic solvents make CMSNs promising supports for surface organometallic chemistry.<sup>72</sup>

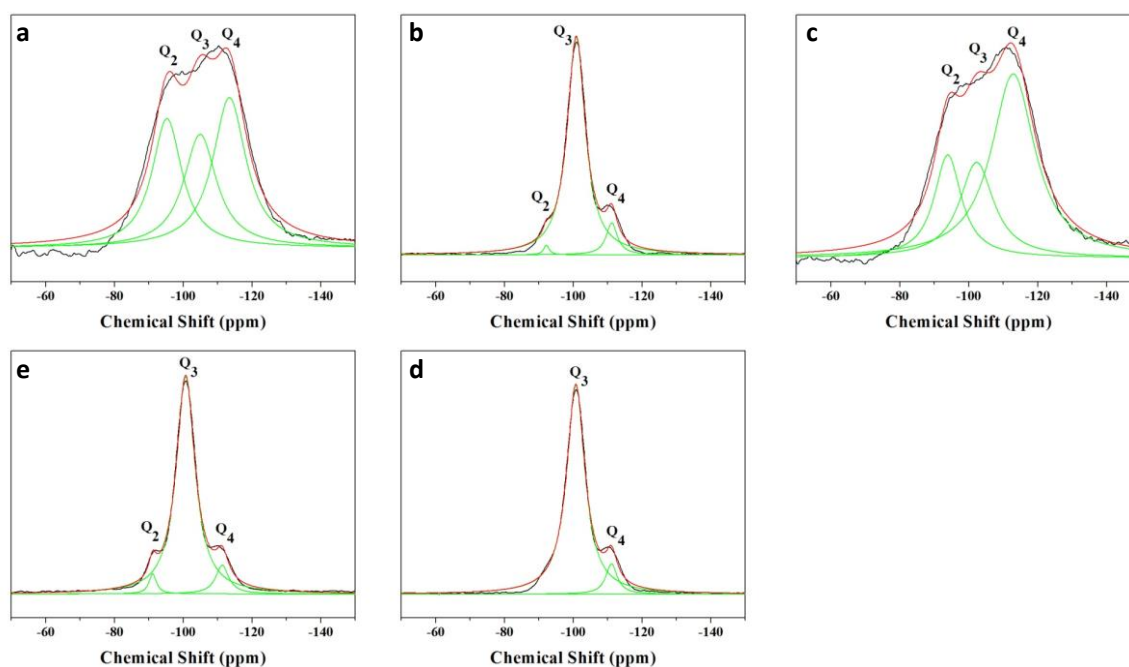


**Figure 2.27**  $^{29}\text{Si}$  CP MAS NMR spectra of PMS samples (a) H/CMSN-4, (b) CMSN-3, (c) CMSN-4, (d) CMSN-5, and (e) H/CMSNs-5.

**Table 2.4**  $Q^3/Q^4$  ratios calculated from  $^{29}\text{Si}$  CP MAS NMR spectra of PMSNs prepared by using different ethanol and surfactant concentrations under study.

Material	$Q^3/Q^4$
HMSN-1	8.90
HMSN-2	8.70
H/CMSN-3	8.73
CMSN-1	10.09
CMSN-2	8.25
CMSN-3	8.94
C/LMSN-2	8.70
H/CMSN-4	0.75
CMSN-4	10.94
CMSN-5	0.41
CMSN-6	4.96
H/CMSN-5	10.84

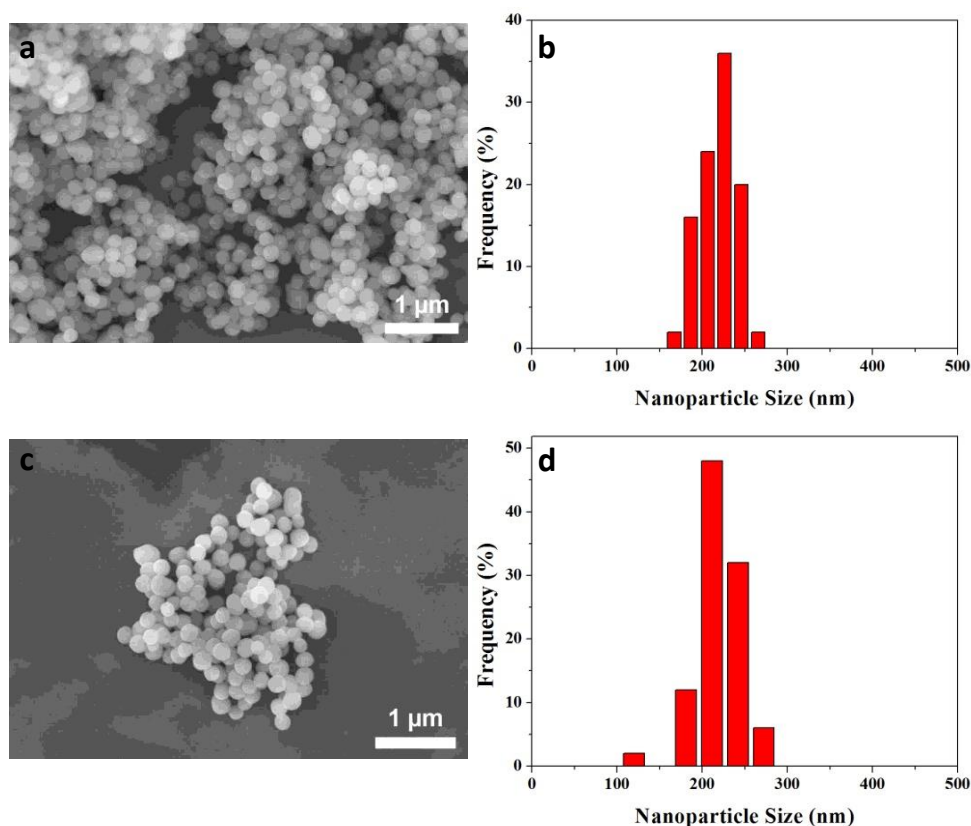


**Figure 2.28** SEM images of CMSN-6 after stirring in n-hexane for 1 day (a) and 7 days (c), and corresponding particle size distributions of CMSN-6 for 1 day (b) and 7 days (d). The average particle sizes of CMSN-6 are  $217 \pm 3.1$  nm after stirring for 1 day and  $219 \pm 3.8$  nm for 7 days.

## 2.4 Conclusions

Monodisperse MCM-48 nanospheres are readily prepared by optimizing the molar composition of the TEOS-CTAB-NaOH-H<sub>2</sub>O-EtOH system (TEOS = tetraethyl orthosilicate, CTAB = cetyltrimethylammonium bromide, EtOH = ethanol). Increasing amounts of EtOH affect the surfactant packing structure driving the formation of periodic mesoporous silica with hexagonal, mixed hexagonal/cubic, purely cubic, and mixed cubic/lamellar mesostructures. This is accompanied by a morphology evolution from mixture of ellipses and spheres to regular rod-like shape, further to uniform spheres, and finally to a mixture of spheres and flakes. In particular, highly monodisperse and uniform mesoporous silica nanospheres with MCM-48 structure (CMSN-n; cubic mesoporous silica nanoparticles) are quite easily obtained, while the monodispersity and particle size can be readily controlled via ethanol concentration.<sup>9–13</sup> On the other hand, at a given ethanol concentration, high-quality CMSN-n can only be fabricated in a narrow range of surfactant concentration with a high stirring rate ( $\geq 600$  rpm). It can be hypothesized that such structural mesophase transformations are due to ethanol-driven changes of the surfactant packing structure and charge matching at the surfactant/silicate interface. The respective morphology evolution of the mesoporous nanoparticles can be elucidated by an ethanol-controlled hydrolysis rate of TEOS and the condensation degree of oligomeric silicate species via a nucleation and growth process. Importantly, the present strategy allows for the

simultaneous control of MSN long-range ordering and morphology. The synthesis protocols are facile and effective, as well as environmentally benign since ethanol can be recovered by evaporation and be reused. The high-quality CMSN-n with adjustable nanoparticle size can apply to catalysis, adsorption, separation and drug delivery alike.

## 2.5 References

1. a) C. T. Kresge, M. E. Leonowicz, W. J. Roth, J. C. Vartuli and J. S. Beck, *Nature*, **1992**, 359, 710-712; b) J. S. Beck, J. C. Vartuli, W. J. Roth, M. E. Leonowicz, C. T. Kresge, K. D. Schmitt, C. T. W. Chu, D. H. Olsen, E. W. Sheppard, S. B. McCullen, J. B. Higgins and J. L. Schlenker, *J. Am. Chem. Soc.*, **1992**, 114, 10834-10854.
2. a) Y. Wan and D. Zhao, *Chem. Rev.*, **2007**, 107, 2821-2860; b) D. Tarn, C. E. Ashley, M. Xue, E. Carnes, J. I. Zink and C. J. Brinker, *Acc. Chem. Res.*, **2013**, 46, 792-801.
3. a) R. Schmidt, M. Stöcker, D. Akporiaye, E.H. Tørstad and A. Olsen, *Micro. Mater.*, **1995**, 5, 1-7; b) V. Alfredsson and M. W. Anderson, *Chem. Mater.*, **1996**, 8, 1141-1146; c) F. Kleitz, S. H. Choi and R. Ryoo, *Chem. Commun.*, **2003**, 2136-2137; d) T. W. Kim, F. Kleitz, B. Paul and R. Ryoo, *J. Am. Chem. Soc.*, **2005**, 127, 7601-7610.
4. a) K. Mukhopadhyay, B. R. Sarkar and R. V. Chaudhari, *J. Am. Chem. Soc.*, **2002**, 124, 9692-9693; b) A. Papat, J. Liu, Q. Hu, M. Kennedy, B. Peters, G. Q. M. Lu and S. Z. Qiao, *Nanoscale*, **2012**, 4, 970-975; c) E. Choi, J. Lu, F. Tamanoi, J. I. Zink, *Z. Anorg. Allg. Chem.*, **2014**, 640, 588-594.
5. a) B. G. Trwyn, S. Giri, I. I. Slowing and V. S.-Y. Lin, *Chem. Commun.*, **2007**, 3236-3245; b) I. I. Slowing, J. L. Vivero-Escoto, B. G. Trewyn and V. S.-Y. Lin, *J. Mater. Chem.*, **2010**, 20, 7924-7937.
6. A. Papat, B. P. Ross, J. Liu, S. Jambhrunkar, F. Kleitz and S. Z. Qiao, *Angew. Chem. Int. Ed.*, **2012**, 51, 12486-12489.
7. a) T. M. Suzuki, M. Yamamoto, K. Fukumoto, Y. Akimoto and K. Yano, *J. Catal.*, **2007**, 251, 249-257; b) T. M. Suzuki, T. Nakamura, E. Sudo, Y. Akimoto and K. Yano, *Micro. Meso. Mater.*, **2008**, 111, 350-358.
8. a) E. Yamamoto, M. Kitahara, T. Tsumura and K. Kuroda, *Chem. Mater.*, **2014**, 26, 2927-2933; b) L. Bai, Z. Xie, W. Wang, C. Yuan, Y. Zhao, Z. Mu, Q. Zhong and Z. Gu, *ACS Nano*, **2014**, 8, 11094-11100.
9. a) K. Schumacher, C. D. F. von Hohenesche, K. K. Unger, R. Ulrich, A. Du Chesne, U. Wiesner and H. W. Spiess, *Adv. Mater.*, **1999**, 11, 1194-1198; b) K. Schumacher, M. Grün and K. K. Unger, *Micro. Meso. Mater.*, **1999**, 27, 201-206.
10. B. Boote, H. Subramanian and K. T. Ranjit, *Chem. Commun.*, **2007**, 4543-4545.
11. T.-W. Kim, P.-W. Chung and V. S. Y. Lin, *Chem. Mater.*, **2010**, 22, 5093-5104.
12. P. K. Chen, N. C. Lai, C. H. Ho, Y. W. Hu, J. F. Lee and C. M. Yang, *Chem. Mater.*, **2013**, 25, 4269-4277.
13. K. Yano, M. B. Katz, X. Pan and N. Tatsuda, *J. Colloid Interf. Sci.*, **2014**, 418, 61-65.
14. a) J. C. Vartuli, K. D. Schmitt, C. T. Kresge, W. J. Roth, M. E. Leonowicz, S. B. McCullen, S. D. Hellring, J. S. Beck, J. L. Schlenker, D. H. Olson and E. W. Sheppard, *Chem. Mater.*, **1994**, 6, 2317-2326; b) A. Monnier, F. Schüth, Q. Huo, D. Kumar, D. Margolese, R. S. Maxwell, G. D. Stucky, M. Krishnamurty, P. Petroff, A. Firouzi, M. Janicke and B. F. Chmelka, *Science*, **1993**, 261, 1299-1303.
15. a) F. Lu, S. H. Wu, Y. Hung and C. Y. Mou, *Small*, **2009**, 5, 1408-1413; b) S. H. Wu, C. Y. Mou and H. P. Lin, *Chem. Soc. Rev.*, **2013**, 42, 3862-3875.
16. a) R. Ryoo, S. H. Joo and J. M. Kim, *J. Phys. Chem. C*, **1999**, 103, 7435-7440; b) L. Han, K. Miyasaka, O. Terasaki and S. Che, *J. Am. Chem. Soc.*, **2011**, 133, 11524-11533.
17. J. N. Israelachvili, D. J. Mitchell and B. W. Ninham, *J. Chem. Soc., Faraday Trans.*, **1976**, 272, 1525-1568.
18. R. Zana, S. Yiv, C. Strazielle and P. Lianos, *J. Colloid. Interface Sci.*, **1981**, 80, 208-223.

19. C. Treiner, *J. Colloid Interface Sci.*, **1983**, 93, 33-42.
20. E. Valenzuela, E. Abuin and E. Lissi, *J. Colloid Interface Sci.*, **1984**, 102, 46-50.
21. R. Strey, R. Schomacker, D. Roux, F. Nallet and U. Olsson, *J. Chem. Soc., Faraday Trans.*, **1990**, 86, 2253-2261.
22. H. Hoffmann, C. Thunig, U. Munkert, W. Meyer and W. Richer, *Langmuir*, **1992**, 8, 2629-2638.
23. D. Langevin, *Annu. Rev. Phys. Chem.*, **1992**, 43, 341-369.
24. M. E. Morgan, H. Uchiyama, S. D. Christian, E. E. Tucker and J. F. Scamehorn, *Langmuir*, **1994**, 10, 2170-2176.
25. K. Fontell, A. Khan, B. Lindström, D. Maciejewska and S. Puang-Ngern, *Colloid Polym. Sci.*, **1991**, 269, 727-742.
26. J. F. Wall and C. F. Zukoski, *Langmuir*, **1999**, 15, 7432-7437.
27. H. P. Lin, Y. R. Cheng, S. B. Liu and C. Y. Mou, *J. Mater. Chem.*, **1999**, 9, 1197-1201.
28. H. P. Lin, C. P. Kao and C. Y. Mou, *Micro. Meso. Mater.*, **2001**, 48, 135-141.
29. P. Agren, M. Linden, J. B. Rosenholm, R. Schwarzenbacher, M. Kriechbaum, H. Amenitsch, P. Laggner, J. Blanchard and F. Schüth, *J. Phys. Chem. B*, **1999**, 103, 5943-5948.
30. S. Liu, P. Cool, O. Collart, P. Van Der Voort, E. F. Vansant, O. I. Lebedev, G. Van Tendeloo and M. Jiang, *J. Phys. Chem. B*, **2003**, 107, 10405-10411.
31. Q. Huo, J. Feng, F. Schüth and G. D. Stucky, *Chem. Mater.*, **1997**, 9, 14-17.
32. K. M. McGrath, D. M. Dabbs, N. Yao, I. A. Aksay and S. M. Gruner, *Science*, **1997**, 277, 552-556.
33. H. P. Lin, S. Cheng and C. Y. Mou, *Micro. Mater.*, **1997**, 10, 111-121.
34. M. Grün, K. K. Unger, A. Matsumoto and K. Tsutsumi, *Micro. Meso. Mater.*, **1999**, 27, 207-216.
35. G. Büchel, K. K. Unger, A. Matsumoto and K. Tsutsumi, *Adv. Mater.*, **1998**, 10, 1036-1038.
36. K. Yano and Y. Fukushima, *J. Mater. Chem.*, **2004**, 14, 1579-1584.
37. W.-Q. Wang, J.-G. Wang, P.-C. Sun, D.-T. Ding and T.-H. Chen, *J. Colloid Interf. Sci.*, **2009**, 331, 156-162.
38. a) A. Sayari, *J. Am. Chem. Soc.*, **2000**, 122, 6504-6505; b) M. Widenmeyer and R. Anwender, *Chem. Mater.*, **2002**, 14, 1827-1831.
39. a) V. K. LaMer and R. H. Dinegar, *J. Am. Chem. Soc.*, **1950**, 72, 4847-4854; b) V. K. LaMer, *Ind. Eng. Chem.*, **1952**, 44, 1270-1277.
40. a) D. Nagao, H. Osuzu, A. Yamada, E. Mine, Y. Kobayashi and M. Konno, *J. Colloid Interf. Sci.*, **2004**, 279, 143-149; b) Z.-A. Qiao, L. Zhang, M. Y. Guo, Y. L. Liu and Q. S. Huo, *Chem. Mater.*, **2009**, 21, 3823-3829.
41. T. Nakamura, M. Mizutani, H. Nozaki, N. Suzuki and K. Yano, *J. Phys. Chem. C*, **2007**, 111, 1093-1100.
42. a) S. Sadasivan, C. E. Fowler, D. Khushalani and S. Mann, *Angew. Chem. Int. Ed.*, **2002**, 41, 2151-2153; b) T. Suteewong, H. Sai, M. Bradbury, L. A. Estroff, S. M. Gruner and U. Wiesner, *Chem. Mater.*, **2012**, 24, 3895-3905.
43. A. Chang, N.-C. Lai and . Yang, *RSC Advances*, **2012**, 2, 12088-12090.
44. a) Q. Huo, R. Leon, P. M. Petroff and G. D. Stucky, *Science*, **1995**, 268, 1324-1327; b) Q. Huo, D. I. Margolese, U. Ciesla, D. G. Demuth, P. Feng, T. E. Gier, P. Sieger, A. Firouzi, B. F. Chmelka, F. Schüth and G. D. Stucky, *Chem. Mater.*, **1994**, 6, 1176-1191.
45. H.-P. Lin and C.-Y. Mou, *Acc. Chem. Res.*, **2002**, 35, 927-935.
46. Y. Liang, E. S. Erichsen, M. Hanzlik and R. Anwender, *Chem. Mater.*, **2008**, 20, 1451-1458.
47. Q. Huo, D. I. Margolese and G. D. Stucky, *Chem. Mater.*, **1996**, 8, 1147-1160.
48. E. Gianotti, G. Berlier, K. Costabello, S. Coluccia and F. Meneau, *Catal. Today*, **2007**, 126, 203-210.
49. S. Manet, J. Schmitt, M. Impérator-Clerc, V. Zholobenko, D. Durand, C. L. P. Oliveira, J. S. Pedersen, C. Gervais, N. Baccile, F. Babonneau, I. Grillo, F. Meneau and C. Rochas, *J. Phys. Chem. B*, **2011**, 115, 11330-11344.

50. M. J. Hollamby, D. Borisova, P. Brown, J. Eastoe, I. Grillo and D. Shchukin, *Langmuir*, **2012**, 28, 4425-4433.
51. F. Michaux, N. Baccile, M. Impéror-Clerc, L. Malfatti, N. Folliet, C. Gervais, S. Manet, F. Meneau, J. S. Pedersen and F. Babonneau, *Langmuir*, **2012**, 28, 17477-17493.
52. J. Schmitt, M. Impéror-Clerc, F. Michaux, J. -L. Blin, M. -J. Stebe, J. S. Pedersen and F. Meneau, *Langmuir*, **2013**, 29, 2007-2023.
53. J. L. Blin and M. Impéror-Clerc, *Chem. Soc. Rev.*, **2013**, 42, 4071-4082.
54. Z. Yi, L. F. Dumée, C. J. Garvey, C. Feng, F. She, J. E. Rookes, S. Mudie, D. M. Cahill and L. Kong, *Langmuir*, **2015**, 31, 8478-8487.
55. K. Flodström, H. Wennerström and V. Alfredsson, *Langmuir*, **2004**, 20, 680-688.
56. T. Suteewong, H. Sai, R. Hovden, D. Muller, M. S. Bradbury, S. M. Gruner and U. Wiesner, *Science*, **2013**, 340, 337-341.
57. S. H. Tolbert, *Nat. Mater.*, **2012**, 11, 749-751.
58.  $V$  is the total volume of surfactant chains plus any cosolvent or organic molecule between the chains,  $a_0$  is the effective hydrophilic headgroup area at the micelle interface, and  $l$  is the kinetic surfactant chain length, depends on interfacial charge matching and the packing of the surfactant carbon chains. The resulting  $g$  value reflects the curvature of the surfactant packing structure or symmetry, which corresponds to the mesophase: spherical micelles ( $g \leq 1/3$ ), hexagonal packed cylindrical micelles ( $1/3 < g < 1/2$ ), bicontinuous cubic packed gyroidal micelles ( $1/2 < g \leq 2/3$ ) and lamellar phases ( $g \geq 1$ ). Ideal bilayer, bicontinuous, cylindrical, and spherical geometries have  $g$  values 1, 2/3, 1/2 and 1/3, respectively.
59. J. Li, Y. Wei, Y. Deng, D. Gu, X. Yang, L. Zhang, B. Tu and D. Zhao, *J. Mater. Chem.*, **2010**, 20, 6460-659.
60. Y. Xia and R. Mokaya, *J. Mater. Chem.*, **2013**, 13, 657-2362.
61. X. Wang, Y. Zhang, W. Luo, A. A. Elzatahry, X. Cheng, A. Alghamdi, A.M. Abudllah, Y. Deng and D. Zhao, *Chem. Mater.*, **2016**, 28, 2356-2362.
62. T. Suteewong, H. Sai, R. Cohen, S. Wang, M. Bradbury, B. Baird, S.M. Gruner and U. Wiesner, *J. Am. Chem. Soc.*, 2011, 133, 172-175.
63. H. B. S. Chan, P. M. Budd and T. deV. Naylor, *J. Mater. Chem.*, **2001**, 11, 951-957.
64. C. Yu, J. Fan, B. Tian and D. Zhao, *Chem. Mater.*, **2004**, 16, 889-898.
65. K. W. Gallis and C. C. Landry, *Chem. Mater.*, **1997**, 9, 2035-2038.
66. a) Y.-D. Chiang, H.-Y. Lian, S.-Y. Leo, S.-G. Wang, Y. Yamauchi and K. C.-W. Wu, *J. Phy. Chem. C*, **2011**, 115, 13158-13165; b) K. Ikari, K. Suzuki and H. Imai, *Langmuir*, **2006**, 22, 802-806; c) R. Kumar, H-T. Chen, J.L.V. Escoto, V.S.-Y. Lin and M. Pruski, *Chem. Mater.*, **2006**, 18, 4319-4327; d) R. I. Nooney, D. Thirunavukkarasu, Y. M. Chen, R. Josephs and A. E. Ostafin, *Chem. Mater.*, **2002**, 14, 4721-4728; e) K. Yano and Y. Fukushima, *J. Mater. Chem.*, **2003**, 13, 2577-2581.
67. Q. He, X. Cui, F. Cui, L. Guo and J. Shi, *Micro. Meso. Mater.*, **2009**, 117, 609-616.
68. Q. Chen, L. Han, C. Gao and S. Che, *Micro. Meso. Mater.*, **2010**, 128, 203-212.
- 69 J. Xu, Z. Luan, H. He, W. Zhou and L. Kevan, *Chem. Mater.*, **1998**, 10, 3690-2698.
70. J. Trébosc, J. W. Wiench, S. Huh, V. S. -Y. Lin and M. Pruski, *J. Am. Chem. Soc.*, **2005**, 127, 3057-3068.
71. Y.Liang and R. Anwander, *Dalton Trans.*, **2013**, 42, 12521-12545.

## 3 Hierarchical Mesoporous Organosilica/Silica Core-Shell Nanoparticles Capable of Controlled Fungicide Release

### 3.1 Introduction

Mesoporous silica core-shell nanoparticles (MSCSNs) have triggered enormous research interest because of potential synergistic effects due to combining distinct core and shell functionalities.<sup>1-10</sup> Not only can the core component be varied, as shown for magnetic nanoparticles,<sup>1-3</sup> metal nanoparticles,<sup>4-7</sup> quantum dots,<sup>8,9</sup> and nonporous silica nanoparticles,<sup>10</sup> but also the shell is adjustable in thickness,<sup>1,3,6</sup> pore size,<sup>3</sup> and composition.<sup>10</sup> Such tailored properties greatly promote applications of well-defined MSCSNs in areas such as adsorption,<sup>2</sup> enzyme immobilization,<sup>3,11,12</sup> catalysis,<sup>1,4,5</sup> molecular imaging,<sup>8</sup> and drug detection/delivery.<sup>9</sup> Apart from MSCSNs, mesoporous carbon and titania microspheres also exhibit great potential for applications in energy conversion and sensing.<sup>13,14</sup> Recently, hierarchically structured mesoporous silica-based core-shell nanoparticles have become an emerging field.<sup>15-25</sup> Different core-shell pore sizes, uniformly distributed over the entire nanoparticle, are proposed to create a unique nanosystem for further-reaching applications in the aforementioned areas. However, the fabrication of perfectly uniform core-shell nanoparticles requires the coating of a preformed core with a porous shell, which will counteract the formation of multicomposite aggregates of various shapes. Such multistep syntheses are promising in controlling the core and shell properties, but are considered tedious and not easy to handle. Hence, a simple procedure for the fabrication of MSCSNs, ideally a one-pot synthesis, seems more attractive.<sup>4,6,7,17,22-24</sup>

Organic-inorganic hybrid mesoporous silica nanoparticles are a unique class of materials exploiting the combined functionalities of the organic and inorganic components and minimizing any intrinsic drawbacks of the individual components.<sup>26</sup> Diverse sets of functional entities/structures are routinely implemented into core-shell frameworks to afford hybrid multifunctional nanoparticles with intriguing application potential (Table 1).<sup>27-39</sup> However, to the best of our knowledge, organic-inorganic hybrid mesoporous silica nanostructures with distinct compositions in the core and shell and bimodal hierarchical pore structures have not been disclosed to date. This is surprising, since such nanosystems featuring distinct compartments are categorized as promising candidates for the immobilization of molecules with different sizes/amphiphilicities<sup>21</sup> and for the enhancement of selectivity in catalytic reactions.<sup>40,41</sup> The preparation of perfectly uniform CSNs with different topologies, various compositions, and hierarchical pore structures is a major technological and scientific challenge.

Herein, we report the synthesis and application of hierarchically structured mesoporous silica core-shell nanoparticles (HSMSCSNs) with periodic mesoporous organosilica (PMO) core and mesoporous silica (MS) shell. Crucially, the new HSMSCSNs are accessible through a facile one-pot, two-step process involving the coating of a hexagonal or cagelike cubic PMO core with a hexagonal MS layer at the interface of an oil (*n*-hexane)/water system. Additionally,

the adsorption and controlled release of the triazole fungicide propiconazole by such HSMSCSNs were investigated in detail, and a mechanism is proposed.

**Table 3.1** Selected examples of hybrid nanoparticles with core-shell frameworks.<sup>a</sup>

Structure	Core Composition	Shell Composition	Application	Reference
Yolk-Shell	amino-functionalized MSN	sulfuric acid-functionalized PMO	acid-base cascade	27
Yolk-Shell	Pt NPs adsorbed MSN	PMO	hydrogenation	29
Yolk-Shell	silica nanosphere	PMO	selective alcohol oxidation	31
Yolk-Shell	MSN-PMO hybrid material	MSN-PMO hybrid material	hemolytic activity	34
Yolk-Shell	thioether-functionalized MSN-PMO hybrid material	thioether-functionalized MSN-PMO hybrid material	photothermal treatment, tumor imaging	35
Yolk-Shell	Fe <sub>3</sub> O <sub>4</sub> and Au NPs	MSN-PMO hybrid material	o-nitroaniline reduction	38
Hollow	-	PMO	hemolytic activity, drug delivery	30
Hollow	-	MSN-PMO hybrid material	hemolytic activity, protein loading	32
Hollow	-	MSN-PMO hybrid material	cytotoxicity, ultrasound imaging	36
Hollow	-	MSN-PMO hybrid material	contaminants removal	37
Dual-Compartment	silica-coated NPs upconversion	MSN and PMO	drug delivery	28

<sup>a</sup> MSN = mesoporous silica nanoparticle; NP = nanoparticle; PMO = periodic mesoporous organosilica

## 3.2 Experimental Section

### 3.2.1 Chemicals

Ethanol (EtOH, 99.9%, Sigma-Aldrich), methanol (MeOH, ≥99.8%, Sigma-Aldrich), tetraethyl orthosilicate (TEOS, ≥99.0%, Sigma-Aldrich), ammonium hydroxide solution (~25 wt%, Sigma-Aldrich), hexadecyltrimethylammonium bromide (CTAB, ≥98%, Sigma-Aldrich), bis(triethoxysilyl)ethane (97%, BTEE, ABCR), bis(triethoxysilyl)methane (BTEM, 97%, ABCR), *n*-hexane (95%, Fisher Scientific), propiconazole (Sigma-Aldrich, analytical standard) and hydrochloric acid (HCl, ≥37%, Sigma-Aldrich), were used as received. Deionized water was used as a solvent for all syntheses.

### 3.2.2 Synthesis of HSMSCSNs

In a 250 mL round-bottom flask, CTAB (0.12 g) was dissolved in a mixture of MeOH (20 mL), water (75 mL) and 25 wt% ammonia aqueous solution (1 mL) and the mixture was stirred (700 rpm) at ambient temperature for 45 min. Then, BTEE (0.2 mL) was added with stirring. After being stirred at the same stirring rate for 24 h, extra CTAB (0.33 g) was added and the suspension was stirred for a further 30 min. Subsequent addition of TEOS (1.5 mL) dissolved in *n*-hexane (20 mL) resulted in a biphasic system. Afterwards, the suspension was stirred (170 rpm) for a further 24 h to fabricate core-shell nanoparticles. The final nanoparticles were separated by centrifugation and washed with ethanol twice. The surfactant CTAB was removed by heating the as-made nanoparticles (0.25 g) in a refluxing mixture of solution of EtOH (160 mL) and 37% HCl (4 mL) at 75 °C for 3 h, and the particles were then separated by centrifugation. The extraction procedure was repeated 3 times. The final template-free HSMSCSNs were washed with ethanol twice and dried at 75 °C overnight. For the synthesis of methylene-containing HSMSCSNs (denoted Me-HSMSCSN), BTEE was replaced by BTEM while all other reagents/conditions stayed the same.



### 3.2.3 Adsorption and Controlled Release of Propiconazole

HSMSCSNs (200 mg) were stirred with 80 mL of an *n*-hexane solution containing 0.76 mg/mL propiconazole at ambient temperature for 7 days. The propiconazole-loaded nanoparticles (denoted HSMSCSN-P) were then separated by centrifugation and dried at 70 °C overnight. The amount of adsorbed propiconazole was determined by comparing the UV/Vis absorbance of the solution at 270.8 nm before and after adsorption. For probing the release of propiconazole, HSMSCSN-P (34 mg), suspended in PBS phosphate buffer solution (45 mL, 10 mM, pH 7.1), was sonicated for 3 min. The resultant suspension was then stirred at ambient temperature for 48 h, and the amount of propiconazole released into PBS was determined by measuring the UV/Vis absorbance of the supernatant at 270.8 nm at defined time intervals.

### 3.2.4 Characterization

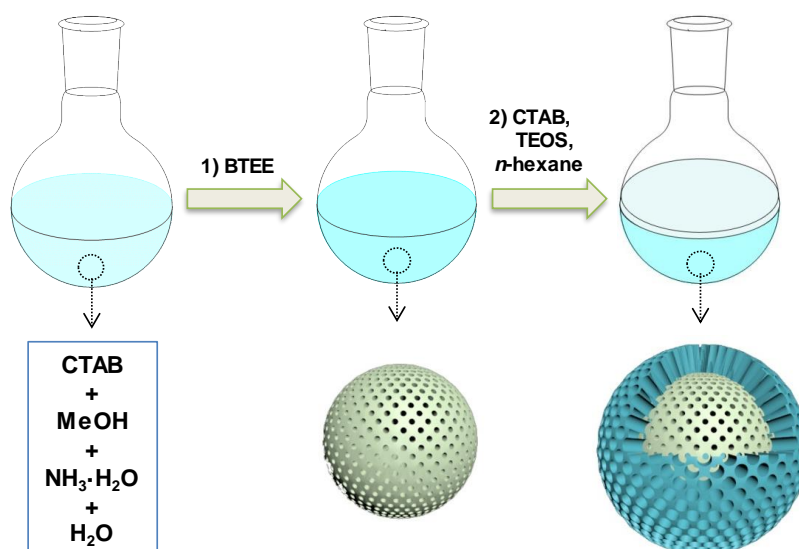
Nitrogen physisorption was carried out on a Micrometrics ASAP 2020 volumetric adsorption apparatus at 77.4 K. Samples were degassed at 120 °C for 6 h under vacuum ( $< 5 \mu\text{mHg}$ ) prior to the measurements. The specific surface area was calculated by the *Brunauer-Emmett-Teller* (BET) method. The pore volume was calculated from the total nitrogen adsorption at  $P/P_0 = 0.995$ . The pore size distribution was obtained from the adsorption branch of the nitrogen isotherm by the *Barret-Joyner-Haldenda* (BJH) method. Transmission electron microscopy (TEM) images were recorded with a JEOL JEM 2010 microscope operated at 160 kV. For TEM observations, the finely powdered materials were dispersed in ethanol (99.9 %) under ultrasonic vibration. A drop of suspension was loaded onto a copper grid covered with a holey carbon film. For some materials, scanning/transmission electron microscopy (S/TEM) images were obtained on a Hitachi SU 8030 microscope operated at an acceleration voltage of 30 kV.  $^{29}\text{Si}$  and  $^{13}\text{C}$  CP MAS NMR spectra were recorded at ambient temperature with a Bruker ASX300 instrument equipped with MAS hardware and using a  $\text{ZrO}_2$  rotor with an inside diameter of 7 mm. Low angle powder X-ray diffraction (PXRD) patterns were obtained on a Bruker D8 Advance Diffractometer by using monochromatic  $\text{CuK}\alpha$  radiation ( $\lambda = 1.5406 \text{ \AA}$ ) in the  $2\theta$  range of  $0.5\text{-}10.0^\circ$  in the step/scan mode with the step width of 0.00825 and accumulation time of 2 s/step. Diffuse-reflectance infrared Fourier transform (DRIFT) spectra were recorded with a Nicolet 6700 FTIR spectrometer with KBr reference spectrum, a resolution of  $4 \text{ cm}^{-1}$ , and 256 scans in the range of  $4000\text{-}400 \text{ cm}^{-1}$ . UV/Vis spectra were obtained with a PG Instruments T60 UV/Vis spectrophotometer in the scan range of 200-800 nm with a step width of 0.2 nm.

## 3.3 Results and Discussion

### 3.3.1 Synthesis and Characterization of HSMSCSNs with Ethylene-Bridged PMO Core and MS Shell

The HSMSCSNs with PMO core and MS shell were synthesized according to a one-pot approach involving a continuous two-step process (Scheme 3.1). Monodisperse PMO

nanoparticles were prepared by a surfactant-assisted sol-gel process with bis(triethoxysilyl)ethane (BTEE) as precursor, cetyltrimethylammonium bromide (CTAB) as structure-directing agent (SDA), and MeOH/H<sub>2</sub>O solvent mixture in the presence of ammonia. In a subsequent second step, additional CTAB and tetraethyl orthosilicate (TEOS) dissolved in *n*-hexane were added to this suspension to give an oil/water biphasic reaction system. The TEOS dissolved in *n*-hexane is hydrolyzed at the oil/water interface to generate silicate species, which further interact with CTAB surfactant preadsorbed on the surface of PMO nanoparticles under the applied basic conditions. This interaction can occur along various directions/sites of CTAB packings and involve micelles from both the first and second steps. The newly formed silicate-CTAB composites are further extended along the direction of CTAB packing at the oil/water interface and deposited onto the surface of the PMO nanoparticles with the formation of the core-shell structure. Owing to the presence of *n*-hexane as an expander during the extension of the packing structure of adsorbed CTAB, the diameter of the CTAB micelles formed is larger than that prevailing for the formation of the PMO nanoparticles in the first step. Removal of the surfactant by EtOH/HCl extraction affords the envisioned HSMSCSNs.



**Scheme 3.1** Synthesis scheme for HSMSCSNs.

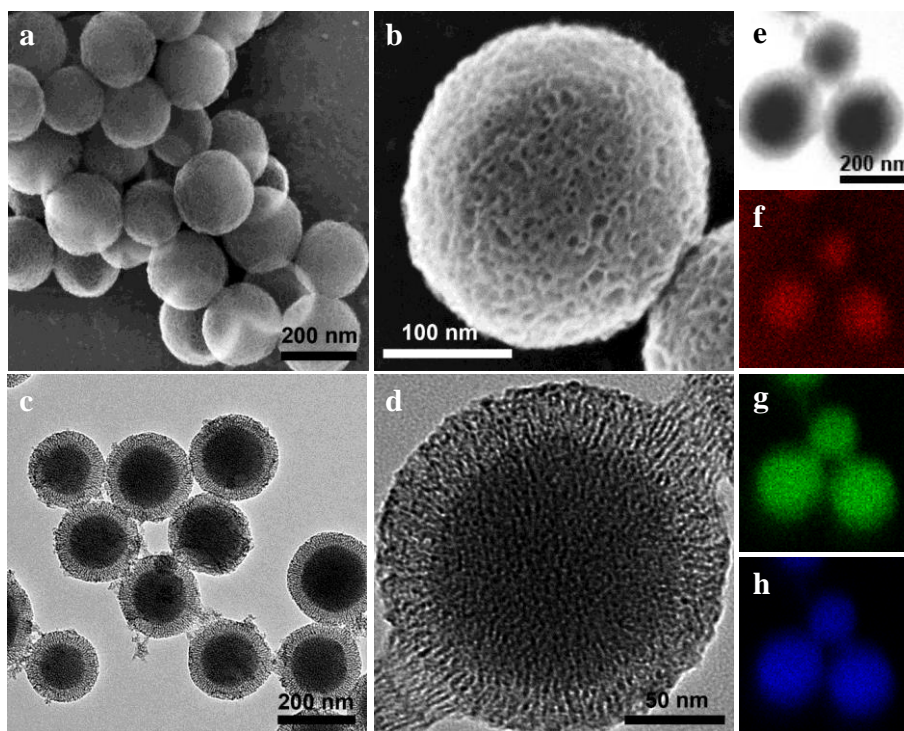


**Figure 3.1** (a, b) SEM, (c, d) TEM and (e) STEM images of HSMSCSNs and energy-dispersive X-ray spectroscopic elemental mapping of C (f), O (g) and Si (h).

Representative SEM images of HSMSCSNs (Figure 3.1a and b) clearly indicate spherical morphology with rough surface and quite uniform particle size. The average particle size was determined to be  $210 \pm 3.9$  nm by measuring 50 random nanoparticles from the SEM images (Figure 3.2). This is in good agreement with the average particle size of  $211 \pm 3.2$  nm obtained from TEM images (Figure 3.3a). In addition, the TEM images (Figure 3.1c) revealed a characteristic spherical core-shell structure with an average core size of  $146 \pm 2.8$  nm (Figure 3.3b) and a shell thickness of  $32 \pm 1.8$  nm. The high-resolution TEM (HRTEM) image clearly shows a wormlike pore structure with a radial pore distribution. Also, different core-shell pore sizes are observed and a few CSNs are connected by a necklike structure with the same pore size as the shell structure (Figure 3.1d). Moreover, interfacial mesopores penetrating from the shell into the core further ensure efficient access to the core compartment, which is also essential for the determination of the core pore size by nitrogen physisorption. The increased shell pore diameter corroborates the role of the extra added CTAB and *n*-hexane. Moreover, the interfacial pores, which seemingly originate from the core, confirm extension of the inner CTAB packing structure along the same direction through addition of extra CTAB, as well as the importance of mass transfer between core and shell. Furthermore, the powder XRD (PXRD) pattern (Figure 3.4a) shows two diffraction peaks at  $2\theta = 1.5$  and  $2.0^\circ$  with  $d = 5.9$  and  $4.4$  nm. It is very difficult to precisely determine any mesophase, but this pattern probably implies the existence of dual pores with different pore sizes. Nitrogen physisorption analysis of HSMSCSNs (Figure 3.4b) revealed a type IV isotherm with three distinct capillary condensation steps at  $P/P_0 = 0.25\text{--}0.4$ ,  $0.5\text{--}0.75$ , and  $0.95\text{--}1.0$ , which indicates mesopore

characteristics typical of different uniform core-shell pore diameters and high textural porosity from particle packing. The *BJH* pore size distribution (Figure 3.4b, inset) clearly corroborated two types of uniform mesopore sizes of 2.7 and 5.6 nm, which is in good agreement with the suggested dual pores from the PXRD pattern. The specific *BET* surface area and the total pore volume of the HSMSCSNs were determined to be  $1196 \text{ m}^2 \text{ g}^{-1}$  and  $1.68 \text{ cm}^3 \text{ g}^{-1}$ , respectively.

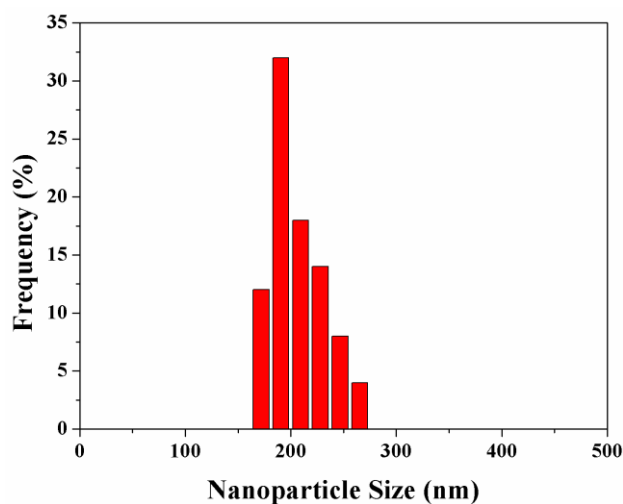


**Figure 3.2** Particle size distribution of HSMSCSN obtained by examining 50 random particles from SEM images.

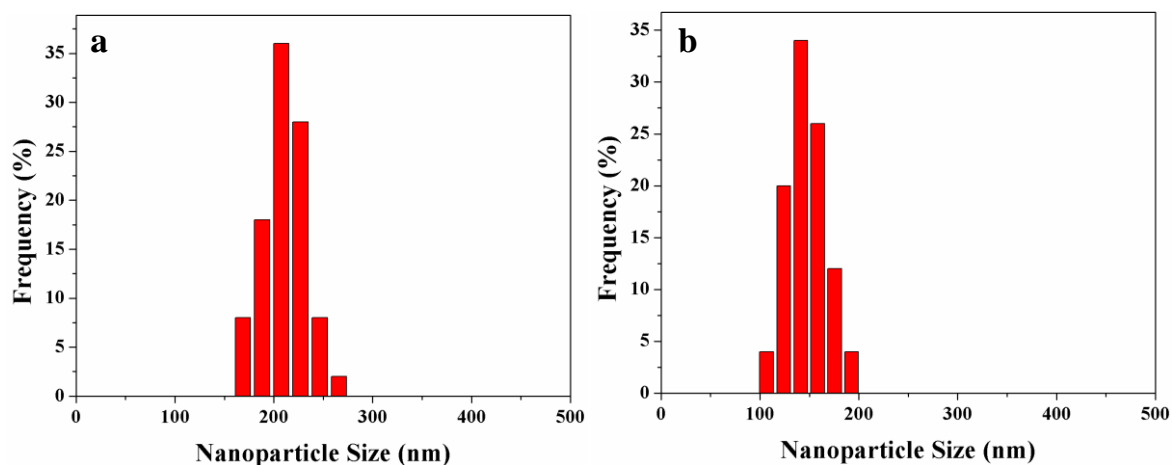


**Figure 3.3** (a) Overall particle size distribution and (b) core size distribution of HSMSCSN obtained by examining 50 random particles from TEM images.

To verify the core-shell chemical composition, energy-dispersive X-ray spectroscopic elemental mapping was performed (Figure 3.1e–h). The selected three single nanoparticles clearly show compositional differences of the core and shell domains, corroborating organosilica and all-silica compositions for core and shell, respectively. The composition of HSMSCSN was also confirmed by  $^{13}\text{C}/^{29}\text{Si}$  CP MAS NMR spectroscopy, which showed a  $^{13}\text{C}$  signal at 4 ppm assignable to the carbon atoms of the Si-CH<sub>2</sub>CH<sub>2</sub>-Si-bridged organosilica framework<sup>31,37</sup> and  $^{29}\text{Si}$  signals at -55, -61, -91, -98, and -107 ppm, attributable to  $\text{T}^2[\text{CSi}(\text{OSi})_2(\text{OX})_2]$ ,  $\text{T}^3[\text{CSi}(\text{OSi})_3]$ ,  $\text{Q}^2[\text{Si}(\text{OSi})_2(\text{OX})_2]$ ,  $\text{Q}^3[\text{Si}(\text{OSi})_3(\text{OX})]$  (X=H or Et), and

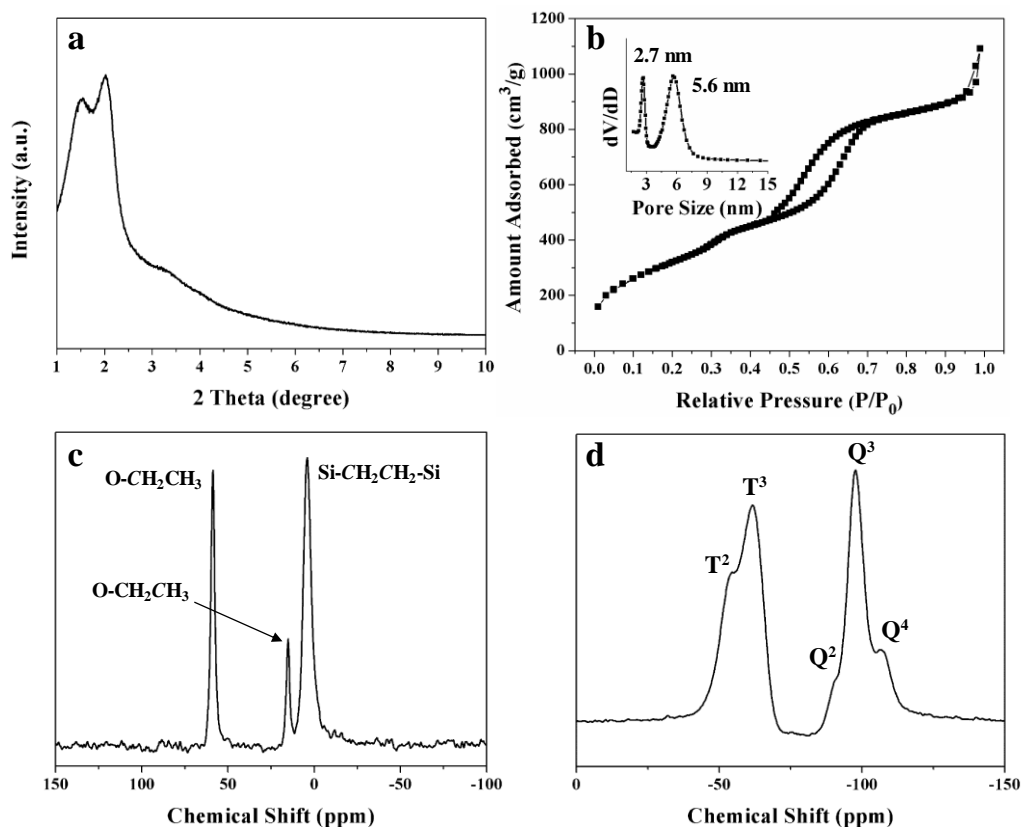


**Figure 3.4** (a) PXRD pattern, (b) nitrogen physisorption isotherm (the inset is the corresponding BJH pore size distribution), (c)  $^{13}\text{C}$  CP MAS NMR spectrum, and (d)  $^{29}\text{Si}$  CP MAS NMR spectrum of HSMSCSN.

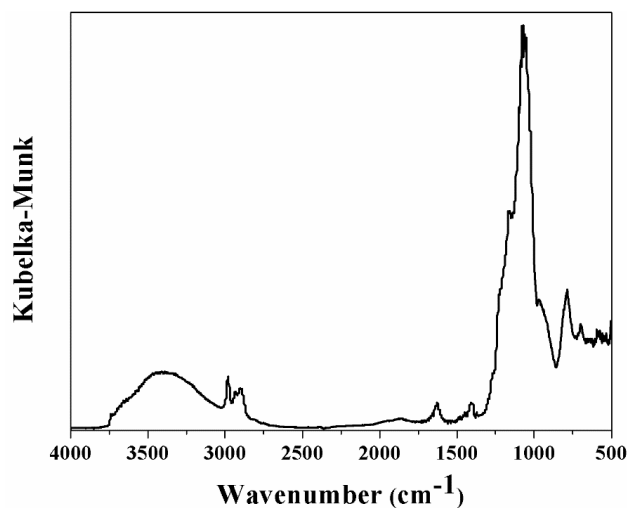


**Figure 3.5** DRIFT spectrum of HSMSCSN.

$\text{Q}^4[\text{Si}(\text{OSi})_4]$  species (Figure 3.4c,d), respectively.<sup>31,34,37,42</sup> The additional carbon signals at 15 and 59 ppm belong to nonhydrolyzed ethoxy groups of the BTEE and TEOS precursors and/or surface ethoxy groups formed during the surfactant-extraction process.<sup>31,43-45</sup> The  $^{13}\text{C}$  signals of CTAB were not detected, and this indicated complete template removal. The DRIFT spectrum of HSMSCSNs (Figure 3.5) shows vibrational bands at 2800-3000, 1450, and 1410  $\text{cm}^{-1}$  (C-H), 1160  $\text{cm}^{-1}$  (Si-C), 786  $\text{cm}^{-1}$  (Si-O), and 1064  $\text{cm}^{-1}$  (Si-O-Si),<sup>37,46</sup> in line with the

formation of HSMSCSNs. All these characterization data demonstrate successful fabrication of the organic-inorganic hybrid mesoporous silica core-shell nanoparticles with hierarchical pore structure.

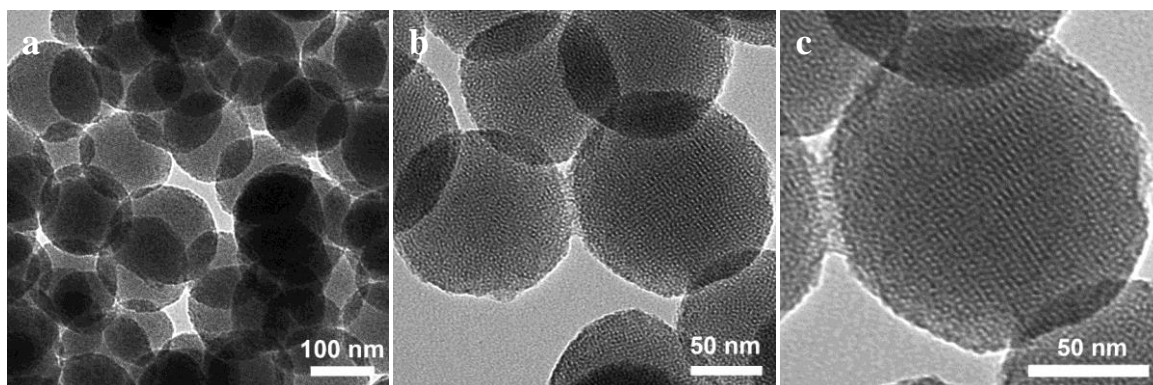


**Figure 3.6** TEM images of monodisperse PMO nanoparticles at different magnifications.

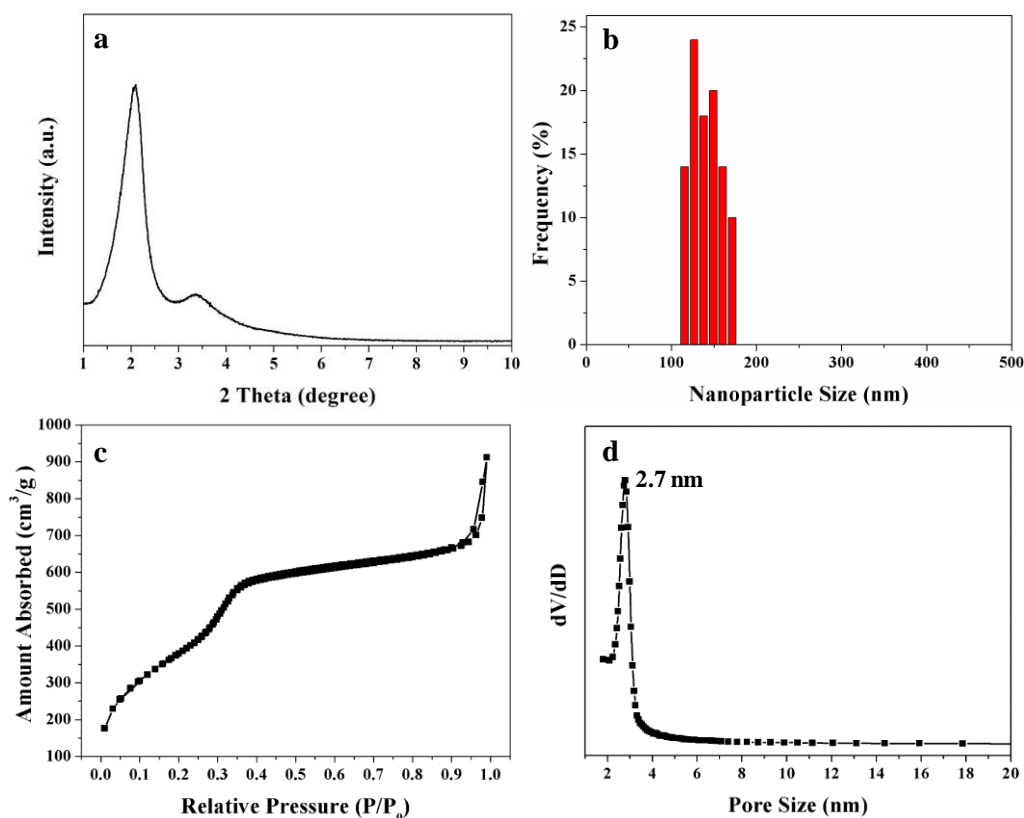


**Figure 3.7** (a) PXRD pattern, (b) particle size distribution obtained by examining 50 random particles from TEM images, (c) nitrogen physisorption, and (d) the corresponding BJH pore size distribution of PMO nanoparticles.

To gain deeper insight into the formation of the hierarchical pore structure of HSMSCSNs, the PMO core structure was synthesized independently. After separating the PMO nanoparticles by centrifugation, the remaining clear reaction solution was further used for the preparation of mesoporous silica in order to simulate shell fabrication under conditions identical to those employed for HSMSCSNs. Monodisperse PMO nanoparticles were obtained

by the sol-gel process described above and showed a distorted hexagonal mesostructure according to HRTEM images (Figure 3.6) and the PXRD pattern (Figure 3.7a). Their average particle size of  $140 \pm 2.5$  nm (Figure 3.7b) is quite similar to the core size of the HSMSCSNs. The type IV nitrogen physisorption isotherm of the monodisperse PMO nanoparticles shows two capillary condensation steps at  $P/P_0 = 0.25$ – $0.4$  (corresponding to a pore size of 2.7 nm) and  $0.9$ – $1.0$  (textural porosity; Figure 3.7c and d), a specific *BET* surface area of  $1433$   $\text{m}^2$   $\text{g}^{-1}$ , and a pore volume of  $1.41$   $\text{cm}^3$   $\text{g}^{-1}$ . It is noteworthy that the pH value of the reaction solution dropped from 13.0 to 12.0 after the PMO nanoparticles were separated.

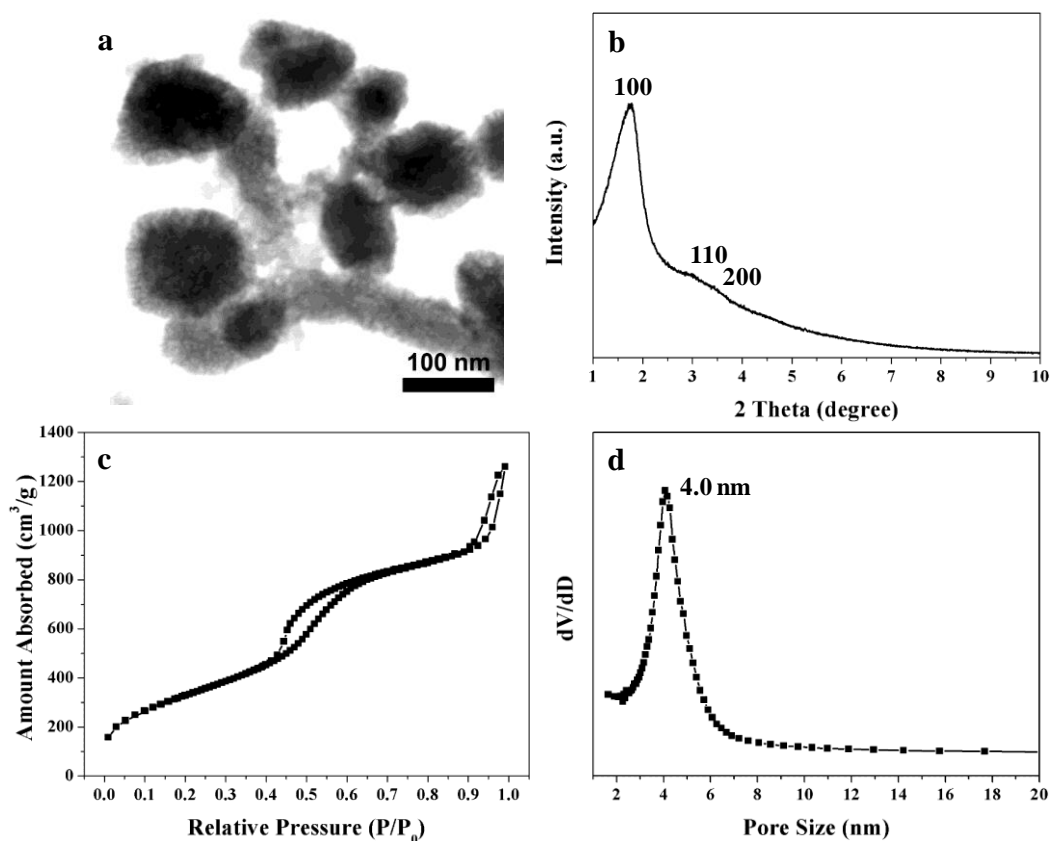


**Figure 3.8** (a) TEM image, (b) PXRD pattern, (c) nitrogen physisorption isotherm, and (d) the corresponding BJH pore size distribution of mesoporous silica synthesized by adding a mixture of 1.5 mL TEOS and 20 mL *n*-hexane into the PMO filtrate in the presence of CTAB, after separation of the PMO nanoparticles.

The mesoporous silica material obtained from the initial filtrate after addition of extra CTAB, *n*-hexane, and TEOS gave TEM images showing the formation of spheres with particle size of 55–180 nm and nanorods with lengths from 100 to 350 nm (Figure 3.8a). The PXRD pattern of this siliceous material clearly indicated three well-resolved diffraction peaks in the  $2\theta$  range of  $1$ – $4^\circ$ , which were indexed as the (100), (110), and (200) planes of a hexagonal mesophase with  $p6mm$  symmetry (Figure 3.8b). Moreover, a type IV isotherm with two capillary condensation steps at  $P/P_0 = 0.4$ – $0.6$  (corresponding to a pore size of 4.0 nm) and  $0.9$ – $1.0$  (textural porosity) were observed by nitrogen physisorption analysis (Figure 3.8c and d). The *BET* specific surface area and pore volume were  $1239$   $\text{m}^2$   $\text{g}^{-1}$  and  $1.95$   $\text{cm}^3$   $\text{g}^{-1}$ , respectively.

According to the above-mentioned results, the latter mesoporous silica clearly has a smaller pore size and different shape than the mesoporous silica shell of HSMSCSNs (5.6 nm). This implies that the PMO nanoparticle core directly affects the pore size and the formation mechanism of the siliceous shell in HSMSCSNs. The pore-enlargement phenomenon observed for the one-pot, two-step preparation of HSMSCSNs is similar to that of recently reported hollow mesoporous titania microspheres and hollow mesoporous silica nanoparticles.<sup>47,48</sup> This pore enlargement is possibly related to the surface curvature of the nanoparticle core and the corresponding very high surface free energy for shell formation.<sup>49</sup> However, the formation of a high-quality porous shell layer also depends on the availability of an extendable surfactant micelle from the core and the packing of newly formed surfactant micelles perpendicular to the surface of the core. Furthermore, the presence of a sufficient amount of condensable surface silanol groups as well as charge matching between surfactant micelles and silicate species at the reaction interface are important.

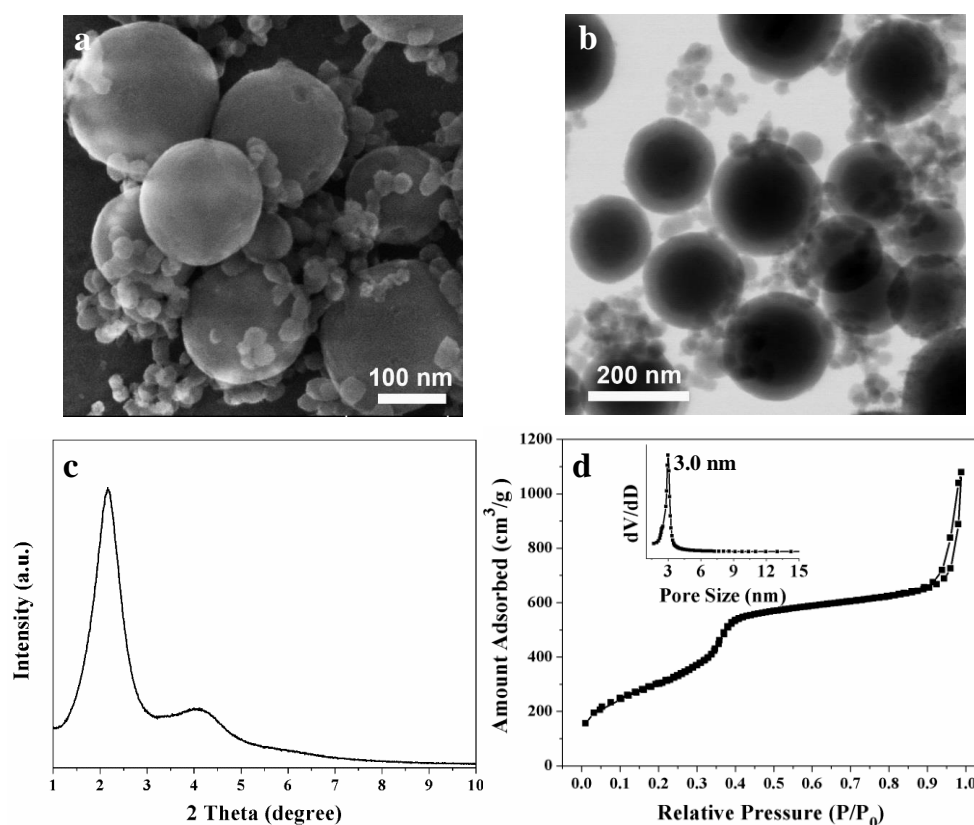


**Figure 3.9** (a) SEM image, (b) TEM image, (c) PXRD pattern, and (d) nitrogen physisorption isotherm (inset: BJH pore size distribution) of organic-inorganic hybrid mesoporous silica nanoparticles synthesized in the absence of *n*-hexane.

The addition of *n*-hexane seems to play a pivotal role in 1) controlling the hydrolysis rate of TEOS, 2) forming an oil/water interface, and hence 3) releasing silicate species from the hydrophobic into the hydrophilic phase. Omitting *n*-hexane in the second step of the reaction system shown in Scheme 3.1 does give access to MSCSNs with an average particle size of 203



$\pm 5.7$  nm (core size:  $143 \pm 5.8$  nm, shell thickness:  $30 \pm 0.4$  nm; Figure 3.9a and b), but a considerable amount of isolated and irregular mesoporous silica nanoparticles were observed to coexist with these CSNs. This implies indirectly that the addition of *n*-hexane effectively slows down the hydrolysis rate of TEOS, thus counteracts the random aggregation of purely siliceous mesoporous material in the second stage (Scheme 3.1), and thereby ensures the formation of the unique uniform HSMSCSNs. Although the PXRD pattern of such MSCSNs shows two diffraction peaks (Figure 3.9c), it markedly differs from that of the HSMSCSNs (Figure 3.4a). In accordance with this, the nitrogen physisorption isotherm of MSCSNs showed two capillary condensation steps corresponding to a pore size of 3.0 nm and void spaces formed by the interparticle contacts (Figure 3.9d). Crucially, no pore-enlargement phenomenon was observed, that is, the core, the shell, and the randomly aggregated mesoporous silica of irregular morphology show similar pore sizes. These findings further verify that *n*-hexane greatly affects the formation of such monodisperse HSMSCSNs.

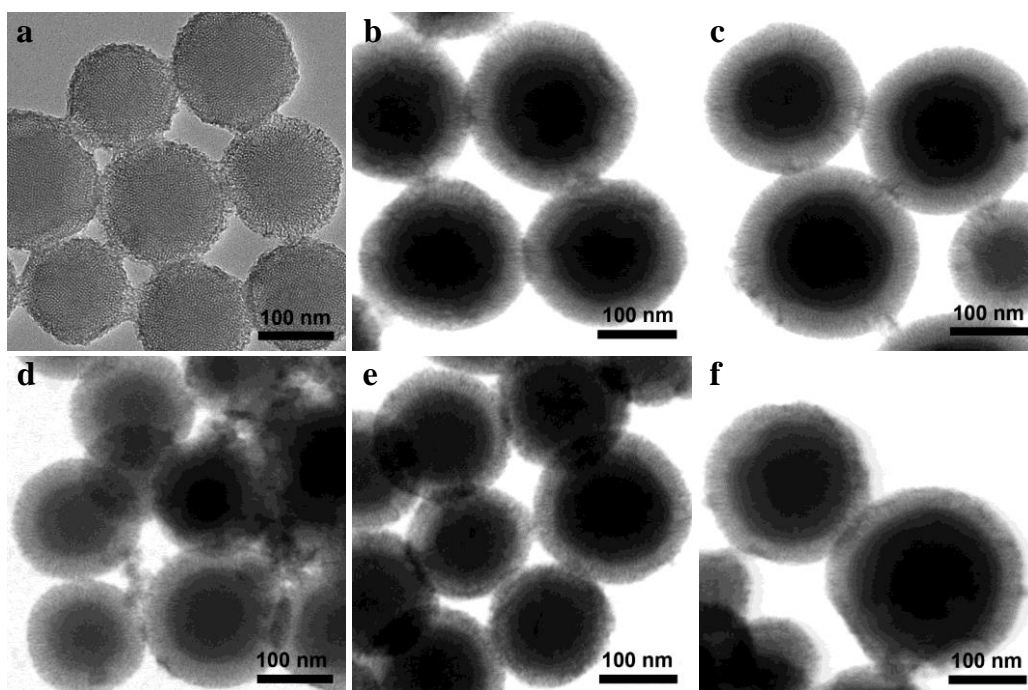


**Figure 3.10** TEM images of materials HSMSCSN-*n* synthesized with different amounts of (organo)silica precursors: (a) HSMSCSN-1, 0.7 mL of TEOS; (b) HSMSCSN-2, 2.2 mL of TEOS; (c) HSMSCSN-3, 3.4 mL of TEOS; (d) HSMSCSN-4, 0.1 mL of BTEE; (e) HSMSCSN-5, 0.3 mL of BTEE; (e) HSMSCSN-6, 0.4 mL of BTEE.

### 3.3.2 Control of Shell Thickness, Core Size and Pore Diameter

Adjusting synthesis parameters such as the amount of silica precursor and the reaction time affects HSMSCSN parameters such as shell thickness, core size, and pore diameter. Under otherwise identical reaction conditions, increasing the amount of TEOS in the second stage (from 0.7 to 2.2 to 3.4 mL) led to the formation of a series of monodisperse materials

HSMSCSN-*n* (*n* = 1, 2, 3) with gradually increased shell thicknesses (from 15 to 34 to 40 nm), while the core size of about 146 nm was preserved (Figure 3.10a-c, Table 3.2).

**Table 3.2** Physicochemical parameters of materials HSMSCSN, HSMSCSN-*n* and Me-HSMSCSN.

	Core formation		Shell formation		Core size (nm)	Shell thickness (nm)	$a_{\text{BET}}$ ( $\text{m}^2 \text{g}^{-1}$ ) <sup>b</sup>	$V_p$ ( $\text{cm}^3 \text{g}^{-1}$ ) <sup>c</sup>	$d_p$ (nm) <sup>d</sup>	
	BTEE/BTME (mL)	$t_s$ (h) <sup>a</sup>	TEOS (mL)	$t_s$ (h) <sup>a</sup>					Core	Shell
HSMSCSN	0.2	24	1.5	24	146	32	1196	1.68	2.7	5.6
HSMSCSN-1	0.2	24	0.7	24	144	15	1237	1.65	2.7	6.2
HSMSCSN-2	0.2	24	2.2	24	145	34	1161	1.63	2.6	5.2
HSMSCSN-3	0.2	24	3.4	24	148	40	1133	1.83	2.6	4.6
HSMSCSN-4	0.1	24	1.5	24	132	32	1263	1.80	2.7	5.3
HSMSCSN-5	0.3	24	1.5	24	164	30	1148	1.66	2.6	5.6
HSMSCSN-6	0.4	24	1.5	24	175	31	1086	1.56	2.6	5.7
HSMSCSN-7	0.2	18	1.5	24	87	30	1175	1.70	2.6	5.6
HSMSCSN-8	0.2	48	1.5	24	157	33	1218	1.80	2.6	5.9
HSMSCSN-9	0.2	24	1.5	18	146	15	1239	1.65	2.7	5.6
HSMSCSN-10	0.2	24	1.5	48	147	46	1168	1.74	2.6	5.9
Me-HSMSCSN	0.2	24	1.5	24	273	32	1294	1.49	3.0	5.9

<sup>a</sup> Stirring time.

<sup>b</sup> Specific BET surface area.

<sup>c</sup> Pore volume at relative pressure  $P/P_0 = 0.995$ .

<sup>d</sup> Pore diameter from adsorption branch of the isotherm.

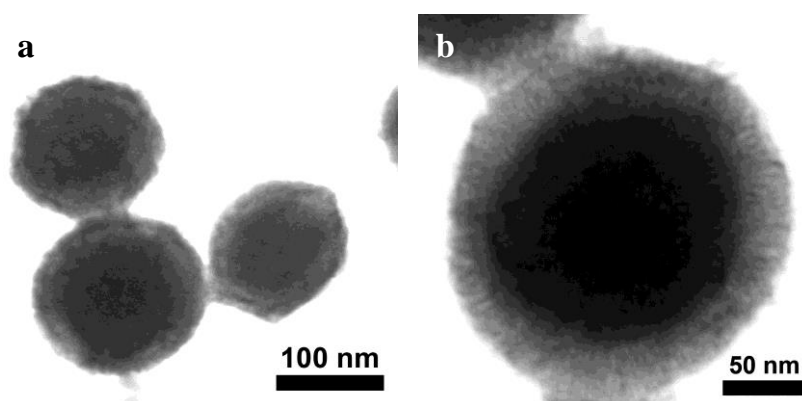


**Figure 3.11** TEM images of (a) HSMSCS-7 and (b) HSMSCSN-8.

Similarly, the core size depends on the amount of BTEE precursor used in the first stage. Gradually increasing the amount of BTEE from 0.1 to 0.3 to 0.4 mL gave materials HSMSCSN-*n* (*n* = 4, 5, 6) with core sizes of 132, 164, and 175 nm, respectively, but an almost constant shell thickness of 31 nm (Figure 3.10d-f, Table 3.2). Moreover, variation of the reaction time in the first stage affected the core size, which ranged from 87 to 157 nm for HSMSCSN-*n* (*n* = 7, 8), at a constant shell thickness of about 33 nm (Figure 3.11 and Table 3.2), whereas in the second stage longer reaction times increased the shell thickness (15 vs. 46 nm) for materials HSMSCSN-*n* (*n* = 9, 10) with constant core size of about 146 nm (Figure 3.12 and Table 3.2). All HSMSCSN-*n* exhibit quite similar PXRD patterns (Figures 3.13 and 3.14), and the nitrogen physisorption analyses revealed overall large BET surface areas (max.  $1263 \text{ m}^2 \text{g}^{-1}$ ), high pore volumes (max.  $1.83 \text{ cm}^3 \text{g}^{-1}$ ), and the characteristic hierarchical pore structure (PMO core:  $\sim 2.6 \text{ nm}$ ; siliceous shell: 4.6-6.2 nm; Figures 3.15-17 and Table 3.2). The

specific BET surface areas and pore volumes are much higher than those previously reported for core-shell-structured materials.<sup>1-3,15-17</sup>

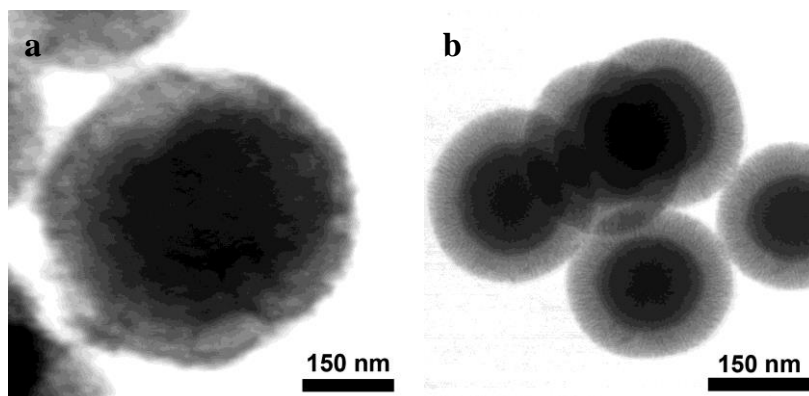


**Figure 3.12** TEM images of (a) HSMSCSN-9 and (b) HSMSCSN-10.

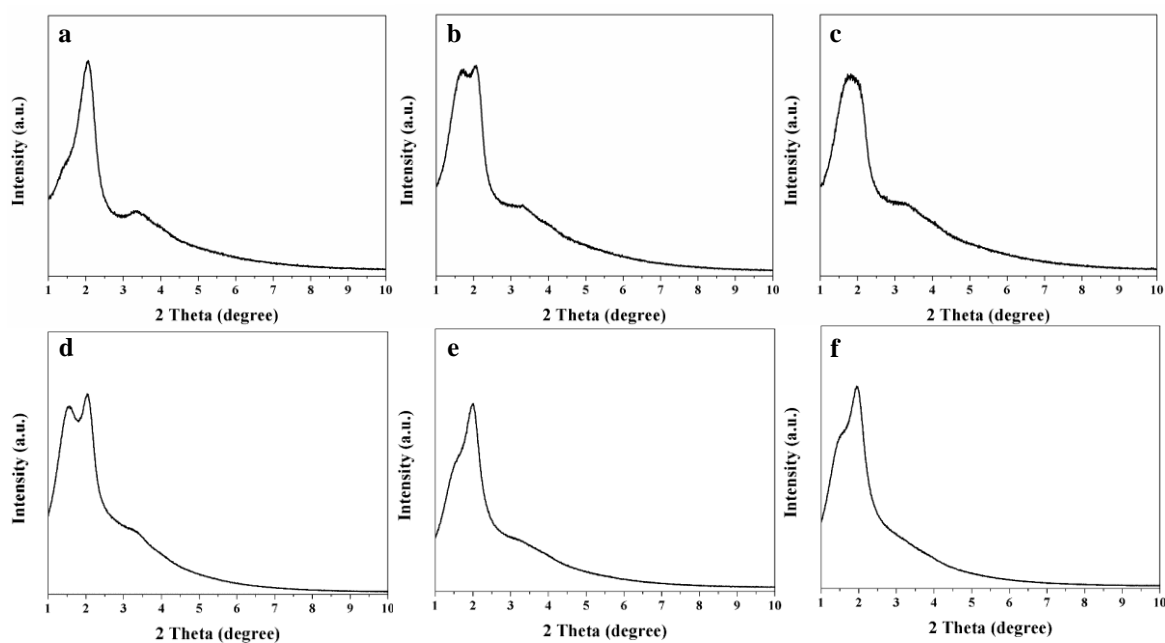


**Figure 3.13** PXRD patterns of (a) HSMSCSN-1, (b) HSMSCSN-2, (c) HSMSCSN-3, (d) HSMSCSN-4, (e) HSMSCSN-5, and (f) HSMSCSN-6.

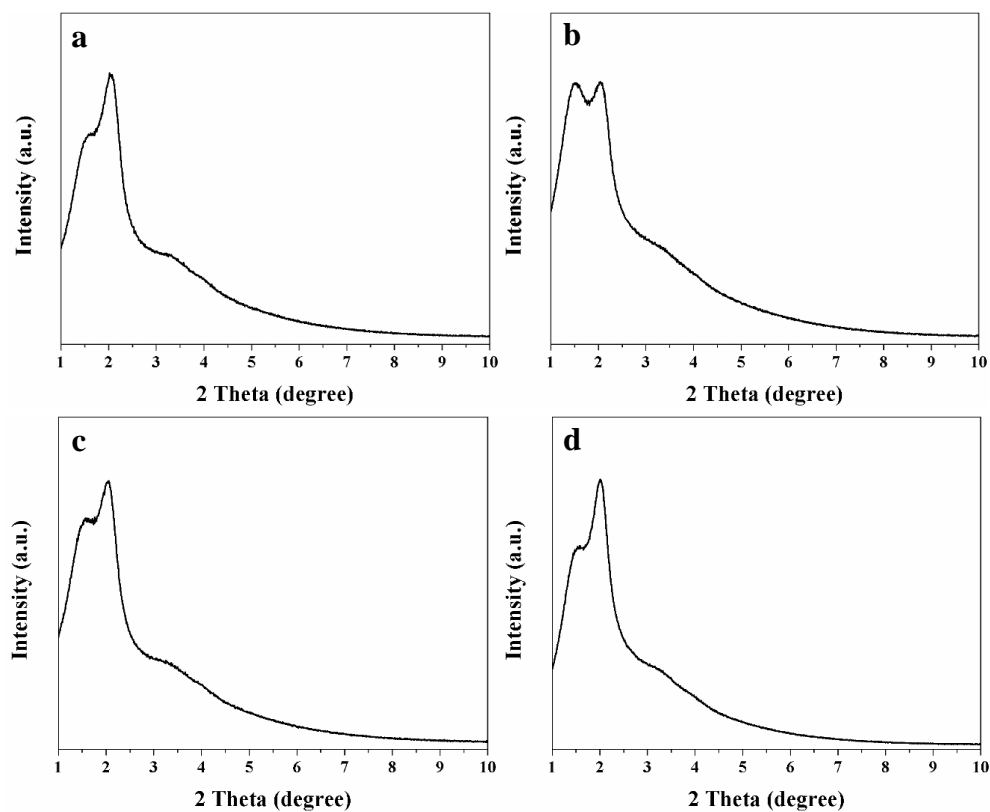


**Figure 3.14** PXRD patterns of (a) HSMSCSN-7, (b) HSMSCSN-8, (c) HSMSCSN-9, and (d) HSMSCSN-10.

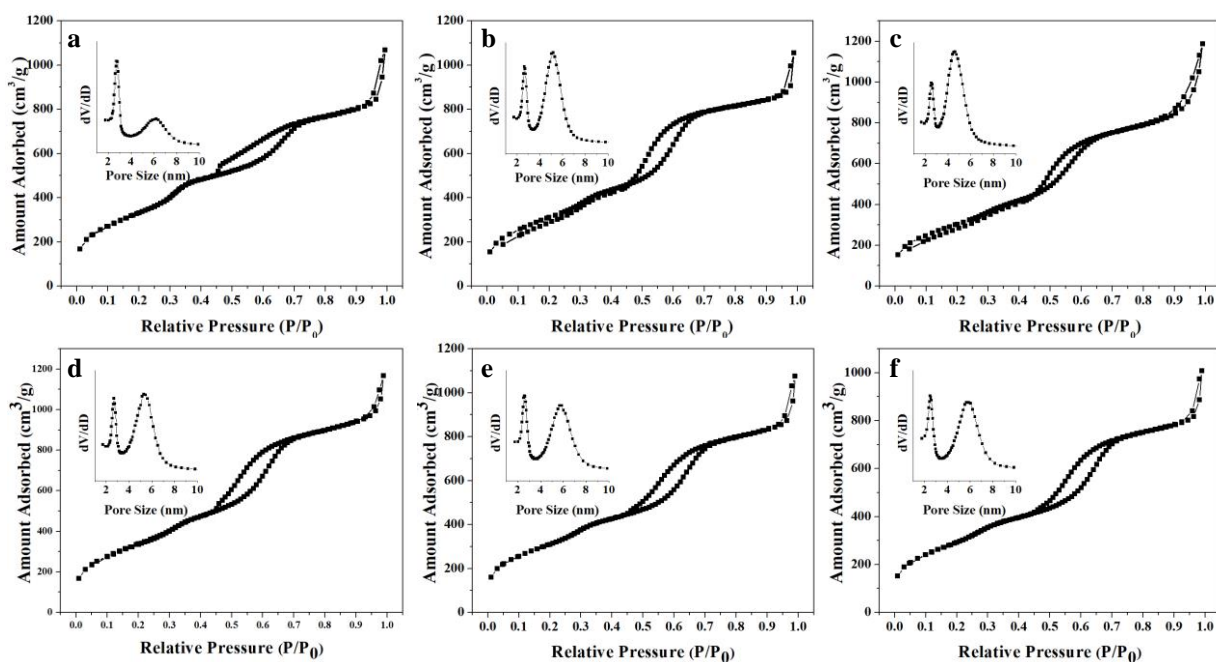


**Figure 3.15** Nitrogen physisorption isotherms and the corresponding BJH pore size distributions of (a) HSMSCSN-1, (b) HSMSCSN-2, (c) HSMSCSN-3, (d) HSMSCSN-4, (e) HSMSCSN-5, and (f) HSMSCSN-6.

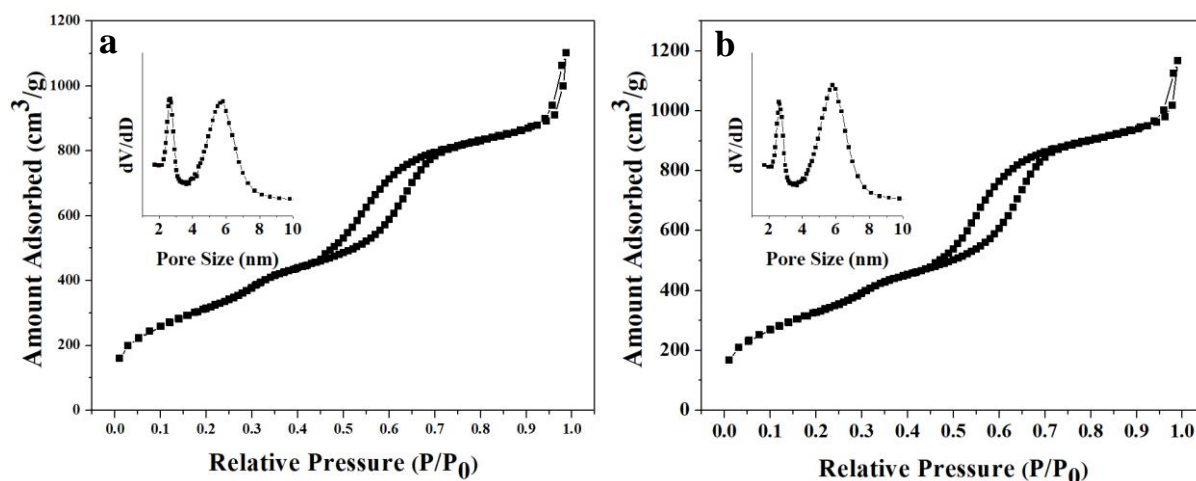


**Figure 3.16** Nitrogen physisorption isotherms and the corresponding BJH pore size distributions of (a) HSMSCSN-7 and (b) HSMSCSN-8.

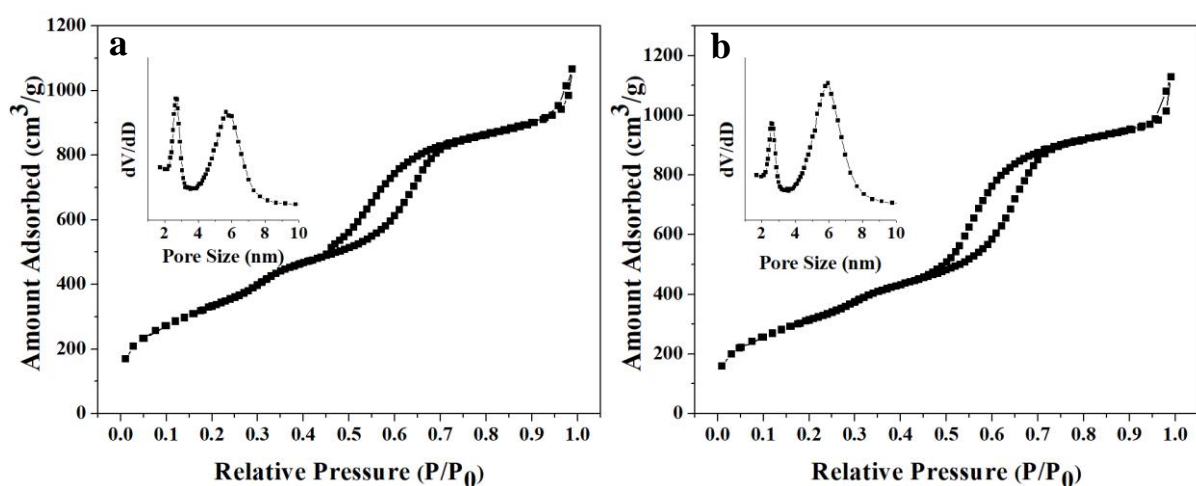


**Figure 3.17** Nitrogen physisorption isotherms and the corresponding BJH pore size distributions of (a) HSMSCSN-9 and (b) HSMSCSN-10.

### 3.3.3 Control of Composition and Topology: Methylene-Bridged HSMSCSNs

The present strategy is versatile and can be used for designing HSMSCSNs with different PMO core compositions. Herein, Me-HSMSCSNs with a methylene-bridged PMO core were obtained when the organosilica precursor was changed from BTEE to bis(triethoxysilyl)methane (BTEM). According to the SEM images, Me-HSMSCSNs have a rough surface and a uniform particle size of  $337 \pm 5.8$  nm (Figures 3.18 and 3.19). This was confirmed by TEM images revealing a core-shell structure with a core size of  $273 \pm 3.3$  nm and a shell thickness of  $32 \pm 0.6$  nm (Figure 3.18b). The PXRD pattern of Me-HSMSCSNs shows a series of well-resolved diffraction peaks in the  $2\theta$  range of  $1.4$ – $4.5^\circ$ , which can be indexed as the (210), (211), (321), (400), (420), and (422) reflections of the cubic  $Pm\bar{3}n$  space group, arising from the PMO core structure (cf. Me-PMO, Figure 3.20).<sup>23, 50–53</sup> The (100) plane indicated by the peak/shoulder at  $2\theta=1.495^\circ$  may represent a distorted hexagonal  $p6mm$  symmetry of the shell layer with large pore size (Figure 3.18c). This topology, consisting of a

cagelike cubic PMO core and large-pore hexagonal siliceous shell features a novel core-shell structure.

For comparison, multicompartment mesoporous silica nanoparticles (mc-MSN) with branched shapes, composed of a core with cagelike cubic mesoporous morphology and up to four branches with hexagonally packed cylindrical mesopores, epitaxially growing out of the cubic core vertices, have been reported.<sup>54</sup> More recently, similarly shaped multipodal hybrid PMO nanoparticles with crystal-like architectures, consisting of a hexagonal core and branches with different compositions, were also prepared by a one-pot, two-step process.<sup>55</sup> The nitrogen physisorption isotherm of Me-HSMSCSN shows two pronounced capillary condensation steps at  $P/P_0 = 0.3-0.45$  and  $0.5-0.75$  (Figure 3.18d), which reveal a bimodal pore characteristic with pore sizes of 3.0 and 5.9 nm in the core and the shell domains, respectively (Figure 3.18d, inset). Furthermore, the chemical composition of Me-HSMSCSN was confirmed by solid-state  $^{13}\text{C}$  and  $^{29}\text{Si}$  NMR spectra (Figure 3.18e and f) verifying methylene moieties of the PMO core with the organosilicon ( $\text{T}^n$ ) species and  $\text{Q}^n$  silicon shell species, respectively.<sup>56</sup> These results further corroborate that the present strategy for HSMSCSN-type materials is simple and efficient as well as versatile and controllable in terms of core/shell chemical composition/functionality and topology.

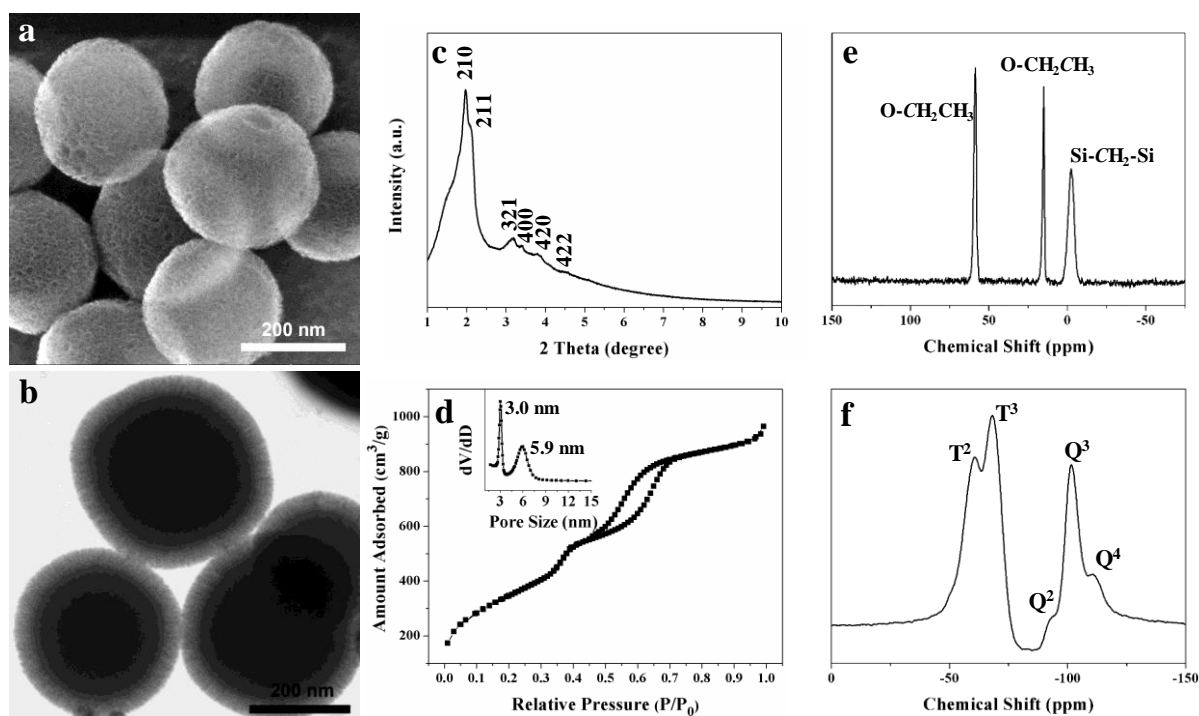


**Figure 3.18** (a) SEM image, (b) TEM image, (c) PXRD pattern, (d) nitrogen physisorption isotherm, the inset is the corresponding BJH pore size distribution, (e)  $^{13}\text{C}$  CP MAS NMR spectrum, and (f)  $^{29}\text{Si}$  CP MAS NMR spectrum of material Me-HSMSCSN.

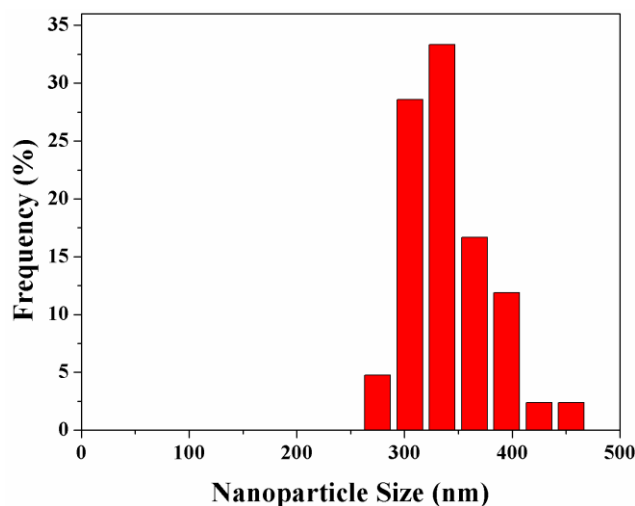


**Figure 3.19** Particle size distribution of Me-HSMSCSN by measuring the sizes of 50 random nanoparticles in the SEM images.

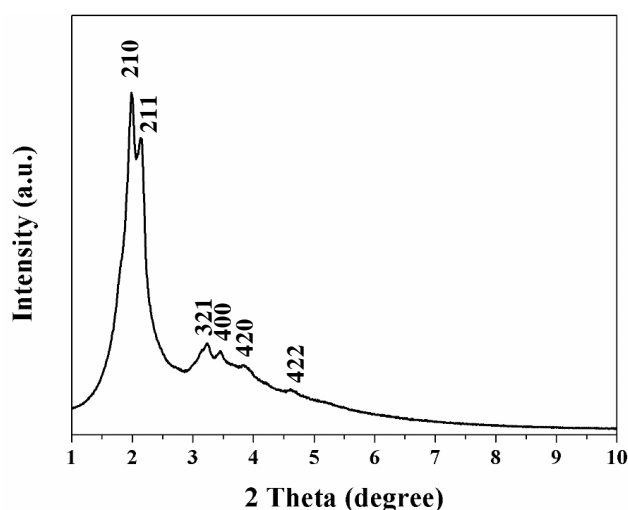


**Figure 3.20** PXRD pattern of Me-PMO nanoparticles.

### 3.3.4 Formation Mechanism of Materials HSMSCSN

On the basis of the role/nature of each starting reagent and the characterization data, a surfactant-directed cosolvent-assisted sol-gel process in the first stage and an *n*-hexane-induced controlled hydrolysis and co-assembly process in the second stage are proposed for the formation of the monodisperse uniform HSMSCSNs. According to previous reports, the surfactant-directed cosolvent-assisted sol-gel process is a traditional route for the preparation of monodisperse PMO nanoparticles.<sup>10,57-60</sup> In the present study, the PMO nanoparticles formed in methanol/water solution. Addition of a TEOS/*n*-hexane solution and extra CTAB to the aqueous PMO slurry gave an oil/water biphasic system. Under static conditions, hydrolysis of TEOS is largely hindered. However, under mild stirring the oil phase at the interface is transformed into thermodynamically stable small microemulsion droplets, inside which TEOS is slowly hydrolyzed. The resulting silicate species are transferred to the aqueous phase<sup>61</sup> and can now interact with the surface silanol groups of the preformed highly reactive PMO

nanoparticles.<sup>37</sup> The emerging inorganic/organic interface layer with small silicate species connected to the organosilica framework extends further along the surface curvature of original or newly formed CTAB surfactant micelles, driven by electrostatic interactions between surfactant and silicate species. The shell thickness of thus fabricated core-shell structure depends on the amount of TEOS used and the reaction time. Crucially, *n*-hexane plays a dual role: on the one hand, to slow down the hydrolysis rate of TEOS and, on the other hand, to expand the surfactant CTAB micelles. This is evidenced by the formation of spontaneously nucleated silicate-CTAB micelle composites in the absence of *n*-hexane, which randomly deposit on the surface of the PMO nanoparticles to form aggregates without uniform core-shell structures.<sup>19,25,62</sup> With respect to nucleation, the formation of random nanoparticles and core-shell nanoparticles is dominated by homogeneous and heterogeneous nucleation, respectively, the latter of which is favored due to the lower energy barrier.<sup>19,63</sup> Hence, in the present case, the presence of *n*-hexane in the reaction system greatly decelerates the hydrolysis rate of TEOS, and the stirring-driven hydrolyzed silicate species, assembling at the interface between hydrophobic and hydrophilic phases, are transferred to the surface of preformed PMO nanoparticles to form silicate oligomers via heterogeneous nucleation. The electrostatic interactions between silicate oligomers and CTAB enable these inorganic-organic composites to slowly extend and form a shell layer with an enlarged pore structure. The mesochannels align along new or original pore directions, which are perpendicular to the surface of PMO core particles. Due to the slow hydrolysis rate of TEOS, homogenous nucleation, and hence the formation of isolated mesoporous silica nanoparticles, is negligible. In contrast, in the absence of *n*-hexane, TEOS hydrolysis is greatly enhanced, so that homogeneous and heterogeneous nucleation occur simultaneously. Since the rate of heterogeneous nucleation is much faster than that of homogeneous nucleation, the silicate-CTAB micelle composites mainly nucleate at the surface of PMO nanoparticles to form core-shell structures, but to a minor extent also independently aggregate to form isolated core-free silica nanoparticles (Figure 3.9a and b).

Secondly, the addition of *n*-hexane is beneficial for the fabrication of a hierarchical mesopore array. In the absence of *n*-hexane, the core-shell nanoparticles accompanied by silica aggregates show only a unimodal pore size of 3 nm (Figure 3.9d), which is similar to the pore size of archetypal mesoporous silica MCM-41 prepared by using CTAB as SDA under basic conditions.<sup>1,2</sup> As revealed by materials HSMSCSN-*n*, during the process of formation of the *n*-hexane-assisted uniform core-shell structures, the pore size of the shell layer can be enlarged to a maximum of 5.9 nm (Table 3.2). This can be interpreted by *n*-hexane acting as a swelling agent, since it can readily diffuse into the hydrophobic core of the CTAB micelle and thereby expand the micelle size, aided by the stirring during shell formation.<sup>3,23,24,64-66</sup> Moreover, TEOS dissolved in *n*-hexane can also be adsorbed into the core of CTAB micelles by hydrophobic interactions.<sup>65</sup> Along with TEOS hydrolysis and condensation of silicate species at the *n*-hexane/water interface, the negatively charged silicate oligomers interact with the swollen



surfactant micelles and are deposited perpendicular to the surface of PMO nanoparticles by a self-assembly process to form a shell layer with enlarged pore size. The resulting materials feature uniform core-shell structures with hierarchical pore size. Due to fast heterogeneous nucleation purely siliceous aggregation is suppressed. The pore size of the shell layer is affected by the stirring rate,<sup>3</sup> while the amount of *n*-hexane used in the second stage has a bearing on the shell thickness (Figure 3.21). A smaller amount of *n*-hexane (10 mL) gives rise to a higher TEOS concentration in the oil phase and therefore faster hydrolysis and condensation rates at the oil/water interface, which result in HSMSCSNs with a shell thickness of 34 nm (cf. 40 mL *n*-hexane: 22 nm).

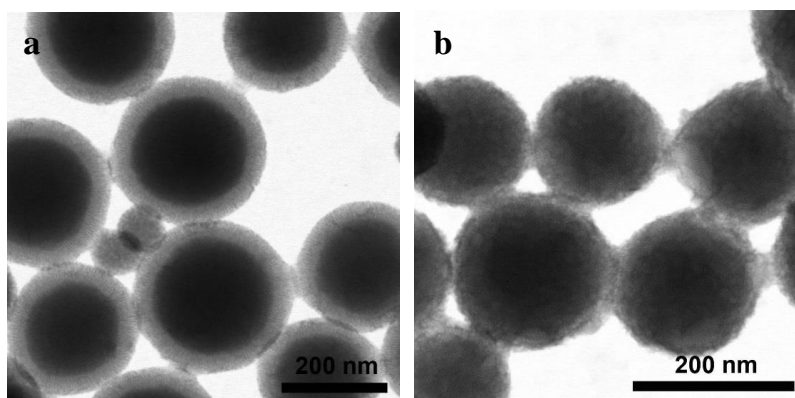


**Figure 3.21** TEM images of HSMSCSNs synthesized with different amounts of *n*-hexane in the second stage: (a) 10 mL, (b) 40 mL. The resultant core-shell nanoparticles show shell thicknesses of (a) 34 nm and (b) 22 nm.

### 3.3.5 Adsorption and Controlled Release of Propiconazole on Material HSMSCSN

The present high surface area/large-volume HSMSCSN material was probed as a carrier for the triazole fungicide propiconazole. We envisaged that the distinct core-shell chemical compositions and topologies as well as the hierarchical pore structure of the organic-inorganic hybrid frameworks might have an impact on the adsorption/desorption behaviour of guest molecules. Propiconazole is a systemic fungicide for controlling harmful microorganisms and preventing fungus attack, and its controlled release is of significance in terms of environmental protection and efficient utilization.<sup>67</sup> We investigated the adsorption behaviour of propiconazole on HSMSCSNs in *n*-hexane solution and its controlled release from propiconazole-loaded HSMSCSNs (denoted HSMSCSN-P) in phosphate buffer solution (PBS, pH 7.1). The adsorption and release of propiconazole by HSMSCSNs were monitored by the change of the UV/Vis absorbance peak of propiconazole at 270.8 nm. After 7 d adsorption on HSMSCSN the markedly decreased peak intensity (Figure 3.22a) implied that most of the propiconazole was adsorbed into the HSMSCSNs. The loading was 262 mg g<sup>-1</sup>. The successful loading of propiconazole was also proven by distinct pore parameters of parent HSMSCSN and HSMSCSN-P from nitrogen physisorption analyses (Figure 3.22b). The observed significant decreases of the specific *BET* surface area (1196 → 547 m<sup>2</sup> g<sup>-1</sup>), pore size (3.0, 5.9 → 2.1, 5.1 nm), and pore volume (1.68 → 0.82 cm<sup>3</sup> g<sup>-1</sup>) reflect the adsorption of propiconazole

into the HSMSCSNs and imply that propiconazole is adsorbed into both pore domains. In contrast, the morphology and topology of HSMSCSN-P (Figure 3.23) did not change significantly compared to parent HSMSCSN. Investigation of the desorption behaviour of propiconazole from a dispersion of HSMSCSN-P in PBS revealed a three-stage release profile over a 48 h period (Figure 3.24). During the first stage (initial 3 h) rapid release of about 74.3 % of propiconazole occurred. In the following 3 h period, the amount of propiconazole in PBS stayed constant, that is, no additional desorption of fungicide took place. Interestingly, the release of propiconazole started again after 6 h and eventually reached 79.5 % in PBS after 48 h. This three-stage release process is quite similar to that of ibuprofen or bovine  $\beta$ -lactoglobulin in core/yolk-shell-structured bimodal mesoporous silica nanoparticles as nanocarriers.<sup>17,24,25</sup> Therefore, it can be reasoned that the stepwise release is associated with the unique hierarchical pore structure.

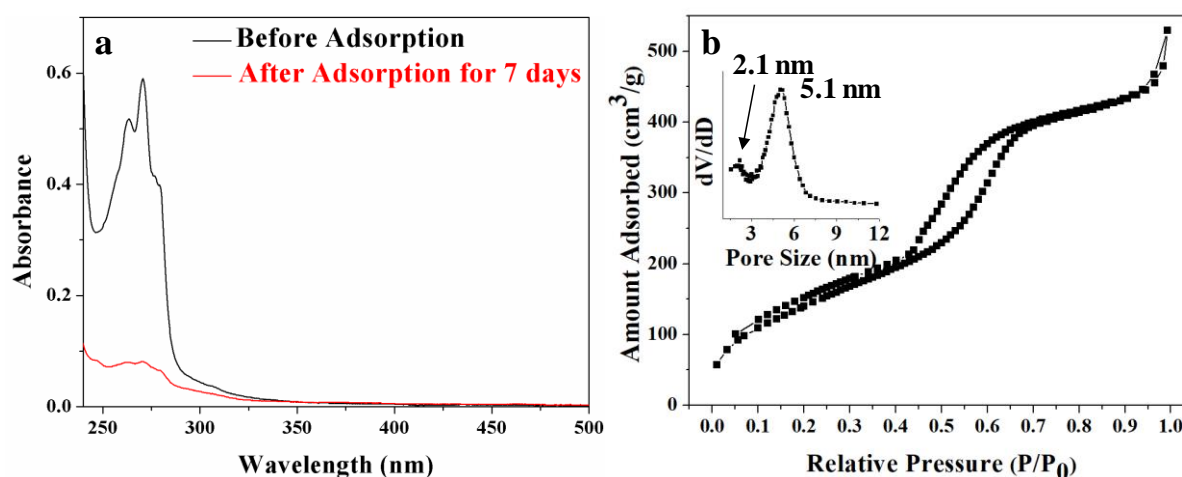


**Figure 3.22** (a) UV-Vis spectra of the propiconazole-*n*-hexane solution before and after adsorption onto HSMSCSN, (b) nitrogen physisorption isotherm of HSMSCSN-P, the inset is the corresponding BJH pore size distribution.

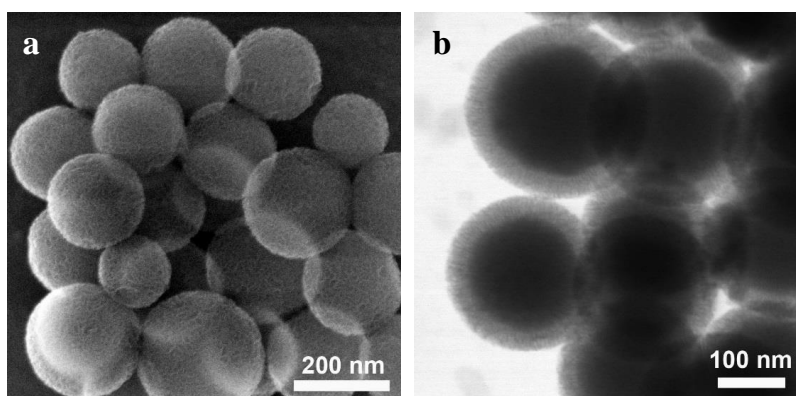


**Figure 3.23** (a) SEM and (b) TEM images of HSMSCSN-P.

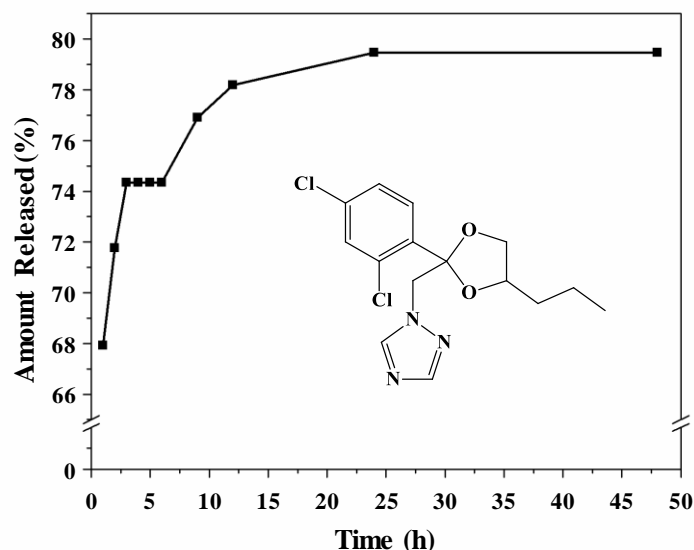


**Figure 3.24** Cumulative release curve of propiconazole from material HSMSCSN-P.

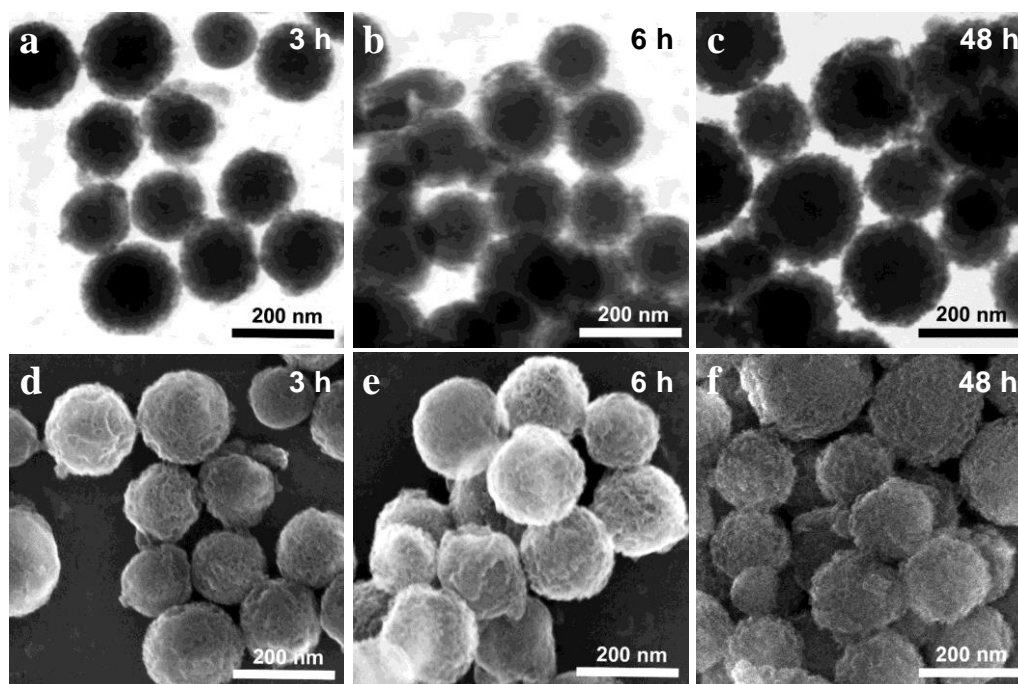


**Figure 3.25** TEM and SEM images of samples of material HSMSCSN-P separated from the PBS during different time periods of stirring.

To probe the release mechanism, the release process of propiconazole from HSMSCSN was tracked by S/TEM images and nitrogen physisorption. To this end, a sample of HSMSCSN-P from the release system was separated at a chosen time interval and dried at 75 °C overnight. After stirring for 3 h in PBS, the TEM image showed that the shell thickness of HSMSCSN-P had decreased to 16 nm and that the radial shell pore structure was partially destroyed, as revealed by the appearance of small fragments (Figure 3.25). Moreover, enhanced roughening of the surface with obvious defects was observed in the SEM image. These results demonstrate that the mesoporous silica shell layer is degraded in PBS. This phenomenon is in line with the

degradation of protein-loaded mesoporous silica in a buffer: the degradation rate of large-pore silica nanoparticles is much faster than that of those with small pore size.<sup>24,68</sup> The rapid degradation of the shell layer is attributed to the large pore size and the low degree of condensation of the surface silica framework. On extending the stirring time to 6 and 48 h, the particle surface becomes rougher and rougher, but the shell thickness remains constant at about 16 nm, and no degradation of the PMO core is observed, which evidences the high stability of PMO.<sup>30</sup>

In addition, the nitrogen physisorption isotherms of HSMSCSN-P separated at each time interval (3 h, 6 h and 48 h) clearly show two condensation steps at  $P/P_0$  values of 0.2-0.35 and 0.9-1.0, corresponding to core mesopores and the void space of interparticle contacts, respectively (Figure 3.26). Adsorption and desorption at low relative pressure are irreversible. The pore size of HSMSCSN-P separated after being stirred for 3 h was 2.1 nm, which is less than the pore size of the original core (2.7 nm), but it is similar to that of propiconazole-loaded HSMSCSNs before the release of propiconazole, which implies that propiconazole molecules are preserved in the pores of the core structure. Also, the original large-pore structure (shell layer) seems for the most part to be destroyed, since the second capillary condensation step at  $P/P_0 = 0.45-0.7$  disappeared. During this initial period rapid release of propiconazole is achieved by fast degradation of the shell layer and/or the destruction of the large-pore structure. This observation is in accordance with the release of guest molecules induced by the degradation of nanocarriers previously reported by Shen et al. and Croissant et al.<sup>24,69</sup> In their studies, the nanocarriers were entirely degraded into small fragments during the release process. Remarkably, in our study no release of propiconazole was detected during the second stage of stirring between 3 and 6 h. More interestingly, the pore parameters of HSMSCSN-P after stirring for 6 h were quite similar to those of the sample stirred for 3 h, as were the morphology and topology, except that a long stirring time leads to the formation of increasing amounts of small fragments stemming from partial exfoliation of the shell structure (Figure 3.25b and e). However, the PMO core remains intact during the entire release process even if the release time is extended to 48 h (Figure 3.25c and f). This high stability of the PMO core can be attributed to the nondegradable nature of PMO nanoparticles in PBS.<sup>70</sup> The temporary release plateau (no release of propiconazole) during 3-6 h is attributable to enhanced interactions between the organosilica framework and propiconazole molecules and the relatively small pore size of PMO core, which greatly impede any fast diffusion of propiconazole molecules into PBS. For HSMSCSN-P stirred for 48 h, the pore size slightly increased to 2.2 and 2.8 nm due to the slow release of propiconazole entrapped in the PMO core by diffusion and partial recovery and enlargement of the original pore size of the PMO core. This three-stage release profile for propiconazole in the HSMSCSN host is a characteristic reflection of the unique hierarchical bimodal pore structure and of the distinct compositions of core and shell. It can be anticipated that, depending on the envisaged application, the release amount/rate in each stage would be adjustable by rationally changing the properties of MS shell and PMO core, such as

shell thickness, pore size, and core composition. It is therefore possible to conclude that such HSMSCSNs are promising candidates for the adsorption and the controlled release of various drugs.

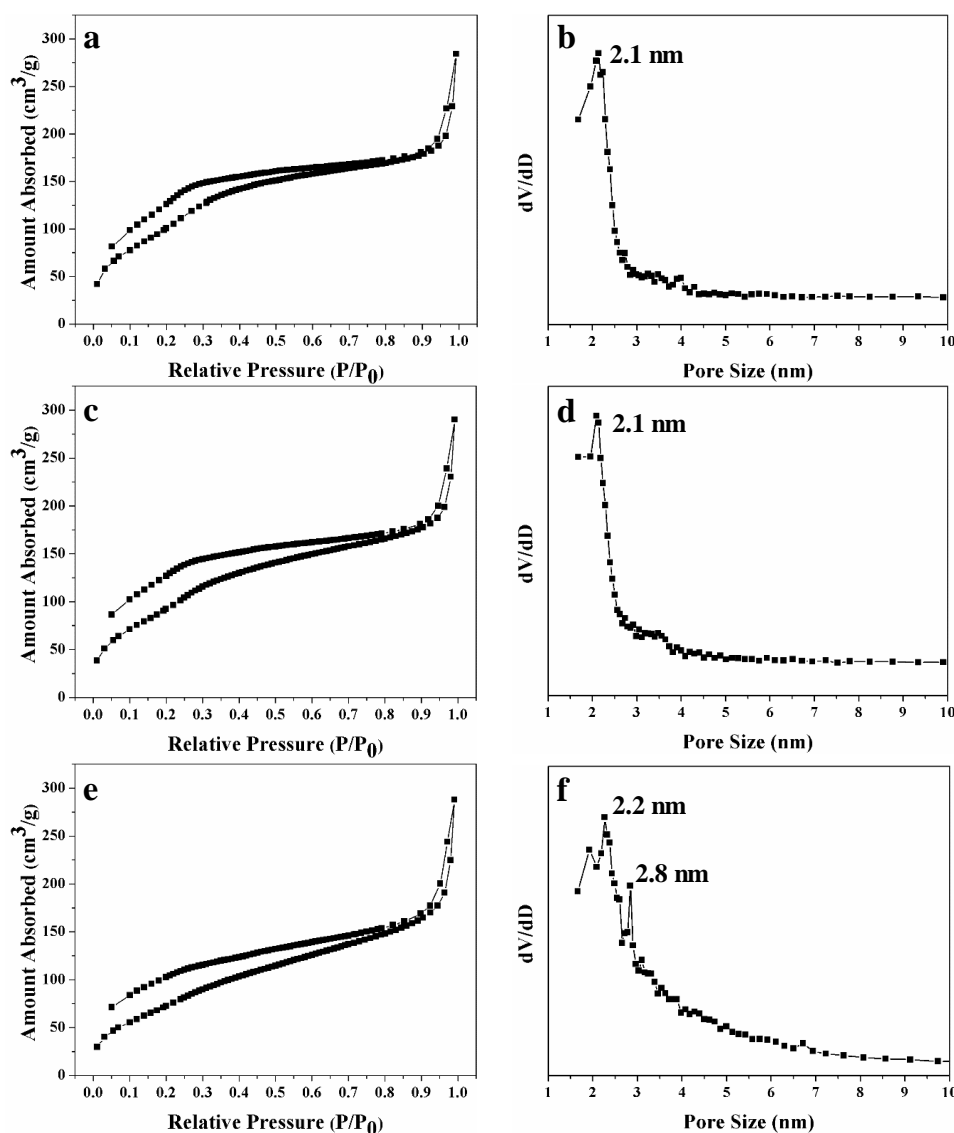


**Figure S3.22** Nitrogen physisorption isotherms and the corresponding BJH pore size distributions of samples HSMSCSN-P separated from the PBS at different time periods under stirring conditions: (a, b) 3 h, (c, d) 6 h, (e, f) 48 h.

### 3.4 Conclusions

A simple and efficient one-pot, two-step strategy has been designed for the preparation of HSMSCSNs with hexagonal or cage-like cubic periodic mesoporous organosilica PMO core and hexagonal mesoporous silica MS shell. By adjusting the synthesis parameters, such HSMSCSNs can feature distinct shell thicknesses (15–46 nm), core sizes (87–273 nm), pore diameters (2.6–6.2 nm), particle sizes (147–337 nm), and core pore configurations (channel versus cage-like). While core formation by a cosolvent-assisted sol-gel process has been established recently, combined shell fabrication by *n*-hexane-assisted controlled hydrolysis and

heterogeneous nucleation at the core surface, involving the self-assembly of swollen surfactant (CTAB) micelles, seems to be unprecedented. The role of *n*-hexane is dual and decisive for the fabrication of high-quality uniform HSMSCSNs, by ensuring the formation of a hierarchical pore structure by controlled TEOS hydrolysis and by acting as a micelle expander. Finally, all HSMSCSN materials have very high surface areas (1086-1294 m<sup>2</sup> g<sup>-1</sup>) and large pore volumes (1.56-1.83 cm<sup>3</sup> g<sup>-1</sup>), which make them promising multicompartiment drug nanocarriers. This could be demonstrated for the HSMSCSN-promoted adsorption and controlled release of the fungicide propiconazole. The observed three-stage release profile characterized by rapid release/temporary plateau/slow release periods reflects the distinct compositions and bimodal pore structure of HSMSCSNs, and can be explained by partial degradation of the large-pore shell layer and slow diffusion within as well as slight pore enlargement of the PMO core. The present investigation paves the way for future applications of HSMSCSN materials in drug delivery and release, continuous multistep catalysis, as well as adsorption and separation of proteins/enzymes.

### 3.5 References

1. Y. Deng, Y. Cai, Z. Sun, J. Liu, C. Liu, J. Wei, W. Li, C. Liu, Y. Wang and D. Zhao, *J. Am. Chem. Soc.*, **2010**, 132, 8466-8473.
2. Y. Deng, D. Qi, C. Deng, X. Zhang and D. Zhao, *J. Am. Chem. Soc.*, **2008**, 130, 28-29.
3. Q. Yue, J. Li, W. Luo, Y. Zhang, A. A. Elzatahry, X. Wang, C. Wang, W. Li, X. Cheng, A. Alghamdi, A. M. Abdullah, Y. Deng and D. Zhao, *J. Am. Chem. Soc.*, **2015**, 137, 13282-13289.
4. J. Chen, R. Zhang, L. Han, B. Tu and D. Zhao, *Nano Res.*, **2013**, 6, 871-879.
5. S. H. Joo, J. Y. Park, C.-K. Tsung, Y. Yamada, P. Yang and G. A. Somorjai, *Nat. Mater.*, **2008**, 8, 126-131.
6. L. Han, H. Wei, B. Tu and D. Zhao, *Chem. Commun.*, **2011**, 47, 8536-8538.
7. J.-T. Song, X.-S. Zhang, M.-Y. Qin and Y.-D. Zhao, *Dalton Trans.*, **2015**, 44, 7752-7756.
8. J. Pan, D. Wan and J. Gong, *Chem. Commun.*, **2011**, 47, 3442-3444.
9. R. Gui, A. Wan and H. Jin, *Analyst*, **2013**, 138, 5956-5964.
10. S. Haffer, M. Tiemann and M. Fröba, *Chem. Eur. J.*, **2010**, 16, 10447-10452.
11. M. Hartmann and W. Schwieger, *Chem. Soc. Rev.*, **2016**, 45, 3311-3312.
12. M. Hartmann and X. Kostrov, *Chem. Soc. Rev.*, **2013**, 42, 6277-6289.
13. W. Luo, T. Zhao, Y. Li, J. Wei, P. Xu, X. Li, Y. Wang, W. Zhang, A. A. Elzatahry, A. Alghamdi, Y. Deng, L. Wang, W. Jiang, Y. Liu, B. Kong, D. Zhao, *J. Am. Chem. Soc.* **2016**, 138, 12586-12595.
14. T. Zhao, W. Luo, Y. Deng, Y. Luo, P. Xu, Y. Liu, L. Wang, Y. Ren, W. Jiang, *Nano Energy* **2016**, 26, 16-25.
15. X. Qian, D. Xiong, A. M. Asiri, S. B. Khan, M. M. Rahman, H. Xu and D. Zhao, *J. Mater. Chem. A*, **2013**, 1, 7525-7532.
16. X. Qian, J. Du, B. Li, M. Si, Y. Yang, Y. Hu, G. Niu, Y. Zhang, H. Xu, B. Tu, Y. Tang and D. Zhao, *Chem. Sci.*, **2011**, 2, 2006-2016.
17. D. Niu, Z. Ma, Y. Li and J. Shi, *J. Am. Chem. Soc.*, **2010**, 132, 15144-15147.
18. L. Xu, Y. Ren, H. Wu, Y. Liu, Z. Wang, Y. Zhang, J. Xu, H. Peng and P. Wu, *J. Mater. Chem.*, **2011**, 21, 10852-10858.
19. B. Xi, Y. C. Tan and H. C. Zeng, *Chem. Mater.*, **2016**, 28, 326-336.
20. Z. Li and H. C. Zeng, *J. Am. Chem. Soc.*, **2014**, 136, 5631-5639.

21. Y. Fang, G. Zheng, J. Yang, H. Tang, Y. Zhang, B. Kong, Y. Lv, C. Xu, A. M. Asiri, J. Zi, F. Zhang and D. Zhao, *Angew. Chem. Int. Ed.*, **2014**, 53, 5366-5370.
22. H. Ishii, T. Ikuno, A. Shimojima and T. Okubo, *J. Colloid Interface Sci.*, **2015**, 448, 57-64.
23. X. Wang, Y. Zhang, W. Luo, A. A. Elzatahry, X. Cheng, A. Alghamdi, A. M. Abdullah, Y. Deng and D. Zhao, *Chem. Mater.*, **2016**, 28, 2356-2362.
24. D. Shen, J. Yang, X. Li, L. Zhou, R. Zhang, W. Li, L. Chen, R. Wang, F. Zhang and D. Zhao, *Nano Lett.*, **2014**, 14, 923-932.
25. J. Liu, S. Z. Qiao, S. Budi Hartono and G. Q. Lu, *Angew. Chem. Int. Ed.*, **2010**, 49, 4981-4985.
26. Y. Chen and J. Shi, *Adv. Mater.*, **2016**, 28, 3235-3272.
27. Y. Yang, X. Liu, X. Li, J. Zhao, S. Bai, J. Liu and Q. Yang, *Angew. Chem. Int. Ed.*, **2012**, 51, 9164-9168.
28. X. Li, L. Zhou, Y. Wei, A. M. El-Toni, F. Zhang and D. Zhao, *J. Am. Chem. Soc.*, **2014**, 136, 15086-15092.
29. J. Peng, G. Lan, M. Guo, X. Wei, C. Li and Q. Yang, *Chem. Eur. J.*, **2015**, 21, 10490-10496.
30. Y. Chen, P. Xu, H. Chen, Y. Li, W. Bu, Z. Shu, Y. Li, J. Zhang, L. Zhang, L. Pan, X. Cui, Z. Hua, J. Wang, L. Zhang and J. Shi, *Adv. Mater.*, **2013**, 25, 3100-3105.
31. J. Liu, H. Q. Yang, F. Kleitz, Z. G. Chen, T. Yang, E. Strounina, G. Q. Lu and S. Z. Qiao, *Adv. Funct. Mater.*, **2012**, 22, 591-599.
32. Y. Yang, S. Bernardi, H. Song, J. Zhang, M. Yu, J. C. Reid, E. Strounina, D. J. Searles and C. Yu, *Chem. Mater.*, **2016**, 28, 704-707.
33. X. Li, L. Zhou, Y. Wei, A. M. El-Toni, F. Zhang and D. Zhao, *J. Am. Chem. Soc.*, **2015**, 137, 5903-5906.
34. Z. Teng, S. Wang, X. Su, G. Chen, Y. Liu, Z. Luo, W. Luo, Y. Tang, H. Ju, D. Zhao and G. Lu, *Adv. Mater.*, **2014**, 26, 3741-3747.
35. Z. Teng, X. Su, B. Lee, C. Huang, Y. Liu, S. Wang, J. Wu, P. Xu, J. Sun, D. Shen, W. Li and G. Lu, *Chem. Mater.*, **2014**, 26, 5980-5987.
36. Z. Teng, X. Su, Y. Zheng, J. Zhang, Y. Liu, S. Wang, J. Wu, G. Chen, J. Wang, D. Zhao and G. Lu, *J. Am. Chem. Soc.*, **2015**, 137, 7935-7944.
37. H. Zou, R. Wang, Z. Shi, J. Dai, Z. Zhang and S. Qiu, *J. Mater. Chem. A*, **2016**, 4, 4145-4154.
38. Y. Yang, J. Liu, X. Li, X. Liu and Q. Yang, *Chem. Mater.*, **2011**, 23, 3676-3684.
39. H. Zou, R. Wang, X. Li, X. Wang, S. Zeng, S. Ding, L. Li, Z. Zhang and S. Qiu, *J. Mater. Chem. A*, **2014**, 2, 12403-12412.
40. C. M. A. Parlett, M. A. Isaacs, S. K. Beaumont, L. M. Bingham, N. S. Hondow, K. Wilson and A. F. Lee, *Nat. Mater.*, **2016**, 15, 178.
41. C. M. A. Parlett, K. Wilson and A. F. Lee, *Chem. Soc. Rev.*, **2013**, 42, 3876-3893.
42. B. J. Melde, B. T. Holland, C. F. Blanford and A. Stein, *Chem. Mater.*, **1999**, 11, 3302-3308.
43. W. Guo, F. Kleitz, K. Cho and R. Ryoo, *J. Mater. Chem.*, **2010**, 20, 8257-8265.
44. J. Liu, S. Bai, H. Zhong, C. Li and Q. Yang, *J. Phys. Chem. C*, **2010**, 114, 953-961.
45. J. Liu, Q. Yang, L. Zhang, H. Yang, J. Gao and C. Li, *Chem. Mater.*, **2008**, 20, 4268-4275.
46. X. Mei, D. Chen, N. Li, Q. Xu, J. Ge, H. Li, B. Yang, Y. Xu and J. Lu, *Soft Matter*, **2012**, 8, 5309-5316.
47. Y. Liu, K. Lan, A. A. Bagabas, P. Zhang, W. Gao, J. Wang, Z. Sun, J. Fan, A. A. Elzatahry and D. Zhao, *Small*, **2016**, 12, 860-867.
48. Z. Teng, X. Su, Y. Zheng, J. Sun, G. Chen, C. Tian, J. Wang, H. Li, Y. Zhao and G. Lu, *Chem. Mater.*, **2013**, 25, 98-105.
49. J. M. Rosenholm, J. Zhang, W. Sun and H. Gu, *Microporous Mesoporous Mater.*, **2011**, 145, 14-20.
50. S. Guan, S. Inagaki, T. Ohsuna and O. Terasaki, *J. Am. Chem. Soc.*, **2000**, 122, 5660-5661.
51. Y. Liang, M. Hanzlik and R. Anwender, *J. Mater. Chem.*, **2005**, 15, 3919-3928.
52. Y. Liang, M. Hanzlik and R. Anwender, *J. Mater. Chem.*, **2006**, 16, 1238-1253.

53. Y. Liang, E. S. Erichsen, M. Hanzlik and R. Anwender, *Chem. Mater.*, **2008**, 20, 1451-1458.
54. T. Suteewong, H. Sai, R. Hovden, D. Muller, M. S. Bradbury, S. M. Gruner and U. Wiesner, *Science*, **2013**, 340, 337-341.
55. J. Croissant, X. Cattoën, M. Wong Chi Man, P. Dieudonné, C. Charnay, L. Raehm and J.-O. Durand, *Adv. Mater.*, **2015**, 27, 145-149.
56. T. Asefa, M. J. MacLachlan, H. Grondley, N. Coombs and G. A. Ozin, *Angew. Chem. Int. Ed.*, **2000**, 39, 1808-1811.
57. W. Guo, J. Wang, S.-J. Lee, F. Dong, S. S. Park and C.-S. Ha, *Chem. Eur. J.*, **2010**, 16, 8641-8646.
58. N. Ma, Y. Deng, W. Liu, S. Li, J. Xu, Y. Qu, K. Gan, X. Sun and J. Yang, *Chem. Commun.*, **2016**, 52, 3544-3547.
59. X. Du, X. Li, L. Xiong, X. Zhang, F. Kleitz and S. Z. Qiao, *Biomaterials*, **2016**, 91, 90-127.
60. J. G. Croissant, X. Cattoën, M. Wong Chi Man, J.-O. Durand and N. M. Khashab, *Nanoscale*, **2015**, 7, 20318-20334.
61. K. D. Hartlen, A. P. T. Athanasopoulos and V. Kitaev, *Langmuir*, **2008**, 24, 1714-1720.
62. W. Li, J. Yang, Z. Wu, J. Wang, B. Li, S. Feng, Y. Deng, F. Zhang and D. Zhao, *J. Am. Chem. Soc.*, **2012**, 134, 11864-11867.
63. X. Y. Liu, *J. Chem. Phys.*, **2000**, 112, 9949-9955.
64. Y. Yang, Y. Niu, J. Zhang, A. K. Meka, H. Zhang, C. Xu, C. X. C. Lin, M. Yu and C. Yu, *Small*, **2015**, 11, 2743-2749.
65. Y. Zhang, Q. Yue, Y. Jiang, W. Luo, A. A. Elzatahry, A. Alghamdi, Y. Deng and D. Zhao, *CrystEngComm*, **2016**, 18, 4343-4348.
66. C. Xu, M. Yu, O. Noonan, J. Zhang, H. Song, H. Zhang, C. Lei, Y. Niu, X. Huang, Y. Yang and C. Yu, *Small*, **2015**, 11, 5949-5955.
67. X. Chen and C. Yang, *J. Agr. Food Chem.*, **2009**, 57, 2441-2446.
68. A. Yildirim and M. Bayindir, *J. Mater. Chem. A*, **2015**, 3, 3839-3846.
69. J. Croissant, X. Cattoën, M. W. C. Man, A. Gallud, L. Raehm, P. Trens, M. Maynadier and J.-O. Durand, *Adv. Mater.*, **2014**, 26, 6174-6180.
70. C. Urata, H. Yamada, R. Wakabayashi, Y. Aoyama, S. Hirose, S. Arai, S. Takeoka, Y. Yamauchi and K. Kuroda, *J. Am. Chem. Soc.*, **2011**, 133, 8102-8105.



## 4 Ultrafast Myoglobin Adsorption into Double-Shelled Hollow Mesoporous Silica Nanospheres

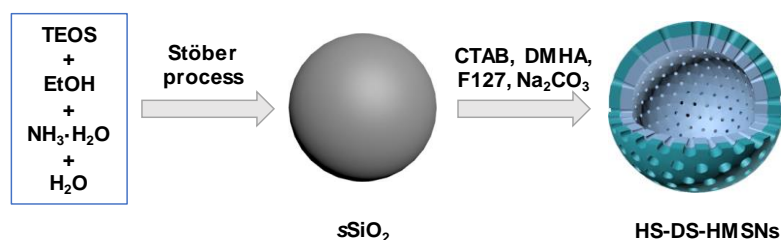
### 4.1 Introduction

Benefiting from their unique properties, such as high surface area, low density, and large cavities, hollow nanostructured materials feature promising applications in micro-/nanoreactors, catalysis, energy storage and biomedicine.<sup>1-10</sup> Among these various hollow nanostructured materials, hollow mesoporous silica nanospheres (HMSNs) in particular show distinct advantages for vast biomedical and catalytic applications due to an easily modifiable surface structure, a nontoxic and biocompatible silica framework as well as a readily accessible hollow cavity via the mesochannels.<sup>8-10</sup> Hence the successful fabrication of HMSNs was particularly striking. A variety of strategies involving hard/soft templating techniques,<sup>11-15</sup> self-templating methods,<sup>16,17</sup> surface-catalyzed dual templating approaches,<sup>18</sup> self-transformation routes,<sup>19</sup> Ostwald ripening processes,<sup>20</sup> and sequential heterogeneous nucleation approaches,<sup>21,22</sup> have been extensively adopted to synthesize HMSNs of distinct compositions, different particle sizes<sup>17-19</sup> and diverse pore sizes/structures<sup>11,12,14,15,18</sup> as well as adjustable shell thicknesses.<sup>13,19,20,22</sup>

While the feasibility of single-shelled HMSNs is not surprising, double/multiply-shelled HMSN materials are becoming more and more the focus of attention.<sup>20,22-26</sup> Large empty spaces between shell layers of distinct pore sizes and structures qualify double/multiple-shelled HMSN as promising candidates for catalysis and drug release.<sup>24,26</sup> Traditional preparation processes of double-shelled HMSNs are tedious and time-consuming.<sup>23,24</sup> One-pot techniques are advantageous in terms of ease and efficiency<sup>20,22,25,26</sup> but the pore size of the shell layers of the HMSNs obtained is usually small and nonadjustable, which exceedingly counteracts a successful diffusion of large molecules, in particular, large nanoobjects and biomolecules. Although double-shelled HMSNs with pore sizes of 9.3 nm were recently reported,<sup>22</sup> a dense structure of the inner silica shell greatly blocked the extension of the mesopore channels of the outer silica shell into the large cavity of the hollow structure, thus impeding any uptake of guest molecules. From these investigations, it is clear that the fabrication of double/multiply-shelled HMSN materials is still in its infancy, encountering enormous challenges regarding a simple approach to efficiently adjust the double/multiply-shelled structure while preserving the intrinsic advantages of large surface areas, high pore volumes as well as hierarchical pore diameters.

Herein, a facile new approach has been developed to prepare hierarchically-structured double-shelled hollow mesoporous silica nanospheres (HS-DS-HMSNs). As shown in Scheme 4.1, solid silica nanospheres ( $s\text{SiO}_2$ ) produced via the Stöber process are treated with a basic solution in the presences of cationic surfactant CTAB (hexadecyltrimethylammonium bromide), neutral amine DMHA (*N,N*-dimethylhexadecylamine) and nonionic polymer

Pluronic F127 to form as-made HS-DS-HMSNs. After removal of the surfactant and organic expander, the resulting materials display a high monodispersibility, uniform particle size, characteristic hollow structure and adjacent double shells with different pore sizes and thicknesses. The formation mechanism of such HS-DS-HMSNs is addressed. Moreover, a series of HS-DS-HMSN-type materials with various particle/pore sizes and shell thicknesses were prepared by adjusting the synthesis parameters. Finally, by taking advantage of the large surface area, high pore volume and radially aligned pore structure, the adsorption ability of the HS-DS-HMSN-type materials for myoglobin is investigated.



**Scheme 4.1** The illustration of the preparation process of hierarchically structured double-shelled hollow mesoporous silica nanospheres (HS-DS-HMSNs).

## 4.2 Experimental Section

### 4.2.1 Chemicals

All the chemicals were used as received without further purification. Ethanol (99.9%), tetraethylorthosilicate (TEOS,  $\geq 99\%$ ), ammonium hydroxide solution (25 wt%), hexadecyltrimethyl-ammonium bromide (CTAB,  $\geq 98\%$ ), *N,N*-dimethylhexadecylamine (DMHA,  $\geq 95\%$ ), *N,N*-dimethyloctylamine (DMOA,  $\geq 95\%$ ), non-ionic triblock copolymer Pluronic F127 (EO<sub>100</sub>PO<sub>70</sub>EO<sub>100</sub>, EO = ethylene oxide, PO = propylene oxide), sodium carbonate (Na<sub>2</sub>CO<sub>3</sub>,  $\geq 99\%$ ), hydrochloric acid (HCl,  $\geq 37\%$ ) and myoglobin (Mb,  $\geq 90\%$ ) were purchased from Sigma-Aldrich. Deionized water was used in all experiments.

### 4.2.2 Synthesis of *s*SiO<sub>2</sub>

Monodisperse *s*SiO<sub>2</sub> with average particle size of 363 nm was synthesized according to the Stöber method.<sup>27</sup> Typically, 10 mL of TEOS mixed with 184 mL of ethanol was stirred at ambient temperature for several minutes. A mixture of 16 mL of 25 wt% ammonium hydroxide solution and 4 mL of H<sub>2</sub>O was then added under stirring. After being stirred for 4 h, the resultant *s*SiO<sub>2</sub> was separated by centrifugation, followed by washing with ethanol twice and dried at 80 °C for 18 h. For the preparation of *s*SiO<sub>2</sub> with average particle size of 177 nm, 12 mL of 25 wt% ammonium hydroxide solution was used at otherwise identical conditions.

### 4.2.3 Synthesis of HS-DS-HMSN

In a typical preparation procedure, 0.4 g of *s*SiO<sub>2</sub> was first suspended in 80 mL of H<sub>2</sub>O by sonication for 30 min. To the stable suspension, 0.1 g of CTAB and 0.1 mL of DMHA were then added and stirred at ambient temperature for 30 min, followed by adding 0.04 g of F127.

The stirring was further lasted for a further 15 min. Afterwards, 2.5 g of  $\text{Na}_2\text{CO}_3$  was added and the resulting mixture was stirred at 45 °C for 24 h. The as-made product was separated by centrifugation and washed with water once and ethanol once. The organic composites involving template CTAB and expander DMHA were removed by sonication in the mixture of 80 mL of ethanol and 3 mL of 37% HCl for 15 min.<sup>28</sup> This process was repeated twice and the final material was dried at 80 °C overnight. For all HS-DS-HMSN-type materials, the same preparation process was applied except that some reaction parameters were changed. These materials were denoted HS-DS-HMSN-x (x is the sample number). The detailed preparation conditions are listed in Table 4.1.

#### 4.2.4 Characterization

Nitrogen physisorption analysis was carried out on a Micrometrics ASAP 2020 volumetric adsorption apparatus at 77.4 K. The sample was degassed at 120°C for 6 h under a pressure < 5  $\mu\text{mHg}$  vacuum prior to the measurement. The specific surface area was calculated by *Brunauer-Emmett-Teller* (BET) method. The pore volume was calculated from the total nitrogen adsorption amount at  $P/P_0 = 0.995$ . The pore size distribution was obtained from the adsorption branch of the isotherm by the *Barret-Joyner-Haldenda* (BJH) method. Low angle powder X-ray diffraction (PXRD) pattern was obtained with a Bruker D8 Advance Diffractometer using monochromatic  $\text{CuK}\alpha$  radiation ( $\lambda = 1.5406 \text{ \AA}$ ) in the  $2\theta$  range of 0.5 to 10.0° in the step/scan mode with the step width of 0.00825 and accumulation time of 2 s/step. Dynamic Light Scattering (DLS) and Zeta potential measurements were conducted on a Malvern Zetasizer Nano-ZS at ambient temperature. Scanning /transmission electron microscopy (S/TEM) images were gained on a Hitachi SU 8030 microscope operated at an acceleration voltage of 30 kV. The sample was prepared by dispersing the powdery sample in ethanol and loading one drop of the suspension onto the copper grid covered with holy carbon film. UV-Vis spectra were obtained with a T60 UV-Vis spectrophotometer (PG Instruments). Sonication was operated in a Bandelin sonorex digtec ultrasonic bath.

#### 4.2.5 Myoglobin (Mb) Adsorption

An Mb solution was prepared by dissolving 10 mg of Mb in 45 mL of 10 mM phosphate buffer solution (pH 6.4). Then 34 mg of HS-DS-HMSN or HS-DS-HMSN-x was added into the Mb solution and stirred at ambient temperature for adsorption. Small amounts (3 mL) of the suspension were withdrawn at defined time intervals, and centrifuged. The supernatant was analysed by UV-Vis absorbance at 407.8 nm to ascertain the adsorption amount.

### 4.3 Results and Discussion

#### 4.3.1 Synthesis and Characterization of HS-DS-HMSN

The monodisperse bulk silica particles  $s\text{SiO}_2$ , used in this study were obtained according to the Stöber method.<sup>27</sup> The TEM image revealed that  $s\text{SiO}_2$  has a uniform size of  $363 \pm 2.1 \text{ nm}$

(Figure 4.1a and Figure 4.2), while the PXRD pattern did not show any diffraction peaks (Figure 4.3a). The nonporous nature of  $s\text{SiO}_2$  was confirmed by a small BET specific surface area ( $15 \text{ m}^2 \text{ g}^{-1}$ ), low pore volume ( $0.04 \text{ cm}^3 \text{ g}^{-1}$ ), and the virtually non-existent pore-size distribution (Figure 4.3b, insert), as obtained from nitrogen physisorption analysis. After being treated in a basic aqueous solution in the presences of CTAB, DMHA and F127 for 24 h, the TEM images revealed that the  $s\text{SiO}_2$  had transformed into monodisperse hollow nanospheres with a double-layer structure in the shell (Figure 4.1b and c). By measuring 50 random particles, the average particle size, cavity size, inner and outer shell thicknesses of such HS-DS-HMSN are  $324 \pm 3.9 \text{ nm}$ ,  $171 \pm 3.6 \text{ nm}$ ,  $41 \pm 0.7 \text{ nm}$  and  $35 \pm 0.4 \text{ nm}$ , respectively (Figure 4.4). The TEM image of a single HS-DS-HMSN shows that the inner-shell pore size is smaller than that of the outer shell (Figure 4.1d). The pores of the two layers are perpendicularly aligned and interconnected at the interface. Such radially oriented mesochannels extending to the large hollow cavity might be beneficial for the uptake of guest molecules from the external surface to inner large cavity. SEM images clearly indicated a relatively coarse surface of the HS-DS-HMSN compared to the parent  $s\text{SiO}_2$  (Figure 4.1e), revealing a change of the surface structure (nonporous versus mesoporous). Note that a single crushed sphere, which is shown in Figure 4.1f, clearly confirmed the existence of a large internal cavity, further corroborating the formation of hollow spheres. Importantly, the conversion of  $s\text{SiO}_2$  into HS-DS-HMSN did not alter its high monodispersibility in aqueous solution. The dynamic light scattering (DLS) profile displayed only one peak ( $458 \text{ nm}$ ) with low polydispersity index ( $\text{PDI} = 0.06$ ) (Figure 4.5), verifying a uniform particle size and excellent monodispersity in aqueous solution. The slightly larger particle size resulting from the DLS measurement is caused by the solvent layer effect, affording a comparatively large hydrodynamic size of the primary particles.

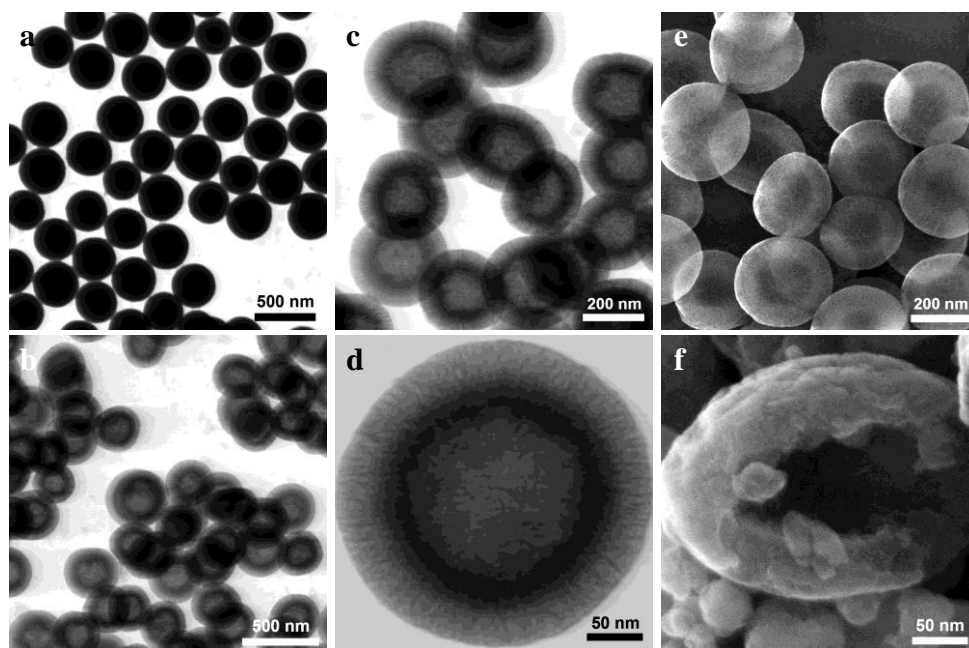


**Figure 4.1** (a) TEM image of  $s\text{SiO}_2$ , (b-d) TEM images of HS-DS-HMSN with different magnifications, (e) SEM image of HS-DS-HMSN, and (f) SEM image of partially crushed HS-DS-HMSN.

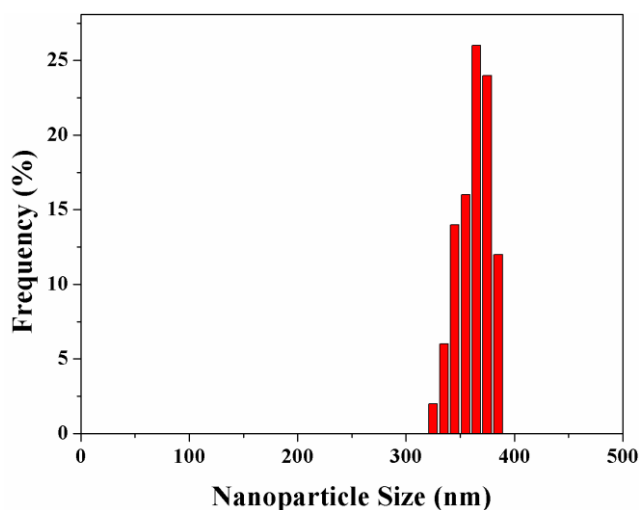


**Figure 4.2** The particle size distribution of  $s\text{SiO}_2$  by measuring 50 random particles from the TEM images.

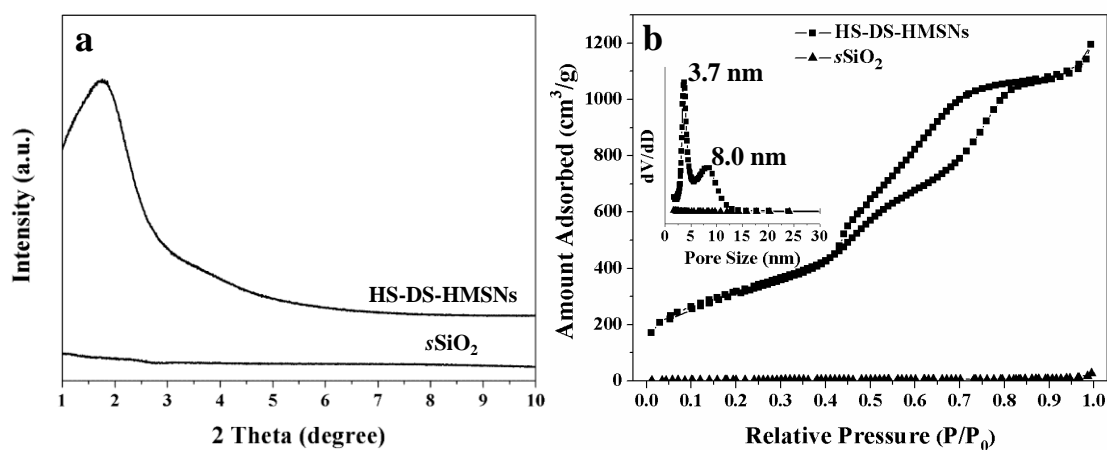


**Figure 4.3** (a) PXRD patterns, and (b)  $\text{N}_2$  physisorption isotherms of  $s\text{SiO}_2$  and HS-DS-HMSNs, the inset in (b) is the corresponding BJH pore size distributions.

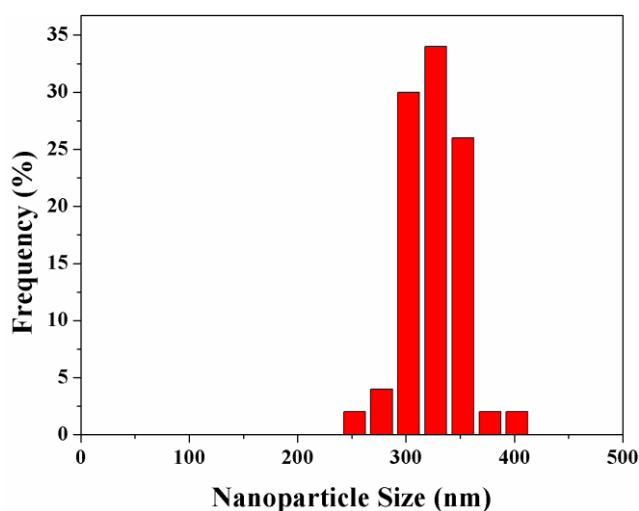


**Figure 4.4** The particle size distribution of HS-DS-HMSNs by measuring 50 random particles from the TEM images.

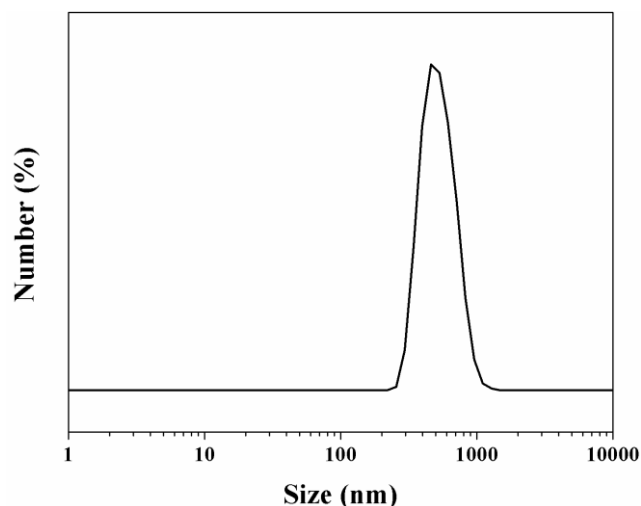


**Figure 4.5** Dynamic light scattering (DLS) of HS-DS-HMSNs suspended in water.

The PXRD pattern of our HS-DS-HMSNs shows only one broad peak centered at the  $2\theta$  angle of  $1.7^\circ$  with a  $d$  value of 5 nm (Figure 4.3a), originating from the shell mesostructure. The small hierarchically mesoporous domains as well as the curved feature of the shell result in the less distinct diffraction peaks from both layers.<sup>16</sup> Nitrogen physisorption analysis of HS-DS-HMSN revealed a type IV isotherm with three sharp condensation steps at  $P/P_0 = 0.4-0.6$ ,  $0.6-0.85$ , and  $0.95-1.0$ , respectively (Figure 4.3b), characteristic of mesopores with different pore sizes and interparticle voids. The BJH pore size distribution clearly features two different pore sizes of about 3.7 and 8.0 nm (Figure 4.3b, insert), corresponding to the pores in the inner and outer shells, respectively. In contrast to the nitrogen physisorption isotherms of hollow structures observed in previous studies, which normally show type H4 hysteresis loops,<sup>4,11,13</sup> and inverse H2 type hysteresis loop is observed in the case of HS-DS-HMSN, which is due to the large pore size in the outer shell.<sup>29,30</sup> The BET specific surface area and pore volume of HS-DS-HMSN are  $1168 \text{ m}^2 \text{ g}^{-1}$  and  $1.85 \text{ cm}^3 \text{ g}^{-1}$ , respectively, and hence much higher than those reported previously.<sup>15-17,19,20,22,24,25</sup> The high specific surface area and large pore volume are attributed to the perpendicularly aligned mesochannels in the double shells and the accessible large cavity.

#### 4.3.2 Formation Mechanism of HS-DS-HMSN

In order to investigate the mechanism of formation of such HS-DS-HMSN, more experiments were conducted. Firstly, in the absence of F127 in the preparation solution under otherwise identical conditions, the obtained silica material was composed of aggregated hollow nanoparticles, as confirmed by TEM and SEM images shown in Figure 4.6 a and b. Also this silica material did not show any uniform pore size distribution (nitrogen physisorption analysis, Figure 4.6 c and d). When the amount of F127 used is the half of the amount used in the preparation of HS-DS-HMSN, monodisperse hollow silica nanoparticles with double-layered structure in the shell were obtained (Figure 4.7a). However, aggregation of some isolated and irregular silica nanoparticles with the hollow silica nanospheres (Figure 4.7b) indicated that the

silicate species formed from the dissolution of  $s\text{SiO}_2$  spheres cannot fully condense on the surface of undissolved  $s\text{SiO}_2$  nanoparticles in the presence of surfactant. But the nitrogen physisorption analysis revealed that silica material obtained possessed a hierarchical pore structure with pore sizes of 3.7 and 6.9 nm, corresponding to the inner and outer layers of the shell, respectively. These results imply that F127 acts as the dispersing but not pore expanding agent, by (a) surrounding the nanoparticles via hydrogen bonding, (b) inhibiting the random aggregation and deposition of nanoparticles, and (c) enhancing the controlled directional condensation of silicate onto the surface of undissolved  $s\text{SiO}_2$  spheres.<sup>31-33</sup> In the absence of DMHA in the preparation solution, monodisperse HMSNs with uniform particle size of 328 nm and shell thickness of 55 nm were obtained, as confirmed by TEM (Figure 4.8a). Any double-layered shell structure could not be detected in these HMSNs with both radially and perpendicularly aligned mesochannels (Figure 4.8b). In contrast, some yolk-shell structured silica spheres were observed, implying that the  $s\text{SiO}_2$  spheres were not completely transformed into hollow mesoporous silica spheres. For such HMSNs, the PXRD pattern shows as well one broad diffraction peak at a  $2\theta$  angle of  $2.0^\circ$  with  $d$  value of 4.3 nm (Figure 4.8c). Compared to HS-DS-HMSNs, the diffraction peak slightly shifted to higher  $2\theta$  angle, implying that HMSNs prepared in the absence of DMHA has a smaller pore size. Nitrogen physisorption analysis revealed a type IV isotherm with a type H4 hysteresis loop (Figure 4.8d) and a pore diameter of about 3.0 nm. Therefore, the presence of DMHA contributes to the complete transformation of  $s\text{SiO}_2$  into a hollow structure as well as the formation of double-shelled hierarchical mesostructures with large pore sizes.

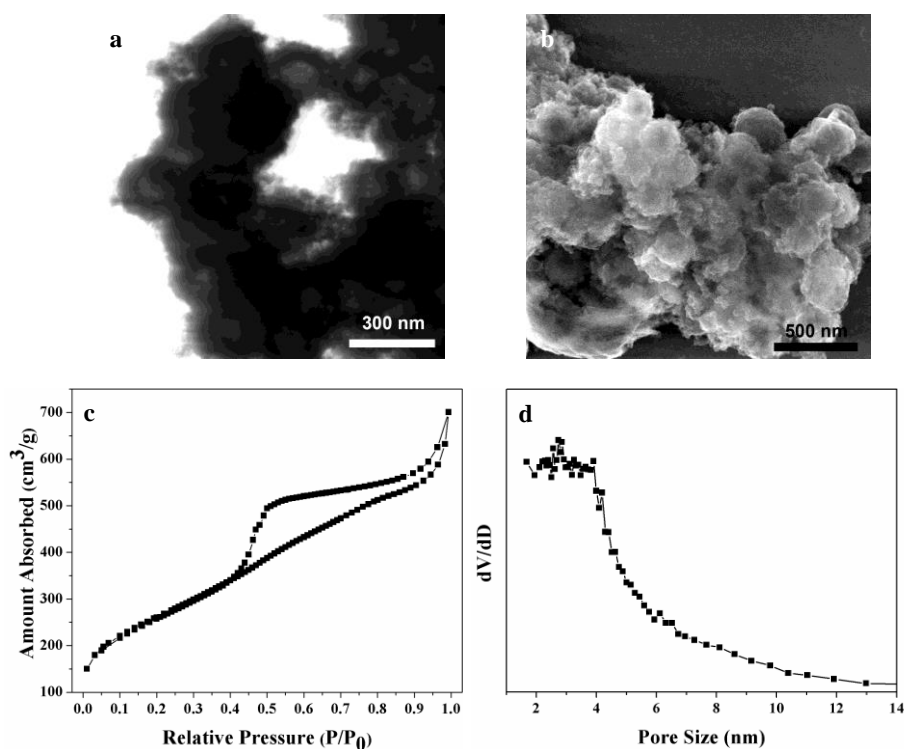


**Figure 4.6** (a) TEM, (b) SEM, (c) nitrogen physisorption isotherm and (d) the corresponding pore size distribution of material prepared in the absence of F127.

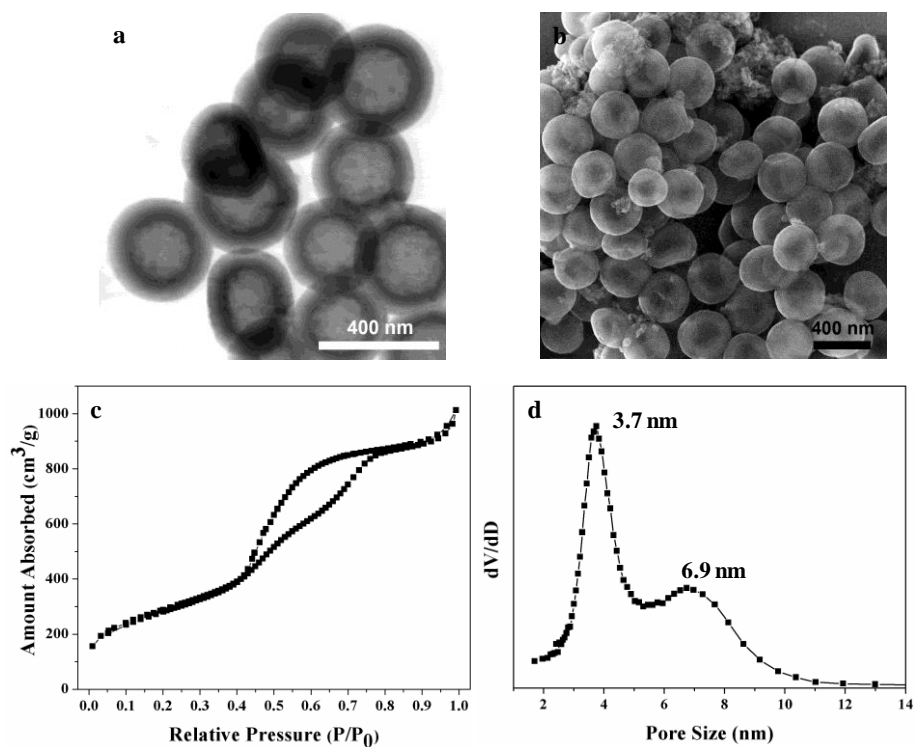


**Figure 4.7** (a) TEM, (b) SEM, (c) nitrogen physisorption isotherm and (d) the corresponding pore size distribution of material prepared in the presence of F127 (0.02 g).

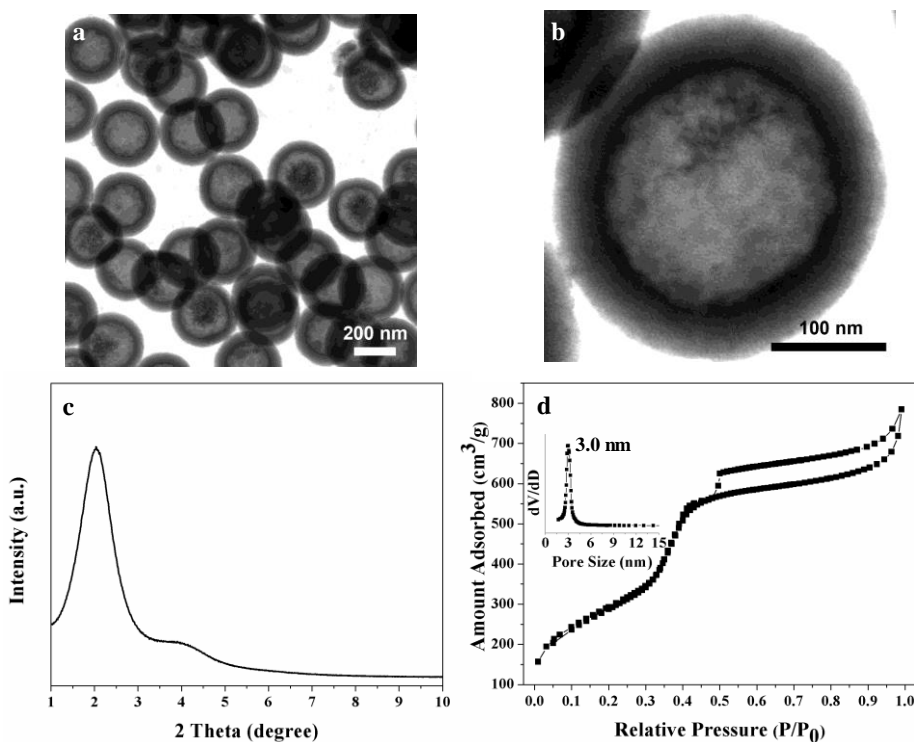


**Figure 4.8** (a, b) TEM images with different magnifications, (c) PXRD pattern and (d) nitrogen physisorption isotherm of material prepared in the absence of DMHA, the inset in (d) is the corresponding pore size distribution.

To understand the formation mechanism of such HS-DS-HMSN more comprehensively, the role of surfactant CTAB has to be elaborated. It is well known that the formation of CTAB



micelles only occurs in the range of concentration higher than its critical micelle concentration of about 0.8-1.1 mM at ambient temperature.<sup>34</sup> Driven by hydrophobic interactions, the neutral DMHA molecules with long hydrocarbon chain spontaneously assemble with CTAB molecules in a parallel manner with respectively opposite head groups.<sup>31,35,36</sup> To shed more light on how DMHA does influence the packing structure of CTAB micelles, three solutions of same amounts of CTAB, H<sub>2</sub>O and Na<sub>2</sub>CO<sub>3</sub> with different amounts of DMHA were prepared and analysed by DLS and zeta potential measurements. The DLS profiles showed that the hydrodynamic size of the CTAB micelle is 3.6 nm in the absence of DMHA, but was enlarged to 6.5 and 8.7 nm by adding 0.05 and 0.1 mL of DMHA into the solution, respectively (Figure 4.9). This verified that the expansion of CTAB micelles is caused by incorporating DMHA into the original CTAB micelles to form dynamically stable DMHA-CTAB assemblies. These results are in good agreement with the pore size of HS-DS-HMSN prepared by a similar micellar system. Moreover, the zeta potential value of the micelles increased from +25 to +27 mV and finally to +30 mV with gradually increasing the amount of DMHA in the solution (from 0 to 0.05 and 0.10 mL). This directly reflects that the incorporation of increasing amounts of DMHA into the CTAB micelles enables more CTAB molecules to enter the DMHA-CTAB micelle system giving rise to new stable DMHA-CTAB micelles of increased positive charge and larger size.

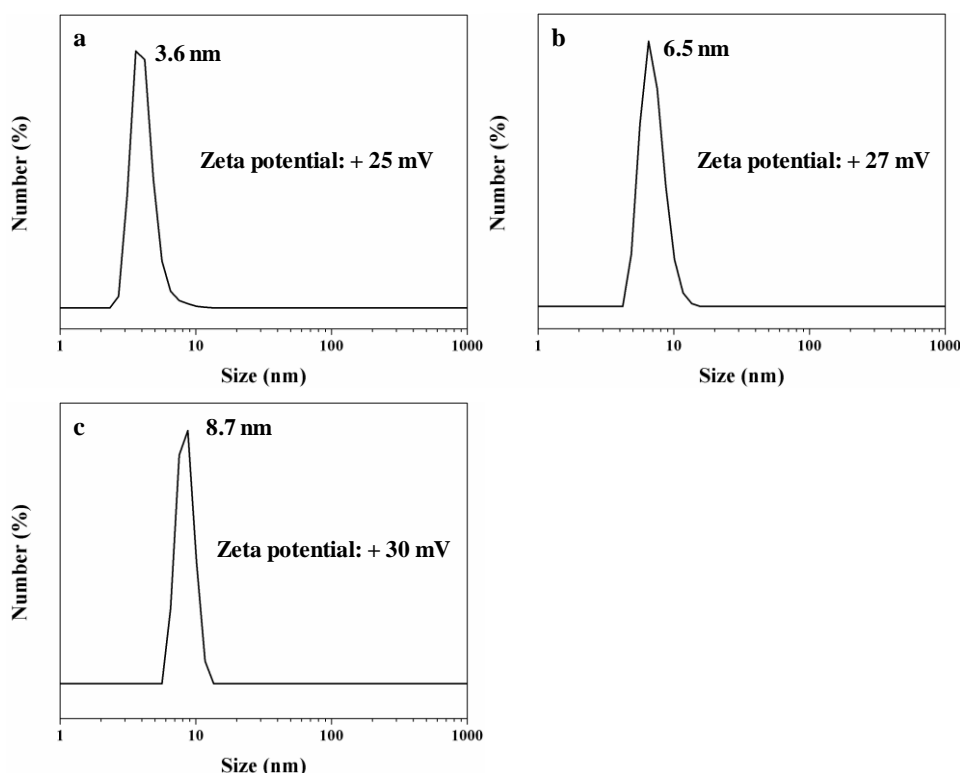


**Figure 4.9** The changes of hydrodynamic size and zeta potential of CTAB micelles along with the increase of DMHA amount. The solutions contain 0.1 g of CTAB, 80 mL of H<sub>2</sub>O, 2.5 g of Na<sub>2</sub>CO<sub>3</sub> and different amount of DMHA: (a) 0 mL, (b) 0.05 mL and (c) 0.1 mL.

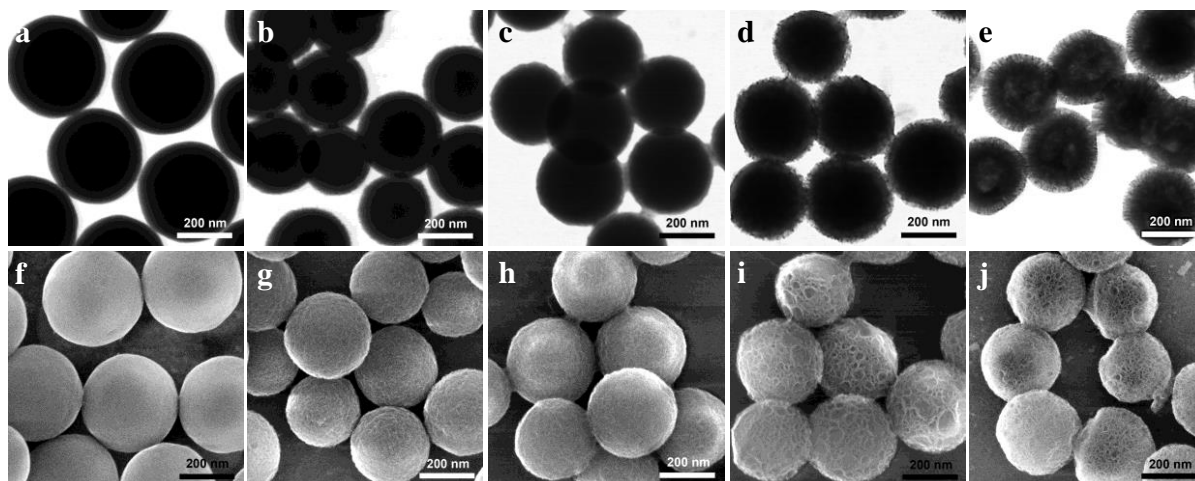


**Figure 4.10** (a-e) TEM and (f-j) SEM images of samples HS-DS-HMSN collected at reaction time (a, f) 1 h, (b, g) 6 h, (c, h) 8 h (d, i) 12 h, and (e, j) 18 h.

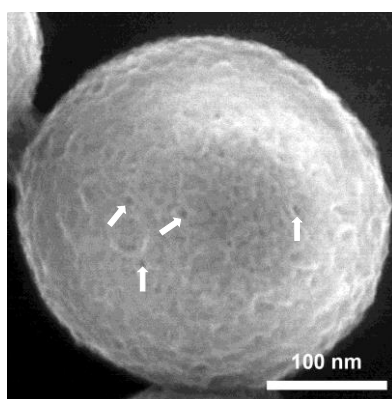


**Figure 4.11** SEM image of a single nanoparticle from the sample withdrawn at 8 h of HS-DS-HMSNs preparation. The white arrows indicate the mesopores with large pore size.

The structure and morphology evolutions of  $s\text{SiO}_2$  into HS-DS-HMSN were monitored by TEM and SEM (Figure 4.10). The size of  $s\text{SiO}_2$  slightly decreased to 357 nm after reacting for 1 h but the spherical morphology and smooth surface were still preserved (Figure 4.10a and f), suggesting that surface fragments of  $s\text{SiO}_2$  started to dissolve in a basic environment. After 6 h, the particle size decreased to 307 nm and the surface became relatively rough (Figure 4.10b and g), implying the formation of different surface structure in the presence of CTAB and DMHA under basic conditions. Note that the formation of core-shell nanoparticles was observed only after a reaction period of 8 h, accomplishing a core size and shell thickness of 285 and 15 nm, respectively (Figure 4.10c and h). At the same time, surface cavity size of about 7.4 nm could be detected on the surface of the core-shell nanoparticles (Figure 4.11), indicating the initial growth of an outer shell with large pores. When the reaction proceeded for 12, 18 and 24 h, the average particle size was 320, 321 and 324 nm, respectively, and the corresponding shell thickness was 35 nm (single shell), 35/38 nm (outer/inner shell) and 35/41 nm (outer/inner shell) (Figure 4.10d, e and Figure 4.1c). Note that the solid core became smaller and smaller over time until complete disappearance, while the formation of the surface

structure of the resultant HS-DS-HMSN also experienced an evolution process from originally smooth (1 h, Figure 4.10f) to very coarse (12 h, Figure 4.10i), to slightly coarse (18 h, Figure 4.10j), and finally to a smooth surface (24 h, Figure 4.10e). More interestingly, once the thickness of the outer shell reached 35 nm, no further remarkable changes were observed for the particle size and the thickness of the outer shell with prolonged reaction time. This implies that the continuous dissolution of the core simultaneously formed a gradually thickened inner shell on the inside wall of the outer shell until the complete disappearance of the core and the formation of a perfectly hollow double-shelled mesoporous silica nanosphere. Overall, this finding directly confirms that the DMHA-CTAB micelles can diffuse into the maximum depth of the  $s\text{SiO}_2$  via dissolution and that small mesopore arrays are formed in the inner shell by self-assembly of CTAB and silicate species generated by the dissolution of the solid silica core.

Based on the above-mentioned results and discussion, a plausible formation mechanism of HS-DS-HMSNs is proposed as follows. Addition of  $\text{Na}_2\text{CO}_3$  into a mixed suspension of  $s\text{SiO}_2$ , CTAB, DMHA and  $\text{H}_2\text{O}$ , results in a pH value of 10 of the suspension. Under such basic conditions,  $s\text{SiO}_2$  can dissolve and convert into silicate species.<sup>16,37,38</sup> The gradual decrease of the average particle size during 1 to 6 h implied that the dissolution of the solid silica spheres started from the outmost layer and proceeded inwards evenly (Figure 4.10a and b). The produced silicate species simultaneously assembled with stable DMHA-CTAB micelles and deposited on the surface of  $s\text{SiO}_2$  via the heterogeneous nucleation process,<sup>39</sup> leading to the formation of the outer shell of HS-DS-HMSN. With the continuous dissolution of solid silica spheres and the formation of new mesoporous silica attached to the surface of  $s\text{SiO}_2$ , self-assembled DMHA-CTAB micelles in the confined space between the solid silica core and newly formed mesoporous silica shell became more and more difficult. When the diffusion of DMHA onto the surface of the solid silica core came to an halt, also the growth of the large-pore outer shell stopped. But dissolution of the solid silica core proceeded and the concentration of the silicate species located inside the outer shell gradually increased. These silicate species further assembled with CTAB micelles to form the inner shells with smaller pore size attached to the inside wall of the outer shell without any void between the inner and outer shell. This process lasted until the formation of a perfectly hollow cavity. In fact, during the process of outer shell formation, the silicate anions preferred to assemble with DMHA-CTAB micelles (due to their high positive charge (Figure 4.9)), forming larger pores that depend on the amount of DMHA used in the system (Figure 4.1b-d and Figure 4.3b). Hence, HS-DS-HMSNs possess two different pore sizes of about 3.7 and 8.0 nm attributable to the inner and outer shells, respectively. Therefore, it is plausible that HMSNs prepared in the absence of DMHA show a single pore size of 3.0 nm (vide supra, Figure 4.8). Moreover, shell formation consumes silicate species from the solution thus enforcing further dissolution of  $s\text{SiO}_2$ , which on the other hand further support the growth of a mesoporous shell. More significantly, no void between the core/shell and shell/shell is observed in the shell growth process. This result is opposite to that previously reported.<sup>16,37</sup> The dissolution of  $s\text{SiO}_2$  and the self-assembly and deposition of the

silicate-DMHA-CTAB composite occurs simultaneously with different rate, thereby leading to a final particle size which is equal to or less than that of parent  $s\text{SiO}_2$ . In fact, the release of silicate species by  $s\text{SiO}_2$  dissolution and the growth of the inner/outer shells are quite slow, and the growth of the shell with the preserved core-shell structure is a pseudomorphic transformation process.<sup>40,41</sup> In addition, the newly formed silicate-CTAB-DMHA composites deposit onto the inner surface of outer shell rather than the etched  $s\text{SiO}_2$  cores owing to the much lower curvature and interfacial energy of the outer shell.<sup>42</sup> In summary, the dissolution of solid silica spheres under basic conditions and formation of HS-DS-HMSN-type materials is proposed to proceed via a co-surfactant-expanded micelle-assisted self-assembly process involving a heterogeneous nucleation deposition. The diffusion depth of DMHA and CTAB decides the thickness of inner and outer shell during the formation of HS-DS-HMSN-type materials.

Table 4.1 Structure properties of HS-DS-HMSN-x.

	$s\text{SiO}_2$ [g] <sup>a</sup>	DMHA /DMOA [mL] <sup>b</sup>	Particle Size [nm]	Cavity Size [nm]	Shell Thickness [nm]		$d_p$ [nm] <sup>c</sup>		$a_{\text{BET}}$ [m <sup>2</sup> g <sup>-1</sup> ] <sup>d</sup>	$V_p$ [cm <sup>3</sup> g <sup>-1</sup> ] <sup>e</sup>
					Inner Shell	Outer Shell	Inner Shell	Outer Shell		
<b>HS-DS-HMSN-1</b>	0.4	0.05	279	145	37	30	3.3	5.4	1128	1.50
<b>HS-DS-HMSNs</b>	0.4	0.1	324	171	41	35	3.7	8.0	1168	1.85
<b>HS-DS-HMSN-2</b>	0.4	0.3	364	226	33	36	3.7	8.0	1133	1.84
<b>HS-DS-HMSN-3</b>	0.4	0.1	162	82	20	20	3.4	5.3	1133	1.89
<b>HS-DS-HMSN-4</b>	0.4	0.061	262	152	18	37	3.1	3.7	1162	1.41

[a]  $s\text{SiO}_2$  with a particle size of 363 nm was used for the preparation of HS-DS-HMSN, HS-DS-HMSN-1, HS-DS-HMSN-2 and HS-DS-HMSN-4,  $s\text{SiO}_2$  with a particle size of 177 nm was used for the preparation of HS-DS-HMSN-3.

[b] DMHA was used for the preparation of HS-DS-HMSN, HS-DS-HMSN-1, HS-DS-HMSN-2 and HS-DS-HMSN-3, DMOA was used for the preparation of HS-DS-HMSN-4.

[c] Pore size from adsorption branch of the nitrogen physisorption isotherm.

[d] Specific BET surface area.

[e] Pore volume at relative pressure  $P/P_0 = 0.995$ .

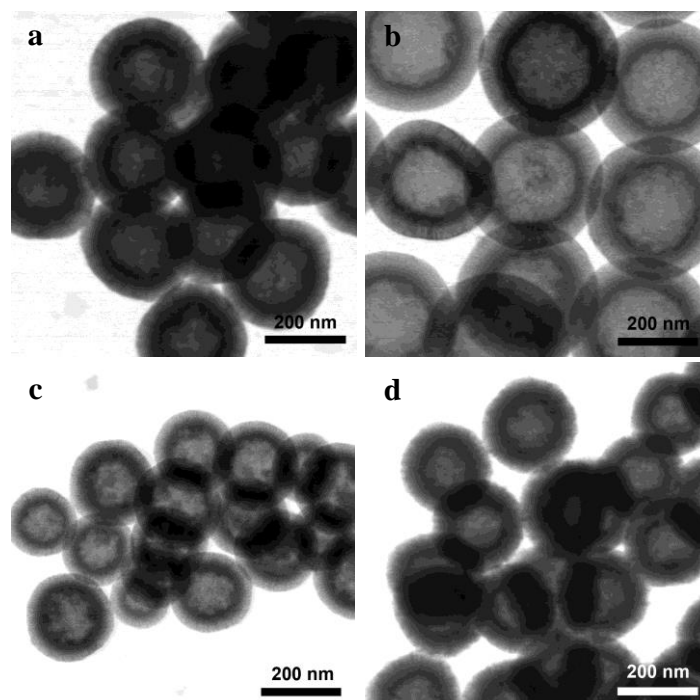


**Figure 4.12** TEM images of (a) HS-DS-HMSN-1, (b) HS-DS-HMSN-2, (c) HS-DS-HMSN-3, and (d) HS-DS-HMSN-4.

### 4.3.3 Control of HS-DS-HMSN Structural Properties

The aforementioned facile synthesis approach can be used to prepare a series of HS-DS-HMSN-*x* with controllable shell thickness and tunable pore/particle size (*x* represents the sample number. Table 4.1). HS-DS-HMSN-1 prepared in the presence of 0.05 mL of DMHA showed a particle size of 279 nm, thicknesses of the inner and outer shells of 37 and 30 nm and corresponding pore sizes of 3.3 and 5.4 nm, respectively (Figure 4.12a and Figure 4.13a). When 0.3 mL of DMHA were used, the resultant material HS-DS-HMSN-2 featured a particle size of 364 nm and inner and outer shell thicknesses of 33 and 36 nm, respectively (Figure 4.12b). The pore sizes in the double shell were 3.7 and 8.0 nm (Figure 4.13b). However, when the amount of DMHA was further increased, the materials obtained possessed similar nanoparticle size, inner and outer thicknesses with pore diameters similar to HS-DS-HMSN-2. These findings imply that the addition of DMHA tends to increase the particle size and outer shell thickness as well as the enlargement of the pore sizes in both shells. The expansion of the CTAB micelles relies on the amount of DMHA used. Although increasing amounts of DMHA can theoretically further expand the CTAB micelles, the formation of stable DMHA-CTAB micelles is a key for the fabrication of the mesopore structure. Hence the maximum pore size in the outer shell is hit at ca. 8.0 nm under the prevailing conditions. Moreover, the positively charged DMHA-CTAB micelles can readily assemble with silicate anions via strong electrostatic interactions and deposit on the surface of *s*SiO<sub>2</sub> as the large pore shell at an earlier *s*SiO<sub>2</sub> dissolution stage.

Increasing amounts of DMHA and its maximal diffusion depth enable the increase of the outer shell thickness and of the particle size. However, when *s*SiO<sub>2</sub> with an average size of 177 nm was used as silica source for the preparation of HS-DS-HMSN-3 (Figure 4.14), the obtained material showed an average size of 162 nm (Figure 4.12c), similar thickness of about 20 nm and pore sizes of 3.4 and 5.3 nm of the inner and outer shells, respectively (Figure 4.13c). If an equimolar amount of *N,N*-dimethyloctylamine (DMOA) instead of DMHA was employed, the resultant material HS-DS-HMSN-4 displayed a particle size and thicknesses of the inner/outer shell of 152 and 18/37 nm, respectively (Figure 4.12d). The corresponding pore sizes in the inner and outer shells were 3.1 and 3.7 nm (Figure 4.13d). The relatively small pore sizes are probably attributed to the shorter carbon chain length of DMOA assembling with CTAB to form DMOA-CTAB micelles with smaller size. All these investigations confirm that the particle size of HS-DS-HMSN-*x* mainly depends on the size of *s*SiO<sub>2</sub>, and that the thickness and pore size of the inner and outer shells rely on the amount and carbon chain length of co-surfactants such as DMHA or DMOA. All HS-DS-HMSN-*x* materials under study possess large surface areas ranging from 1128 to 1168 m<sup>2</sup> g<sup>-1</sup> and high pore volumes ranging from 1.41 to 1.89 cm<sup>3</sup> g<sup>-1</sup>. These adjustable structural properties will greatly extend the applications of HS-DS-HMSN-*x* materials in relevant fields.

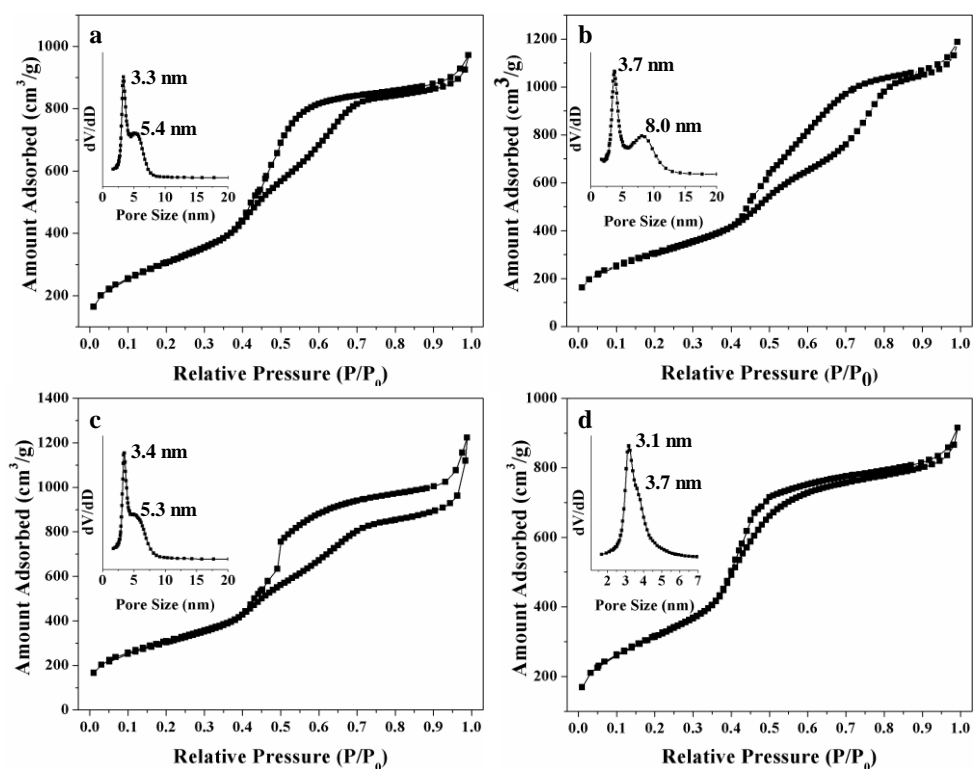


**Figure 4.13** Nitrogen physisorption isotherms and the corresponding pore size distributions of (a) HS-DS-HMSN-1, (b) HS-DS-HMSN-2, (c) HS-DS-HMSN-3, and (d) HS-DS-HMSN-4.

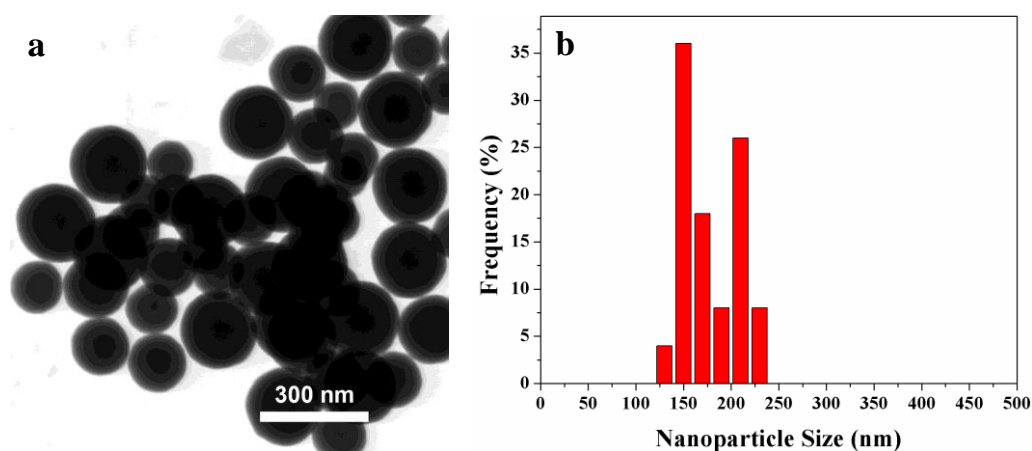


**Figure 4.14** (a) TEM image and (b) the particle size distribution of  $s\text{SiO}_2$  with average particle size of 177 nm.

#### 4.3.4 Myoglobin Adsorption onto HS-DS-HMSN

The adsorption of proteins from solution onto solid surfaces is of significance in terms of stability enhancement as well as ease of separation and recovery for reuse.<sup>43</sup> Mesoporous silicas are good host materials for protein adsorption.<sup>44,45</sup> However, long adsorption times and relatively low protein loadings are still major issues. By taking advantage of the uniform particle size, high surface area, large pore volume and perpendicularly aligned pore structure, the protein adsorption behaviors of HS-DS-HMSN and HS-DS-HMSN-*x* were investigated. Myoglobin (Mb) with the dimension of  $2.8 \times 3.2 \times 4.5$  nm and isoelectric point (IP) of 7.0 was used as a model protein.<sup>44,46</sup> The adsorption of Mb was carried out in a phosphate buffer

solution (pH 6.4), in which Mb molecules and the silica framework are positively and negatively charged, respectively. Driven by the strong electrostatic interactions, Mb molecules are drawn into the mesochannels of HS-DS-HMSN. The time-dependent adsorption amount curves are shown in Figure 4.15a. Remarkably, materials HS-DS-HMSN, HS-DS-HMSN-2, and HS-DS-HMSN-3 exhibit an unusual ultrafast adsorption rate and high loading capacities. In all three cases, the adsorption equilibria are reached after 120 min with Mb loadings of about 290 mg g<sup>-1</sup> (Table 4.2). These loading amounts are the highest reported so far.<sup>46-49</sup> For comparison, HS-DS-HMSN-1 and HS-DS-HMSN-4 show lower loadings of 193 and 205 mg g<sup>-1</sup>, respectively. Furthermore, HMSN with single shell (Figure 4.8) exhibits the lowest loading amount of 96 mg g<sup>-1</sup>, proving that the double shell is a crucial factor for gaining high loading.

To further investigate the adsorption behaviors, a pseudo-second-order model was adopted to analyze the adsorption process (Figure 4.15b). The adsorption equation is as follows

$$\frac{t}{q_t} = \frac{1}{\kappa q_e^2} + \frac{t}{q_e}$$

where  $\kappa$  is the equilibrium rate constant,  $q_e$  is the adsorption amount of Mb when equilibrium is reached, and  $q_t$  is the adsorption amount of Mb at time  $t$ . The correlation coefficient  $R^2$  (Table 4.2) indicates the adsorption behavior of each material fits the pseudo-second-order kinetic model very well.

Materials HS-DS-HMSN, HS-DS-HMSN-2, HS-DS-HMSN-3 and HMSN have comparatively larger  $\kappa$  values than those of HS-DS-HMSN-1 and HS-DS-HMSN-4, revealing much faster adsorption Mb rates.

For HS-DS-HMSN, the adsorption of Mb leads to a rapid decrease of the surface area (1168 → 177 m<sup>2</sup> g<sup>-1</sup>) and pore volume (1.85 → 0.31 cm<sup>3</sup> g<sup>-1</sup>) as well as drop in pore size below 2 nm (Figure 4.16), implying that Mb molecules have been adsorbed into both the cavity and the mesochannels of HS-DS-HMSN. Herein, the high immobilization amount of Mb is attributed to the large pore volume of HS-DS-HMSN (Table 4.1).

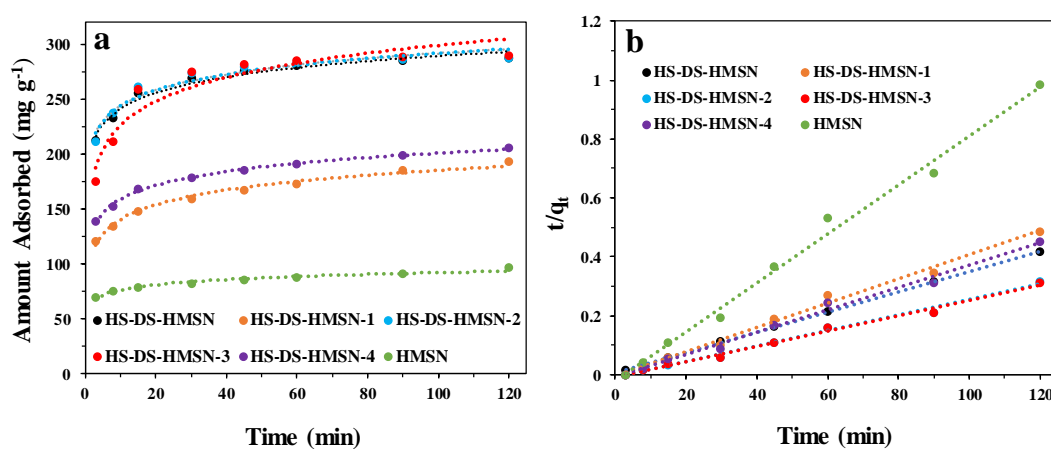


**Figure 4.15** (a) Mb adsorption amounts as a function of time on HS-DS-HMSN-type materials and HMSN, (b) linear fits of experimental data using pseudo-second-order kinetic model.

Table 4.2 Mb adsorption capacities and kinetic parameters on HS-DS-HMSN-x and HMSN<sup>a</sup>

	Mb Capacity [ $\text{mg g}^{-1}$ ]	$\kappa$ [ $\text{g mg}^{-1} \text{min}^{-1}$ ]	$R^2$
HS-DS-HMSN-1	193	0.00057	0.9974
HS-DS-HMSN	286	0.00136	0.9999
HS-DS-HMSN-2	287	0.00178	0.9999
HS-DS-HMSN-3	289	0.00163	0.9999
HS-DS-HMSN-4	205	0.00082	0.9987
HMSN	96	0.00155	0.9971

[a] Material HMSN with a single shell was prepared under the same conditions as used for HS-DS-HMSN, but without the addition of DMHA.

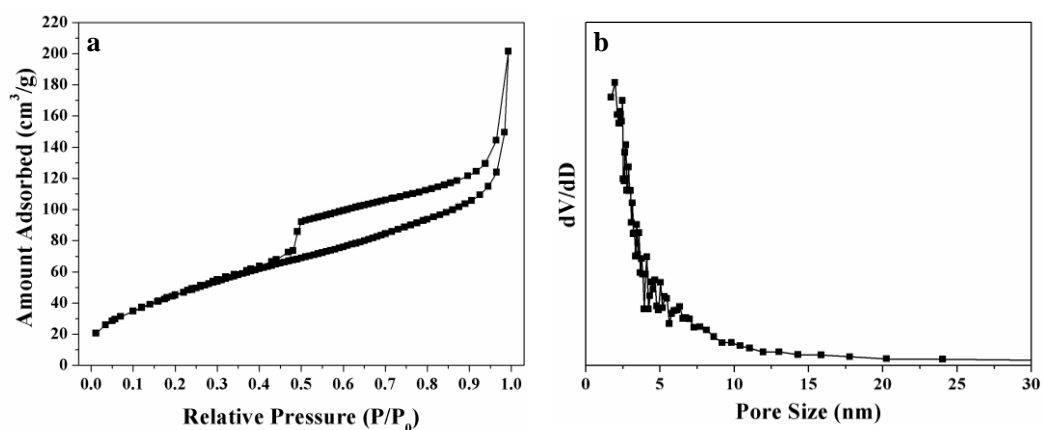


**Figure 4.16** (a) Nitrogen physisorption and (b) the corresponding pore size distribution of Mb loaded HS-DS-HMSNs.

Previous studies have shown that both the mesostructure and the morphology of mesoporous silica have significant impacts on protein adsorption.<sup>11,14,31,50,51</sup> Mesoporous silica with large pore size and high pore volume favor high loading amounts,<sup>14,50,51</sup> while small particle size and regular morphology of mesoporous silica are beneficial to fast adsorption.<sup>11,14,52</sup> In our case, the ultrafast adsorption rate can be rationalized as follows: (a) the uniform particle size and the radially aligned pore structure of HS-DS-HMSNs with large pore openings on the surface endow ready diffusion of Mb molecules into the hollow cavity, (b) the high monodispersibility of non-aggregated HS-DS-HMSNs in aqueous solution make the pore openings of each nanoparticle fully accessible to Mb molecules (Figure 4.5), (c) the short transport pathway for Mb molecules through the shell,<sup>11</sup> and (d) the template removal process via gentle solvent extraction rather than calcination ensures that most framework silanol groups are still preserved,<sup>53</sup> which provides a more hydrophilic and negatively charged pore wall for the adsorption of positively charged Mb molecules. For HS-DS-HMSN, HS-DS-HMSN-2 and HS-DS-HMSN-3, the shell pore sizes are significantly larger than the dimension of Mb, while their similar pore volumes ( $1.84\text{-}1.89 \text{ cm}^3 \text{ g}^{-1}$ ) and surface areas ( $1133\text{-}1162 \text{ m}^2 \text{ g}^{-1}$ ) contribute to very similar Mb adsorption features. Considering the similarly large pore sizes of HS-DS-HMSN-1 the lower Mb loading amount is attributed to the comparatively lower pore volume ( $1.50 \text{ cm}^3 \text{ g}^{-1}$ ). Since the pore sizes of HMSN the inner shell of HS-DS-HMSN-4 are less than the dimension of Mb, its adsorptions should experience a diffusion limitation and thus lead to



a lower adsorption amount. Regarding adsorption kinetics, the same pore sizes and similar particle sizes of HS-DS-HMSN and HS-DS-HMSN-2 give rise to similar adsorption rates (Table 2). However, the smaller pore sizes of HS-DS-HMSN-1 and HS-DS-HMSN-4 led to a limited Mb diffusion, and thus smaller rate constants. Although the pore sizes of HS-DS-HMSN-3 are similar to those of HS-DS-HMSN-1, the small particle size of HS-DS-HMSN-3 may contribute to the rapid adsorption. For mono-shell material HMSN, the pore size of 3.0 nm indicates that Mb molecules could be adsorbed only onto the outer surface of the nanoparticles, implying that the adsorption equilibrium is attained rapidly.

#### 4.4 Conclusions

In summary, we have successfully developed a facile approach to prepare hierarchically structured double-shelled hollow mesoporous silica nanoparticles by simply treating solid silica nanospheres with basic solution in the presences of CTAB, DMHA and F127. All HS-DS-HMSN-type materials obtained feature a high monodispersibility, uniform particle size, adjacent double shells with different pore sizes, large hollow cavity, high surface area and large pore volume. The particle/pore/cavity sizes and thicknesses of double shells can be easily modulated by adjusting co-surfactant amount and the size of solid silica spheres. Dissolution of solid silica spheres under basic condition and the co-surfactant-expanded micelle-assisted self-assembly process via a heterogeneous nucleation deposition is proposed to explain the formation of HS-DS-HMSN-type materials. The maximum of access of co-surfactant such as DMHA or DMOA formed the stable DMHA/DMOA-CTAB micelle decides the maximal thickness of outer shell with large pore and minimal thickness of inner shell in the case of complete disappearance of solid silica spheres. Owing to the structure advantages and high monodispersibility in aqueous solution, HS-DS-HMSN-type materials with large pore and large pore volume demonstrate ultrafast myoglobin adsorption speed with high loading amount. The facile preparation process and the distinct structure advantages provide HS-DS-HMSN-type materials with great application potentials in drug/gene delivery, bio-imaging, catalysis etc.

#### 4.5 References

1. X. Wang, J. Feng, Y. Bai, Q. Zhang and Y. Yin, *Chem. Rev.*, **2016**, 116, 10983-11060.
2. L. Yu, H. Hu, H. B. Wu and X. W. Lou, *Adv. Mater.*, **2017**, 29, 1604563.
3. G. Prieto, H. Tüysüz, N. Duyckaerts, J. Knossalla, G.-H. Wang and F. Schüth, *Chem. Rev.*, **2016**, 116, 14056-14119.
4. G.-H. Wang, J. Hilgert, F. H. Richter, F. Wang, H.-J. Bongard, B. Spliethoff, C. Weidenthaler and F. Schüth, *Nat. Mater.*, **2014**, 13, 293-300.
5. Y. Zhang, B. Y. W. Hsu, C. Ren, X. Li and J. Wang, *Chem. Soc. Rev.*, **2015**, 44, 315-335.
6. Y. Si, M. Chen and L. Wu, *Chem. Soc. Rev.*, **2016**, 45, 690-714.
7. Q. Zhang, W. Wang, J. Goebel and Y. Yin, *Nano Today*, **2009**, 4, 494-507.
8. X. Du and J. He, *Nanoscale*, **2011**, 3, 3984-4002.
9. Y. Chen, H.-R. Chen and J.-L. Shi, *Acc. Chem. Res.*, **2014**, 47, 125-137.
10. X. Fang, X. Zhao, W. Fang, C. Chen and N. Zheng, *Nanoscale*, **2013**, 5, 2205-2218.

11. Y. Chen, H. Chen, L. Guo, Q. He, F. Chen, J. Zhou, J. Feng and J. Shi, *ACS Nano*, **2010**, 4, 529-539.
12. Y. Chen, C. Chu, Y. Zhou, Y. Ru, H. Chen, F. Chen, Q. He, Y. Zhang, L. Zhang and J. Shi, *Small*, **2011**, 7, 2935-2944.
13. H. Blas, M. Save, P. Pasetto, C. Boissière, C. Sanchez and B. Charleux, *Langmuir*, **2008**, 24, 13132-13137.
14. J. Liu, C. Li, Q. Yang, J. Yang and C. Li, *Langmuir*, **2007**, 23, 7255-7262.
15. Y. Zhang, Q. Yue, Y. Jiang, W. Luo, A. A. Elzatahry, A. Alghamdi, Y. Deng and D. Zhao, *CrystEngComm*, **2016**, 18, 4343-4348.
16. X. Fang, C. Chen, Z. Liu, P. Liu and N. Zheng, *Nanoscale*, **2011**, 3, 1632-1639.
17. X. Fang, Z. Liu, M.-F. Hsieh, M. Chen, P. Liu, C. Chen and N. Zheng, *ACS Nano*, **2012**, 6, 4434-4444.
18. C. C. Yec and H. C. Zeng, *ACS Nano*, **2014**, 8, 6407-6416.
19. Z. Teng, X. Su, Y. Zheng, J. Sun, G. Chen, C. Tian, J. Wang, H. Li, Y. Zhao and G. Lu, *Chem. Mater.*, **2013**, 25, 98-105.
20. D. P. Wang and H. C. Zeng, *Chem. Mater.*, **2011**, 23, 4886-4899.
21. H. Zhang, M. Yu, H. Song, O. Noonan, J. Zhang, Y. Yang, L. Zhou and C. Yu, *Chem. Mater.*, **2015**, 27, 6297-6304.
22. H. Song, Y. A. Nor, M. Yu, Y. Yang, J. Zhang, H. Zhang, C. Xu, N. Mitter and C. Yu, *J. Am. Chem. Soc.*, **2016**, 138, 6455-6462.
23. C.-C. Huang, W. Huang and C.-S. Yeh, *Biomaterials*, **2011**, 32, 556-564.
24. Y. Chen, H. Chen, M. Ma, F. Chen, L. Guo, L. Zhang and J. Shi, *J. Mater. Chem.*, **2011**, 21, 5290-5298.
25. J. Liu, S. B. Hartono, Y. G. Jin, Z. Li, G. Q. Lu and S. Z. Qiao, *J. Mater. Chem.*, **2010**, 20, 4595-4601.
26. Y. Yang, X. Liu, X. Li, J. Zhao, S. Bai, J. Liu and Q. Yang, *Angew. Chem. Int. Ed.*, **2012**, 51, 9164-9168.
27. W. Stöber, A. Fink and E. Bohn, *J. Colloid Interface Sci.*, **1968**, 26, 62-69.
28. K. Moeller, J. Kobler and T. Bein, *Adv. Funct. Mater.*, **2007**, 17, 605-612.
29. M. Thommes, *Chem. Ing. Tech.*, **2010**, 82, 1059-1073.
30. K. Morishige, M. Tateishi, F. Hirose and K. Aramaki, *Langmuir*, **2006**, 22, 9220-9224.
31. J. Gu, K. Huang, X. Zhu, Y. Li, J. Wei, W. Zhao, C. Liu and J. Shi, *J. Colloid Interface Sci.*, **2013**, 407, 236-242.
32. T.-W. Kim, P.-W. Chung and V. S. Y. Lin, *Chem. Mater.*, **2010**, 22, 5093-5104.
33. K. Suzuki, K. Ikari and H. Imai, *J. Am. Chem. Soc.*, **2004**, 126, 462-463.
34. M. A. Bahri, M. Hoebeke, A. Grammenos, L. Delanaye, N. Vandewalle and A. Seret, *Colloids Surf. A*, **2006**, 290, 206-212.
35. B. Xi, Y. C. Tan and H. C. Zeng, *Chem. Mater.*, **2016**, 28, 326-336.
36. A. Sayari, *Angew. Chem. Int. Ed.*, **2000**, 39, 2920-2922.
37. T. Zhang, J. Ge, Y. Hu, Q. Zhang, S. Aloni and Y. Yin, *Angew. Chem. Int. Ed.*, **2008**, 47, 5806-5811.
38. X. Li, T. Zhao, Y. Lu, P. Wang, A. M. El-Toni, F. Zhang and D. Zhao, *Adv. Mater.*, **2017**, 29, 1701652.
39. X. Y. Liu, *J. Chem. Phys.*, **2000**, 112, 9949-9955.
40. T. Martin, A. Galarneau, F. Di Renzo, F. Fajula and D. Plee, *Angew. Chem. Int. Ed.*, **2002**, 41, 2590-2592.
41. Q. Yu, J. Hui, P. Wang, B. Xu, J. Zhuang and X. Wang, *Nanoscale*, **2012**, 4, 7114-7120.
42. Z. Teng, S. Wang, X. Su, G. Chen, Y. Liu, Z. Luo, W. Luo, Y. Tang, H. Ju, D. Zhao and G. Lu, *Adv. Mater.*, **2014**, 26, 3741-3747.

- 
43. J. D. Andrade and V. Hlady, Protein adsorption and materials biocompatibility: A tutorial review and suggested hypotheses, Springer, Berlin, Heidelberg, 1986.
  44. S. Hudson, J. Cooney and E. Magner, *Angew. Chem. Int. Ed.*, **2008**, 47, 8582-8594.
  45. M. Hartmann, *Chem. Mater.*, **2005**, 17, 4577-4593.
  46. T. Itoh, R. Ishii, T. Ebina, T. Hanaoka, Y. Fukushima and F. Mizukami, *Bioconjug. Chem.*, **2006**, 17, 236-240.
  47. A. Katiyar, L. Ji, P. Smirniotis and N. G. Pinto, *J. Chromatogr. A*, **2005**, 1069, 119-126.
  48. W. Shui, J. Fan, P. Yang, C. Liu, J. Zhai, J. Lei, Yan, D. Zhao and X. Chen, *Anal. Chem.*, **2006**, 78, 4811-4819.
  49. H. H. P. Yiu, C. H. Botting, N. P. Botting and P. A. Wright, *Phys. Chem. Chem. Phys.*, **2001**, 3, 2983-2985.
  50. J. Zhang, S. Karmakar, M. Yu, N. Mitter, J. Zou and C. Yu, *Small*, **2014**, 10, 5068-5076.
  51. C. Xu, M. Yu, O. Noonan, J. Zhang, H. Song, H. Zhang, C. Lei, Y. Niu, X. Huang, Y. Yang and C. Yu, *Small*, **2015**, 11, 5949-5955.
  52. J. Sun, H. Zhang, R. Tian, D. Ma, X. Bao, D. S. Su and H. Zou, *Chem. Commun.*, **2006**, 1322-1324.
  53. X. Wang, Y. Zhang, W. Luo, A. A. Elzatahry, X. Cheng, A. Alghamdi, A. M. Abdullah, Y. Deng and D. Zhao, *Chem. Mater.*, **2016**, 28, 2356-2362.



## 5 Gold-loaded Mesoporous Organosilica-Silica Core-Shell Nanoparticles as Catalytic Nanoreactors

### 5.1 Introduction

Nanoreactors with tailor-made structures and compositions have shown superior performances in many catalytic reactions by accelerating the reaction kinetics, enhancing the selectivity, and improving the recycling of the catalysts.<sup>1,2</sup> Among them, core-shell nanoparticles of distinct compositions and pore structures were shown to be highly active and selective in many catalytic reactions.<sup>3</sup> Recently, substantial efforts have been devoted to the application of core-shell mesoporous silica nanoparticles (CSMSNs) in catalysis because of their intriguing properties.<sup>4-11</sup> Various monodisperse CSMSNs with catalytically active noble metal nanoparticles (MNPs) as the core and mesoporous silica (MS) as the shell have been successfully designed.<sup>6-8</sup> The mesoporous channels not only protect the active surface of the loaded MNPs and prevent from their aggregation, but also facilitate the easy access and diffusion of reactants and products. In general, the catalytic activity of noble MNPs strongly depends on the particle size and their stability, in particular, noble MNPs less than 5 nm in size show a high catalytic performance. Such small and stable noble MNPs were often carefully prepared by unconventional method, and their stability is ensured by stabilizers or supports. The mesochannels of ordered mesoporous silica can be an effective means for building a nanoreactor for catalytically active MNPs of controlled particle size and concomitant chemical/physical stabilization.<sup>12</sup> CSMSNs featuring distinct pore structures provide numerous sites in the core domain for the loading of catalytically active ultrasmall metal NPs, with the shell acting as protective physically-separated layer.<sup>9-11</sup> Overall, CSMSNs have emerged as promising functional support material for fabricating heterogeneous catalysts. For example, Pd-loaded porous carbon@MS core-shell NPs exhibited stable catalytic activity towards benzyl alcohol oxidation due to that the MS coating prevented the sintering and leaching of Pd NPs during the reaction.<sup>9</sup> A Pd-loaded MS-coated hydrophobic poly(ionic liquid) created a hydrophobic@hydrophilic hybrid core-shell structured nanoreactor demonstrating a good dispersibility in water. The specific enrichment of the hydrophobic substrates in the hydrophobic core made such core-shell NPs as efficient nanocatalysts in aqueous catalytic reactions.<sup>10</sup> Integrated nanocatalysts consisting of metal-loaded mesoporous silica NPs as the core and metal-organic framework (MOF) material ZIF-8 as the shell has served as molecule-selective reactors for controlled hydrogenation of alkenes and exclusion of cyclohexene.<sup>11</sup>

Despite enormous research endeavors, the fabrication and application of functional core-shell nanosystems displaying high catalytic efficiency has remained challenging. For MNPs, the particle size distribution and dispersity exert a vital influence on the catalytic performance. Therefore, it is of utmost importance to prevent the small-sized loaded MNPs from aggregation and leaching. Secondly, the modulated design of the shell configuration of the CSMSNs also

requires attentions. To tackle these two problems, herein, we targeted the synthesis of a heterogenous catalyst composed of a hierarchically structured thiol group-functionalized mesoporous organosilica core which is encapsulated by mesoporous silica shell nanoparticles (SH-MON@MS) and loaded with small-sized Au nanoparticles. The SH-MON@MS core-shell nanoparticles were prepared via a two-step approach, in which the thiol group-functionalized mesoporous organosilica nanoparticles (SH-MONs) were first synthesized via a surfactant-assisted sol-gel process, followed by their encapsulation with as mesoporous silica shell utilizing a *n*-hexane-induced controlled hydrolysis and assembly process. The resultant SH-MON@MS featured a hierarchical pore structures with pore sizes of 1.5 and 5.0 nm in the core and shell, respectively. Furthermore, the thiol group-functionalized core enables the exclusively loading of Au nanoparticles in the core domain. Thus obtained Au/SH-MON@MS features the following advantages: i) a mesoporous silica shell with large pore size (5.0 nm) minimizing the diffusion limitations of reactant and product molecules;<sup>13</sup> ii) the organic moieties of the mesoporous organosilica core framework provides a hydrophobic microenvironment beneficial to the enrichment of organic substrates; iii) ultrasmall Au NPs stabilized by the thiol groups in the mesochannels ensure efficient catalytic conversions. By taking advantages of such a hierarchical structure and distinct composition, the catalytic activities of Au/SH-MON@MS in the reduction of 4-nitrophenol with NaBH<sub>4</sub> to 4-aminophenol and the aerobic oxidation of benzyl alcohol to benzaldehyde were investigated in detail.

## 5.2 Experimental Section

### 5.2.1 Chemicals

All chemicals were used as received: ethanol (EtOH, 99.9 %, Sigma-Aldrich), tetraethyl orthosilicate (TEOS,  $\geq 99$  %, Sigma-Aldrich), ammonium hydroxide solution (NH<sub>3</sub>·H<sub>2</sub>O, 25 wt%, Sigma-Aldrich), hexadecyltrimethylammonium bromide (CTAB,  $\geq 98$ %, Sigma-Aldrich), hydrochloric acid (HCl,  $\geq 37$ %, Sigma-Aldrich), methanol (MeOH,  $\geq 99.9$ %, Sigma-Aldrich), benzyl alcohol ( $\geq 99$ %, Sigma-Aldrich), tetrachloroauric acid (HAuCl<sub>4</sub>, Sigma-Aldrich), *n*-hexane (95 %, Fisher Chemical), toluene (HPLC grade, Fisher Chemical), (3-mercaptopropyl)trimethoxysilane (MPTMS, 95 %, Alfa Aesar), potassium carbonate (K<sub>2</sub>CO<sub>3</sub>, 99 %, Alfa Aesar), bis(triethoxysilyl)ethane (BTEE, 97 %, ABCR), sodium borohydride (NaBH<sub>4</sub>, 96 %, AppliChem), 4-nitrophenol (4-NP, 99 %, TCI), and naphthalene (analytical standard, Sigma-Aldrich). Deionized water was used in all the experiments.

### 5.2.2 Synthesis of Thiol Group-Functionalized Mesoporous Organosilica Nanoparticles (SH-MONs)

SH-MONs were synthesized via a surfactant-assisted sol-gel co-condensation process. A mixture of EtOH (40 mL), H<sub>2</sub>O (150 mL), 25 wt% NH<sub>3</sub>·H<sub>2</sub>O (2 mL), and CTAB (0.25 g) was stirred at ambient temperature for 45 min to form a clear solution. The pre-mixed BTEE (0.6

mL) and MPTMS (0.2 mL) were then added under stirring. After being further stirred for 24 h, SH-MONs were separated by centrifugation and washed with EtOH twice. The organic template was removed by refluxing the as-synthesized nanoparticles suspended in a mixture of EtOH (160 mL) and 37% HCl (4 mL) at 75 °C for 3 h, then the solid was collected by centrifugation. This process was repeated for 5 times in order to completely remove the template. The resulting template-free SH-MONs were dried at ambient temperature overnight in a vacuum oven. Elemental analysis (wt %) for SH-MONs: N 0.16, C 23.50, H 6.19, S 4.25.

### 5.2.3 Synthesis of Core-Shell-Structured SH-MON@MS Nanoparticles

As-synthesized SH-MONs suspended in 60 mL of methanol solution were added into a clear solution of H<sub>2</sub>O (240 mL), CTAB (2.0 g) and 25 wt% NH<sub>3</sub>·H<sub>2</sub>O (0.4 mL). After being sonicated for 1 h and vigorously stirred at 70 °C for 1 h, a solution of pre-mixed *n*-hexane (40 mL) and TEOS (1.5 mL) was added to form a biphasic reaction system, which was gently stirred at 70 °C for 24 h to prepare the core-shell-structured nanoparticles. Then diluted HCl solution (0.1 M) was added to the reaction system to adjust the pH value to 7.0. After being stirred at the same temperature for further 24 h, the core-shell-structured nanoparticles were centrifuged and washed with EtOH twice. The organic template and *n*-hexane were removed by using same method as for aforementioned SH-MONs. The resultant template-free core-shell-structured SH-MON@MS nanoparticles were dried at ambient temperature overnight in a vacuum oven. Elemental analysis (wt %) for SH-MON@MS: N 0.17, C 12.65, H 2.87, S 3.76.

### 5.2.4 Synthesis of Au-loaded SH-MON@MS

To specifically load Au nanoparticles into the core of SH-MON@MS core-shell nanoparticles, SH-MON@MS (0.1 g) was first suspended in EtOH (100 mL) by sonication for 30 min. An HAuCl<sub>4</sub> solution (7 mL, 1 mM) was then added and the mixture stirred at ambient temperature for 6 h. The Au(III) ions-loaded SH-MON@MS core-shell nanoparticles were separated by centrifugation, and washed with EtOH three times to completely wash out all free Au(III) ions, then the solid was resuspended in EtOH (50 mL). A freshly prepared NaBH<sub>4</sub>-EtOH solution (15 mL, 0.267 mg/mL) was added and the suspension was stirred at ambient temperature for 18 h. The Au-loaded SH-MON@MS (Au/SH-MON@MS) nanoparticles were finally centrifuged and washed with H<sub>2</sub>O once, followed by EtOH once, then dried at ambient temperature overnight in a vacuum oven. The calculated Au loading is 1.38 wt%. Elemental analysis (wt%) for Au/SH-MON@MS: N 0.15, C 11.55, H 3.04, S 3.06.

### 5.2.5 Catalytic Reduction of 4-Nitrophenol

The catalytic activity of Au/SH-MON@MS in aqueous solution was investigated using the reduction of 4-nitrophenol (4-NP) with NaBH<sub>4</sub> to 4-aminophenol (4-AP) as a model reaction. Au/SH-MON@MS (0.2 mg) was suspended in H<sub>2</sub>O (2.5 mL) in a cuvette by sonication for 1 min. A 4-NP aqueous solution (100 μL, 5 mM) was added. The reaction was initiated by adding

a freshly prepared NaBH<sub>4</sub> aqueous solution (200  $\mu$ L, 200 mM) into the mixture. The reaction progress was monitored by measuring the UV-Vis spectra as a function of the reaction time.

### 5.2.6 Catalytic Aerobic Oxidation of Benzyl Alcohol

The catalytic activity of Au/SH-MON@MS was further demonstrated by the aerobic oxidation of benzyl alcohol to benzaldehyde. Au/SH-MON@MS (60 mg) and K<sub>2</sub>CO<sub>3</sub> (66 mg) were added to a mixture of toluene (5 mL) and benzyl alcohol (0.05 mL). The mixture was sonicated for 1 min and then refluxed at 90 °C for 12 h. Then, a minor amount of the suspension was withdrawn and centrifuged. The clear supernatant was analysed by gas chromatography (GC) using naphthalene as an internal standard to determine the conversion and selectivity. The used nanocatalyst was collected by centrifugation and washed with H<sub>2</sub>O and EtOH several times and dried at ambient temperature overnight in a vacuum oven before reusing it in the next catalytic run.

### 5.2.7 Characterization

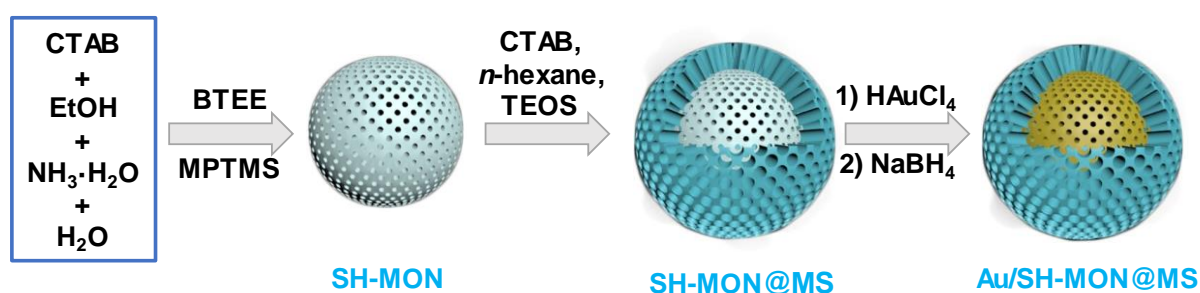
Nitrogen physisorption analysis was carried out on a Micrometrics ASAP 2020 volumetric adsorption apparatus at 77.4 K. The sample was degassed at 150 °C for 6 h under a pressure < 5  $\mu$ mHg vacuum prior to the measurement. The specific surface area was calculated by the *Brunauer-Emmett-Teller* (BET) method. The pore volume was calculated from the total nitrogen adsorption amount at  $P/P_0 = 0.995$ . The pore size distribution was obtained from the adsorption branch of the isotherm by the *Barret-Joyner-Haldenda* (BJH) method. The low and wide angle powder X-ray diffraction (PXRD) patterns were obtained on a Bruker D8 Advance Diffractometer using monochromatic CuK $\alpha$  radiation ( $\lambda = 1.5406 \text{ \AA}$ ) in the step/scan mode with the step width of 0.00825 and accumulation time of 2 s/step in the  $2\theta$  range of 0.5-10.0° and 10-90°, respectively. Scanning/transmission electron microscope (S/TEM) images were gained with a Hitachi SU 8030 microscope operated at an acceleration voltage of 30 kV. A finely powdered sample was dispersed in ethanol by sonication, and one drop of such suspension was loaded onto the copper grid covered with holey carbon film. <sup>29</sup>Si and <sup>13</sup>C CP MAS NMR spectra were recorded at ambient temperature on a Bruker ASX300 instrument equipped with MAS hardware and using a ZrO<sub>2</sub> rotor with an inside diameter of 7 mm. UV-Vis spectra were obtained with a T60 UV-Vis spectrophotometer (PG Instruments). Gas chromatography (GC) analysis was conducted in a Perkin Elmer Clarus 580 gas chromatograph equipped with a 30 m Velocity Wax capillary column.

## 5.3 Results and Discussion

As shown in Scheme 1, the core-shell structured Au/SH-MON@MS were successfully synthesized applying a 3-step procedure. The thiol group-functionalized mesoporous organosilica NP (SH-MONs) core was first fabricated via a surfactant-assisted sol-gel co-condensation process by adding a BTEE/MPTMS mixture into a solution of CTAB, EtOH, NH<sub>3</sub>·H<sub>2</sub>O and H<sub>2</sub>O. Subsequent separation of the SH-MONs ensures that any organosilicate



and SH-contained silicate species in the mother solution cannot be incorporated into the shell structure during the second step, meaning that the functional thiol groups (-SH) do exist only in the core. The as-synthesized SH-MONs were then re-suspended in a CTAB-MeOH-H<sub>2</sub>O solution for the further growth of a MS shell. In the shell formation process, a biphasic reaction system was used, in which TEOS dissolved in *n*-hexane was used as the oil phase. After an *n*-hexane-induced controlled hydrolysis and condensation process of TEOS, the formed silicate species or silicate oligomer is proposed to self-assemble on the surface of SH-MON via a surfactant-assisted heterogeneous nucleation process, thus generating the core-shell structured SH-MON@MS NPs with SH-MON as the core and MS as the shell. Finally, the loading with Au nanoparticles was conducted by treating SH-MON@MS with a HAuCl<sub>4</sub> solution, followed by reduction with NaBH<sub>4</sub> to afford Au/SH-MON@MS NPs.



**Scheme 5.1** Schematic illustration of the preparation process of Au/SH-MON@MS.

TEM and SEM images revealed that SH-MONs have a spherical morphology with a slightly rough surface and quite uniform particle size (Figure 5.1a and b). The average particle size from the TEM images was determined by measuring 50 random particles and calculated to be  $98 \pm 1.8$  nm (Figure 5.2). After coating with the mesoporous silica shell, the core-shell structure of SH-MON@MS NPs was confirmed by TEM (Figure 5.1c). The average particle size increased to  $128 \pm 2.0$  nm with a core size of  $97 \pm 1.9$  nm and shell thickness of  $15 \pm 0.1$  nm (Figure 5.3). Moreover, the SH-MON@MS exhibited the characteristic spheres with a slightly coarse surface (Figure 5.1d). For SH-MON NPs, the nitrogen physisorption analysis revealed a type IV isotherm with two capillary condensation steps at  $P/P_0 = 0.1-0.2$  and  $0.9-1.0$ , corresponding to a pore size of ca. 1.5 nm and the interparticle voids, respectively (Figure 5.4). The *BET* specific surface area and pore volume were  $1104 \text{ m}^2 \text{ g}^{-1}$  and  $1.14 \text{ cm}^3 \text{ g}^{-1}$ , respectively. Compared to SH-MON, the nitrogen physisorption isotherm of SH-MON@MS shows an additional capillary condensation at  $P/P_0 = 0.45-0.70$ , which corresponds to larger pores of 5.0 nm in the shell (Figure 5.4 and inset). In addition, large pore arrays of the core-shell structured SH-MON@MS were easily observed from S/TEM images in Figure 5.1c and d, confirming the formation of large mesopores in the shell layer. The mesoporous organosilica core framework was not affected during the formation of MS shell layer, which was corroborated by the almost identical core size and the pore diameter of core of SH-MON@MS (1.5 nm) compared to that of SH-MONs. However, for SH-MON@MS, the *BET* specific surface markedly decreased

( $840 \text{ m}^2 \text{ g}^{-1}$ ) while the pore volume slightly increased ( $1.18 \text{ cm}^3 \text{ g}^{-1}$ ), which is in good agreement with the formation of a large pore structure in the shell layer. Note that the PXRD patterns of SH-MONs and SH-MON@MS (Figure 5.5) clearly revealed a characteristic single-pore structure of the SH-MONs from one diffraction peak at  $2\theta = 2.5^\circ$  and a double-pore structure of SH-MON@MS from two diffraction peaks at  $2\theta = 1.7$  and  $2.5^\circ$  without long-range ordering of pore arrays. These characteristics are in good accordance with the results of core-shell structured materials recently reported.<sup>14,15,16</sup> The formation mechanism of such advanced materials with hierarchical pore structure is very similar to that reported by us.<sup>16</sup>

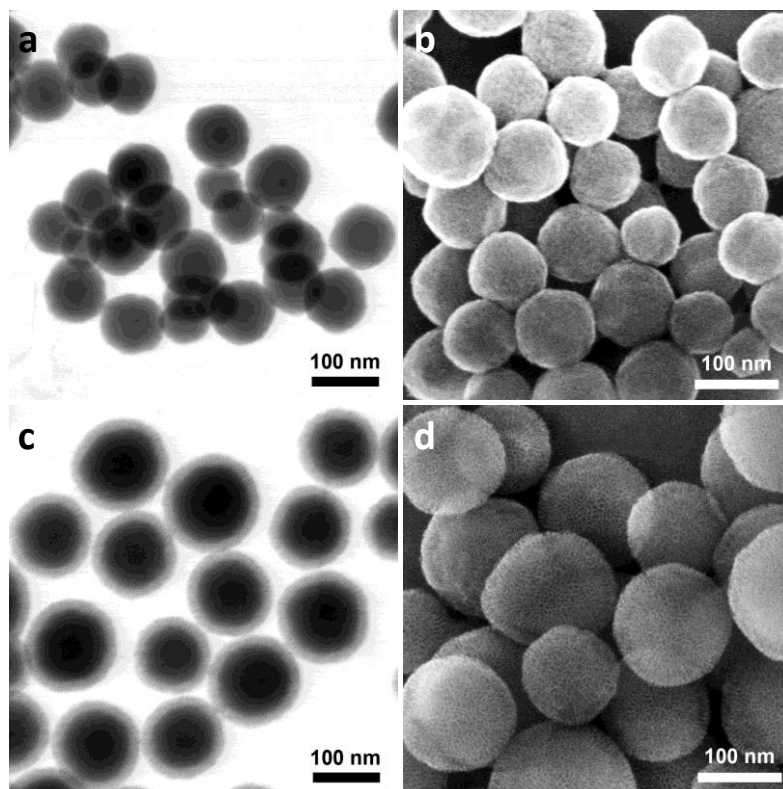


**Figure 5.1** TEM and SEM images of (a, b) SH-MON and (c, d) SH-MON@MS.

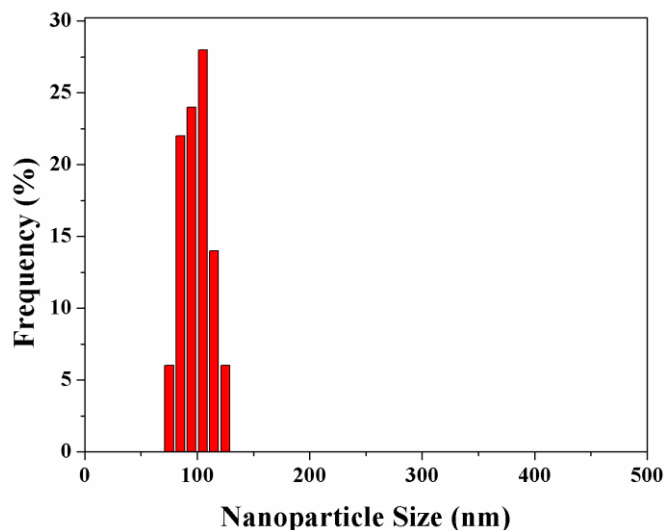


**Figure 5.2** Particle size distribution of SH-MON by measuring 50 random particles from the TEM images.

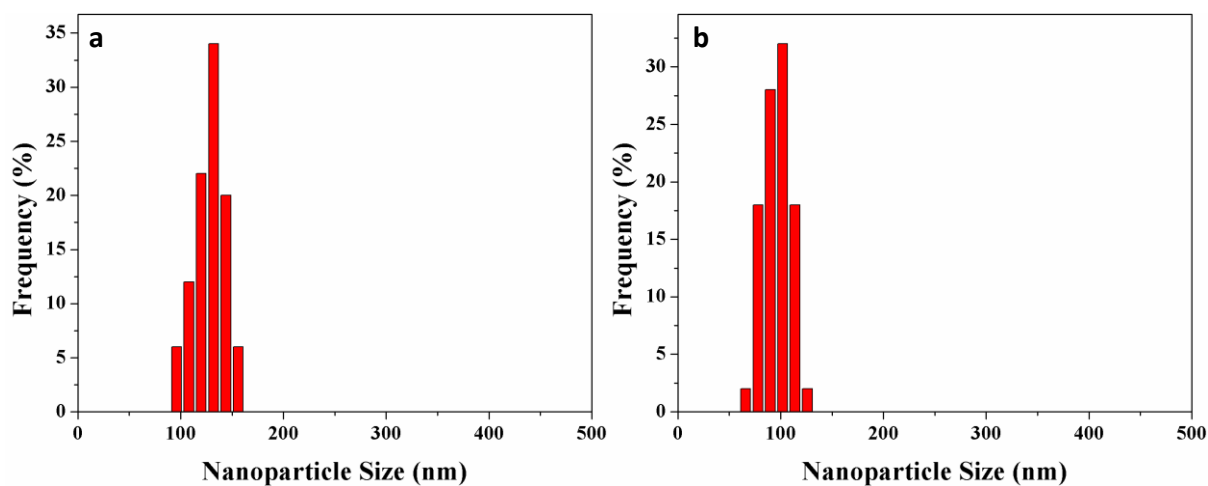


**Figure 5.3** (a) Overall particle size distribution and (b) the core size distribution of SH-MON@MS by measuring 50 random particles from the TEM images.

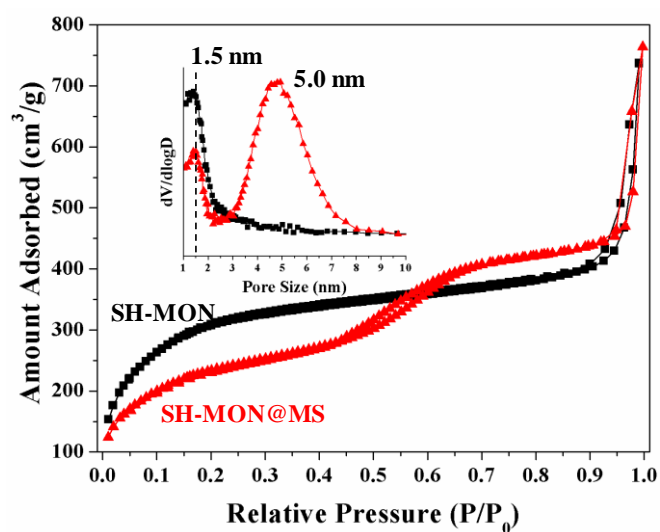


**Figure 5.4** Nitrogen physisorption isotherms of SH-MON and SH-MON@MS, the inset is the corresponding BJH pore size distribution.

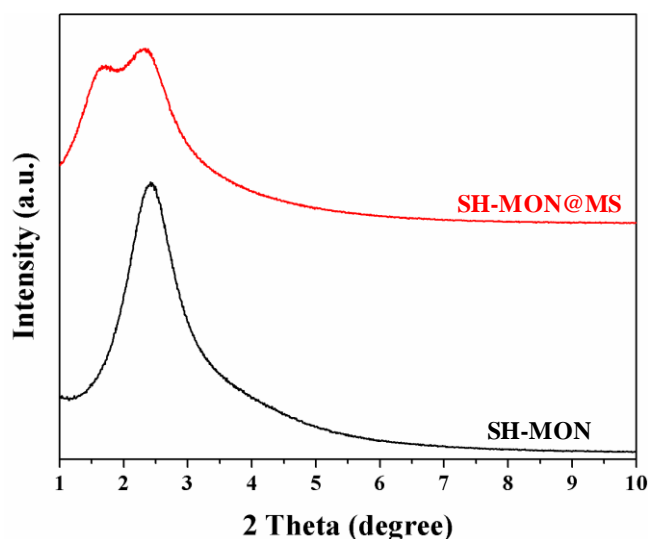


Figure 5.5 Low-angle PXRD patterns of SH-MON and SH-MON@MS.

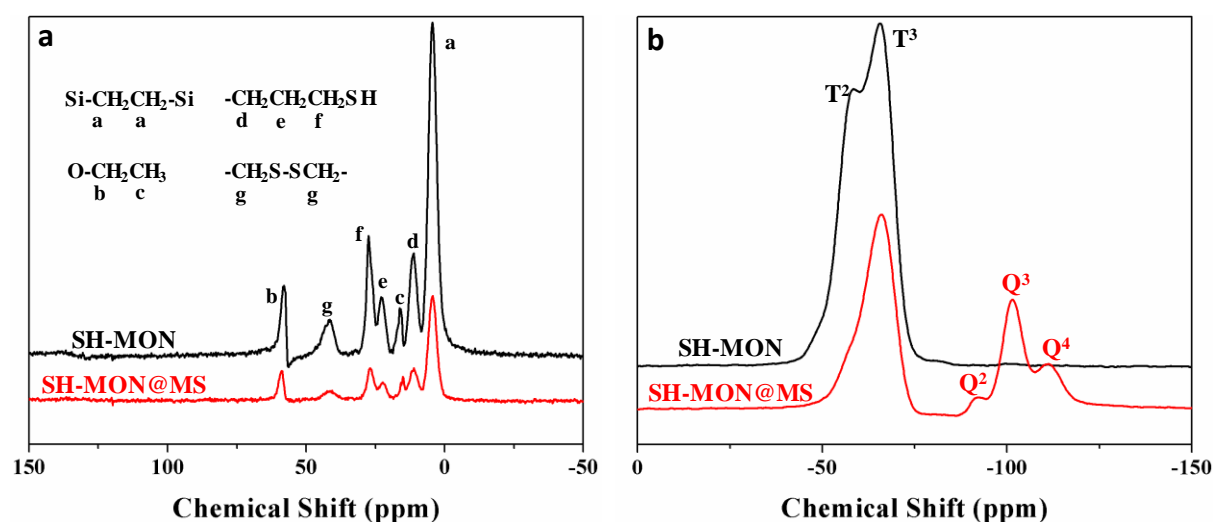
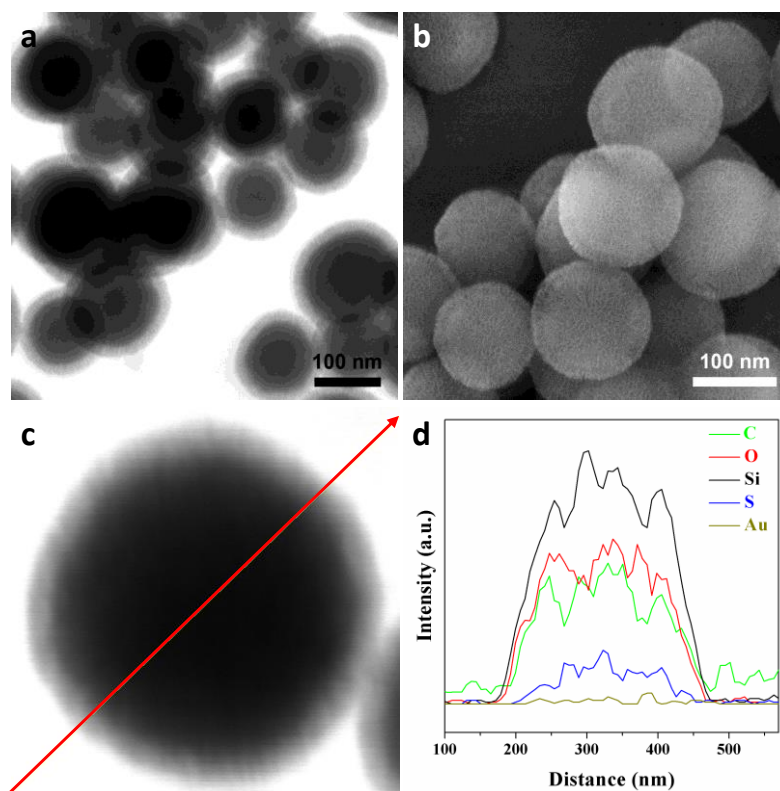


Figure 5.6 (a)  $^{13}\text{C}$  CP MAS NMR and (b)  $^{29}\text{Si}$  CP MAS NMR of SH-MON and SH-MON@MS.

The composition of the successfully synthesized SH-MONs and core-shell structured SH-MON@MS, was further confirmed by  $^{13}\text{C}$  and  $^{29}\text{Si}$  CP MAS NMR spectroscopy, as shown in Figure 5.6a and b. For both materials, carbon signals from the bridging ethylene groups ( $\delta = 4.5$  ppm), mercaptopropyl groups ( $\delta = 11, 23, 27$  ppm), and bis(propyl) disulfide groups ( $\delta = 41$  ppm) were detected, respectively, which are in good agreement with those reported previously.<sup>17,18,19</sup> The broad peak at  $\delta = 41$  ppm was attributed to the disulfide group formed under basic preparation conditions.<sup>17,18</sup> The peaks at  $\delta = 16$  and  $58$  ppm could be attributed to the ethoxy group as originated from the unhydrolyzed silicon precursors or/and formed during the solvent extraction process.<sup>20</sup> It is notable that the peak intensity of the  $^{13}\text{C}$  NMR spectrum from material SH-MON@MS is remarkably lower than that of SH-MONs due to the relatively decreased content of organosilica in the core-shell nanoparticle. Carbon signals of CTAB surfactant were not observable in the spectra, confirming complete removal of the template, which was in good agreement with the elemental analysis result. The  $^{29}\text{Si}$  CP MAS NMR

spectrum of SH-MONs showed two peaks derived from T<sup>2</sup> (RSi(OSi)<sub>2</sub>(OH),  $\delta = -58$  ppm) and T<sup>3</sup> (RSi(OSi)<sub>3</sub>,  $\delta = -65$  ppm)<sup>18</sup> (Figure 5.3b), but for SH-MON@MS, except from the characteristic silicon species T<sup>2</sup> and T<sup>3</sup> from the organosilica framework, silicon species Q<sup>n</sup> (n = 4, 3, 2) corresponding to Q<sup>4</sup> (Si(OSi)<sub>4</sub>,  $\delta = -111$  ppm), Q<sup>3</sup> (Si(OSi)<sub>3</sub>(OH),  $\delta = -101$  ppm) and Q<sup>2</sup> (Si(OSi)<sub>2</sub>(OH)<sub>2</sub>,  $\delta = -91$  ppm) assignable to the inorganic silica framework were observed, further corroborating the existence of an inorganic silica shell.<sup>19</sup>

On the basis of above-mentioned characterizations, the SH-MON@MS core-shell nanoparticles with hierarchical pore sizes of 1.5 and 5.0 nm in the core and shell have been successfully synthesized. Crucially, the distinct composition of a thiol group-functionalized mesoporous organosilica core and pure mesoporous silica shell makes such SH-MON@MS a promising support material for loading of metal nanoparticles and hence to prepare metal-based heterogeneous catalysts. Herein, Au nanoparticles were loaded into the core domain of SH-MON@MS by applying the reaction of HAuCl<sub>4</sub> with the thiol groups to form a Au(I)-thiolate complex,<sup>21,22</sup> and subsequent reduction with NaBH<sub>4</sub> to generate metallic Au nanoparticles. Accordingly, SH-MON@MS core-shell nanoparticles were suspended in a slightly yellowish HAuCl<sub>4</sub> solution and stirred for 6 h to form a colorless suspension, indicating the successful reaction between HAuCl<sub>4</sub> and the thiol groups. Upon addition of a NaBH<sub>4</sub>-ethanol solution, the color of the nanoparticles changed to grey, confirming the formation of metallic Au nanoparticles stabilized by thiol groups inside the mesochannels. TEM and SEM images showed that the core-shell structure and the surface morphology were not affected by the Au loading (Figure 5.7a and b). Any isolated Au nanoparticles could not be observed in the shell. An EDX line scanning of a single Au/SH-MON@MS revealed the composition difference between the core and shell domains (Figure 5.7c and d). While the elements Si and O distribute over the entire nanoparticle, Au, C and S are located/reside only in the core domain. Nitrogen physisorption analysis of Au/SH-MON@MS showed that the core pore size slightly decreased and the shell pore size remained unchanged (Figure 5.8), which is in good agreement with the TEM/SEM measurements and the EDX line scanning results, confirming that the loading of Au nanoparticles was exclusively occurred in the core. Compared to SH-MON@MS, the specific BET surface area and the pore volume of Au/SH-MON@MS decreased to 788 m<sup>2</sup> g<sup>-1</sup> and 0.95 cm<sup>3</sup> g<sup>-1</sup>, respectively. Both the low-angle and wide-angle PXRD patterns for Au/SH-MON@MS showed similar diffraction peaks as that of SH-MON@MS (Figure 5.9 and 5.10), due to that such ultrasmall-sized Au nanoparticles as well as a very low content can be hardly monitored by X-ray diffraction. The interconnected pore structure of Au/SH-MON@MS with pore sizes of 1.4 and 5.0 nm in the core and shell, the high surface area, and the large pore volume are beneficial for the diffusion of reactant and product, proposing Au/SH-MON@MS as an efficient nanocatalyst.



**Figure 5.7** (a) TEM and (b) SEM images of Au/Si-MON@MS, (c, d) EDX line scanning profile for a single Au/Si-MON@MS nanoparticle.

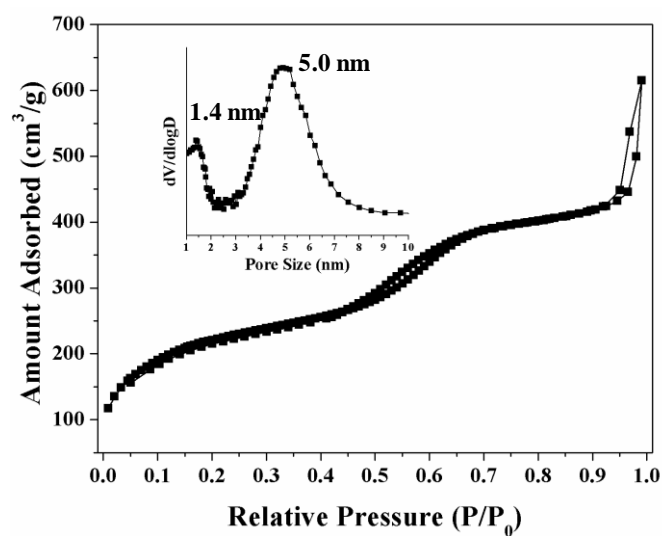


**Figure 5.8** Nitrogen physisorption isotherm of Au/Si-MON@MS, the inset is the BJH pore size distribution.

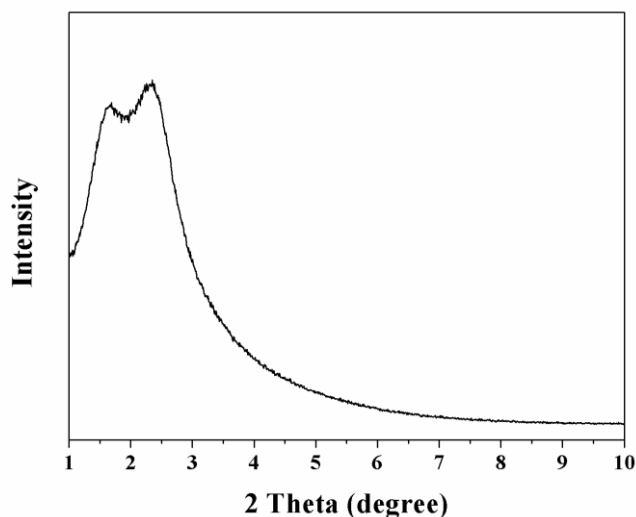


**Figure 5.9** Low-angle PXRD pattern of Au/SO-MON@MS.

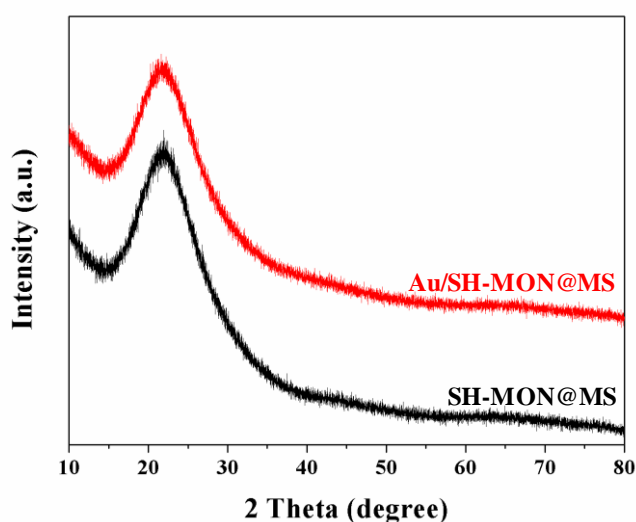


**Figure 5.10** Wide-angle PXRD patterns of Au/SO-MON@MS and SO-MON@MS.

To evaluate the catalytic activity of Au/SO-MON@MS, the catalytic reduction of 4-nitrophenol (4-NP) with NaBH<sub>4</sub> to 4-aminophenol (4-AP) in aqueous solution was chosen as a model reaction. The reduction of harmful 4-NP into less toxic 4-AP by noble metal-based nanocatalysts is regarded as an efficient, green, and environmentally benign method.<sup>23-25</sup> The colour of the 4-NP solution changed from light yellow into bright yellow after the addition of NaBH<sub>4</sub>, implying the deprotonation of 4-NP in the alkaline solution. The bright yellow color of the reaction solution gradually faded in the presence of Au/SO-MON@MS. With increasing reaction time, the corresponding characteristic absorbance peak of 4-NP at 400 nm in the UV-Vis spectrum decreased (Figure 5.11a). Meanwhile, the absorbance of deprotonated 4-AP at 233 nm gradually increased, indicating the reduction of 4-NP to 4-AP. The conversion of 4-NP reached to 98% after 11 min. As an excessive amount of NaBH<sub>4</sub> was used, the reaction kinetic of the reduction of 4-NP could be considered as pseudo-first-order. Figure 5.6b exhibits the plot of  $\ln(C_t/C_0)$  versus reaction time, where  $C_t$  and  $C_0$  represent the concentrations of 4-

NP at the defined and initial time, respectively. The kinetic constant of the reaction was determined by the slope of fitted plot as  $0.39 \text{ min}^{-1}$ . It is important to note that when the same amount of SH-MON@MS was added into an otherwise identical reaction solution, the absorbance at 400 nm didn't show any changes (Figure 5.11b), confirming that the loaded Au NPs acted as a catalyst for this reaction. After the catalytic reaction, the Au/SH-MON@MS showed a rough surface due to the degradation of the mesoporous silica shell in the reaction solution (Figure 5.12a and b). Furthermore, large aggregated Au nanoparticles were also observed, implying that the interaction between Au nanoparticles and SH-MON@MS was not as strong to prevent the Au nanoparticles from aggregation of during the reaction.

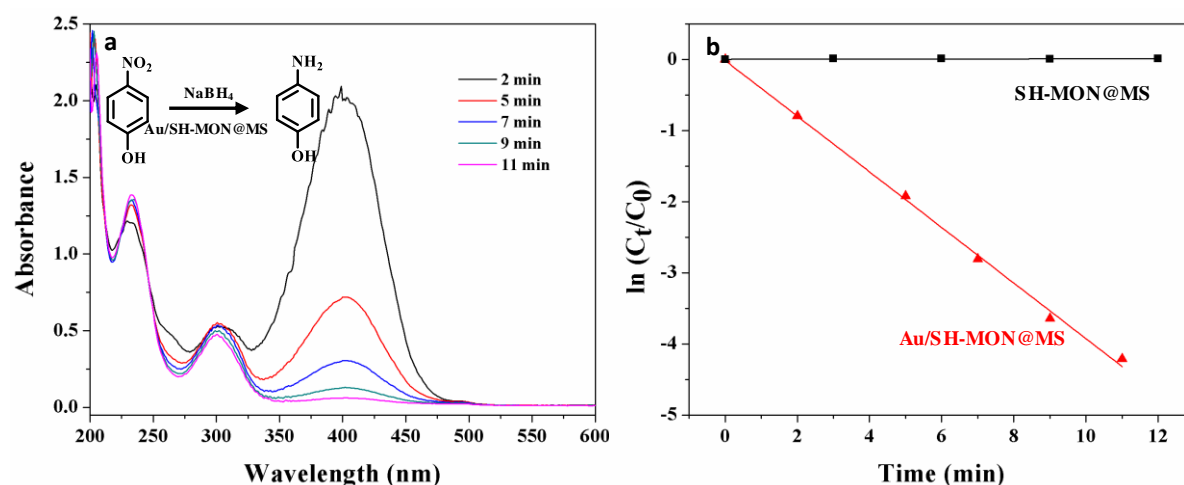


**Figure 5.11** Reduction of 4-nitrophenol to 4-aminophenol catalysed by Au/SH-MON@MS: (a) UV-Vis spectra of the reaction solution at different reaction times, (b) the kinetic plots of  $\ln(C_t/C_0)$  versus the reaction time in the presence of SH-MON@MS and Au/SH-MON@MS.

The aerobic oxidation of benzyl alcohol to benzaldehyde in toluene was chosen as a probe reaction to investigate the catalytic activity of Au/SH-MON@MS in an organic solvent. The reaction of benzyl alcohol to benzaldehyde is an environmentally friendly transformation under conditions using atmospheric oxygen as the sole oxidant.<sup>9,10</sup> The produced benzaldehyde can be used as a high-value chemical for many industrial applications. Running the reaction at 90 °C for 12 h, Au/SH-MON@MS exhibited an excellent performance with a high conversion of benzyl alcohol (95%) and high selectivity for benzaldehyde (96%) (Figure 5.13). Next, the recycling and re-use of this heterogeneous catalyst was collected examined. While the conversion of benzyl alcohol dropped to 60% and 19% in the second and third run, respectively, the selectivity for benzaldehyde was kept at about 96% in each cycle (Figure 5.13). The Au/SH-MON@MS catalyst collected after 3 cycles was analyzed by SEM and TEM, showing a degraded mesoporous silica shell and slightly aggregated Au nanoparticles (Figure 5.12c and d). During the catalytic reaction, the aggregation of Au nanoparticles and degradation of the mesoporous silica shell greatly reduced the active sites and thus decreased the catalytic activity, further confirming the importance of highly active and small-size MNPs as well as a protective mesoporous silica shell.



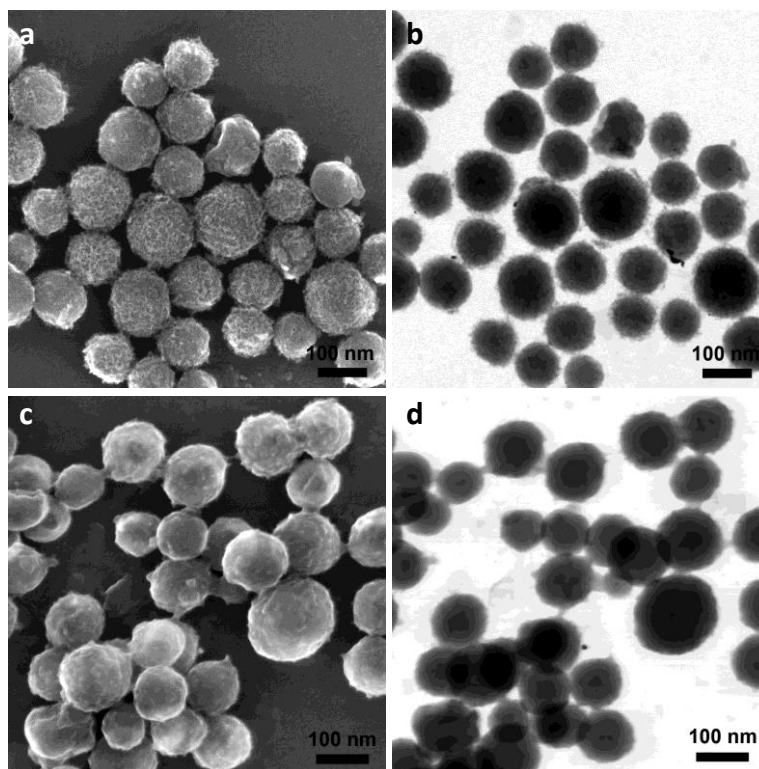


**Figure 5.12** TEM and SEM images of Au/SH-MON@MS after the catalytic reduction of 4-NP to 4-AP (a, b), and the catalytic oxidation of benzyl alcohol (c, d).

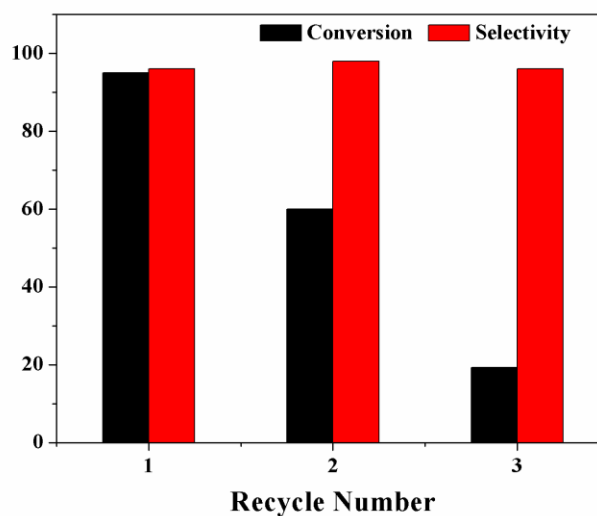


**Figure 5.13** Catalytic performance of Au/SH-MON@MS in the catalytic oxidation of benzyl alcohol after twofold recycling.

## 5.4 Conclusions

Hierarchically structured core-shell nanoparticles consisting of a thiol group-functionalized mesoporous organosilica as the core and mesoporous silica as the shell (SH-MON@MS) have been prepared via a two-step process. The obtained monodisperse SH-MON@MS feature an average particle size of ca. 130 nm with a core size of ca. 100 nm and a shell thickness of ca. 15 nm. The large shell pores of 5.0 nm diameter gave efficient access to the micropore structure

of thiol-functionalized core, and hence allowed for an effective loading with ultra-small gold nanoparticles in the core domain. The 5.0 nm-sized shell mesopores of the resultant Au/SH-MON@MS material also ensured efficient substrate diffusion to the catalytically active gold nanoparticles. Such Au/SH-MON@MS revealed good performance in the catalytic reduction of 4-nitrophenol to 4-aminophenol with NaBH<sub>4</sub>, and high conversion and selectivity in the aerobic oxidation of benzyl alcohol to benzaldehyde. However, degradation of the “thin” mesoporous silica shell and aggregation of the loaded Au nanoparticles greatly affected the active sites and hence the catalytic activity, as shown by a recycling/re-use study. The recycling properties of catalyst Au/SH-MON@MS might be further improved by optimizing the shell structure such as by fine-tuning the shell thickness and pore configuration/size and surface modification.

## 5.5 References

1. D. M. Vriezema, M. Comellas Aragonès, J. A. A. W. Elemans, J. J. L. M. Cornelissen, A. E. Rowan and R. J. M. Nolte, *Chem. Rev.*, **2005**, 105, 1445-1490.
2. R. J. R. W. Peters, I. Louzao and J. C. M. van Hest, *Chem. Sci.*, **2012**, 3, 335-342.
3. M. B. Gawande, A. Goswami, T. Asefa, H. Guo, A. V. Biradar, D.-L. Peng, R. Zboril and R. S. Varma, *Chem. Soc. Rev.*, **2015**, 44, 7540-7590.
4. W. Li and D. Zhao, *Adv. Mater.*, **2013**, 25, 142-149.
5. J. Liu, S. Z. Qiao, Q. H. Hu and G. Q. Lu, *Small*, **2011**, 7, 425-443.
6. S. H. Joo, J. Y. Park, C.-K. Tsung, Y. Yamada, P. Yang and G. A. Somorjai, *Nat. Mater.*, **2008**, 8, 126.
7. J. Chen, R. Zhang, L. Han, B. Tu and D. Zhao, *Nano Res.*, **2013**, 6, 871-879.
8. L. Han, H. Wei, B. Tu and D. Zhao, *Chem. Commun.*, **2011**, 47, 8536-8538.
9. S. Zhang, A. Han, Y. Zhai, J. Zhang, W.-C. Cheong, D. Wang and Y. Li, *Chem. Commun.*, **2017**, 53, 9490-9493.
10. Y. Yang, M. Ambroggi, H. Kirmse, Y. Men, M. Antonietti and J. Yuan, *Chem. Mater.*, **2015**, 27, 127-132.
11. B. Xi, Y. C. Tan and H. C. Zeng, *Chem. Mater.*, **2016**, 28, 326-336.
12. L. Chen, J. Hu and R. Richards, *J. Am. Chem. Soc.*, **2009**, 131, 914-915.
13. E. Le Roux, Y. Liang, M. P. Storz and R. Anwender, *J. Am. Chem. Soc.*, **2010**, 132, 16368-16371.
14. D. Shen, J. Yang, X. Li, L. Zhou, R. Zhang, W. Li, L. Chen, R. Wang, F. Zhang and D. Zhao, *Nano Lett.*, **2014**, 14, 923-932.
15. Q. Yue, J. Li, W. Luo, Y. Zhang, A. A. Elzatahry, X. Wang, C. Wang, W. Li, X. Cheng, A. Alghamdi, A. M. Abdullah, Y. Deng and D. Zhao, *J. Am. Chem. Soc.*, **2015**, 137, 13282-13289.
16. L. Luo, Y. Liang, E. S. Erichsen and R. Anwender, *Chem. Eur. J.*, DOI: 10.1002/chem.201800135.
17. T. M. Suzuki, T. Nakamura, E. Sudo, Y. Akimoto and K. Yano, *Microporous Mesoporous Mater.*, **2008**, 111, 350-358.
18. J. Croissant, X. Cattoën, M. W. C. Man, A. Gallud, L. Raehm, P. Trens, M. Maynadier and J.-O. Durand, *Adv. Mater.*, **2014**, 26, 6174-6180.
19. J. Liu, H. Q. Yang, F. Kleitz, Z. G. Chen, T. Yang, E. Strounina, G. Q. Lu and S. Z. Qiao, *Adv. Funct. Mater.*, **2012**, 22, 591-599.
20. W. Guo, F. Kleitz, K. Cho and R. Ryoo, *J. Mater. Chem.*, **2010**, 20, 8257-8265.
21. P. Wu, P. Bai, Z. Lei, K. P. Loh and X. S. Zhao, *Microporous Mesoporous Mater.*, **2011**, 141, 222-230.
22. Y. X. Zhang and H. C. Zeng, *Adv. Mater.*, **2009**, 21, 4962-4965.

23. T. Yang, L. Wei, L. Jing, J. Liang, X. Zhang, M. Tang, M. J. Monteiro, Y. Chen, Y. Wang, S. Gu, D. Zhao, H. Yang, J. Liu and G. Q. M. Lu, *Angew. Chem. Int. Ed.*, **2017**, 56, 8459-8463.
24. J. G. Kim, A. Kumar, S. J. Lee, J. Kim, D.-G. Lee, T. Kwon, S. H. Cho and I. S. Lee, *Chem. Mater.*, **2017**, 29, 7785-7793.
25. X. Du, C. Zhao, Y. Luan, C. Zhang, M. Jaroniec, H. Huang, X. Zhang and S.-Z. Qiao, *J. Mater. Chem. A*, **2017**, 5, 21560-21569.



## 6 Appendix

### 6.1 Publications

**Leilei Luo**, Yucang Liang, Egil Sev. Erichsen and Reiner Anwander, Monodisperse Mesoporous Silica Nanoparticles of Distinct Topology, *Journal of Colloid and Interface Science*, 2017, 495, 84-93.

**Leilei Luo**, Yucang Liang, Egil Sev. Erichsen and Reiner Anwander, Hierarchical Mesoporous Organosilica/Silica Core-Shell Nanoparticles Capable of Controlled Fungicide Release, *Chemistry-a European Journal*, 2018, 24, 7200-7209.

**Leilei Luo**, Yucang Liang, Thomas Chassé and Reiner Anwander, Ultrafast Myoglobin Adsorption into Double-Shelled Hollow Mesoporous Silica Nanospheres, *Particle & Particle Systems Characterization*, submitted.

**Leilei Luo**, Lorenz Bock, Yucang Liang and Reiner Anwander, Gold-loaded Mesoporous Organosilica-Silica Core-Shell Nanoparticles as Catalytic Nanoreactors, *manuscript, to be submitted*.

Carla S. Lorenz, Anna-J. Wicht, Leyla Guluzada, **Leilei Luo**, Leonie Jager, Barbara Crone, Uwe Karst, Rita Triebkorn, Yucang Liang, Reiner Anwander, Stefan B. Haderlein, Carolin Huhn and Heinz-R. Köhler, Nano-sized Al<sub>2</sub>O<sub>3</sub> reduces acute toxic effects of thiacloprid on the non-biting midge *Chironomus riparius*, *PLOS One*, DOI: 10.1371/journal.pone.0179786.

### 6.2 Presentations

#### 6.2.1 Poster Presentation

**Leilei Luo**, Leyla Guluzada, Carla S. Lorenz, Yucang Liang, Stefan B. Haderlein, Heinz-R. Köhler and Reiner Anwander, Al<sub>2</sub>O<sub>3</sub> Nanoparticles: Performance in the Sorption of Pesticides and Effects on Aquatic Invertebrates, Jahrestagung des SETAC GLB, September 5-8, 2016, Tübingen, Germany.

**Leilei Luo**, Yucang Liang, Egil Severin Erichsen and Reiner Anwander, One-pot Synthesis of Hierarchically Structured Mesoporous Silica Core-Shell Nanoparticles with Organosilica Core and Inorganic Silica Shell for Controlled Release, 8<sup>th</sup> International Symposium Nanoporous Materials (NANO-8), July 9-12, 2017, Ottawa, Canada.

Elisabeth Früh, **Leilei Luo**, Yucang Liang, Leyla Guluzada, Reiner Anwander, Stefan B. Haderlein, Sandra Dietz, Effect of Particle-associated Fungicides, Jahrestagung des SETAC GLB, September 5-8, 2016, Tübingen, Germany.

Carla S. Lorenz, Leonie Jäger, Leyla Guluzada, **Leilei Luo**, Yucang Liang, Reiner Anwander, Stefan B. Haderlein and Heinz R. Köhler, Effect of Al<sub>2</sub>O<sub>3</sub> Nanoparticles on the Toxicity of the Neonicotinoid Insecticide Thiacloprid, Jahrestagung des SETAC GLB, September 7-10, 2015, Zürich, Switzerland.

### **6.2.2 Oral Presentation**

**Leilei Luo**, One-pot Synthesis of Hierarchical Mesoporous Core-Shell Nanoparticles with Organosilica Core and Inorganic Silica Shell, 2017 CGCA South Workshop, October 21, 2017, Würzburg, Germany.

## 6.3 Curriculum Vitae

### Personal Information

Name: Luo, Leilei  
Gender: Male  
Date of Birth: September 10, 1988  
Place of Birth: Wuhu, Anhui Province, P. R. China  
Nationality: Chinese

### Education

01/2014-07/2018 PhD study, Institute of Inorganic Chemistry, Department of Chemistry, Faculty of Science, Eberhard Karls Universität Tübingen, Germany  
07/2012-10/2013 PhD application phase  
09/2009-06/2012 Master of Science in Physical Chemistry, Nanjing University, Nanjing, P. R. China  
09/2005-06/2009 Bachelor of Science in Chemistry, Anhui Normal University, Wuhu, P. R. China

### Awards and Scholarships

09/2008 Excellent student scholarship, Anhui Normal University  
09/2011 Wenruo Jiang scholarship, Nanjing University  
06/2012 Honar of excellent graduate student, Nanjing University

### Language Skills

Mandarin (Mother language); English (Fluent); German (Basic)

